Azinium and Azolium Salts as Fluorometric/Colorimetric Chemosensors

THESIS

Submitted in partial fulfillment of the requirements for the degree of

DOCTOR OF PHILOSOPHY

by

PRAGYA

ID. NO. 2019PHXF0013P

Under the supervision of

Prof. BHARTI KHUNGAR

BIRLA INSTITUTE OF TECHNOLOGY AND SCIENCE, PILANI
PILANI CAMPUS, RAJASTHAN, INDIA
2024

BIRLA INSTITUTE OF TECHNOLOGY AND SCIENCE PILANI (RAJASTHAN)

CERTIFICATE

This is to certify that the thesis entitled **"Azinium and Azolium Salts as Fluorometric/Colorimetric Chemosensors"** submitted by **Pragya**, ID No. **2019PHXF0013P** for the award of Ph. D. degree of the institute embodies the original work done by her under my supervision.

Signature in full of the Supervisor:
Name in capital block letters: **BHARTI KHUNGAR**
Designation: Professor

Date: 23/10/2024

Dedicated to

Maa - Papa

&

Bhai...

TABLE OF CONTENTS

Acknowledgements

At the beginning, I dedicate this work to Mahadev & Mata Rani, whose grace has bestowed upon me the strength, knowledge, and ability to undertake and complete this journey of academic pursuit. The divine wisdom has illuminated my path and granted me strength and perseverance to overcome challenges along the way. I am deeply grateful for the unwavering support, guidance, and blessings of those who accompanied me on this journey. Their assistance and encouragement have helped me directly or indirectly to achieve this milestone of my life.

First of all, I am extremely thankful to my Supervisor Prof. Bharti Khungar. In the journey of academic pursuit, she been the guiding star that illuminated my path through the darkest of nights. Her unwavering belief in my abilities, even when I faltered, had been a source of profound inspiration. The tireless dedication to my growth and success had been a testament to her exceptional mentorship. With each milestone reached, I have felt the weight of her encouragement, the warmth of support, and the depth of investment in my journey. Her wisdom, patience, and unwavering faith in my potential have propelled me forward when doubts threatened me. As I pen these words, I am overwhelmed with gratitude for the countless hours she had devoted to shaping my academic pursuits and nurturing my intellectual curiosity. Her guidance has not only enriched this thesis but has also left an indelible mark on my scholarly endeavours and personal growth. I am forever indebted for her your unwavering support, guidance, and belief in me.

I would like to express my gratitude to the former and current Vice Chancellor, Birla Institute of Technology & Science Pilani, Director, Dean, and Associate Dean, AGSRD, BITS Pilani Pilani Campus for granting me the opportunity to pursue my PhD studies and for providing the required resources and support. I would like to express my sincere gratitude to the office personnel of AGSRD for their invaluable secretarial assistance in ensuring the timely submission of the numerous evaluation documents. I would like to express my gratitude to the former and current Head of the Department, DRC, Chemistry, BITS Pilani, Pilani Campus for their official support and encouragement. I would like to express my gratitude to BITS Pilani for granting me an Institute fellowship during my doctoral program. Furthermore, I would like to express our sincere gratitude to DST-FIST for their provision of instruments.

I wish to acknowledge Prof. R. Krishnan from Department of Chemistry, BITS Pilani, Hyderabad Campus for providing us single X-ray crystal analysis. I would also like to express my gratitude to Prof. Prabhat Nath Jha and Sonali Jain from the Department of Biological Sciences at BITS Pilani, Pilani Campus, for performing biological studies. I am grateful to the

members of my Doctoral Advisory Committee, Prof. Ajay K. Sah and Prof. Madhushree Sarkar for their great cooperation during my Ph.D. Their insightful advice for improving my proposal and seminar at the outset greatly influenced my decision to start my research. I thank them for their unceasing feedback and edits that have helped me polish my thesis.

I am profoundly thankful for the cooperation and affection extended by all the respected teachers who have played a pivotal role in shaping my academic journey. I extend my heartfelt gratitude to all the esteemed professors for their unwavering support and guidance: Prof. S. C. Sivasubramanian, Prof. Dalip Kumar, Prof. R. K. Roy, Prof. Indresh Kumar, Prof. Prashant Uday Manohar, Prof. Saumi Ray, Prof. Inamur R. Laskar, Prof. Anil Kumar, Prof. Paritosh Shukla, Prof. Rajeev Sakhuja, Prof. Surojit Pande, Prof. Shamik Chakraborty, and Prof. Bibhas R. Sarkar, Prof. Mrinmoyee Basu, Prof. P. K. Jana, Prof. Avik Kumar Pati, Prof. Partha sarathi Addy, Prof. Satyajit Patra, Prof. Nitika Grover and Prof. Amrita Chakarborty. Thanks to all the office staff Mr. Soni, Mr. Virender Tomar, Mrs. Pushpalata, Mr. Ashok, Mr. Suresh of the Department for their help during PhD tenure. A special thanks to Mrs. Pushpa ji for her adoring support and care all the time during my PhD.

I am very much thankful to my respected secondary school teachers (Mahoday, R. N Jha Sir and Yadav Sir) for inculcating wisdom at my young age. I am highly grateful to my BSc college teacher Late Dr. Amrita Singh for supporting me in making me understand chemistry in a better way. Dr. Sr. M. Reema AC and Dr. Sr. Maria Tanisha AC (Patna Womens College) for shaping me into a better person in all aspects.

My special thanks to my group members Vaishali ma'am, Payal, Nidhi, and Antima for helping in my research work. A special thanks to Nitika for helping me in every situation. I am very thankful to my lab members, Santosh Sir, Vikki Sir, Anuvasita, and Parmisthi. Special thanks to seniors Amol Sir, Mahesh Sir, Prachi ma'am, Sonam ma'am, Dhritabrata Pal sir for giving me troubleshoots in my PhD. I am thankful to Vishal Sir, Vimal Sir, Myona ma'am, Bintu Sir, Pramod Sir, Saumona ma'am for their help and charming company during my PhD. Thanks to other research scholars from the dept. for their respect and care in my PhD.

A special thanks to my batch mates (Prakriti, Narshima, Prakash, Monika, Mamta, Divya) for their company during course-work and afterwards in my PhD. A special thanks to my other friends (Yadav Nagre, Ram Prasad Bhatt and Vishaka) for their well-wishing in my PhD. This academic journey won't be easy without Neha and Dhananjay (Trio of Wierdos) for their friendship and company. Their belief in me and willingness to offer both emotional support and valuable insights have been invaluable. I am deeply grateful to Shivani for her unwavering support, encouragement, and friendship throughout my doctoral journey. I am fortunate to have

such a remarkable friend by my side. A special thanks to Mr. Jayesh (Gujju Bhai) for his cherished companion and unwavering support. I would like to extend my thanks to Sushmita for being a supportive junior. A heartfelt gratitude to Ms. Sakshi Maan for endless memories. A special thanks to Ms. Disha, Mr. Somanth, Mr. Saurojit, Ms. Ritu, Mr. Divyanshu, and Mr. Prashant Tripathi for your generosity I deeply appreciate it. I also extend my gratitude to Ms. Manisha, Ms. Arzoo, Mr. Prakash, Ms. Sakshi, Mr. Ajeet, Ms. Priyanka, Mr. Atul, Mr. Imtiaz, Ms. Nandani, Ms. Sonika, Mr. Bharat, Ms. Karishma, Mr. Sumit, Ms. Heena, Mr. Prashant, Ms. Astha, Ms. Sakshi, Ms. Meenu, Ms. Amol, Ms. Subhangi, Ms. Shruti, Ms. Ritu, Ms. Pinky, Ms. Arpit, Ms. Nancy, Mr. Subhendu and Research Scholars of department of chemistry for their support. I extend my love and gratitude to Mr. Sumant and Mr. Prakash for their support in my PhD tenure. A special thanks Ms. Nishi Rani for always being my rock; your friendship means the world to me.

In deepest reverence, I dedicate this thesis to my beloved parents, Mr. Promod Kumar Singh and Mrs. Sandhya Singh. Their unwavering love has been the guiding force behind every step of my academic journey. From the earliest stages of my education to the culmination of this thesis, their boundless support, sacrifices, and belief in my abilities have been a constant source of strength. Their sacrifices, often unseen but deeply felt, have paved the path for my success. Their encouragement in times of doubt and their celebration of every achievement, no matter how small, have been the pillars on which I have leaned. Through their example, they have instilled in me the values of diligence, perseverance, and integrity. This thesis stands as a testament to their unwavering commitment and enduring love. To my parents, I owe everything. I thank them for being my guiding light, my champions, and my greatest inspiration. I personally thank my loving brother, Dr. Ishan Chandra for his utmost moral support, love and care in all the aspects of my life.

This doctoral journey won't be complete without the *Ashirward* of my grandparents, Late Harendra Singh, Late Sunaina Singh, Late Ram Kirat Singh and Late Girja Devi.

I am very thankful to my Masi's (Rekha Singh, Sulekha Singh, Poornima Singh, Nirupama Singh, Chitra Singh) and Mama's (Abhishek and Ajitesh) for their boundless dedication and for instilling in me the values of perseverance and resilience. A special thanks to my brothers (Bittu, Mithu, Akku, Nittu, Pumpum, Vivek, Mohak, Ansh and Chiku) and sister (Betu, Tutu and Piku) for being the best siblings.

Thanks to my Bade papa "Dr. N. K. P Singh" and Badi Maa "Aruna Singh" for their encouragement, guidance, and belief in me that have fuelled my aspirations and sustained me

through the challenges I am thankful to my Dr. Bhawani Chandra and Mr. Madhav Chandra (Bhaiya) and Dr. Vijeta Singh (Bhabhi) for their support during difficult times.

In humble gratitude, this thesis is dedicated to the Divine, whose presence has illuminated my path and granted me strength throughout this endeavour.

ABSTRACT

The thesis entitled "**Azinium and Azolium Salts as Fluorometric/Colorimetric Chemosensors**" deals with the synthesis and application of Azinium (pyrazinium and pyridinium) and Azolium (imidazolium) salts. These salts are structurally characterized and utilized for selective sensing of analytes. The synthesized chemosensors are also used in different applications such as cell imaging, latent fingerprinting, development of microfluidic channels, smartphone-based colorimetric read-out, and real soil, water and urine sample analysis. The thesis is divided into five chapters.

Chapter 1 of the thesis describes an overview of the fundamentals of chemosensing, along with a summary of sensing mechanisms such as Photoinduced electron transfer (PET), Excited state intramolecular electron transfer (ESIPT), Ground state charge transfer complex formation (GSC) etc. The literature for pyrazine, pyridinium and imidazolium-based chemosensors and their photophysical properties, and sensing mechanisms have been incorporated in this chapter.

Chapter 2 of the thesis includes detailed information about the materials, methods, and instruments used during the research work.

Chapter 3 of the thesis discusses the development of pyrazinium salts as fluorometric/colorimetric chemosensors. This chapter is divided into three sections.

Section 3A describes the synthesis of a thiophene-appended pyrazinium salt, **BTPyz** and its potential application for selective and sensitive detection of TNP in aqueous medium by fluorescence turn-off mechanism. The quenching efficiency, quenching constant and limit of detection is found to be 93.4%, 3.8×10^{-4} M, and 11.6 nM, respectively. The synthesized chemosensor is also employed for TNP detection on paper strips, real water and soil samples.

Section 3B presents the synthesis and characterization of a benzene-appended pyrazinium salt, **BPPyz**. **BPPyz** is highly selective toward TNP as indicated by the decrease in fluorescence intensity, it also exhibits a quick response for sulfite anion with the naked eye through a colour change brought by a small hypsochromic shift in absorption spectra. Colorimetric response of **BPPyz** for sulfite is monitored using the built-in camera of a smartphone.

Section 3C discusses the synthesis and characterization of pyrene-appended pyrazinium salt, **MPyPyz** for the detection of TNP and nitrite ions. The chemosensor shows fluorescence turn-off in the presence of both the analytes

Chapter 4 describes the development of Schiff base-appended pyridinium- and imidazolium-salts as fluorometric/colorimetric chemosensors and is divided into two parts.

Section 4A deals with the synthesis and characterization of a Schiff base-appended pyridinium-salt, **BzPySB**. The detailed photophysical properties of this chemosensor are investigated for

the selective and sensitive turn-on fluorescence response for Al^{3+} in a pure aqueous medium. Theoretical studies provide additional support to the experimental data. This pyridinium salt is applied for cell imaging in plants and MCF-7 cells. Furthermore, a portable film for the detection of Al^{3+} in water is successfully developed and the solid-state luminescence property of **BzPySB** is utilized for latent fingerprinting.

Section 4B describes the synthesis and characterization of Schiff base-appended imidazolium salt (**IsImSB**) and its application as a colorimetric chemosensor for copper ion detection in a pure aqueous medium. Copper ion detection is also performed in real water, urine samples and on filter paper strips. This chapter explains the development of microfluidic paper-based analytical devices (μPADs), as a simple colorimetric sensor for selective recognition of Cu^{2+}.

Chapter 5 summarizes the overall thesis work conducted and the future scope of the research work.

LIST OF FIGURES

List of Tables

List of Abbreviations and Symbols

Abbreviation/Symbol	Description
η	Refractive index
σ	Standard deviation
N	Frequency
°C	Degree centigrade
Å	Angstrom
K	Kelvin
T	Temperature
Φ	Quantum yield
E	Energy
F	Oscillator strength
%	Percentage
K_B	Binding constant
B3LYP	Becke three-parameter exchange functional and Lee-Yang-Parr correlation functional
J	Coupling constant
Calcd.	Calculated
$CHCl_3$	Chloroform
CHEF	Chelation induced enhanced fluorescence
Cl-DNB	1-Chloro 2,4-dinitrobenzene
$CDCl_3$	Deuterated chloroform
D	Doublet
dd	Doublet of doublet
DMF	N,N-Dimethylformamide
DCM	Dichloromethane
DL	Detection limit
DMSO	Dimethylsulfoxide
DMSO-d_6	Deuterated dimethylsulfoxide
DFT	Density functional theory
DNP	2,4-Dinitrophenol
3,4-DNT	3,4-Dinitrotoluene
DNBA	3,5-Dinitrobenzoic acid
3,5-DNT	3,5-Dinitrotoluene

λ_{em}	Emission wavelength
λ_{ex}	Excitation wavelength
Equiv.	Equivalent
ESI	Electron spray ionization
ESIPT	Excited state intramolecular proton transfer
EtOH	Ethanol
EtOAc	Ethyl acetate
EDTA	Ethylenediaminetetraacetic Acid
Et	Ethyl
R_0	Förster radius
FTIR	Fourier-transform infrared spectroscopy
Glu	Glutamate
GSC	Ground state complex
h	Hour
HOMO	Highest occupied molecular orbital
HRMS	High-resolution mass spectrometry
HEPES	4-(2-Hydroxyethyl)-1-piperazineethanesulfonic acid
Hz	Hertz
ICT	Internal charge transfer
IEF-PCM	Integral equation formalism- polarizable continuum model
τ	Lifetime
LUMO	Lowest unoccupied molecular orbital
LC-MS	Liquid chromatography-mass spectrometry
λ_{max}	Maximum wavelength
M	Molar
m	Multiplet
mmol	Millimole
m	Meta
μM	Micromolar
mp	Melting point
MW	Microwave

mg	Milligram
MHz	Mega hertz
min	Minute
mL	Milliliter
MeOH	Methanol
NAC	Nitroaromatic compound
NB	Nitrobenzoic acid
nm	Nanometer
nM	Nanomolar
k_{nr}	Non-radiative decay rate constant
NM	Nitromethane
NMR	Nuclear magnetic resonance spectroscopy
NMP	N-Methyl-2-pyrrolidone
NBA	4-Nitrobenzoic acid
NP	4-Nitrophenol
NT	4-Nitrotoluene
NB	Nitrobenzene
NM	Nitromethane
o	Ortho
ORTEP	Oak ridge thermal ellipsoid plot
PA	Picric acid
PET	Photo-induced electron transfer
ppb	Parts per billion
ppt	Parts per trillion
ppm	Parts per million
PET	Photoinduced electron transfer
Q-TOF	Quadrupole time-of-flight
q	Quartet
k_r	Radiative decay rate constant
RET	Resonance energy transfer
r.t.	Room temperature
J_λ	Spectral overlap integral
K_{sv}	Stern-Volmer quenching constant
s	Singlet

SDS	Sodium dodecyl sulfate
S-V	Stern-Volmer
TLC	Thin layer chromatography
TMS	Tetramethylsilane
Ts	Toluenesulfonyl
t	Triplet
t	Tertiary
TCSPC	Time correlated single photon counting
TFA	Trifluoroacetic acid
THF	Tetrahydrofuran
TNP	2,4,6-Trinitrophenol
TNP	2,4,6-Trinitrophenol
UV	Ultraviolet
v/v	Volume per volume
Vis	Visible
XRD	X-ray diffraction

Chapter 1

Introduction

Chapter 1

1.1 INTRODUCTION

1.1.1 Background of Chemical Sensing

Czarnick defines the chemosensor as a "molecule of abiotic origin that signals the presence of matter or energy.[1-2] It is a device that transforms chemical information obtained from a chemical reaction of the analyte or the physical property of a system into a detectable analytical signal. It operates by incorporating chemically selective sites to interact with specific analytes leading to various detectable changes.[3] These changes serve as signals that can be measured or correlated with the concentration of the analyte enabling both identification and determination of the substance. Compared with traditional analysis instruments, chemosensors are portable, simple to use, easily synthesized, and miniature in size which can deliver real-time application in the presence of a contaminant in soil, water, or other environmental samples.[4-6] Chemical sensors contain the following three basic functional units:

(a) Receptor: It binds to the targeted species and chemical information is transformed into a form of energy.

(b) Transducer: It transforms the energy carrying the chemical information into a useful analytical signal.

(c) Signaling or read-out unit: It reads and quantifies the binding event.[7-8]

According to the operating principles chemosensors can be classified into six types viz., optical, electrochemical, mass-sensitive, magnetic, thermometric, and other radiation-detecting type. Out of these, optical sensors are the chemosensors that use electromagnetic rays as a source of the signal to detect analytes in the UV-vis, IR and near-infrared regions.[9-11] These sensors are based on different optical principles like absorbance, reflectance, and luminescence as well as other optical properties like refractive index, fluorescence lifetime, and scattering of light. The optical sensor comprises a molecular binding site, a chromophore or fluorophore which when bound with an analyte changes the optical properties (absorption or fluorescence). Optical sensors offer numerous advantages over conventional sensors in terms of sensitivity, selectivity, and the ability to detect in wide variety of electromagnetic wavelengths.[12-14] Optical chemosensors are further classified into following two types (**Figure 1.1**).

(a) Colorimetric Chemosensors: The observation of color change has been utilized as a technique for sensor signal transduction for quite a long time due to the possibility of obtaining qualitative and quantitative data *via* the naked eye without referring to any complex techniques.[15-17] The core

of these sensors is the incorporation or involvement of signaling moiety which is a chromophore resulting in chromogenic response.[17] Colorimetric chemosensors rely on the transformation of chemical information into colour signals, visible to naked eye.

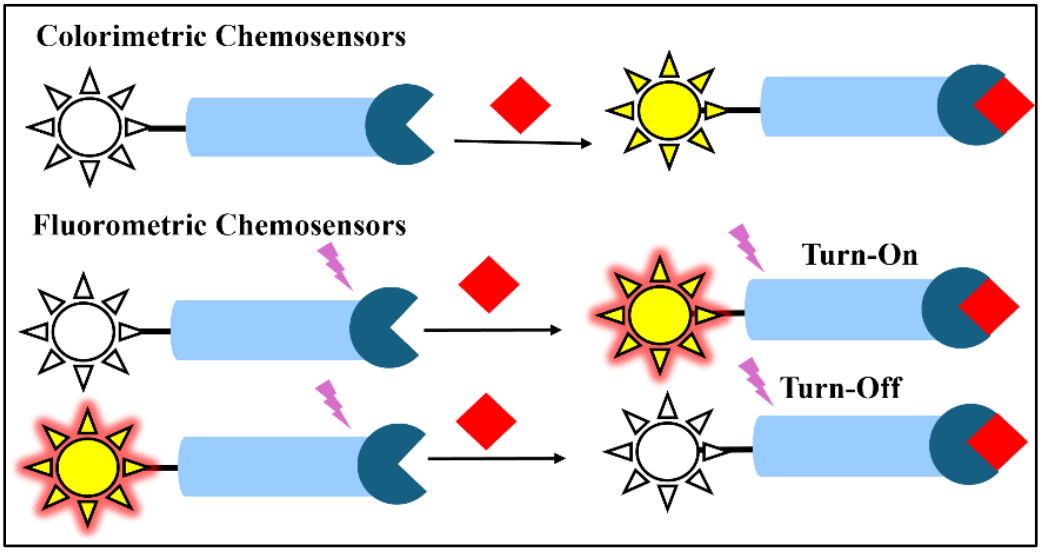

Figure 1.1: Schematic representation of optical chemosensors

Colorimetric sensors rely on changes in electron densities on the conjugated molecule to produce a shift in absorption band (bathochromic or hypsochromic) along with color change.The presence of conjugation in the system along with electron-donating and electron-withdrawing groups influences the absorption spectra of the molecule.[18-19] The decrease in the energy gap between the ground state and excited state of the molecule results in a bathochromic (red) shift, while increase leads to a hypsochromic (blue) shift. The introduction of electron-donating and electron-withdrawing groups affects the photophysical properties of the sensor.[19-20] When a cation binds to the electron-donating group, it reduces the donating capability of the donor group leading to a decrease in the conjugation of the system resulting in ligand-metal charge transfer (LMCT) causing a blue shift in the absorption band.[21] In contrast, metal ion binding to the electron-acceptor group enhances its electron-withdrawing character, and the absorption spectrum is red-shifted leading to the formation of MLCT.[22-23] This results in the excited state being more stable than the ground state, leading to a red shift in the absorption spectra.

(b) Fluorometric Chemosensors: Fluorescence is considered one of the most useful technologies for optical readout.[24-25] Fluorescence chemosensors are the molecules whose fluorescent properties change in response to the interaction with the analyte.[26-27] They have gained considerable attention

due to quick response time, sensitivity, straightforward performance, and real-time detection. A fluorescent chemosensor is developed by connecting a receptor (ionophore) to a fluorophore responsible for converting the recognition into the photophysical signal like fluorescence spectra, quantum yield, and lifetime.[28-29] The photophysical properties can be altered by binding a particular analyte to the receptor leading to a fluorescence signal with either an enhancement (turn-on) or quenching (turn-off) of fluorescence. In 1867, Goppelsroder reported the first fluorescent chemosensor to detect aluminum ions via formation of a morin chelate which was strongly fluorescent.

Fluorescence involves the transfer of electrons to a higher energy level when the molecule is electronically stimulated.[30-31] The excited state will eventually return to the lowest energy level through one of three processes: photochemical reaction, radiative decay or non-radiative decay. During a typical fluorescence process, an electron is excited from the highest occupied molecular orbital (HOMO) to the lowest unoccupied molecular orbital (LUMO) of the molecule, resulting in the formation of a singlet excited state.[32-33] The energy of the emitted radiation decreases as the excited state undergoes vibrational relaxation before emitting a photon. The decrease in energy of the emitted radiation from the absorbed radiation is observed as a red shift in the emission spectrum,[34] commonly known as the "Stokes shift".

1.1.2 Signaling Mechanisms for Chemosensor

Photophysical properties like changes in fluorescent intensity, emission spectra, and molecular decay life after interacting with an analyte involve different photophysical signaling mechanisms like Photoinduced Electron Transfer (PET), Intramolecular Charge Transfer (ICT), Fluorescence Resonance Energy Transfer (FRET), Ground State Complex (GSC) formation, Inner Filter Effect (IFE) and excimer/exciplex formation through different types of non-covalent interactions.[35-36] In addition to this other sensing mechanism such as Aggregation Caused Quenching (ACQ), Aggregation Induced Emission (AIE), Excited State Intramolecular Proton Transfer (ESIPT), C=N isomerization, have also been reported for the detection of analytes.

(a) Photoinduced electron transfer

A PET sensor absorbs energy, and the electron is promoted from the HOMO of the fluorophore to the LUMO. At the same time, the HOMO of the free receptor is at a higher level and facilitates PET from the HOMO of the free receptor to the HOMO of the fluorophore resulting in the blocking of emission transition or quenching of fluorescence. When an analyte binds with the receptor, the

redox potential of the receptor (donor) increases hence, the relevant HOMO is lowered than the HOMO of the fluorophore. Consequently, no PET occurs and hence there is fluorescent enhancement of chromophore[37-39] (**Figure 1.2a**).

(b) Ground-state complex (GSC)

The formation of a non-fluorescent compound between the analyte and the fluorophore before being excited forms a ground state complex (GSC). The newly formed compound exhibits unique photophysical properties, such as a noticeable absorption spectrum and the capability to undergo non-radiative decay[40-41] (**Figure 1.2b**). The fluorescence intensity in the GSC is determined by the concentration of the quencher, which can be calculated from the association constant (K_s).

$K_s = [F-Q]/[F][Q]$

where, $[F-Q]$ = concentration of GSC, [F] = concentration of flurophore, U = concentration of uncomplexed flurophore and [Q] = concentration of quencher

(c) Intramolecular Charge Transfer (ICT)/Photoinduced Charge Transfer (PCT)

ICT typically occurs in molecules with a D-π-A (Donor-π-Acceptor) or D-A structural arrangement. ICT-based probes undergo changes in electron density inside the recognition group when they interact with the intended analyte (**Figure 1.2c**). These changes can occur due to bond cleavage, substitution, or substrate coordination, resulting in the creation of a 'push-pull' system within the molecule.[42-44]

(d) Fluorescence Resonance Energy Transfer (FRET)

It is a distance-dependent physical phenomenon that occurs between the electronically excited states of two dissimilar fluorophores in which excited energy is transferred from a donor to an acceptor fluorophore through non-radiative dipole-dipole coupling (**Figure 1.2d**). According to Förster theory, fluorescence resonance energy transfer generally occurs by the following factors: (i) The donor fluorophore and acceptor fluorophore must be in close proximity (10–100 Å)[45-47] (ii) The emission spectrum of the donor fluorophore must overlap with the absorption spectrum of the acceptor fluorophore (iii) The relative orientation of the donor emission dipole moment and acceptor absorption moment must be parallel to each other.

(e) Excited-state intramolecular proton transfer

A photophysical phenomenon that occurs due to the presence of both proton donating-(OH or -NH_2) and accepting (carbonyl oxygen or imine nitrogen) groups that undergo excited-state intramolecular proton transfer (ESIPT) due to increased acidity/basicity. Upon excitation, the

protons migrate from the acidic side to the basic side, resulting in changes in the structure and electronic distribution of the chromophore.[48-50] The fluorophore exists in two tautomeric forms, one is stable in the ground state and the another in the excited state (**Figure 1.2e**).

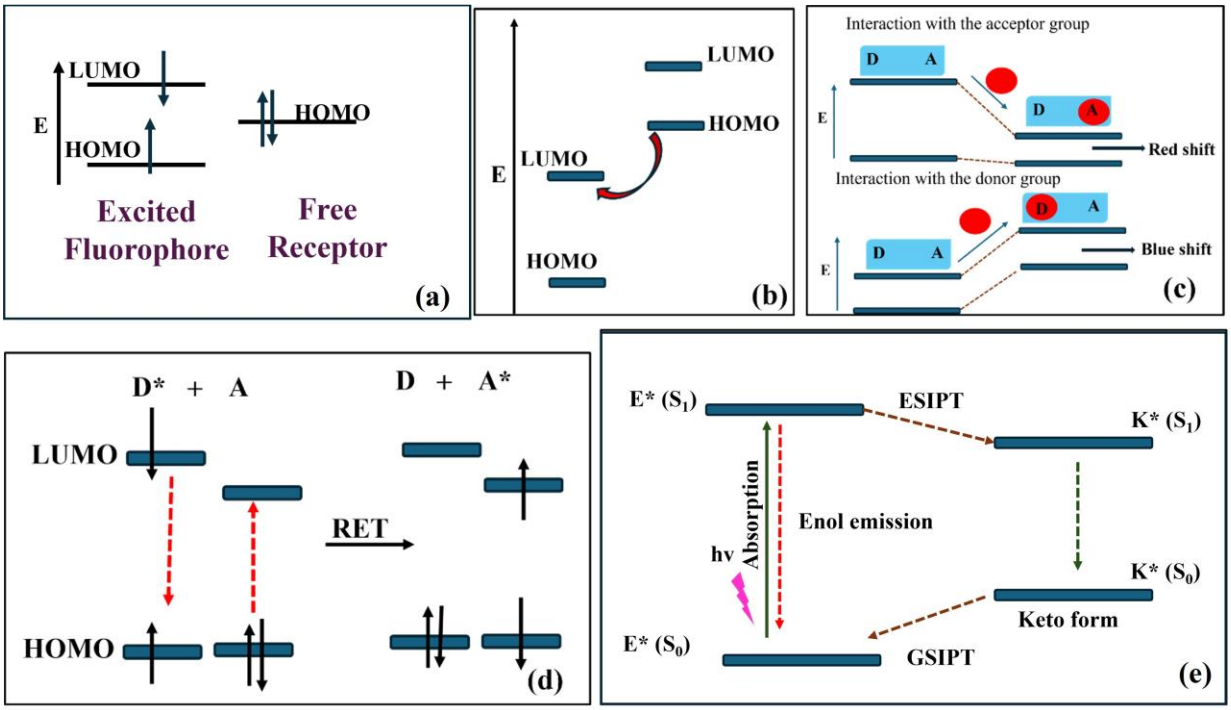

Figure 1.2: Schematic representation of (a) PET (b) GSC (c) ICT (d) RET (e) ESIPT signaling mechanisms

(f) C=N isomerization

This phenomenon investigates the non-fluorescent photophysical properties of conformational restricted compounds. Strong fluorescence can be observed in such compounds by inhibiting C=N bond isomerization *via.*, conformational restriction-induced coordination with a target analyte or rigidifying the structure *via* an intramolecular hydrogen bond leading to fluorescence enhancement[51-52] (**Figure 1.3a**).

(g) Chelation Enhanced Fluorescence (CHEF) and Chelation Enhanced Quenching (CHEQ)

This phenomenon accounts for the complexation of a metal ion resulting in chelation-enhanced fluorescence (CHEF), or chelation-enhanced quenching (CHEQ). CHEF typically results upon chelation of one of the ions that are not inherently quenching (non-redox active, closed shell, e.g., Zn^{2+}, Cd^{2+} and CHEQ is observed on chelation of an inherently quenching ion[53-54] e.g., Cu^{2+}, Hg^{2+}, Ni^{2+} (**Figure 1.3b**).

(h) Inner filter effect (IFE)

It is non-irradiation energy conversion model resulting from the absorption of the excitation and/or emission light by the absorber in the detection system. IFE is frequently regarded as an error in fluorometric analysis, and the attenuations are sometimes referred to as the primary or secondary inner filter effect because of the absorption of excitation or emission light.[55-57] The term "primary inner filter effect" (p-IFE) describes how different chromophores in a solution or matrix absorb excitation light, whereas the term "secondary inner filter effect" (s-IFE) describes how these same chromophores absorb emission (**Figure 1.3c**).

(i) Aggregation Caused Quenching (ACQ) and Aggregation Induced Emission (AIE)

Aggregation of classical fluorophore (polyaromatic carbons) quenches the light emission, this concentration quenching effect is called as aggregation caused quenching (ACQ). Aggregation induced emission (AIE) is the term used to describe the phenomenon where molecules emit more strongly when they are in an aggregated state compared to when they are in a solution state.[58-62] Various mechanisms have been proposed to explain AIE such as restriction of molecular motions (RIM), suppression of the charge-transfer (CT) state, excimer formation, conical intersection (CI), intramolecular planarization and twisted intramolecular charge transfer (TICT) (**Figure 1.3d**).

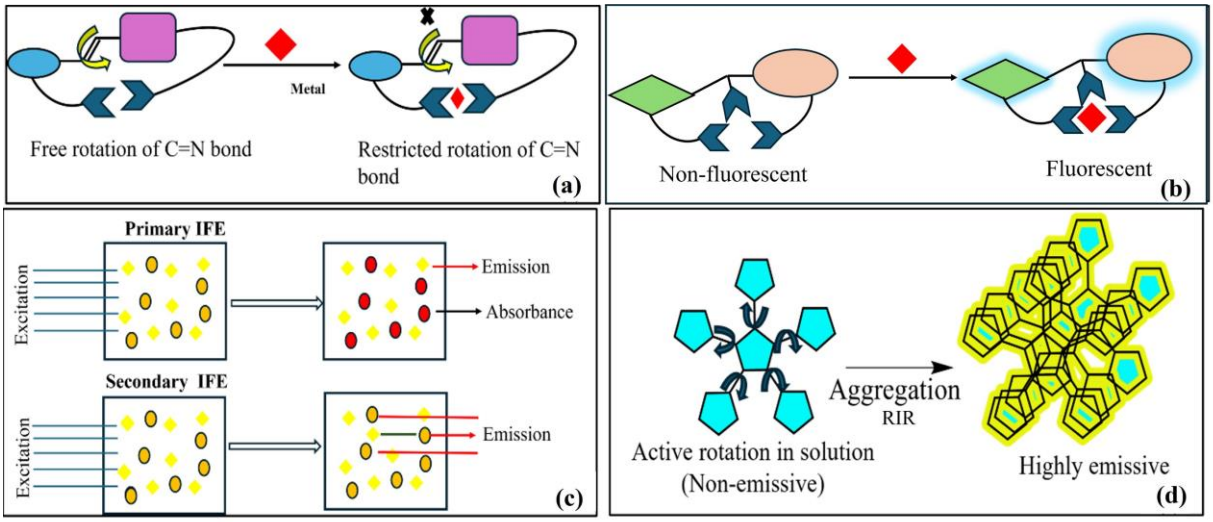

Figure 1.3: Schematic representation of (a) C=N Isomerization (b) CHEF (c) IFE (d) AIE signaling mechanisms

1.1.3 Quenching of fluorescence

The decrease in fluorescence intensity due to excited-state reactions, energy transfer, ground-state complex formation molecular rearrangements is referred to as fluorescence quenching.[63] There are mainly two types of quenching processes: (i) collisional or dynamic quenching and (ii) static quenching.

(a) Collisional quenching

Collisional quenching occurs when the excited-state fluorophore is deactivated upon contact with some other molecules in solution called quencher.[64-65] The decrease in intensity due to collisional quenching is described by Stern-Volmer equation:

$F/F_0 = 1 + K[Q] = 1 + k_q\tau_0\,[Q]$

where K = Stern-Volmer rate quenching constant, k_q = bimolecular quenching constant,

τ_0 = unquenched lifetime, and [Q] = quencher concentration.

The constant K mainly represents the sensitivity of the fluorophore to a quencher.[66-67] A diversity of molecules such as oxygen, halogens, amines, etc. can act as fluorescence quenchers. Quenching by heavy atoms occurs due to spin-orbit coupling and inter-system crossing to the triplet state. Collisional quenching also diminishes the lifetime of the fluorophore.[68]

(b) Static quenching

In a number of cases, the fluorophore can form a stable complex with a quencher. If this ground-state complex is non-fluorescent, then the fluorophore is said to be statically quenched.[69-70] In such cases, the dependence of the fluorescence as a function of the quencher concentration follows the relation:

$F/F_0 = 1 + K_a\,[Q]$

where K_a is the association constant of the complex, $[Q]$ = concenteration of quencher.

Static quenching will not decrease the lifetime of the sample as the fluorophores being uncomplexed are able to emit after excitation.[71]

1.2 CHEMOSESORS FOR ANALYTE DETECTION

From a physiological and economic perspective, the history of people and metals goes back centuries, with the majority of metals playing a substantial role in the advancement of civilization. The recognition and sensing of numerous ionic and neutral species that are biologically and environmentally important has emerged as a significant goal in the field of chemical sensors in

recent years.[72-73] Among the biologically relevant metal ions and anions, the role and toxicity of metal ions like mercury (Hg^{2+}), lead (Pb^{2+}), cadmium (Cd^{2+}), copper (Cu^{2+}), and nickel (Ni^{2+}) could cause a series of diseases like immune dysfunction, nephrosis, and cardiovascular disease. Aluminum, being the most abundant metal, is found in various forms and its exposure and intake are detrimental to plants and humans. Copper, an essential trace mineral and first-row transition metal plays vital roles in energy production and metabolism by acting as a cofactor for enzymes.[74] Similar to metal ions, environmental and biological important anions play numerous indispensable roles in biological system. For example, (a) Sulfite is involved in human redox homeostasis, cell signaling, various physiological and pathological processes (b) Nitrite is a key signaling component in the cellular machinery (c) Fluoride ion has beneficial effects in keeping up dental health or treating osteoporosis (d) Acetate ion has its utility in many enzymes and antibodies (e) Superoxide ion, a reactive oxygen species (ROS), possesses characteristic activity in cell growth and metabolism

Nitroarmoatic compounds (NACs) such as 1,3,5-trinitroperhydro-1,3,5-triazine (RDX), 2,4-dinitrotoluene (2,4-DNT), and 2,4,6-trinitrotoluene (TNT), are commonly used as explosives. 2,4,6-trinitrophenol (TNP) is more lethal than TNT due to its fast detonation velocity and low safety coefficient. It is extensively utilized in leather, dye, pharmaceutical, fireworks industries, and rocket fuel production. Because of its diverse uses, high water solubility, and low degradation, it can easily contaminate water and soil and is therefore recognized as an environmental pollutant. TNP carries health risks, including cancer, skin irritation, liver dysfunction, respiratory organ damage, nausea, and allergies. The allowed concentration of TNP in groundwater is 0.001 mg L^{-1} according to World Health Organisation (WHO). To monitor environmental contamination and terrorist operations, selective and sensitive detection of TNP is needed. Therefore, effective monitoring of various hazardous analytes is of substantial necessity for a sustainable future.

Numerous chemosensors have been reported for selective and rapid detection of analytes. However, persistent challenges include high cost, susceptibility to interference from other analytes, and use of organic solvents have hindered widespread application for environmental and biological samples. Therefore, it is highly desirable to improve the sensitivity of chemosensors to detect analytes at lower concentrations in aqueous medium.[75] Some selective examples of these chemosensors used for analyte detection are discussed.

Two of the pyrazine based chemosensors reported in literature for anion and explosive detection are shown in **Figure 1.4**. Kim and co-workers reported naphthalic Schiff base **1** bearing amino pyrazine for fluoride and cyanide through different channels. The colorimetric response to F^- was due to the deprotonation process while detection of CN^- was based on nucleophilic addition.[76] Pyrazine-based chemosensors have also been reported for explosive detection. Zao et al. reported tetraphenylpyrazine-based **2** manganese metal−organic framework for the detection of TNP. The fluorescence quenching was due to resonance energy transfer from MOF to TNP along with the electrostatic interaction of Lewis acid and base between the N atom of pyrazine and TNP.[77]

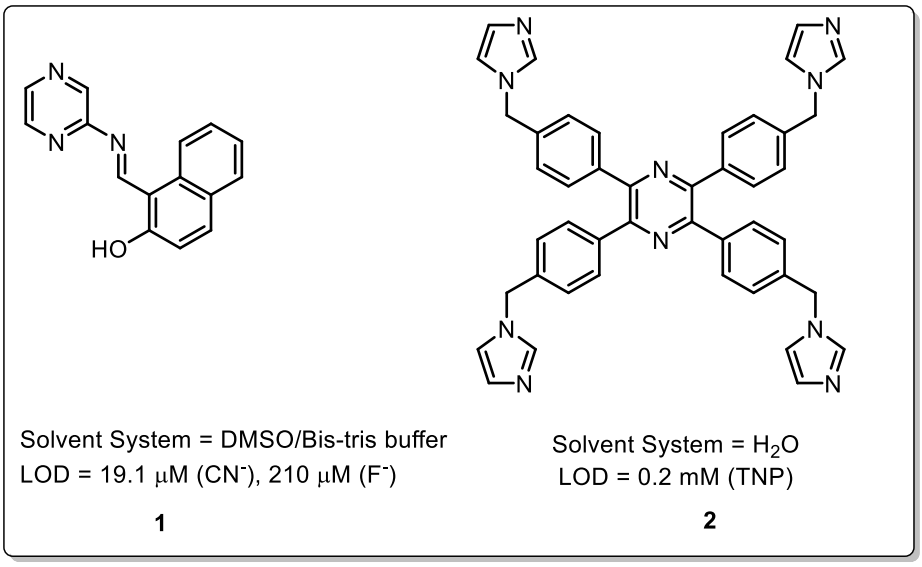

Figure 1.4: Pyrazine-based chemosensors for anion and 2,4,6-trinitrophenol (TNP) detection

Chemosensors for detection of metal ion based on pyrazine are also reported (**Figure 1.5**). Kashyup and co-workers reported BODIPY azine-bearing pyrazine attached Schiff base **3** for Al^{3+} detection. The intermolecular hydrogen bonding in the molecule and the presence of extra nitrogen helped to increase the efficiency of the chemosensor.[78] Li et al. also reported pyrazine-derived hydrazone Schiff base ligand **4** bearing quinoline unit as a turn-on fluorescent chemosensor for Al^{3+} detection. The reason was attributed to the inhibition of the PET phenomenon upon complexation of **4** with Al^{3+}, resulting in efficient chelation-enhanced fluorescence (CHEF) effect.[79] A pyrazine-2-carbohydrazide-based chemosensor **5** was reported by Napolean and co-workers for Zn^{2+} detection in the partial hydrophilic medium. The complexation of **5** with Zn^{2+} through hydroxy, carbonyl, and imine bonds lead to colorimetric response of **5**.[80] Singh and co-workers synthesized pyrazine-based organo silane **6** for the selective and sensitive detection of

Cu^{2+}. The sensing application was enhanced by the immobilization of organic moiety on the magnetic surface. The fluorescence quenching by Cu^{2+} ions might be attributed to factors like excitation energy transfer from fluorophore to metal d-orbital, charge transfer from fluorophore to Cu^{2+} ion, and heavy metal effect.[81] Malhotra and group reported chromone-based Schiff base with pyrazine **7** as a colorimetric probe for the detection of Cu^{2+}. The intramolecular charge transfer (ICT) process was evident during the complex formation with Cu^{2+}.[82] Rajesh and co-workers reported pyrazine incorporated Schiff base as colorimetric and ratiometric fluorescent chemosensor **8** for Ni^{2+} detection. The significant enhancement of fluorescence intensity was caused by the inhibiting C=N isomerization and promoting CHEF upon binding with Ni^{2+} ion through N and O atoms.[83]

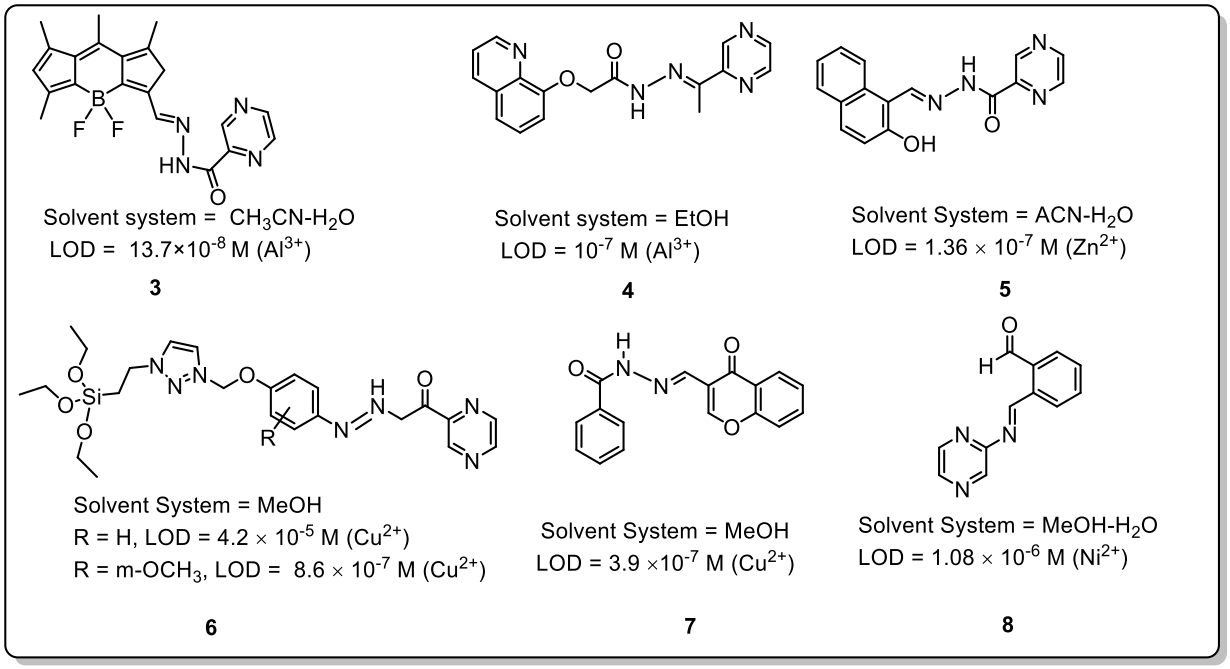

Figure 1.5: Pyrazine-based chemosensors for metal ion detection

The incorporation of pyridinium group in a chemosensor provides specific recognition site for explosive detection because of electrostatic interactions (**Figure 1.6**). Iyer and co-workers reported non-fluorescent polymeric cationic pyridinium bromide **9** for recognition of picric acid (PA) by fluorescence "turn-on" via Indicator displacement assay (IDA) mechanism. Chemosensor **9** worked as a host for an anionic green emitting dye (uranine dye, UD) that acted as an indicator for the detection of TNP by forming an electrostatic complex with **9**.[84] Kumar and co-workers developed a pyridinium-dansyl conjugate based three-dimensional molecular probe **10**, which

showed aggregation-induced emission in water with excellent fluorescence enhancement (Φ = 0.71). It selectively detected TNP and showed dynamic quenching as observed from the decrease in the lifetime.[85] It was shown that picrate anion places itself closer to the dansyl fluorophore due to its decreased cavity length thereby increasing the sensitivity of the probe. A novel cationic conjugated copolymer **11** was reported by Tanwar et al. for selective detection of TNT via an intermediate Meisenheimer complex. The fluorescence quenching was attributed to the combination of static and dynamic quenching processes due to the ground-state and excited-state interaction of probe **11** with the analyte TNT.[86]

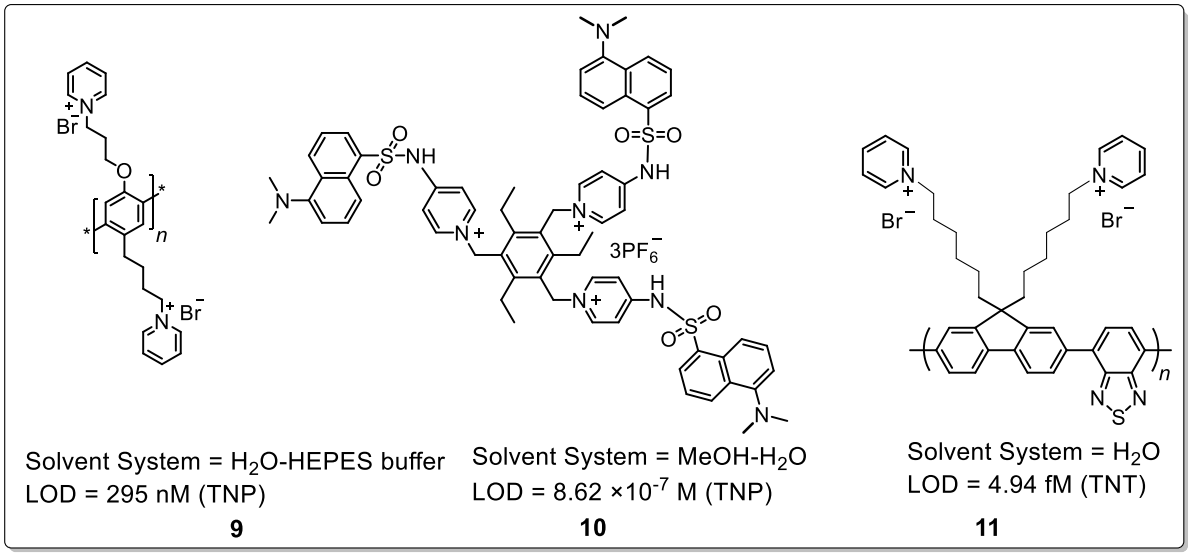

Figure 1.6: Pyridinium salts for nitroaromatic compounds (NACs) detection

Pyridinium salts are also utilized as chemosensors for anion detection via different mechanism (**Figure 1.7**). A ratiometric fluorescence probe **12** was developed by Lin and co-workers for the rapid detection of HClO/ClO^- in living cells. The mechanism for selective detection of HClO/ClO^- was rationalized as regioselective electrophilic addition on the C=C between pyridine and diethyl amine phenol. The presence of pyridinium salt moiety tends to target mitochondria due to electrostatic interaction, but it showed higher targeting ability toward lysosome due to extensive "*p*-*π*" electron-donating ability of diethylamine and hydroxyl in the benzene, which might counteract the positive charge of pyridinium.[87] Kumar and co-workers reported dual fluorescent probe **13** for mitochondrial viscosity and F^-. The fluorescence intensity increased gradually with a change in solvent from the ethanol-glycerol mixture. The change in fluorescence was attributed to a highly viscous environment, free intramolecular rotation between 4-dimethylamino and

pyridine moieties was restricted, and enhanced absorbance and red-fluorescence were observed. **13** showed strong green fluorescence on interaction with F^-. The F^- sensing mechanism was credited to F^- triggered desilylation which was followed by the release of quinone-methide moieties from DMAS to release green fluorescence.[88] Tang and co-workers reported pyridinium salt **14** with push-pull and utilized it for the selective detection of hypochlorite. The decrease in fluorescence intensity was attributed to the oxidation of the conjugated C=C double bonds of pyridinium by hypochlorite.[89] Liu and co-workers reported pyridinium inner salt **15** with strong red emission and good water solubility and utilized it for the CN^- recognition. The mechanism for CN^- selectivity was credited to the addition of CN^- to 4-coumarin by Michael addition inducing the decrease in electron-donating ability of the coumarin group and reduction in intramolecular charge transfer leading to fluorescence quenching.[90]

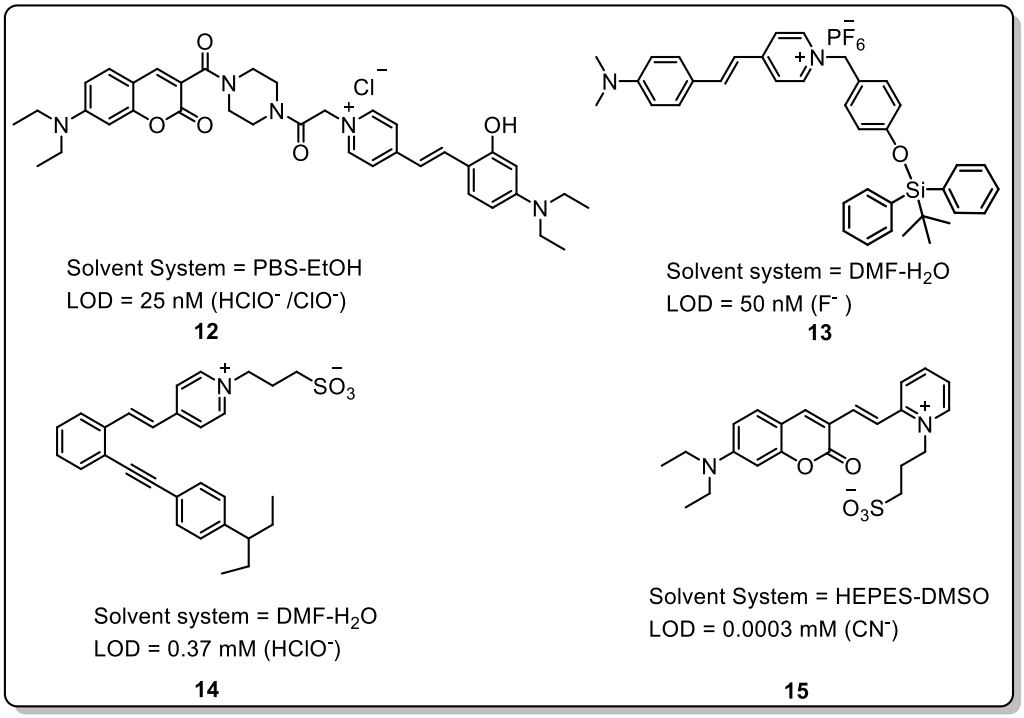

Figure 1.7: Pyridinium salts for anion detection

The π-conjugated pyridinium chemosensors exhibit advantage of detection of anions via aggregation of the conjugated aromatic moieties (**Figure 1.8**). Ni and co-workers developed a fluorescent probe using π-conjugated pyridinium derivatives **16** with positive charges. This probe demonstrated exceptional selectivity in detecting BF_4^- and PF_6^- ions in both neutral solutions and live cells. The system demonstrated a unique detection signal output for selectively identifying

anions by utilizing the process of aggregation self-assembly, which was facilitated by several non-covalent interactions including ionic binding, van der Waals forces, and π–π stacking.[91] Su et al. reported a water-soluble cationic fluorescent probe **17** with AIE characteristics that detected charge-diffuse anions namely SCN^-, PF_6^-, and HSO_3^- through ionic interactions and variable hydrophobicity. The sensing mechanism of **17** for the detection was ascribed to the binding strength between the anions and **17**, which enabled the target anions to initiate the aggregation of **17** via electrostatic ionic bonding, van der Waals forces between the alkyl chains, and π-stacking of the conjugated aromatic moieties.[92]

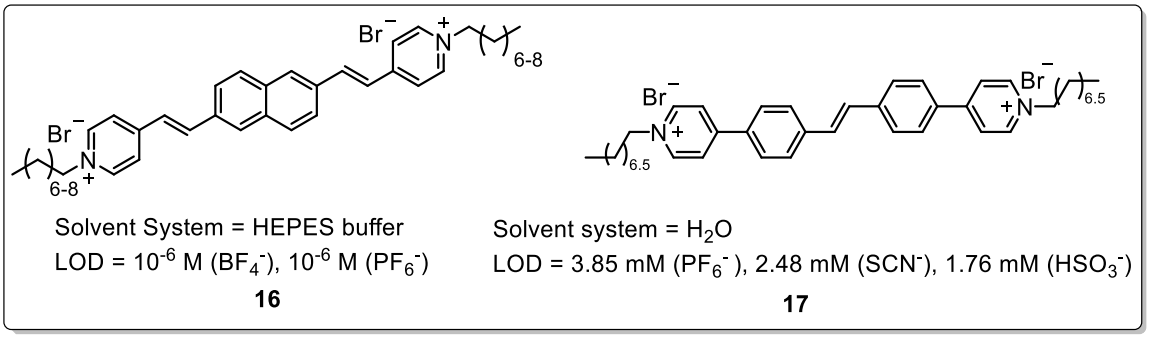

Figure 1.8: Bi-Pyridinium salts for anion detection

Pyridinium salts are also reported for the detection of metal ions (**Figure 1.9**). Xu and co-workers reported styryl-pyridinium salts **18** for Cu^{2+} sensing. The quenching of fluorescence upon binding with Cu^{2+} was attributed to the transfer of a lone pair of electrons of nitrogen atom on the DPA group of the probe **18**, triggering a distorted rotation of the C-N bond. Therefore, the intramolecular charge transfer (ICT) effect was suppressed by the paramagnetic nature and the heavy metal ion effect of the copper ion, leading to the quenching of the fluorescence emission spectrum.

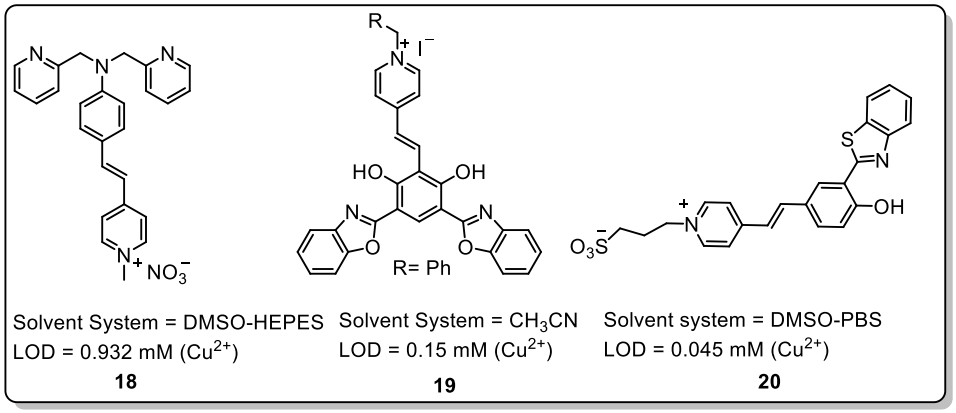

Figure 1.9: Pyridinium salts for metal ion detection

Rajapakshe et al. reported chemosensor **19** by incorporating a vinyl pyridinium segment. The Cu^{2+} induced fluorescence quenching in **19** occurs mainly via a static quenching mechanism by forming a **19**-Cu complex of the phenoxide anion by deprotonation of the phenolic group in the probe which enabled the metal-to-ligand electron transfer (MCLT) process.[93] An ESIPT probe based on pyridinium salt **20** was designed and synthesized by Zhou and co-workers. The probe was highly sensitive to Cu^{2+}. The probe exhibited intense orange fluorescence emission which was quenched in the presence of Cu^{2+} via dynamic or static mechanism.[94]

Imidazolium salt based receptors exhibit selective recognition of nitroaromatic compounds and have presently gained attention (**Figure 1.10**). Kumar and co-workers synthesized pyrene appended imidazolium salt **21** for the selective detection of TNP. The quenching of **21** with TNP was attributed to development of π-π interaction between pyrene rings and TNP facilitating the energy transfer.[95] Two water-soluble anthracene- and pyrene-based imidazolium chemosensors (**22** and **23**) were reported by Pherkkhuntod et al. and were demonstrated to exhibit highly efficient NACs detection in aqueous media. **22** and **23** showed fluorescent quenching upon the addition of NACs and probe **23** was more sensitive as compared to **22**. The cation-anion interactions between the imidazolium and picrate ions caused fluorescent quenching through PET and charge transfer involving a dark S_1 excited state.[96]

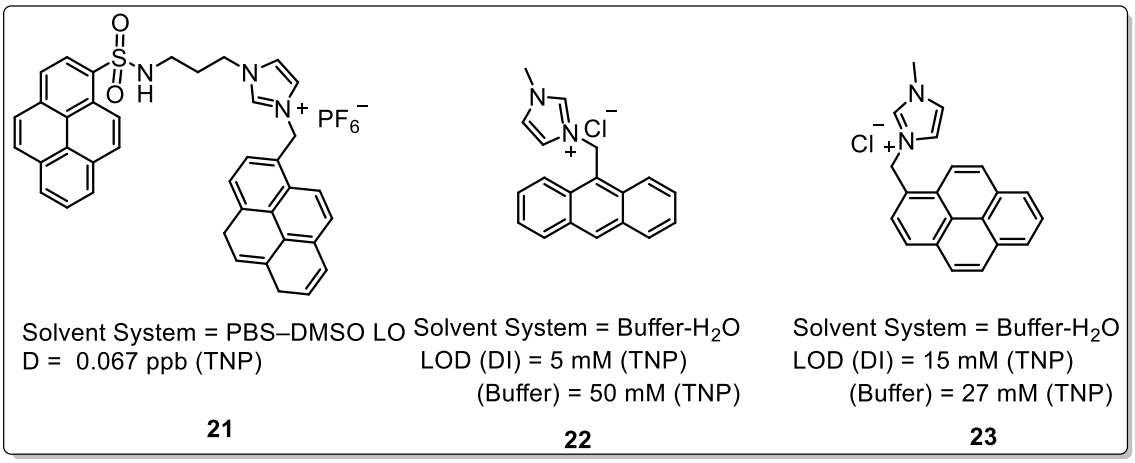

Figure 1.10: Imidazolium salts for NACs detection

Hydrophobic chemosenors suffers from low selectivity and sensitivity in non-aqeous medium, which is circumvented by incorporating imidazolium groups as receptors (**Figure 1.11**). Imidazolium conjugated polyelectrolyte (PMI), **24** synthesized by Iyer and co-workers was developed using the post-functionalization polymerization method. PMI showed remarkable

selectivity for TNP by immediate fluorescence quenching by 95% in purely aqueous media and on solid platforms. The high quenching efficiency of TNP compared to other nitro-compounds was explained via deprotonation of the strongly acidic phenolic –OH group in aqueous media, resulting in anion exchange with the polymer PMI. The complex thus formed may facilitate the ground state charge transfer between PMI and picrate along with the energy transfer process. Theoretical calculations validated the molecular interactions involved in supramolecular assembly.[97] Iyer and co-workers reported a di-imidazolium receptor by conjugating it with naphthalene diimide (NDMI) **25**, which was explored as an optical and electrical sensor for nitroaromatic compounds. Halide ions interacted with **25** via hydrogen bonding interaction. The strong π-π stacking interaction between TNP and **25** resulted in a change in photophysical properties. The prepared sensor was capable of detecting TNP in vapour states as well.[98]

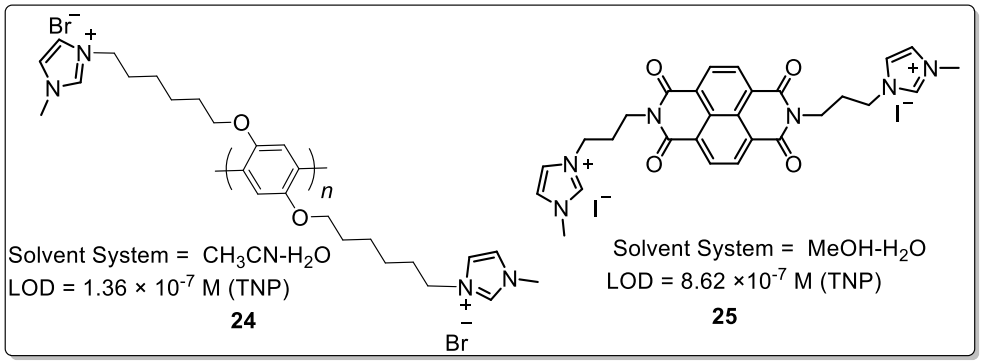

Figure 1.11: Bis-imidazolium salts for NACs detection

Imidazolium salts are utilized for anion detection (**Figure 1.12**) with good selectivity and sensitivity. Chae and co-workers reported an imidazolium bearing dansyl based probe with dicynovinyl group containing substrate with different alkyl chain **26** for CN^- detection. Investigations revealed that the substrate combined with cationic probe **26** to produce supramolecular self-assemblies after reacting with a nucleophilic CN^-.[99] Tomapatanaget and co-workers reported a naked-eye fluorescent probe **27** based on naphthalimide and imidazolium moieties for fluoride detection. The fluorescence response of **27** was significantly quenched in the presence of fluoride ion upon the interaction between an acidic amide proton and acidic C2 proton of the imidazolium ring.[100] An AIE-based imidazolium fluorescent chemosensor, **28** was designed and synthesized for the selective and sensitive detection of carbonate ion (CO_3^{2-}) in aqueous solution by Cheng et al. **28** contains a triphenylamine-based red emission core, imidazolium and amide anions donors, and a long alkyl chain. The recognition mechanism for carbonate was

credited to the formation of the bigger aggregate of nanoparticles with carbonate ions, limiting effective aggregation and decreasing fluorescence.[101] A series of cyclophane fluorescent probe based on acridine combined with imidazolium through ether linkages **29** were developed by Lin and co-workers. The sensors showed excellent selectivity towards Fe^{3+} in aqueous solution and H_2PO_4 in acetonitrile solution, with notable color change under UV-vis light and evident changes in fluorescence spectra. The sensing mechanism for Fe^{3+} was attributed to the formation of a rigid system after binding with Fe^{3+} causing the photoinduced electron transfer (PET) effect whereas the selectivity of H_2PO_4 was credited to H_2PO_4 anion formed hydrogen bonds with the two hydrogen atoms of imidazolium in the macrocyclic sensor.[102]

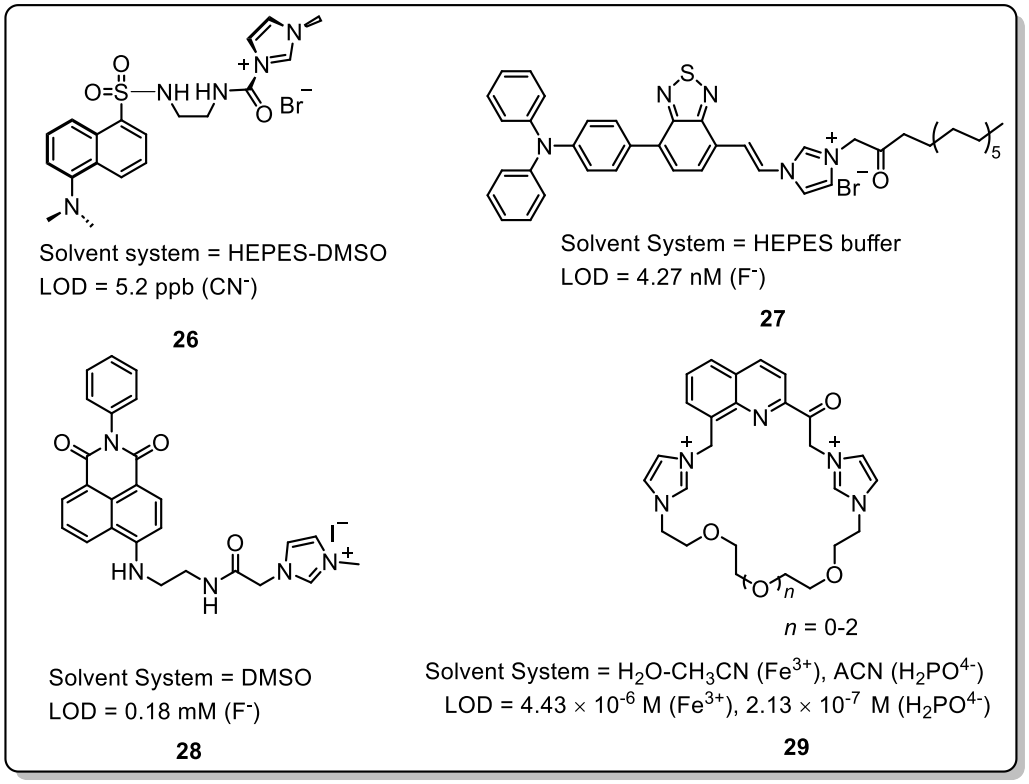

Figure 1.12: Imidazolium salts for anion detection

AIE based chemosensors with incorporation of bis-imidazloium salt for better selectivity and sensitivity are also reported for anion detection (**Figure 1.13**). Cao and co-workers reported cleft-type tetraphenylethylene appended imidazolium with 1,2-phenyl (**30**) or 1,2-phenylmethyl (**31**) for investigating their anion binding ability. **30** showed high affinity towards polyphosphate and SO_4^{2-} with the increase in fluorescence in aqueous solution. The response of **31** was reported to be weaker for polyphosphates, but not for SO_4^{2-}. The sensing mechanism explained the complexation

of **30**/**31** with these anions leading to an increase in aggregation state, enhancing its fluorescence.[103] Xiong et al. reported imidazolium linked AIE-active macrocyclophane **32** for the selective ratiometric fluorescence sensor for pyrophosphate anion in aqueous medium in the presence of zinc ion. The sensing mechanism was credited to macrocycle bearing imidazolium units which were able to bind pyrophosphate anion in its cavity through electrostatic and dipole interaction. The complex of **32** and pyrophosphate coordinated with Zn^{2+} resulting in aggregation and change in fluorescence.[104]

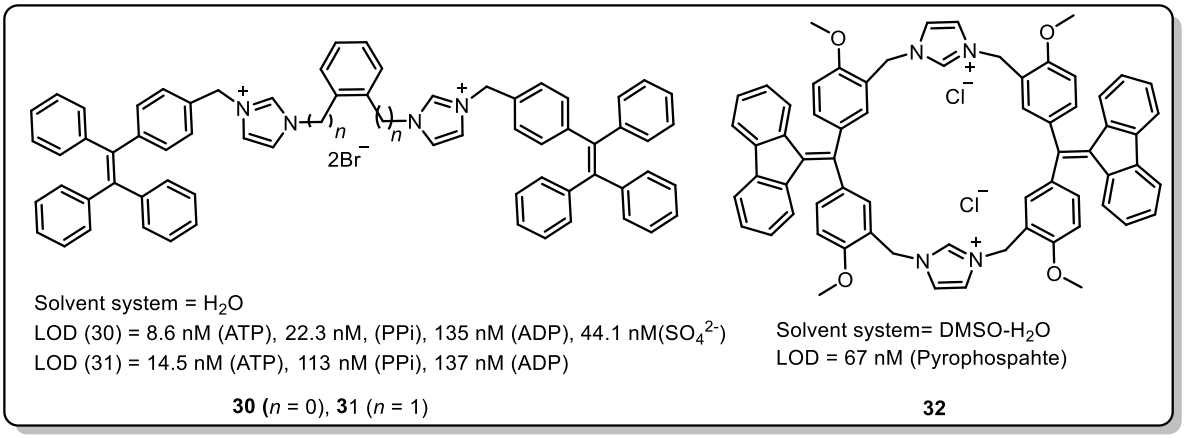

Figure 1.13: Bis-imidazolium salts for anion detection

Imidazolium salts are also reported for metal ion detection (**Figure 1.14**). Griebeler et al. reported thiazolidine-based chiral ionic liquids **33** for the detection of Cu^{2+}. It was hypothesized that nitrogen and sulfur atoms of the thiazolidine ring were involved in the complexation. The quenching of fluorescence was also observed due to the formation of a non-fluorescent complex in the ground state.[105]

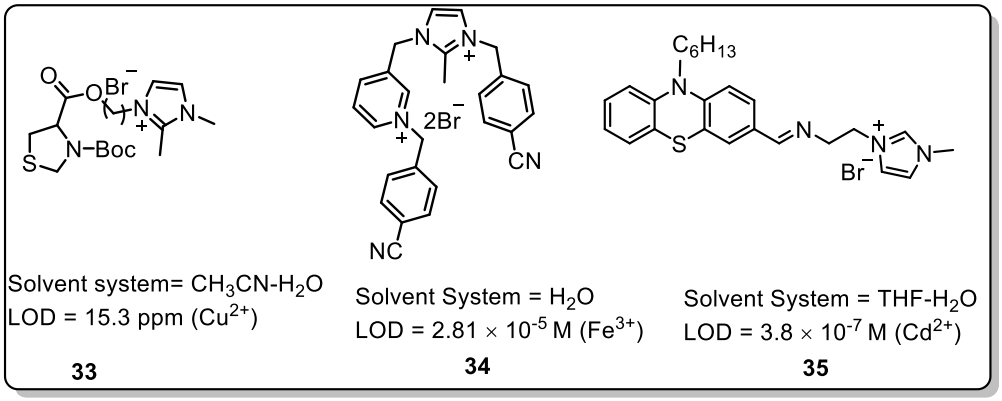

Figure 1.14: Imidazolium salts for metal ion detection

A series of N, N'-disubstituted imidazolium salts **34** were synthesized for selective detection of Fe^{3+} ions in pure aqueous media by Chaudhary and Milton. The sensors showed fluorescence turn-off in the presence of Fe^{3+}. The paramagnetic property of Fe^{3+} ions was responsible for fluorescence quenching upon binding of Fe^{3+} to the recognition sites.[106] Barot et al. reported aggregation-induced emission (AIEE)-active imidazolium ionic liquid functionalized phenothiazine-based Schiff-Base **35** for the nanomolar detection of Cd^{2+}. The active involvement of the -C=N group of **35** was found to be responsible for the complexation process.[107]

Bis-imidazolium salts are reported for their effectiveness in detecting metal ions (**Figure 1.15**). Zhou and co-workers reported a salicylaldehyde bis-Schiff base decorated with imidazolium ionic liquid **36** as a colorimetric/ratiometric sensor for the detection of Cu^{2+} and Pd^{2+} in aqueous medium. The interaction of **36** with Cu^{2+} and Pd^{2+} was due to the phenol and imine groups acting as binding sites leading to the formation of complex. Sun and co-workers reported bis-(NHC) derivatives **37** for selective recognition of Al^{3+}. It exhibited excellent fluorescence in the presence of Al^{3+}, while the pyridine analogue does not have selectivity to metal ions. The fluorescence enhancement was attributed to the formation of bis-quinoline-Al complex and extended conjugated system of **37**.[108] Hu et al. synthesized imidazolium chloride ionic liquid-grafted rhodamine B salicylaldehyde hydrazone **38** as a promising multi-ion-responsive probe for the colorimetric detection a of Cu^{2+} and Al^{3+} in 100% aqueous solutions. The sensing mechanism was proposed as an "electrostatic repulsion-induced difference in response time".[109]

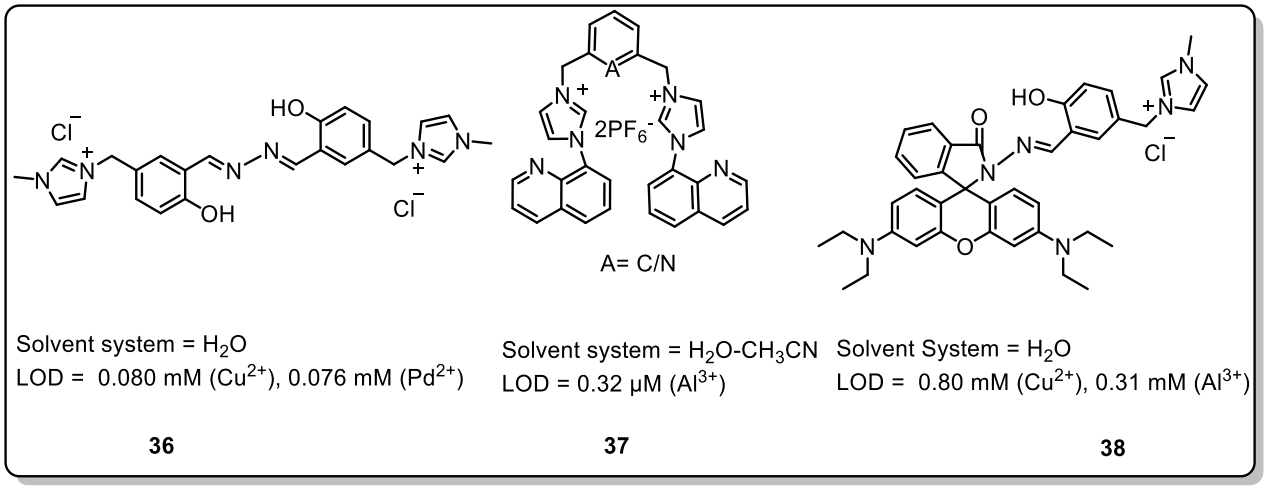

Figure 1.15: Bis-imidazolium salts for metal ion detection

1.3 AIM OF PRESENT STUDY

In recent years, the field of chemical sensors has placed significant emphasis on the detection and analysis of biologically and environmentally significant analytes. However, challenges still exist in developing receptors that selectively bind analytes in water. Changes in ligand design or donor atom selection can provide significant improvements in selectivity, sensitivity, and solvent system. The incorporation of ionic parts leading to azinium and azolium salts may provide hydrophilic properties suitable for high activity, stability, and reusability. The imidazolium and pyridinium salts have been widely reported for their selective response towards various analytes whereas pyrazinium salts are yet to be explored. The salt-like framework presents interesting photophysical properties due to interaction between chemosensor and analyte that results in change of luminescence which can be monitored easily. These chemosensors are widely studied for the recognition of environmentally relevant anions and metal ions. The present thesis focuses on the design and synthesis of azinium and azolium salts to investigate them as potential candidates for chemosensing properties. The chemosensors are also employed for the detection of various analytes viz., metal ions, anions and nitoexplosives in aqueous medium. The efficacy of salt-based chemosensors is investigated by application in a wide range of biological and real-world samples.

1.4 REFERENCES:

1. Martínez, R.; Zapata, F.; Caballero, A.; Espinosa, A.; Tárraga, A.; Molina, P.; *Organic letters*, **2006**, *8* (15), 3235-3238.
2. Dalapati, S.; Alam, M. A.; Jana, S.; Saha, R.; Biswas, S.; Guchhait, N.; *ChemPlusChem*, **2012**, *77* (2), 93-97.
3. Czarnik, A. W.; *Accounts of Chemical Research*, **1994**, *27* (10), 302-308.
4. De Silva, A. P.; Gunaratne, H. N.; Gunnlaugsson, T.; Huxley, A. J.; McCoy, C. P.; Rademacher, J. T.; Rice, T. E.; *Chemical Reviews*, **1997**, *97* (5), 1515-1566.
5. Kim, J. S.; Quang, D. T.; *Chemical Reviews*, **2007**, *107* (9), 3780-3799.
6. Martin, R. B.; *Metal ions in Biological Systems*, **1984**, *17*, 1-49.
7. Stillman, M., Biological Inorganic Chemistry. Structure and Reactivity. Edited by Ivano Bertini, Harry B. Gray, Edward I. Stiefel and Joan S. Valentine. Wiley Online Library: 2007.
8. Albretsen, J.; *Veterinary Medicine-Bonner Springs Then Edwardsville-*, **2006**, *101* (2), 82.
9. Matsuda, K.; Hiratsuka, N.; Koyama, T.; Kurihara, Y.; Hotta, O.; Itoh, Y.; Shiba, K.; *Clinical Chemistry*, **2001**, *47* (4), 763-766.
10. Liu, L.; Zhang, D.; Zhang, G.; Xiang, J.; Zhu, D.; *Organic Letters*, **2008**, *10* (11), 2271-2274.
11. Fung, M. C.; Bowen, D. L.; *Journal of toxicology: Clinical toxicology*, **1996**, *34* (1), 119-126.
12. Tsipouras, N.; Rix, C. J.; Brady, P. H.; *Clinical Chemistry*, **1997**, *43* (2), 290-301.
13. Thompson, D. T., Cyanide: Social, industrial and economic aspects. Springer: 2001.
14. Geller, R. J.; Barthold, C.; Saiers, J. A.; Hall, A. H.; *Pediatrics*, **2006**, *118* (5), 2146-2158.
15. Baird, C.; Cann, M., *Environmental chemistry*. Macmillan: 2005.
16. Gao, Y.; Shi, Z.; Long, Z.; Wu, P.; Zheng, C.; Hou, X.; *Microchemical Journal*, **2012**, *103*, 1-14.
17. Jia, X.; Han, Y.; Liu, X.; Duan, T.; Chen, H.; *Spectrochimica Acta Part B: Atomic Spectroscopy*, **2011**, *66* (1), 88-92.
18. Hrishikesan, E.; Kannan, P.; *Inorganic Chemistry Communications*, **2013**, *37*, 21-25.
19. Lee, E.-M.; Gwon, S.-Y.; Kim, S.-H.; *Spectrochimica Acta Part A: Molecular and Biomolecular Spectroscopy*, **2014**, *120*, 646-649.
20. De Silva, A. P.; Fox, D. B.; Huxley, A. J.; Moody, T. S.; *Coordination Chemistry Reviews*, **2000**, *205* (1), 41-57.

21. Evans, L. S.; Gale, P. A.; Light, M. E.; Quesada, R.; *New Journal of Chemistry*, **2006**, *30* (7), 1019-1025.

22. Meyer, T. J.; *Pure and Applied Chemistry*, **1986**, *58* (9), 1193-1206.

23. Vogler, A.; Kunkely, H.; *Coordination chemistry reviews*, **1998**, *177* (1), 81-96.

24. Wu, D.; Sedgwick, A. C.; Gunnlaugsson, T.; Akkaya, E. U.; Yoon, J.; James, T. D.; *Chemical Society Reviews*, **2017**, *46* (23), 7105-7123.

25. Wu, J.; Liu, W.; Ge, J.; Zhang, H.; Wang, P.; *Chemical Society Reviews*, **2011**, *40* (7), 3483-3495.

26. Wang, P.; Liu, L.; Zhou, P.; Wu, W.; Wu, J.; Liu, W.; Tang, Y.; *Biosensors and Bioelectronics*, **2015**, *72*, 80-86.

27. Thiagarajan, V.; Ramamurthy, P.; Thirumalai, D.; Ramakrishnan, V. T.; *Organic letters*, **2005**, *7* (4), 657-660.

28. Xie, H.; Hu, Q.; Qin, X.; Zhang, Y.; Li, L.; Li, J.; *Spectrochimica Acta Part A: Molecular and Biomolecular Spectroscopy*, **2022**, *283*, 121740.

29. Singh, T. S.; Paul, P. C.; Pramanik, H. A.; *Spectrochimica Acta Part A: Molecular and Biomolecular Spectroscopy*, **2014**, *121*, 520-526.

30. Pan, J.; Tang, F.; Ding, A.; Kong, L.; Yang, L.; Tao, X.; Tian, Y.; Yang, J.; *RSC advances*, **2015**, *5* (1), 191-195.

31. Rajput, J. K.; *Sensors and Actuators B: Chemical*, **2018**, *259*, 990-1005.

32. Ahmed, M.; Faisal, M.; Ihsan, A.; Naseer, M. M.; *Analyst*, **2019**, *144* (8), 2480-2497.

33. Qu, D.-Y.; Chen, J.-L.; Di, B.; *Analytical methods*, **2014**, *6* (13), 4705-4709.

34. Bagchi, B.; Oxtoby, D. W.; Fleming, G. R.; *Chemical physics*, **1984**, *86* (3), 257-267.

35. Mello, J. V.; Finney, N. S.; *Angewandte Chemie*, **2001**, *113* (8), 1584-1586.

36. Cao, D.; Liu, Z.; Verwilst, P.; Koo, S.; Jangjili, P.; Kim, J. S.; Lin, W.; *Chemical Reviews*, **2019**, *119* (18), 10403-10519.

37. Piotrowiak, P.; *Chemical Society Reviews*, **1999**, *28* (2), 143-150.

38. Kavarnos, G. J., Fundamental concepts of photoinduced electron transfer. In *Photoinduced electron transfer I*, Springer: 2005; pp 21-58.

39. Bissell, R. A.; Prasanna de Silva, A.; Nimal Gunaratne, H.; Mark Lynch, P.; Maguire, G. E.; McCoy, C. P.; Samankumara Sandanayake, K.; *Photoinduced Electron Transfer V*, **1993**, 223-264.

40. Ma, Y.; Feng, L.; Liu, J.; Yang, Y.; Chu, T.; *Theoretical Chemistry Accounts*, **2020**, *139*, 1-11.

41. Liu, L.; Sun, B.; Ding, R.; Mao, Y.; *The Journal of Physical Chemistry A*, **2022**, *126* (2), 230-238.

42. Grabowski, Z.; Dobkowski, J.; *Pure and Applied Chemistry*, **1983**, *55* (2), 245-252.

43. Long, L.; Zhou, L.; Wang, L.; Meng, S.; Gong, A.; Zhang, C.; *Analytica Chimica Acta*, **2014**, *812*, 145-151.

44. Zhang, L.-J.; Wang, Z.-Y.; Cao, X.-J.; Liu, J.-T.; Zhao, B.-X.; *Sensors and Actuators B: Chemical*, **2016**, *236*, 741-748.

45. Nohta, H.; Satozono, H.; Koiso, K.; Yoshida, H.; Ishida, J.; Yamaguchi, M.; *Analytical Chemistry*, **2000**, *72* (17), 4199-4204.

46. Song, J.; Huai, M.; Wang, C.; Xu, Z.; Zhao, Y.; Ye, Y.; *Spectrochimica Acta Part A: Molecular and Biomolecular Spectroscopy*, **2015**, *139*, 549-554.

47. Li, C.-Y.; Zhou, Y.; Li, Y.-F.; Zou, C.-X.; Kong, X.-F.; *Sensors and Actuators B: Chemical*, **2013**, *186*, 360-366.

48. Chen, W.-H.; Xing, Y.; Pang, Y.; *Organic letters*, **2011**, *13* (6), 1362-1365.

49. Park, S.; Kwon, J. E.; Kim, S. H.; Seo, J.; Chung, K.; Park, S.-Y.; Jang, D.-J.; Medina, B. M.; Gierschner, J.; Park, S. Y.; *Journal of the American Chemical Society*, **2009**, *131* (39), 14043-14049.

50. Lim, S.-J.; Seo, J.; Park, S. Y.; *Journal of the American Chemical Society*, **2006**, *128* (45), 14542-14547.

51. Pandey, M. D.; Tamrakar, A.; Wani, M. A.; Mishra, G.; Srivastava, A.; Pandey, R.; *Analytical Methods*, **2024**.

52. Dongare, P. R.; Gore, A. H.; *ChemistrySelect*, **2021**, *6* (23), 5657-5669.

53. Mahajan, P. G.; Shin, J. S.; Dige, N. C.; Vanjare, B. D.; Han, Y.; Choi, N. G.; Kim, S. J.; Seo, S. Y.; Lee, K. H.; *Journal of Photochemistry and Photobiology A: Chemistry*, **2020**, *397*, 112579.

54. Venkatesan, V.; Kumar, S. A.; Sahoo, S. K.; *Inorganic Chemistry Communications*, **2019**, *102*, 171-179.

55. Chen, S.; Yu, Y.-L.; Wang, J.-H.; *Analytica Chimica Acta*, **2018**, *999*, 13-26.

56. Panigrahi, S. K.; Mishra, A. K.; *Journal of Photochemistry and Photobiology C: Photochemistry Reviews*, **2019**, *41*, 100318.
57. Kubista, M.; Sjöback, R.; Eriksson, S.; Albinsson, B.; *Analyst*, **1994**, *119* (3), 417-419.
58. Fumoto, T.; Tanaka, R.; Ooyama, Y.; *Dalton Transactions*, **2023**, *52* (16), 5047-5055.
59. Swager, T. M.; *Accounts of chemical research*, **2008**, *41* (9), 1181-1189.
60. Sugiyasu, K.; Honsho, Y.; Harrison, R. M.; Sato, A.; Yasuda, T.; Seki, S.; Takeuchi, M.; *Journal of the American Chemical Society*, **2010**, *132* (42), 14754-14756.
61. Cacialli, F.; Wilson, J.; Michels, J.; Daniel, C.; Silva, C.; Friend, R.; Severin, N.; Samorı, P.; *Nature Material*, **2002**, *1* (3), 160.
62. Lam, J. L. Z. X. J.; *Chemical Communication*, **2001**, 1740-1741.
63. Lakowicz, J. R.; Lakowicz, J. R.; *Principles of fluorescence spectroscopy*, **1983**, 257-301.
64. Steinfeld, J. I.; *Accounts of Chemical Research*, **1970**, *3* (9), 313-320.
65. Ware, W. R.; *The Journal of Physical Chemistry*, **1962**, *66* (3), 455-458.
66. Boaz, H.; Rollefson, G.; *Journal of the American Chemical Society*, **1950**, *72* (8), 3435-3443.
67. Rollefson, G.; Stoughton, R.; *Journal of the American Chemical Society*, **1941**, *63* (6), 1517-1520.
68. Rollefson, G. K.; Boaz, H.; *The Journal of Physical Chemistry*, **1948**, *52* (3), 518-527.
69. Lakowicz, J. R.; Malicka, J.; D'Auria, S.; Gryczynski, I.; *Analytical Biochemistry*, **2003**, *320* (1), 13-20.
70. Ribeiro, M. M.; Franquelim, H. G.; Castanho, M. A.; Veiga, A. S.; *Journal of Peptide Science: an official publication of the European Peptide Society*, **2008**, *14* (4), 401-406.
71. Rahman, M.; Harmon, H. J.; *Spectrochimica Acta Part A: Molecular and Biomolecular Spectroscopy*, **2006**, *65* (3-4), 901-906.
72. Priyangga, K. T. A.; Kurniawan, Y. S.; Ohto, K.; Jumina, J.; *Journal of Multidisciplinary Applied Natural Science*, **2022**, *2* (1), 23-40.
73. Park, G. J.; Jo, H. Y.; Ryu, K. Y.; Kim, C.; *RSC Advances*, **2014**, *4* (109), 63882-63890.
74. Li, L.; Yun, S.; Yuan-Hui, Z.; Lan, M.; Xi, Z.; Redshaw, C.; Gang, W.; *Sensors and Actuators B: Chemical*, **2016**, *226*, 279-288.
75. Sasaki, Y.; Kojima, S.; Hamedpour, V.; Kubota, R.; Takizawa, S.-y.; Yoshikawa, I.; Houjou, H.; Kubo, Y.; Minami, T.; *Chemical Science*, **2020**, *11* (15), 3790-3796.

76. Lee, J. J.; Park, G. J.; Choi, Y. W.; You, G. R.; Kim, Y. S.; Lee, S. Y.; Kim, C.; *Sensors and Actuators B: Chemical*, **2015**, *207*, 123-132.

77. Zou, Y.; Huang, K.; Zhang, X.; Qin, D.; Zhao, B.; *Inorganic Chemistry*, **2021**, *60* (15), 11222-11230.

78. Kashyap, K. S.; Kumar, A.; Hira, S. K.; Dey, S.; *Inorganica Chimica Acta*, **2019**, *498*, 119157.

79. Li, C.-r.; Qin, J.-c.; Wang, G.-q.; Wang, B.-d.; Fu, A.-k.; Yang, Z.-y.; *Inorganica Chimica Acta*, **2015**, *430*, 91-95.

80. Dhanasekaran, K.; Napoleon, A. A.; *Inorganic Chemistry Communications*, **2024**, *161*, 112117.

81. Singh, G.; Suman; Diksha; Sushma; Mohit; Priyanka; Kaur, J.; Saini, A.; Devi, A.; *Journal of Molecular Structure*, **2022**, *1259*, 132512.

82. Tomer, N.; Goel, A.; Ghule, V. D.; Malhotra, R.; *Journal of Molecular Structure*, **2021**, *1227*, 129549.

83. Dhanushkodi, M.; Vinoth Kumar, G. G.; Balachandar, B. K.; Sarveswari, S.; Gandhi, S.; Rajesh, J.; *Dyes and Pigments*, **2020**, *173*, 107897.

84. Tanwar, A. S.; Iyer, P. K.; *ACS Omega*, **2017**, *2* (8), 4424-4430.

85. Tripathi, N.; Singh, P.; Kumar, S.; *New Journal of Chemistry*, **2017**, *41* (17), 8739-8747.

86. Tanwar, A. S.; Parui, R.; Garai, R.; Chanu, M. A.; Iyer, P. K.; *ACS Measurement Science Au*, **2022**, *2* (1), 23-30.

87. Yan, Y. H.; Ma, H. L.; Miao, J. Y.; Zhao, B. X.; Lin, Z. M.; *Analytica Chimica Acta*, **2019**, *1064*, 87-93.

88. Dhiman, S.; Kour, R.; Kaur, S.; Singh, P.; Kumar, S.; *Bioorganic Chemistry*, **2022**, *129*, 106169.

89. Xu, Y.; Zhao, L.; Zhao, Y. H.; Tang, Z.; *Russian Journal of General Chemistry*, **2023**, *93* (9), 2404-2409.

90. Zhao, X.; Sun, Y.; Zhu, Y.; Chen, H.; Wang, Z.; Zhao, S.; Cao, D.; Liu, G.; *Journal of Photochemistry and Photobiology A: Chemistry*, **2018**, *367*, 83-88.

91. Gong, X.; Zhang, Q.-L.; Zhang, S.; Xia, Y.; Bai, Q.; Chen, S.; Ni, X.-L.; *Dyes and Pigments*, **2019**, *163*, 502-508.

92. Su, S.; Zheng, Z.; Zhang, Q.-L.; Ni, X.-L.; *Dyes and Pigments*, **2021**, *185*, 108903.

93. Borchers, A.; Pieler, T.; *Genes (Basel)*, **2010**, *1* (3), 413-26.

94. Zhao, L.; Yue, M.; Zhao, Y. H.; Tang, Z.; Zhou, W.; *Russian Journal of General Chemistry*, **2024**, *94* (3), 660-665.

95. Kumar, A.; Pandith, A.; Kim, H.-S.; *Sensors and Actuators B: Chemical*, **2016**, *231*, 293-301.

96. Pherkkhuntod, C.; Ervithayasuporn, V.; Chanmungkalakul, S.; Wang, C.; Liu, X.; Harding, D. J.; Kiatkamjornwong, S.; *Sensors and Actuators B: Chemical*, **2021**, *330*, 129287.

97. Hussain, S.; Malik, A. H.; Afroz, M. A.; Iyer, P. K.; *Chemical Communication*, **2015**, *51* (33), 7207-10.

98. Kalita, A.; Hussain, S.; Malik, A. H.; Barman, U.; Goswami, N.; Iyer, P. K.; *ACS Applied Material Interfaces*, **2016**, *8* (38), 25326-36.

99. Jeong, E.; Yoon, S.; Lee, H. S.; Kumar, A.; Chae, P. S.; *Dyes and Pigments*, **2019**, *162*, 348-357.

100. Cheng, G.-J.-S.; Liu, Y.-P.; Xiong, Z.; Lang, W.; Zhang, Z.-W.; Cao, Q.-Y.; *Dyes and Pigments*, **2024**, *224*, 112018.

101. Kongwutthivech, J.; Tuntulani, T.; Promarak, V.; Tomapatanaget, B.; *Journal of Fluorescence*, **2020**, *30* (2), 259-267.

102. Zhou, J.; Yuan, Y.-F.; Zhuo, J.-B.; Lin, C.-X.; *Tetrahedron Letters*, **2018**, *59* (11), 1059-1064.

103. Huang, L.-X.; Bai, H.-Y.; Tao, H.; Cheng, G.; Cao, Q.-Y.; *Dyes and Pigments*, **2020**, *181*, 108553.

104. Xiong, J.-B.; Ban, D.-D.; Zhou, Y.-J.; Li, J.-Z.; Chen, S.-R.; Liu, G.-Q.; Tian, J.-J.; Mi, L.-W.; Li, D.-M.; *RSC Advances*, **2022**, *12* (11), 6876-6880.

105. Griebeler, C. H.; Bach, M. F.; Silva, H. C.; Rodembusch, F. S.; Coelho, F. L.; Schneider, P. H.; *Compounds*, **2023**, *3* (3), 430-446.

106. Chaudhary, S.; Milton, M. D.; *Journal of Photochemistry and Photobiology A: Chemistry*, **2018**, *356*, 595-602.

107. Barot, Y. B.; Anand, V.; Vyas, S.; Mishra, R.; *Journal of Molecular Liquids*, **2023**, *376*, 121490.

108. Zhou, W.; Gao, Q.; Liu, D.; Li, C.; Liu, S.; Xia, K.; Han, B.; Zhou, C.; *Spectrochimica Acta Part A: Molecular and Biomolecular Spectroscopy*, **2020**, *237*, 118365.

109. Shuai, H.-J.; Du, X.-G.; Jin, X.-M.; Jin, C.-M.; Sun, J.; *Journal of Molecular Structure*, **2023**, *1275*, 134668.

Chapter 2

Material, Methods and Instrumentation

OVERVIEW

This chapter highlights the information on material and experimental techniques employed for the characterization of pyrazinium, pyridinium, and imidazolium salt based chemosensors. This chapter also describes different instrumentation techniques that have been used for the characterization and analysis of the structure and properties of chemosensors. This chapter provides a list of software used for data interpretation, as well as details of theoretical studies for synthesized chemosensors.

2.1 CHEMICALS AND REAGENTS

List of chemicals and reagents used for the synthesis, catalytic, and sensing applications purchased from different suppliers is given below:

2,4-dihydroxybenzaldehyde was purchased from Alfa Aesar. 1-methylimidazole, palladium (II) acetate, Tetrakis(triphenylphosphine)palladium(0), 1-chloro-4-iodobenzene, 3,4-dinitrotoluene, 3,5-dinitrobenzoic acid, 3,5-dinitrotoluene, 4-nitrobenzoic acid, 4-nitrotoluene, were procured from Sigma Aldrich. Aluminium(III) nitrate nonahydrate, cadmium(II) nitrate tetrahydrate, chromium(III) nitrate nonahydrate, calcium(II) nitrate tetrahydrate, cobalt(II) nitrate hexahydrate, copper(II) nitrate trihydrate, ferric(III) nitrate nonahydrate, ferrous(II) sulfate heptahydrate, lead(II) nitrate, lanthanum(III) nitrate hexahydrate, mercury(II) nitrate monohydrate, magnesium(II) nitrate hexahydrate, manganese(II) nitrate tetrahydrate, nickel(II) nitrate hexahydrate, potassium(I) nitrate, sodium(I) nitrate, silver nitrate, zinc(II) nitrate hexahydrate**,** acetone, acetonitrile (ACN), chloroform ($CHCl_3$), dioxane, dichloromethane (DCM), dimethylformamide (DMF), dimethylsulfoxide (DMSO), ethanol (EtOH), ethyl acetate (EtOAc), ether, hexane, methanol (MeOH), and tetrahydrofuran (THF), DMSO (UV-grade), MeOH (UV-grade) were purchased from Merck. 1,2-dibromoethane, isatin, pyridine, potassium carbonate, sodium hydrogen carbonate, sodium sulfate, 2,6-dichloropyrazine, phenylboronic acid, benzoic acid, 1-chloro-2,4-dinitrobenzene, 2,4-dinitrophenol, 4-nitrophenol, nitrobenzene, nitromethane, potassium carbonate, sodium sulfate, tetrabutylammonium acetate, tetrabutylammonium chloride, tetrabutylammonium bromide, tetrabutylammonium hydrogen sulfate, tetrabutylammonium fluoride, tetrabutylammonium iodide, 2,4,6-trinitrophenol were commercially available from Spectrochem.

2.2 METHODS

The synthesis of the coupling products of 2,6-dichloropyrazine with boronic acid was conducted by microwave irradiation. Progress of the reaction was monitored by TLC on Merck aluminum sheets (silica gel 60 F_{254}). Desired products were purified by column chromatography (silica gel 100–200 mesh, Merck) using a gradient of ethyl acetate and hexane as a mobile phase. The reaction mixture of pyrazinium, pyridinium, and imidazolium salts was washed with ethyl acetate. The obtained solid was washed with diethyl ether and dried under a vacuum.

2.2.1 Job's plot

Job's plot is a method of continuous variation performed by mixing two solutions of the same concentration.[1-3] The solutions are prepared in such a way that the total analytical concentration of the solution remains constant, while the probe (a):analyte (b) ratio varies according to eqn. (2.1)

$$C_a + C_b = k \quad (2.1)$$

where C_a and C_b = analytical concentrations of probe and analyte, respectively, and k is a constant. The absorbance is plotted as a function of the mole fraction of probe or analyte. The resulting curves, called Job's plots, yield a maximum (or minimum) position which indicates the probe:analyte ratio of the complex in solution.

2.2.2 Limit of Detection calculation

The efficiency of a chemosensor is quantified by its Limit of Detection (LOD). As per the International Organisation for Standardisation, LOD refers to the minimum amount of a substance that may be reliably detected, with a specified level of confidence, above the absence of the substance (blank value).[4-5] The detection limit for the linear calibration plot is calculated using eqn. (2.2).

$$\text{Detection limit} = 3\sigma/K \quad (2.2)$$

where σ is the standard deviation of blank measurements, and K is the slope between the plot of fluorescence intensity versus sample concentration. To determine the signal/noise ratio, the fluorescence intensity of the chemosensor in water without an analyte is measured ten times and the standard deviation of blank measurements is determined.

2.2.3 Quantum Yield Calculation

The fluorescence quantum yield is calculated using quinine sulfate as a reference in 0.1 M H_2SO_4 (Φ_R = 0.54)[6-7] and calculated using eqn. (2.3).

$$\Phi_S = \Phi_R \frac{I_S}{I_R} \times \frac{A_R}{A_S} \times \frac{\eta_S^2}{\eta_R^2} \quad (2.3)$$

where I = integrated area under the fluorescence curve, A = absorbance at the excitation wavelength, η = refractive index of the medium, and Φ = fluorescence quantum yield. Subscripts S and R refer to the sample and the reference standard, respectively.

2.2.4 Fluorescence quenching percentage calculation

The fluorescence quenching percentage is calculated using the eqn. (2.4)[8-10]

$$Fluorescence\ quenching\ \% = \left(1 - \frac{I}{I_0}\right) \times 100\% \quad (2.4)$$

where, I_0 = initial fluorescence intensity in the absence of analyte, I = fluorescence intensity in the presence of analyte.

2.2.5 Overlap Integral Calculation

Analytes Overlap integral values is calculated using the eqn. (2.5)[11-13]

$$J(\lambda) = F_D(\lambda)\varepsilon_A(\lambda)\lambda^4 d\lambda \quad (2.5)$$

Where $F_D(\lambda)$ = corrected fluorescence intensity of donor in the range of λ to $\lambda + \Delta\lambda$ with the total intensity normalized to unity; ε_A = molar absorptivity of the acceptor at λ in M^{-1} cm^{-1}.

The Förster distance R_0 is calculated for chemosensor interaction using the eqn. (2.6)

$$R_0 = 0.211\ [(J)Q\ (\eta^{-4})(\kappa^2)]^{1/6} \quad (2.6)$$

Where J = degree of spectral overlap between the donor fluorescence spectrum and the acceptor absorption spectrum; fluorescence quantum yield of the donor (without acceptor); η = refractive index of the medium; κ^2 (dipole orientation factor) = 0.667.

2.2.6 Benesi–Hildebrand plot

The binding constant (K) determined by the Benesi−Hildebrand expression is calculated by the eqn. (2.7)[14-16]

$$1/(A - A_0) = 1/\{K(A_{max} - A_0)[C] + 1/(A_{max} - A_0) \quad (2.7)$$

where, A_0/I_0 and A/I = Absorbance/Fluorescence intensities of chemosensor in the absence and presence of metal ion, and I_{max} = maximum fluorescence intensity of chemosensor in the presence of metal ion. [C] = concentration of the metal, and n = number of metal ions bound to chemosensor here n = 1.

2.2.7 Fluorescence lifetime calculation

The fluorescence lifetime is a measure of the time that a fluorophore spends in the excited state before returning to the ground state by emitting a photon. Average fluorescence lifetimes (τ_{avg}) are calculated from the decay times and pre-exponential factors using the eqn. (2.8)[17]

$$\tau_{avg} = \Sigma\alpha_i \tau_i^2/\Sigma\alpha_i\tau_i \quad (2.8)$$

where α_i = pre-exponential factor corresponding to the i_{th} decay time constant.

2.2.8 Stern-Volmer quenching constant calculation

Collisional quenching occurs when an excited fluorophore comes in contact with a quencher that can facilitate non-radiative transitions to the ground state. The Stern-Volmer equation can be derived by considering fluorescence intensities observed in the absence and presence of a quencher.[18-20] The fluorescence intensity observed for a fluorophore is proportional to its concentration in the excited state. The Stern-Volmer quenching constant, K_{SV} is obtained using the eqn. (2.9)

$$I_0/I = 1 + K_{SV}[Q] \quad (2.9)$$

where I_0 and I = fluorescence intensities of chemosensor in the absence and presence of analyte, respectively, [Q] = concentration of analytes.

2.2.9 Detection of analytes in different samples

Stock solutions of chemosensors and analytes were prepared and diluted to the required concentration in Milli- Q water. Test strips were prepared by impregnating filter paper with chemosensor solution. The real water samples were procured from the Ganga River (Rishikesh, India), tap water from BITS Pilani, Pilani campus, and mineral water was purchased from the local market. The water samples were centrifuged and filtered through a 2.5 μm filter paper. Water samples were spiked with standard analytes solution and absorption and fluorescence spectra were recorded. 2 mg, 5 mg, 7 mg, and 10 mg of analyte were added to 2 gm of finely ground soil samples collected from the garden area of the BITS Pilani, Pilani campus in four different Petri dishes. 100 mg of each soil sample was added to a 2 ml solution of chemosensor. The detection of analytes in urine samples were performed by spiking the samples with the corresponding analytes.

2.2.10 Smartphone-Based Colorimetric Read-Out

For the naked-eye detectable change of probe in the presence of analytes using a smartphone was employed. The change in the RGB values of probe on the addition of analytes was recorded by keeping the smartphone camera about 1 cm away from the vials enclosed inside a paper box. The changes were recorded using a smartphone app, Color Grab, which could directly output the RGB values **(Figure 2.1)**. The standard RGB scale is represented by whole number-values from 0 to 255 for red, green, and blue colors. The values [0,0,0] and [255, 255, 255] correspond to absolute black and white, respectively.[21]

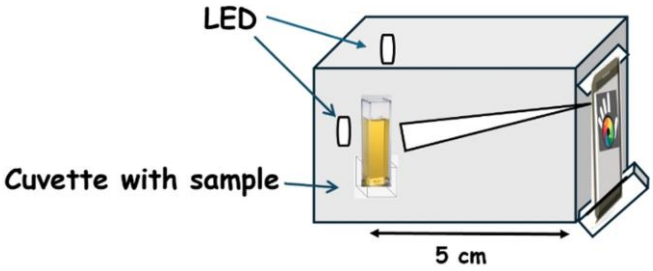

Figure 2.1: Sketch of Photo light box for RGB analysis

2.2.11 Methods for developing latent fingerprints (LFPs)

The visualization of latent fingerprints was performed for chemosensor with solid state luminescent properties. Chemosensor was used either directly or thoroughly ground with the neutral alumina oxide G in 1:15 w/w ratio to yield a homogenous mixture.[22-24] The formulated fingerprint powder exhibited a bright fluorescent color emission when exposed to UV light (365 nm). The fingerprint powder was applied to the latent fingerprints deposited on a microscopic glass plate by a volunteer. The excess powder was removed by a tapping and blowing method and fingerprints developed were photographed under UV light with high resolution camera.

2.2.12 Cytotoxicity Assay

For the cytotoxicity assay MCF-7 cells (6000 cells per well) grown in Dulbecco's Modified Eagle Medium (DMEM) were added to a 96-well plate and incubated at 37°C in an atmosphere of 5% CO_2 and 95% air overnight until 90% confluency was achieved. DMEM was aspirated from the 96-well plate, and different concentrations of probe (0.5, 1, 5, 10, 25, 50 and 100 µM) dissolved in DMEM along with the negative control set (no probe) were added in each well. Cells were incubated for 24 hours, 100 μL of 0.5mg ml-1[3-(4,5-dimethylthiazol-2-yl)-2,5-diphenyltetrazolium bromide] (MTT) dissolved in PBS was added to each well and left for 3-4 hours of incubation. MTT was carefully removed without disturbing the formazan crystals formed

due to the presence of live cells, and DMSO (cell-culture grade) was added to each well for solubilization.[25] The absorbance values were measured using a Multiskan Microplate Spectrophotometer (Thermo Scientific) at 570nm and 630nm wavelengths. The percentage of viable cells was calculated using the formula: viability (%) = (mean absorbance value of drug-treated cells)/(mean absorbance value of control) × 100. The percentage of cell viability versus different concentrations of probe was plotted using GraphPad Prism 8.0.1 Software Inc. The experiment was conducted in biological triplicate.

2.2.13 Cell-culture and imaging

MCF-7 cells were cultured in DMEM supplemented with 10% fetal bovine serum (FBS) and antibiotics (1% penicillin-streptomycin). Cultures were maintained at 37 °C in a humidified atmosphere containing 5% CO_2 and 95% air. Cells were seeded onto coverslips placed in 6-well plates at a density of 1.5×10^6 cells per well and allowed to adhere overnight with the incubation conditions mentioned. Upon reaching 70-80% confluency, the cells were washed with phosphate-buffered saline (PBS) to remove residual media, followed by fixation with 2% paraformaldehyde for 10 minutes. Post-fixation, cells were washed with 1X-PBS and blocked with 2% Bovine serum albumin in 0.1% PBS and subsequently rewashed with PBS. Permeabilization of cells was achieved using 0.1% Triton X-100 in PBS. Following permeabilization, cells were treated with probe (30 μM) dissolved in double-autoclaved Milli-Q water and incubated for 45 minutes at room temperature. Post-incubation, cells were washed twice with PBS to remove cellular debris. Subsequently, cells were treated with analyte solution (30 μM, 1:1 ratio of probe: analyte) for 20 minutes with intermittent PBS washes. Finally, the coverslips were mounted on glass slides using 70% glycerol, and allowed to dry overnight, and fluorescence images were acquired using a Carl Zeiss LSM 880 confocal microscope equipped with a 40X objective lens

2.2.14 Method for development of µPADs

The fabrication of this µPAD involved melting paraffin and iron mould. An iron rod was cut into a 5-branched mold by the laser cutting shop. The chromatography paper was cut into 5 cm × 5 cm plates and securely fastened to the moulds using paperclips.[26-28] To create a µPAD pattern, the chromatography paper was briefly dipped into melted paraffin, allowing it to adhere to the paper. Once the paraffin cooled at room temperature, the mould was carefully removed. An interesting contrast was created on the paper, with one area being hydrophobic and the other area being hydrophilic.

2.3 INSTRUMENTATION

2.3.1 Infrared (IR) spectroscopy

This branch of spectroscopy deals with the absorption of radiations in the infrared region of the electromagnetic spectrum. This region consists of light with longer wavelengths and lower frequencies compared to visible light. The electromagnetic spectrum of the infrared segment is commonly categorized into three regions: near-infrared, mid-infrared, and far-infrared. These divisions are based on their proximity to the visible spectrum. The higher energy near-infrared (near-IR), which falls within the range of approximately 14000-4000 cm^{-1} (0.8-2.5 μm wavelength), can stimulate overtone or harmonic vibrations. The mid-infrared region, spanning from roughly 4000-400 cm^{-1} (2.5-25 μm), can be utilized for investigating the fundamental vibrations and the corresponding rotational-vibrational arrangement. The far-infrared area, which spans from approximately 400 to 10 cm^{-1} (25-1000 μm) and is located next to the microwave zone, consists of low-energy radiation that can be utilized for rotational spectroscopy. Infrared spectroscopy utilizes the phenomenon of molecules selectively absorbing distinct frequencies that are indicative of their molecular structure. These absorptions correspond to resonant frequencies, meaning that the frequency of the absorbed radiation aligns with the frequency of the vibrating bond or group. [29-30] A vibrational mode in a molecule is considered "IR active" only if it is linked to alterations in the permanent dipole. The vibrational spectroscopy is governed by Hooke's law which is used for calculating the approximate stretching frequency of a bond. The infrared spectra (4000-450 cm^{-1}) of the synthesized compounds were recorded on the Perkin Elmer Spectrum 100 FTIR spectrometer (**Figure 2.2)**.

Figure 2.2: FTIR spectrometer (Perkin Elmer Spectrum 100)

2.3.2 Nuclear Magnetic Resonance Spectroscopy

NMR spectroscopy is one of the most powerful tools for structural elucidation, which involves the change of the spin state of a nuclear magnetic moment when the nucleus absorbs electromagnetic radiation in a strong magnetic field. ^{1}H and ^{13}C are commonly used NMR spectroscopic techniques. The absorbed energy, resonance frequency, and the strength of signal intensity are directly proportional to the applied magnetic field. [31-32] Parts per million (ppm) and hertz (Hz) are used to express chemical shifts (δ) and coupling constants (J), respectively. In the ^{1}H NMR spectra, spin multiplicities are represented by the following abbreviations: s = singlet, d = doublet, t = triplet, and m = multiplet.

In the present work, the ^{1}H and ^{13}C NMR, spectra of synthesized compounds were measured on a 400 MHz NMR spectrometer, Bruker AscendTM 400 **(Figure 2.3)** using $CDCl_3$ and DMSO-d_6 as deuterated solvents. The NMR peak integration was performed on MestReNova software.

Figure 2.3: NMR spectrometer (Bruker AscendTM 400)

2.3.3 Mass spectrometry

Mass spectrometry is a powerful analytical technique that allows for the precise measurement of molecular or atomic weight. It has also been extensively utilized for monitoring reactions. The process entails transforming the sample into gaseous ions, either with or without fragmentation. The ions are subsequently separated in the mass spectrometer based on their mass-to-charge ratio (*m/z*) and are then qualitatively and quantitatively detected according to their *m/z* and relative abundance. The results are presented as a plot showing the abundance of ions plotted against their mass-to-charge ratio. Q-TOF (Quadrupole Time-of-Flight) LC-MS offers exceptional precision in determining mass information down to the sub-ppm levels. In Q-TOF, the ions are carefully

controlled within a stable orbit using an electric field created by four parallel electrodes. These ions, each with their unique mass, are then accelerated to an equal kinetic energy. The time it takes for each ion to travel a known distance and reach the detector is precisely measured. By combining a quadrupole and a collision cell with the TOF analyzer, the selectivity is significantly improved. This is achieved by fragmenting specific ions and identifying compounds based on their product ion spectra. Therefore, it is possible to accurately determine the mass of both the precursor and product ions. The mass spectra for different synthesized compounds and reaction intermediates were recorded on 6545 Q-TOF LC/MS, Model-G6545A **(Figure 2.4)**.

Figure 2.4: Mass spectrometer (6545Q-TOF LC/MS)

2.3.4 UV-visible absorption spectroscopy

UV-visible absorption spectroscopy is a widely used analytical technique that provides information about the amount of energy absorbed by a molecule due to electronic transitions from ground state to an excited state. The ultraviolet (UV) range spans from 100 to 400 nm, while the visible spectrum covers wavelengths from 400 to 700 nm. UV-visible light possesses sufficient energy to elevate electrons to a higher electronic state, specifically from the highest occupied molecular orbital (HOMO) to the lowest unoccupied molecular orbital (LUMO). The HOMO and the LUMO are known as bonding and anti-bonding orbitals, respectively and the difference in these energy levels is referred to as the band gap. In order for a photon to be absorbed, its energy must precisely correspond to the band gap. The molecules of distinct chemical structures exhibit varying energy band gaps resulting in different absorption spectra. The π-π^* and n-π^* transitions are the most often observed transitions within the UV-vis range.[33-36] Absorption obeys Beer's Law,

which states that the absorbance (A) of a substance is directly proportional to the product of the molar absorption coefficient (ε), the path length (l), and the concentration (C) eqn. (2.10)

$$A = \varepsilon l C \quad (2.10)$$

The UV-visible spectra were recorded both in solution and solid states. The studies were performed using the Perkin Elmer LAMBDA 950 UV-VIS-NIR Spectrophotometer and JASCO model V-650 (**Figure 2.5**).

Figure 2.5: UV-visible spectrophotometer (a) Perkin Elmer LAMBDA 950 UV-VIS-NIR (b) JASCO V-650

2.3.5 Fluorescence spectroscopy

Fluorescence spectroscopy is a technique that analyzes the emission of fluorescence from a molecule, specifically studying its underlying luminescent properties. Fluorescence is a type of luminescence that happens when photons stimulate a molecule leading to a change in the excited state. A spectrofluorometer is an instrument that irradiates a sample with suitable excitation light and measures the subsequent fluorescence generated by the sample. The emission intensity increases in direct proportion to the concentration of the analyte.[37]

The Steady-state fluorescence measurements were performed using the Horiba Jobin Yvon Fluoromax-4 scanning spectrofluorometer. Spectral measurements were conducted using quartz cuvettes with a path length of 1 cm and excitation and emission slit widths of 3 nm (**Figure 2.6**).

Figure 2.6: Spectrofluorometer (Horiba Jobin Yvon Fluoromax-4)

2.3.6 Time-resolved spectroscopy

Time-resolved or fluorescence lifetime spectroscopy is a powerful tool that allows researchers to investigate the behavior of short-lived intermediate species by extending the capabilities of the steady-state fluorescence technique. During a time-resolved fluorescence experiment, a sample is excited using a pulsed laser. The emissions produced and their decay times are subsequently observed over time. This can be done using either an ultrafast detector or the second pulse of laser light. Studying the decay processes that happen on ultrashort time scales (~10^{-6}-10^{-16} seconds) can be achieved with the assistance of lasers.[38-39] The fluorescence lifetime measurements in this study were conducted using the time-correlated single-photon counting (TCSPC) method with the Horiba Jobin Yvon TCSPC (**Figure 2.7**).

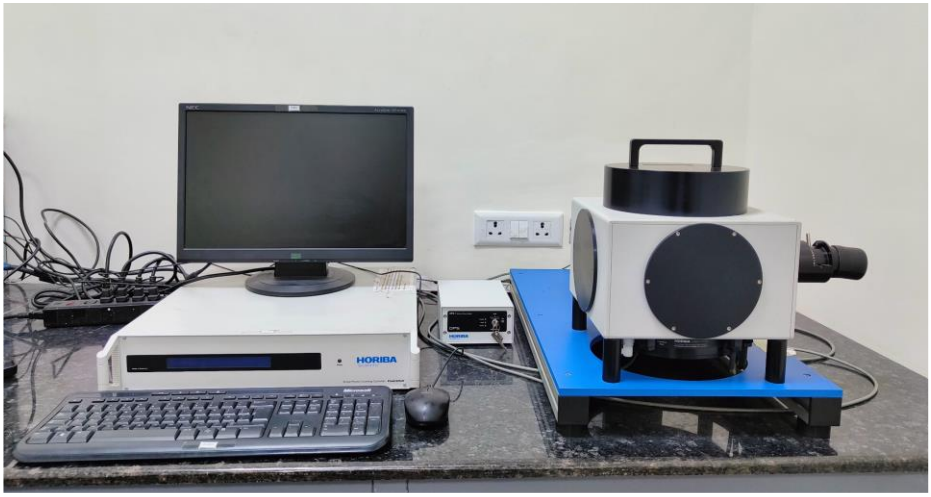

Figure 2.7: Fluorescence lifetime Spectrometer (Horiba Jobin Yvon TCSPC)

2.3.7 Single-crystal X-ray diffraction

Single-crystal X-ray refers to the technique of using X-rays to study the structure of a single crystal. X-ray diffraction is a non-destructive analytical technique that offers comprehensive insights into the internal lattice of crystalline substances. It provides precise information about several aspects, such as unit cell diameters, bond lengths, bond angles, and details of site ordering. X-ray diffraction relies on the constructive interference of monochromatic X-rays and a crystalline material. The X-rays are produced by a cathode ray tube, filtered to provide radiation of a single wavelength, focused to concentrate, and aimed at the sample. When the incident rays interact with the sample, they create constructive interference and a diffracted ray. This occurs when the conditions meet Bragg's Law.[40-41]

The Bragg's law is expressed by eqn. (2.11)

$$n\lambda = 2dsin\theta \quad (2.11)$$

where n = diffraction order, λ = wavelength of X-rays, d = spacing of the crystal layers, θ = incident angle.

The X-ray diffraction (XRD) data were obtained using a Rigaku-Oxford XtaLAB Pro: Kappa dual home/near diffractometer (**Figure 2.8**). The instrument was equipped with a CCD detector and a fine focus-sealed X-ray tube that emitted monochromated MoKα/CuKα radiations. The appropriate crystals were maintained at a temperature of 293 K during the process of collecting data. The process of collecting and reducing data was carried out using CrysAlisPro software. The structures were determined using Olex2 with ShelXT structure solution software employing Intrinsic Phasing and subsequently refined with the ShelXL refinement tool utilizing least squares minimization.

Figure 2.8: Single-crystal X-ray diffractometer (Rigaku-Oxford XtaLAB)

2.3.9 X-ray photoelectron spectroscopy (XPS)

It is also referred to as electron spectroscopy for chemical analysis (ESCA) and is employed to examine the chemical composition of a material surface. It is capable of determining the elemental makeup, chemical properties, and electronic configuration of atoms present in a given material. XPS spectra are acquired by exposing a solid surface to a stream of X-rays and quantifying the kinetic energy of electrons released from the uppermost 1-10 nm layer of the material. A photoelectron spectrum is obtained by quantifying the number of emitted electrons throughout a variety of kinetic energies. The energies and intensities of the photoelectron peaks allow for the

identification and measurement of all surface elements, with the exception of hydrogen.[43-44] K-Alpha model has been used to acquire the XPS data in this thesis (**Figure 2.9**).

Figure 2.9: X-ray photoelectron spectrometer

2.3.8 Microwave synthesis

Microwave irradiation refers to the exposure to electromagnetic radiation within the frequency range of 0.3 GHz to 300 GHz. This range corresponds to wavelengths between 1 mm and 1 m. For microwave heating to occur, the substance must have a dipole moment. A dipole exhibits sensitivity to the external electric field and endeavors to align itself with the field by rotation. The microwaves directly interact with the molecules of the entire reaction mixture, causing a rapid rise in temperature. This allows for improved homogeneity and targeted heating of polar molecules. The reactions under microwaves are fast, with increased reaction rates, and lead to better selectivity [42]. In this thesis, the microwave reactions were performed in a Monowave 300 (Anton Paar, Austria) microwave synthesis reactor with 10 mL standard vials and a Teflon-coated magnetic stir bar (**Figure 2.10**).

Figure 2.10: Microwave synthesis reactor (Monowave 300, Anton Paar)

2.3.9 Computational study

Computational or theoretical study is a methodology used to examine the structural, electrical, and magnetic characteristics of molecules and materials. The electronic ground state (S_0) of molecules were optimized through the application of the density functional theory (DFT)[45] with Becke's three-parameter hybrid exchange functional[46] and Lee−Yang−Parr gradient-corrected correlation (B3LYP density functional)[47]. The 6-311G+(d,p) basis set was utilized for C, H, N, O, Br atoms and LanL2DZ as an effective core potential (ECP) set for aluminum. The TD-B3LYP method was utilized to optimize the structures of the first electronic excited state (S_1) using the Integral Equation Formalism-Polarizable Continuum Model (IEF-PCM) with 6-311G+(d,p) basis set with water as a solvent medium. All these calculations were performed with the Gaussian 09 package.

2.4 REFERENCES

1. Ulatowski, F.; Dabrowa, K.; Balakier, T.; Jurczak, J.; *Journal of Organic Chemistry*, **2016**, *81* (5), 1746-56.
2. Renny, J. S.; Tomasevich, L. L.; Tallmadge, E. H.; Collum, D. B.; *Angewandte Chemie International Edition*, **2013**, *52* (46), 11998-2013.
3. Dong, Y.; Fan, R.; Chen, W.; Wang, P.; Yang, Y.; *Dalton Transactions*, **2017**, *46* (20), 6769-6775.
4. Oleneva, E.; Khaydukova, M.; Ashina, J.; Yaroshenko, I.; Jahatspanian, I.; Legin, A.; Kirsanov, D.; *Sensors (Basel)*, **2019**, *19* (6),
5. Allegrini, F.; Olivieri, A. C.; *Analytical Chemistry*, **2014**, *86* (15), 7858-66.
6. Nawara, K.; Waluk, J.; *Analytical Chemistry*, **2017**, *89* (17), 8650-8655.
7. Zhang, Y.; Wang, D.; Sun, C.; Feng, H.; Zhao, D.; Bi, Y.; *Dyes and Pigments*, **2017**, *141*, 202-208.
8. Wei, X. L.; Xiao, J. B.; Wang, Y.; Bai, Y.; *Spectrochimca Acta A Molecular and Biomolecular Spectroscopy*, **2010**, *75* (1), 299-304.
9. Zou, L.; Harkey, M. R.; Henderson, G. L.; *Phytomedicine*, **2002**, *9* (3), 263-7.
10. Bakar, K. A.; Feroz, S. R.; *Spectrochimca Acta A Molecular and Biomolecular Spectroscopy*, **2019**, *223*, 117337.
11. Tamil Selvan, G.; Varadaraju, C.; Tamil Selvan, R.; Enoch, I.; Mosae Selvakumar, P.; *ACS Omega*, **2018**, *3* (7), 7985-7992.
12. Taya, P.; Maiti, B.; Kumar, V.; De, P.; Satapathi, S.; *Sensors and Actuators B: Chemical*, **2018**, *255*, 2628-2634.
13. Lu, M.; Zhang, X.; Zhou, P.; Tang, Z.; Qiao, Y.; Yang, Y.; Liu, J.; *Chemical Physics Letters*, **2019**, *725*, 45-51.
14. Singh, T. S.; Paul, P. C.; Pramanik, H. A.; *Spectrochimca Acta A Molecular and Biomolecular Spectroscopy*, **2014**, *121*, 520-6.
15. Roy, N.; Pramanik, H. A.; Paul, P. C.; Singh, S. T.; *Journal of Fluorescence*, **2014**, *24* (4), 1099-106.
16. Mulimani, P.; Bhat, M. P.; Patil, P.; Aralekallu, S.; Kapavarapu, R.; Yu, J.; Kurkuri, M.; Kalkhambkar, R. G.; *Journal of Water Process Engineering*, **2024**, *59*, 105030.

17. Heena; Silswal, A.; Sharma, D.; Koner, A. L.; Om, H.; Rana, R.; *Spectrochimca Acta A Molecular and Biomolecular Spectroscopy*, **2024**, *320*, 124575.

18. Cui, F.; Xie, Z.; Yang, R.; Zhang, Y.; Liu, Y.; Zheng, H.; Han, X.; *Spectrochimca Acta A Molecular and Biomolecular Spectroscopy*, **2024**, *314*, 124222.

19. Wang, J.; Chen, L.; Li, Y.; Manley-Harris, M.; *Analytical and Bioanalytical Chemistry*, **2024**, *416* (14), 3433-3445.

20. Ye, Z.; Liu, Y.; Yang, J.; Long, J.; Zeng, H.; Li, H.; Liu, C.; Xu, B.; Wei Ng, K.; Shi, G.; Yi, A.; *Journal of Photochemistry and Photobiology A: Chemistry*, **2024**, *450*, 115431.

21. R, S. K.; Kumar, S. K. A.; Vijayakrishna, K.; Sivaramakrishna, A.; Brahmmananda Rao, C. V. S.; Sivaraman, N.; Sahoo, S. K.; *Inorganic Chemistry*, **2018**, *57* (24), 15270-15279.

22. Jain, A.; De, S.; Saraswat, P.; Haribabu, J.; Santibanez, J. F.; Barman, P.; *Journal of Molecular Structure*, **2024**, *1310*, 138383.

23. Johny Dathees, T.; Narmatha, G.; Prabakaran, G.; Seenithurai, S.; Chai, J. D.; Suresh Kumar, R.; Prabhu, J.; Nandhakumar, R.; *Food Chemistry*, **2024**, *441*, 138362.

24. Ruan, N.; Qiu, Q.; Wei, X.; Liu, J.; Wu, L.; Jia, N.; Huang, C.; James, T. D.; *Journal of American Chemical Society*, **2024**, *146* (3), 2072-2079.

25. Agarwal, D. S.; Singh, R. P.; Lohitesh, K.; Jha, P. N.; Chowdhury, R.; Sakhuja, R.; *Molecular Diversity*, **2018**, *22* (2), 305-321.

26. Al-Jaf, S. H.; Mohammed Ameen, S. S.; Omer, K. M.; *Lab Chip*, **2024**, *24* (8), 2306-2316.

27. Anushka; Bandopadhyay, A.; Das, P. K.; *The European Physical Journal Special Topics* , **2023**, *232* (6), 781-815.

28. Chen, J. L.; Njoku, D. I.; Tang, C.; Gao, Y.; Chen, J.; Peng, Y. K.; Sun, H.; Mao, G.; Pan, M.; Tam, N. F.; *Small Methods*, **2024**, e2400155.

29. Dutta, A.; **2017**, 73-93.

30. Vimont, A.; Thibault-Starzyk, F.; Daturi, M.; *Chemical Society Reviews*, **2010**, *39* (12), 4928-50.

31. Ben-Tal, Y.; Boaler, P. J.; Dale, H. J. A.; Dooley, R. E.; Fohn, N. A.; Gao, Y.; Garcia-Dominguez, A.; Grant, K. M.; Hall, A. M. R.; Hayes, H. L. D.; Kucharski, M. M.; Wei, R.; Lloyd-Jones, G. C.; *Progress in Nuclear Magnetic Resonance Spectroscopy*

32. Claramunt, R. M.; López, C.; Santa María, M. D.; Sanz, D.; Elguero, J.; *Progress in Nuclear Magnetic Resonance Spectroscopy*, **2006**, *49* (3-4), 169-206.

33. Bols, M. L.; Ma, J.; Rammal, F.; Plessers, D.; Wu, X.; Navarro-Jaen, S.; Heyer, A. J.; Sels, B. F.; Solomon, E. I.; Schoonheydt, R. A.; *Chemical Reviews*, **2024**, *124* (5), 2352-2418.

34. Das, A.; De, S.; Das, G.; *Journal of Photochemistry and Photobiology A: Chemistry*, **2021**, *418*, 113442.

35. Kang, J. H.; Lee, S. Y.; Ahn, H. M.; Kim, C.; *Sensors and Actuators B: Chemical*, **2017**, *242*, 25-34.

36. Slassi, S.; Aarjane, M.; El-Ghayoury, A.; Amine, A.; *Spectrochimca Acta A Molecular and Biomolecular Spectroscopy*, **2019**, *215*, 348-353.

37. Instrumentation for Fluorescence Spectroscopy. In *Principles of Fluorescence Spectroscopy*, Lakowicz, J. R., Ed. Springer US: Boston, MA, 2006; pp 27-61.

38. Ghosh, A.; Karedla, N.; Thiele, J. C.; Gregor, I.; Enderlein, J.; *Methods*, **2018**, *140-141*, 32-39.

39. Kapusta, P.; Machan, R.; Benda, A.; Hof, M.; *International Journal of Molecular Sciences*, **2012**, *13* (10), 12890-910.

40. Ameh, E. S.; *The International Journal of Advanced Manufacturing Technology*, **2019**, *105* (7-8), 3289-3302.

41. Dowsett, M.; Wiesinger, R.; Adriaens, M., Chapter 6 - X-ray diffraction. In *Spectroscopy, Diffraction and Tomography in Art and Heritage Science*, Adriaens, M.; Dowsett, M., Eds. Elsevier: 2021; pp 161-207.

42. Nüchter, M.; Ondruschka, B.; Bonrath, W.; Gum, A.; *Green Chemistry*, **2004**, *6* (3), 128-141.

43. J. Tomasi, B. Mennucci and R. Cammi, *Chemical Reviews*, **2005**, 105, 2999–3094.

44. D. Xie, J. Jing, Y.-B. Cai, J. Tang, J.-J. Chen and J.-L. Zhang, *Chemical Science*, **2014**, 5, 2318.

45. M. J. Frisch, G. W. Trucks, H. B. Schlegel, G. E. Scuseria, M. A. Robb, J. R. Cheeseman, G. Scalmani, V. Barone, B. Mennucci, G. A. Petersson, et al., Gaussian 09, Revision C.01, Gaussion, Inc., Wallingford CT, **2009**.

46. A. D. Becke, *The Journal of Chemical Physics*, **1993**, 98, 5648–5652.

47. C. Lee, W. Yang and R. G. Parr, *Physical Review B: Condensed Matter and Materials.*, **1988**, 37, 785–789.

Chapter 3

Pyrazinium Salts for Fluorometric/Colorimetric Detection of TNP and Anions

3.1 INTRODUCTION

Rapid and selective detection of explosives has become a pressing concern in anti-terrorism, homeland security, and environmental safety.[1] Due to their ease of production and deployment, explosive bombs have been by far the most popular type of terrorism, killing thousands of people and causing massive property damage.[2] Concerns regarding environmental contamination at the sites of production and storage of explosives have also been raised by the widespread use of explosives for military purposes.[3-5] Nitroaromatic compounds (NACs) like 2,4,6-trinitrotoluene (TNT) and 2,4-dinitrotoluene (2,4-DNT) are commonly used as military explosives and are also the main constituents of unexploded landmines across the globe.[6] 2,4,6-TNP has been a serious concern due to its hazardous effect on the environment and human health.[7-9] Amongst the primary class of nitrogen-containing explosives, TNP, commonly known as picric acid (PA), has emerged as a potential explosive superior to TNT.[10-12] TNP is extensively used as a reagent in the pharmaceutical, dye, leather, textile, and explosive manufacturing industries. It is also employed as rocket fuel, a component in matches and batteries, and a sensitizer in photographic emulsions.[13-15] It is a chemical intermediate in producing picramic acid and chloropicrin.[16-18] Due to phenol and nitro functionalities, it possesses potential health hazards such as skin and eye irritation, respiratory system damage, and liver/ kidney malfunction.[19-20] It leads to water and soil pollution due to good water solubility (14 g L^{-1} at 20 °C) and low degradation rate in the biosystem.[21-23] The low vapor pressure of TNP (5.8×10^{-9} Torr at 25 °C) indicates its existence in both vapor and particulate phases.[23-25] TNP as a soil impurity is expected to have high mobility (K_{OC} =180) due to its high-water solubility. Therefore, TNP is categorized as a severe water contaminant in the list of priority pollutants by the environmental protection agency (EPA). The allowed concentration of TNP in groundwater is 0.001 mg L^{-1} according to WHO.[25-27]

Sulfite is used as an antioxidant, antibacterial, and enzyme inhibitor in food and beverages. Ingress of sulfite to the human body is through SO_2, an environmental pollutant released by unrestricted combustion of fossil fuels and volcanic activity. In an aqueous solution at neutral pH, SO_2 exists in an equilibrium between sulfite ions (SO_3^{2-}) and bisulfite ions (HSO_3^-). The abnormal level of exogenous sulfite in humans induces the free radical reaction, changing the oxidation and antioxidant levels and causing symptoms such as allergies, asthma, diarrhea, and hypotension.[28] Abnormal endogenous sulfite has been linked to neurological diseases and lung cancer.[29] WHO

considers a daily sulfite intake of less than 0.7 mg/kg.[30] Therefore, detecting sulfite with selectivity and sensitivity in the environment is essential.

Nitrite (NO_2^-) is an important anion in human physiology and is recognized as a key signaling component in the cellular machinery and acts as a vasodilator.[31-33] Nitrite is also believed to be the natural storage form of nitric oxide (NO) in blood and tissues.[34-36] It also plays a crucial role in the nitrogen cycle in soils.[37-38] Nitrite is commonly used in various industries, such as dyeing and bleaching, as well as in agriculture as fertilizer.[39-41] The utilization of nitrite is restricted in physiological systems due to the potential negative impact it can have on human health, especially in children and pregnant women.[42] Exposure to high nitrite concentrations can lead to methemoglobinemia.[43] Furthermore, the reaction between nitrite and secondary amines found in the human body can result in the formation of N-nitrosamines, which have been linked to cancer.[44] The permissible level of nitrite in drinking water by the World Health Organization and the Environmental Protection Agency is 1 mg/L. For these reasons, nitrite detection is important from the therapeutic and toxicity perspectives.[45]

Various instrumental techniques are employed to detect TNP, such as gas chromatography-mass spectrometry (GC-MS),[46] high-performance liquid chromatography (HPLC),[47] surface-enhanced Raman spectroscopy,[48] and ion-mobility spectroscopy.[49]

The conventional methods to detect sulfite include official Monier-William's methods,[50] titrimetry,[51] electrochemistry, chromatography,[52] flow injection analysis, and capillary electrophoresis.[53] Pyrazoline,[54] Bodipy,[55] coumarin,[56] and fluorescein[57] based molecules are designed to detect SO_3^{2-}. The mechanism involved in sulfite ion detection includes hydrogen bond-inhibited C=N isomerization,[58] hydrogen bonding recognition,[59] deprotection of the levulinate group,[60] Michael addition reaction, and nucleophilic reaction.

Several analytical methods have been developed to detect NO_2^- ions viz., chemiluminescence, capillary electrophoretic, electrochemical detection, chromatographic, spectrophotometric, fluorimetric, and colorimetric methods.

Fluorescence-based detection has gained tremendous attention because of its high sensitivity, ease of use, and rapid execution time.[61-62] Several fluorescent chemosensors reported in the literature for analyte detection are associated with drawbacks such as less water solubility, analyte interference, and low detection limit. Therefore, it is necessary to develop fluorescent

chemosensors with multianalyte sensing, low detection limit, and high-water solubility. Therefore, developing a fluorescent chemosensor with aqueous solubility is vital.

The literature review of benzimidazolium, pyridinium, and imidazolium salts as water-soluble chemosensors for TNP (**Figure 3.1**) are discussed. Khungar and co-workers reported pyridinium-based chemosensor **1** for the nanomolar detection of TNP. The selective and sensitive fluorescence quenching of **1** was attributed to ground state charge transfer complex formation and resonance energy transfer. Theoretical calculations were performed to validate the molecular interactions involved.[63] Coumaryl-linked 2-methyl-imidazolium chemosensors **2** were reported for nanomolar detection of PA in an aqueous medium. The characteristic coumarin absorption maxima at 325 nm, which on the addition of PA (100 μM) showed a bathochromic shift to 340 nm. The results of UV-vis, time-resolved fluorescence, and DFT studies showed that GSC formation is the predominant mechanism for fluorescence quenching.[64] Thenmozhi and co-workers reported water-soluble fluorescent chemosensor **3** having a strong cyan-blue color assigned to the excited state intramolecular proton transfer (ESIPT) process. The probe was employed for the colorimetric and fluorescence detection of TNP in aqueous medium. The blue shift for the absorption band and the decrease in emission intensity were ascribed to the GSC formation between TNP and **3** in a 1:1 stoichiometric ratio.[65] Phenazine-tagged benzimidazolium IL salophen fluorescent chemosensor **4** was reported for TNP detection in aqueous and solid-state environments by colorimetric and fluorometric methods. The decrease in fluorescence intensities in the presence of TNP was ascribed to hydrogen bonding between the phenazine (N atoms) of **4** and the –OH group of TNP. The probe was effectively applied for the detection using an electrospun nanofiber of **4** which showed considerable variation in the fluorescence intensities of nanofibers during the detection of TNP as evident from the change in morphology.[66] Benzimidazolium-based coumaryl hydrid chemosenor **5** was employed for selective nanomolar detection of TNP. The interaction between chemosensor **5** and PA was elucidated by the red shift in the absorption band and the appearance of a new band, indicating the GSC formation with TNP. The chemosensor was also applied for the visual detection of TNP on thin layer chromatographic plate.[67]

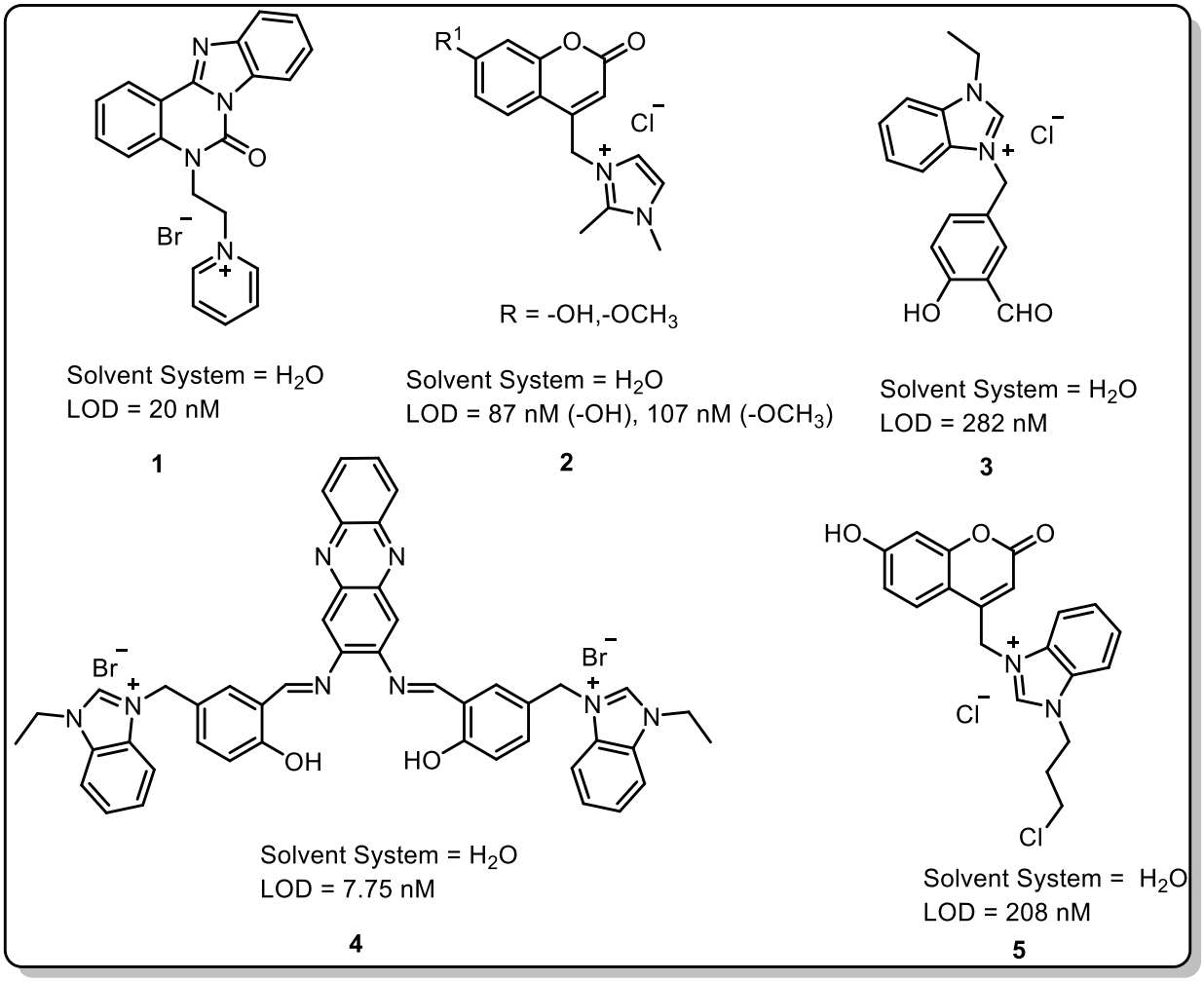

Figure 3.1: Chemosensors for detection of TNP

Different chemosensors for sulfite detection are shown in **Figure 3.2**. A colorimetric and NIR fluorescent chemosensor **6** incorporating electron-donating 7-diethylamino-azacoumarin conjugated with an electron-withdrawing pyridinium moiety was reported. The addition of sulfite led to disruption in conjugation inhibiting the ICT process. A fluorescence chemosensor **7** displayed observable chromogenic and NIR fluorescence turn-on response on the interaction of SO_3^{2-} with quinolinium skeleton via 1, 4-Michael addition reaction.[68] A bis-chalcone-based colorimetric probe **8** was used for the detection of sulfite ions in aqueous medium. The presence of a cationic micellar medium promoted the Michael addition reaction between the probe and SO_3^{2-} ions.[69] The chemosensor **9** appended with phenanthrene imidazole fluorophore showed fluorescence enhancement on the addition of sulfite ions. A nucleophilic addition mechanism blocked the π-conjugation in the probe and thus hindered the ICT.[70] Two off–on ratiometric

pyrazoline-based sensors **10, 11** exhibited weak charge transfer fluorescence which was blocked after the attack of sulfite ions to the α,β-unsaturated ketone part.[71]

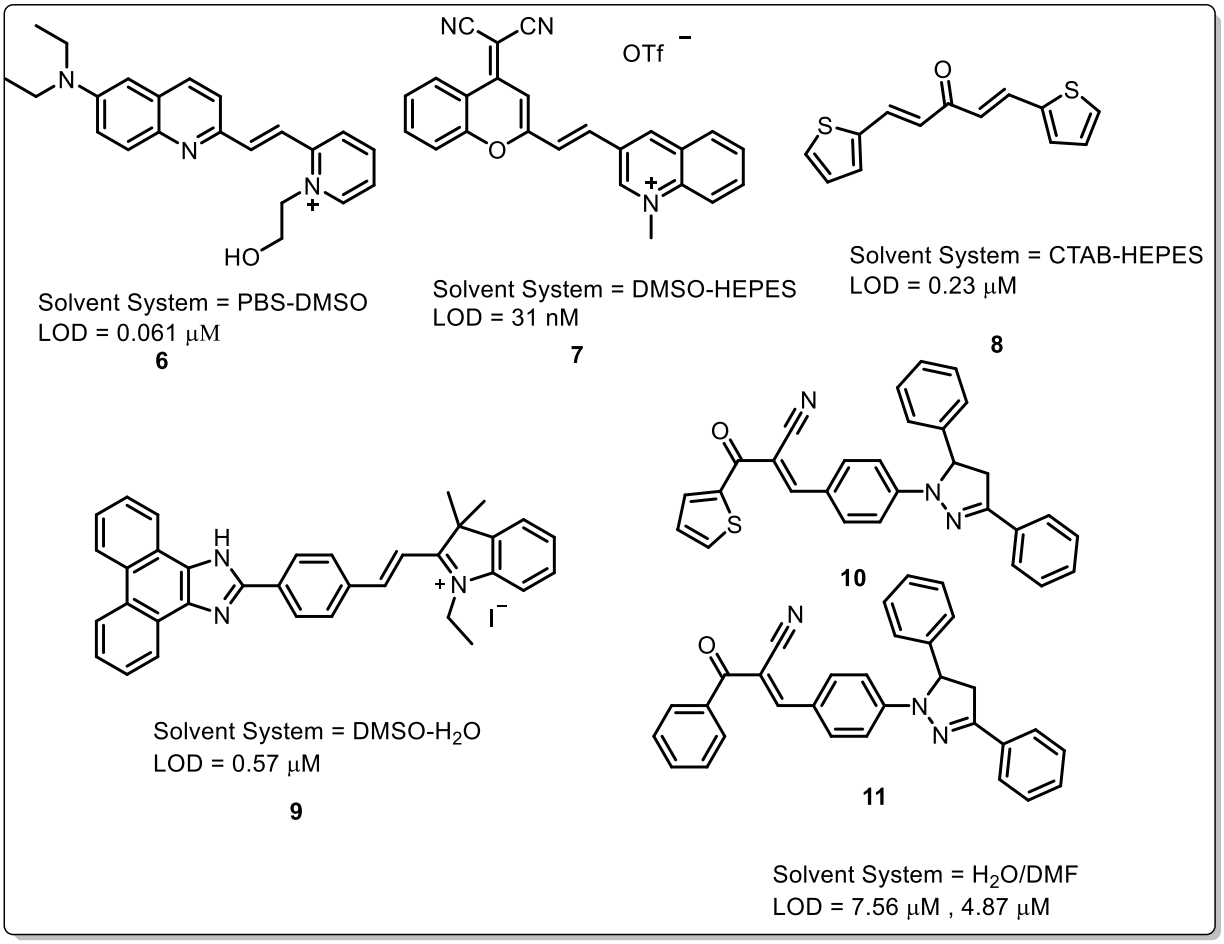

Figure 3.2: Chemosensors for detection of sulfite ions

Figure 3.3 shows different molecules reported for nitrite ion detection based on the fluorescence method. A chemosensor **12** using a benzimidazole that selectively detected nitrite through fluorescence quenching stemming from an unusual nitration reaction was reported.[72] A carboxyimide derivative **13** was reported as a colorimetric and fluorogenic sensor to determine NO_2^- with a rapid response. The fluorescence enhancement upon the addition of NO_2^- was due to PET and reduced ICT effect on the formation of the triazole-based product. IR780 dye as a near-infrared (NIR) probe **14** was utilized for its colorimetric response to NO_2^- ions with excellent selectivity. The mechanism was attributed to the production of nitric oxide radical (•NO) from HNO_2 which further oxidized to $•NO_2$ in the presence of oxygen. In acidic conditions, the reaction between IR780 and NO_2^- followed a radical pathway.[73] 2-(1H-benzimidazol-2-yl) aniline-based

chemosensor **15** underwent diazotization followed by intramolecular cyclization to form a non-fluorescent benzotriazine derivative, thereby rendering **15** as a turn-off probe for nitrite ion.[74] A near-infrared-emitting probe **16** for detecting nitrite based on an intramolecular azo-coupling mechanism was developed. Under strong acidic conditions, the 4-(2-aminophenyl) moiety of **16** underwent a diazotization reaction in the presence of nitrite followed by intramolecular electrophilic aromatic substitution reaction between the aryldiazonium moiety and the 7-(diethylamino) coumarin moiety to yield a heterotetracyclic fluorophore. Finally, under strongly acidic conditions, the pyridazine nitrogen became protonated to form a purple dye. Upon reaction with nitrite under acidic conditions, the color of the fluorescence changed from colorless to red.[75]

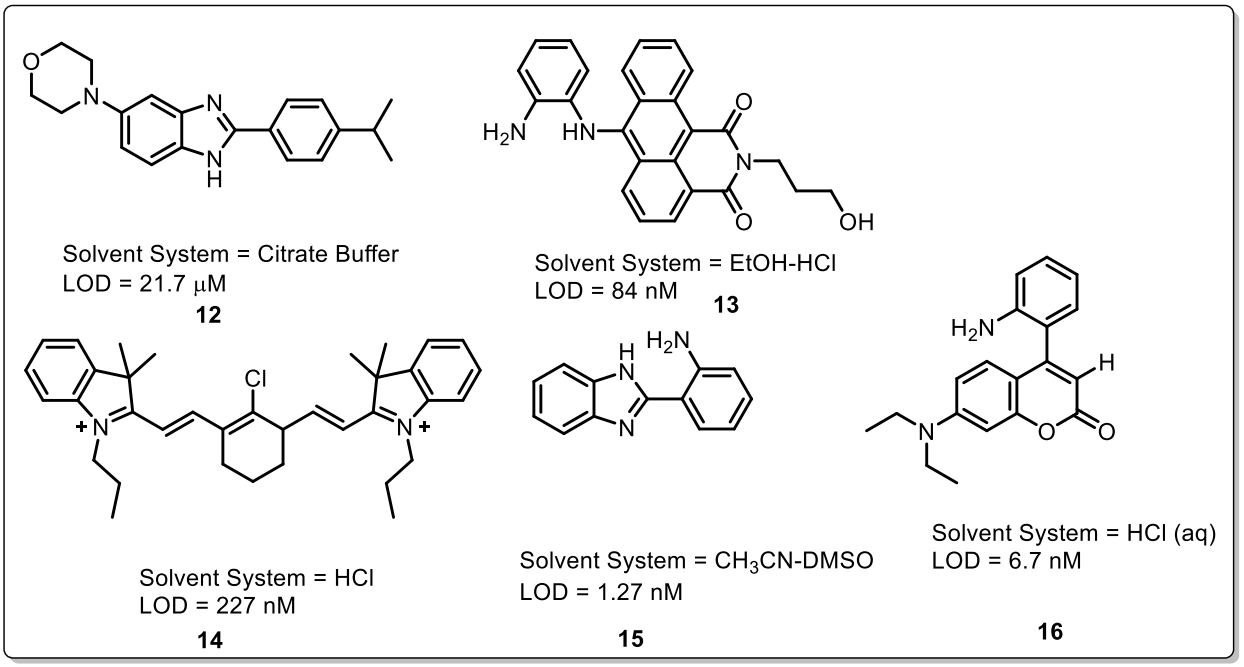

Figure 3.3: Chemosensors for detection of nitrite ions

Pyrazinium salts as chemosensors are yet to be explored in the field of chemosensors. Pyrazines are a class of photostable molecules with wide application in luminescent materials, semiconductors, and sensors.[76-78] Moreover, the pyrazine nucleus offers scope for the quaternization of one of the N atoms enhancing its hydrophilicity thus enabling the sensing in aqueous medium. In order to rationalize the ease of synthesis, desirable photophysical properties, and chemosensing in an aqueous medium, we devised a straightforward approach to synthesize pyrazinium salts, **BTPyz, BPPyz,** and **MPyPyz** under solvent-free conditions for detection of TNP and anions.

SECTION 3A

Thiophene-Appended Pyrazinium Salt for Detection of TNP

In this section a thiophene-appended pyrazinium salt, **BTPyz** is synthesized and well characterized. It is utilized for the detection of TNP via turn-off mechanism. It is also employed for TNP detection in real water and soil samples.

3A.1 EXPERIMENTAL SECTION

3A.1.1 Synthesis of 2,6-bis(thiophen-2-yl) pyrazine (TPyz)

An oven-dried glass vial was charged with 2,6-dichloropyrazine (0.340 mmol), thiophene-2-boronic acid (0.748 mmol), $Pd(OAc)_2$ (3.75 mg, 0.017 mmol), K_2CO_3 (92.75 mg, 0.680 mmol) and dimethylformamide (2.5 mL). The reaction was irradiated in the microwave at 120 °C for 50 min. After completion of the reaction (monitored by TLC), the reaction mixture was allowed to attain room temperature. The reaction mixture was poured into water (20 mL) and extracted with ethyl acetate (3 × 15 mL). The combined organic layers were dried over anhydrous Na_2SO_4 and evaporated under reduced pressure. The resulting crude mixture was purified by column chromatography (silica gel 100–200 mesh) using ethyl acetate/*n*-hexane (5:95) as an eluent. **TPyz** was obtained as a white solid, (60 mg, 73% yield); mp = 95–98 °C; ^{1}H NMR (400 MHz, $CDCl_3$) δ 8.78 (s, 2H), 7.77 (dd, *J* = 3.6, 1.2 Hz, 2H), 7.54 (dd, *J* = 4.8, 1.2 Hz, 2H), 7.21 (dd, *J* = 5, 3.8 Hz, 2H). ^{13}C{^{1}H} NMR (100 MHz, $CDCl_3$) δ 150.9, 140.4, 136.2, 130.5, 129.5, 127.2; HRMS (ESI) *m*/*z*: $[M+H]^+$ calcd for $C_{12}H_8N_2S_2$, 245.0129, found 245.0191.

3A.1.2 Synthesis of 1-benzyl-3,5-di(thiophen-2yl) pyrazin-1-ium bromide (BTPyz)

A mixture of **TPyz** (50 mg, 0.204 mmol) and benzyl bromide (42.055 mg, 0.244 mmol) were taken in round bottom flask and stirred for 8 h at 75 °C. Reaction mixture was washed with ethyl acetate. The obtained bright yellow solid was filtered and dried under vacuum, (59 mg, 70% yield); mp = 220–226 °C; ^{1}H NMR (400 MHz, DMSO-d_6) δ 9.55 (s, 2H), 8.16 (dd, *J* = 3.6, 1.2 Hz, 2H), 7.99 (dd, *J* = 4.6, 1.0 Hz, 2H), 7.71 – 7.70 (m, *J* = 3.6 Hz, 1H), 7.69 (d, *J* = 2 Hz, 1H), 7.48 (d, *J* = 2.0 Hz, 1H), 7.47 (d, *J* = 2.0 Hz, 2H), 7.35 (dd, *J* = 5.0, 3.8 Hz, 2H), 5.82 (s, 2H). ^{13}C{^{1}H} NMR (100 MHz, DMSO-d_6) δ 53.1, 138.4, 134.4, 133.1, 131.2, 130.2, 130.1, 130.0, 129.6, 129.5, 65.2; HRMS (ESI) *m*/*z*: $[M-Br]^+$ calcd for $[C_{19}H_{15}N_2S_2]^+$, 335.0586; found 335.0665.

3A.1.3 Synthesis of BTPyz-TNP complex

To a solution of **BTPyz** (20 mg, 0.049 mmol) in 1.0 mL ethanol, TNP (55.1 mg, 0.245 mmol) was added dropwise and stirred for 6 h. The yellowish-green precipitate obtained was filtered, washed with ethanol and ether successively and dried under vacuum, (25 mg, 92.5% yield); mp = 235–240

°C; ^{1}H NMR (400 MHz, DMSO-d_6) δ 9.55 (s, 2H), 8.58 (s, 2H), 8.17 – 8.11 (m, 2H), 7.98 (dd, *J* = 5.2, 1.2 Hz, 2H), 7.73 – 7.64 (m, 2H), 7.47 (dd, *J* = 5.0, 1.8 Hz, 3H), 7.34 (dd, *J* = 5.0, 3.8 Hz, 2H), 5.81 (s, 2H). The crystal of the complex was obtained in an acetonitrile and methanol solvent mixture.

3A.2 RESULTS AND DISCUSSION

3A.2.1 Synthesis and Characterization

The synthetic route for **BTPyz** is outlined in Scheme 3A.1. In the first step**,** 2,6-bis(thiophen-2-yl) pyrazine (**TPyz)** was synthesized via a microwave-assisted palladium-catalyzed reaction of 2,6-dichloropyrazine with thiophene-2-boronic acid and was characterized by different spectroscopic techniques.

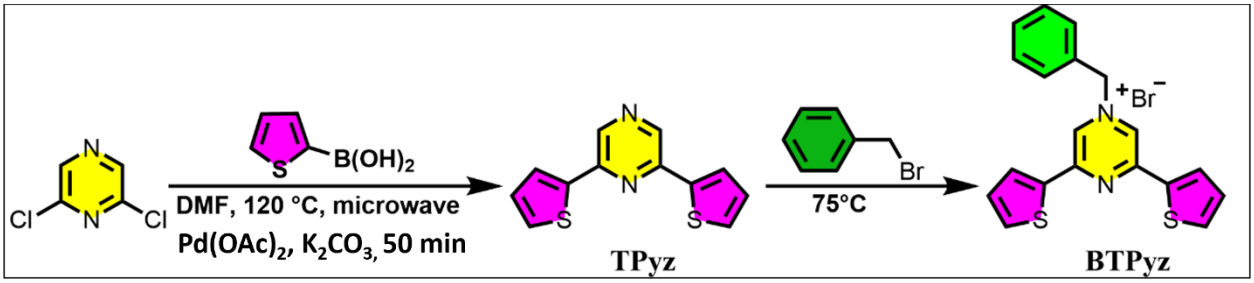

Scheme 3A.1: Synthetic route for **BTPyz**

TPyz on nucleophilic addition reaction with benzyl bromide provided **BTPyz.** The synthesized **TPyz** and **BTPyz** were well characterized by ^{1}H, ^{13}C NMR spectroscopy, high-resolution mass spectrometry. In the ^{1}H NMR spectra of **TPyz**, the appearance of singlet at 8.77 ppm for pyrazinium proton and aromatic protons 7.19–7.77 ppm confirmed the synthesis of Suzuki coupling product (**Figure A1, Appendix-A**). The ^{13}C NMR also supported the formation **TPyz**, with pyrazinium carbon at 155.9 ppm and aromatic carbons in the range of 129.54–153.16 ppm (**Figure A2, Appendix-A**). The HRMS of **TPyz** exhibited a peak at *m/z* = 245.0191 (*m/z*, calcd. 245.0129) due to [**TPyz**+H]$^{+}$ (**Figure A3, Appendix-A**).

The ^{1}H NMR of **BTPyz** showed a singlet at 5.82 ppm due to benzylic proton, and thirteen aromatic protons were observed in the range of 7.35–9.56 ppm (**Figure 3A.1**). The ^{13}C NMR also supported the formation **BTPyz**, benzylic carbon appeared at 65.2 ppm, and aromatic carbons were found in the range of 129.54–153.16 ppm (**Figure 3A.2**). In ESI-MS spectra of **BTPyz**, a peak corresponding to [**BTPyz**-Br] $^{+}$ appeared at *m/z* 335.0665 (*m/z*, calcd. 335.0586) (**Figure 3A.3**).

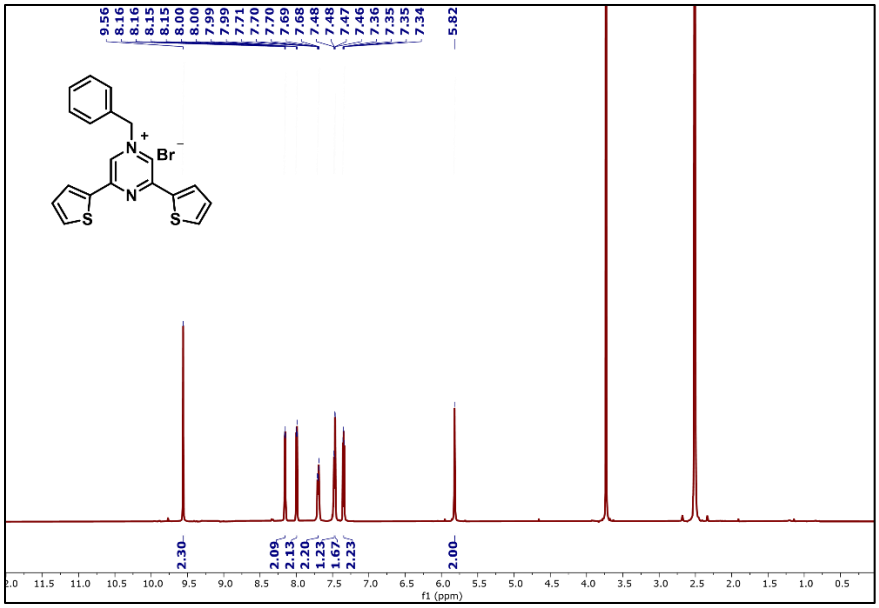

Figure 3A.1: ^{1}H NMR of **BTPyz** in DMSO-d_6

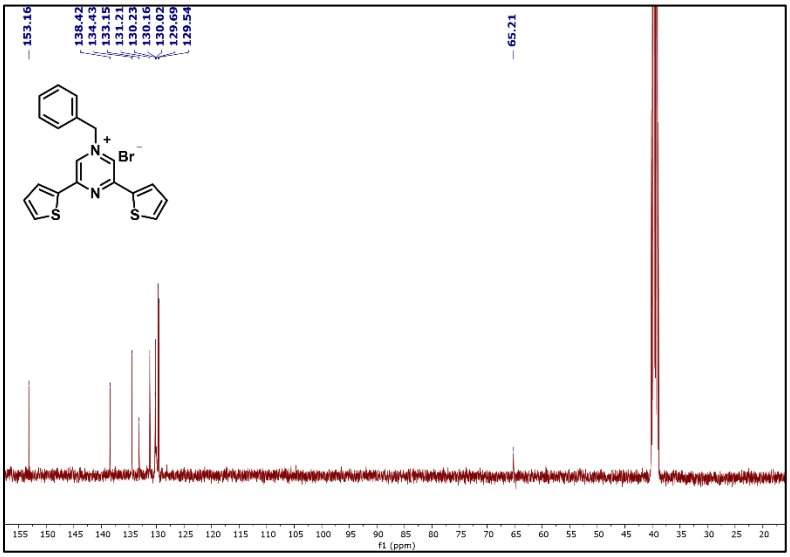

Figure 3A.2: ^{13}C NMR of **BTPyz** in DMSO-d_6

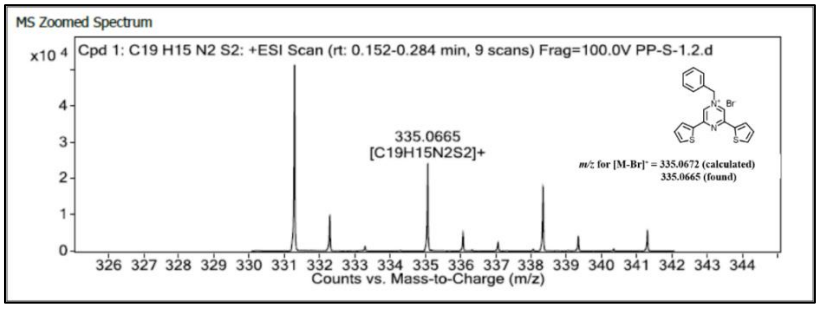

Figure 3A.3: HRMS of **BTPyz**

The structure of **BTPyz** was further confirmed by single-crystal X-ray crystallography. The single crystal of **BTPyz** was obtained from an acetonitrile-methanol solvent mixture. **BTPyz** ($C_{19.5}H_{17}BrN_2O_{0.5}S_2 = 2C_{19}H_{15}BrN_2S_2.1CH_3OH$) crystallized in the monoclinic $P2_1/n$ space group. Its asymmetric unit shown in **Figure 3A.4** consist of two organic molecular cations and two bromide counter anions, along with one methanol solvent molecule. The single-crystal XRD data and cell parameters are summarized in **Table A2**, **Appendix-A**.

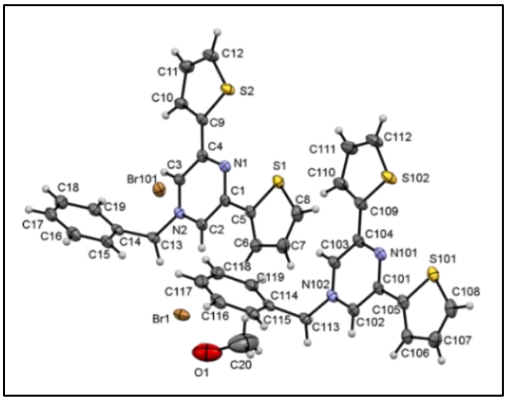

Figure 3A.4: ORTEP diagram of **BTPyz (**CCDC 2110747) showing thermal ellipsoids at 50% probability level

The UV-vis absorption spectra of **BTPyz** in aqueous solution showed two well-separated absorption bands at 305 nm and 406 nm ascribed to π-π^* and n-π^*, respectively. Upon excitation at 406 nm, **BTPyz** exhibited emission maxima at 524 nm (Φ = 0.47) with yellowish-green fluorescence (**Figure 3A.5a**). The UV-vis and emission spectra of **BTPyz** were also recorded in MeOH and ACN, minimal shifts were observed in the absorption bands, implying no change in the ground state energy distribution of **BTPyz**. In the emission spectra, due to a decrease in the solvent polarity, the peak shifted to 514 nm in MeOH and 519 nm in ACN (**Figure 3A.5b**).

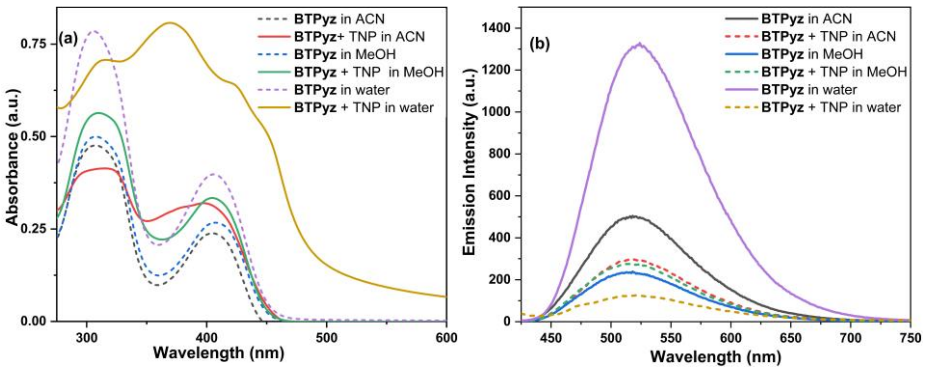

Figure 3A.5: (a) Absorption (b) Fluorescence spectra of **BTPyz** (5×10^{-5} M) towards TNP in different solvents

3A.2.2 Response of BTPyz toward TNP

Due to its fluorescent nature and water solubility, **BTPyz** was explored as a chemosensor for TNP in aqueous medium. The fluorescence intensity of **BTPyz** decreased with the addition of TNP, indicating **BTPyz** as a fluorescent turn-off chemosensor. To inspect the selectivity of TNP, the studies were executed with other analytes, viz. BA, *p*-cresol, 2,4-DNP, 3,4-DNT, NB, 4-NBA, NM, 4-NP, and 4-NT (**Figure 3A.6a**). In the UV-vis spectra, the intensity of band at 305 nm increased on the addition of 4-NP and 2,4-DNP while a new absorption appeared at 370 nm on the addition of TNP. All analytes exhibited negligible fluorescence quenching except NP and 2,4-DNP (**Figure 3A.6b**). The fluorescence quenching efficiencies of compounds containing only one hydroxyl group followed the order TNP>2,4-DNP>NP>*p*-cresol, which is in good agreement with the acidity of these compounds. Quenching percentage for TNP, NP, 2,4-DNP and *p*-cresol were found to be 93.4%, 17.4%, 37% and 1%, respectively. Therefore, **BTPyz** displayed good selectivity for TNP compared to the other analytes (**Figure A4, Appendix-A**).

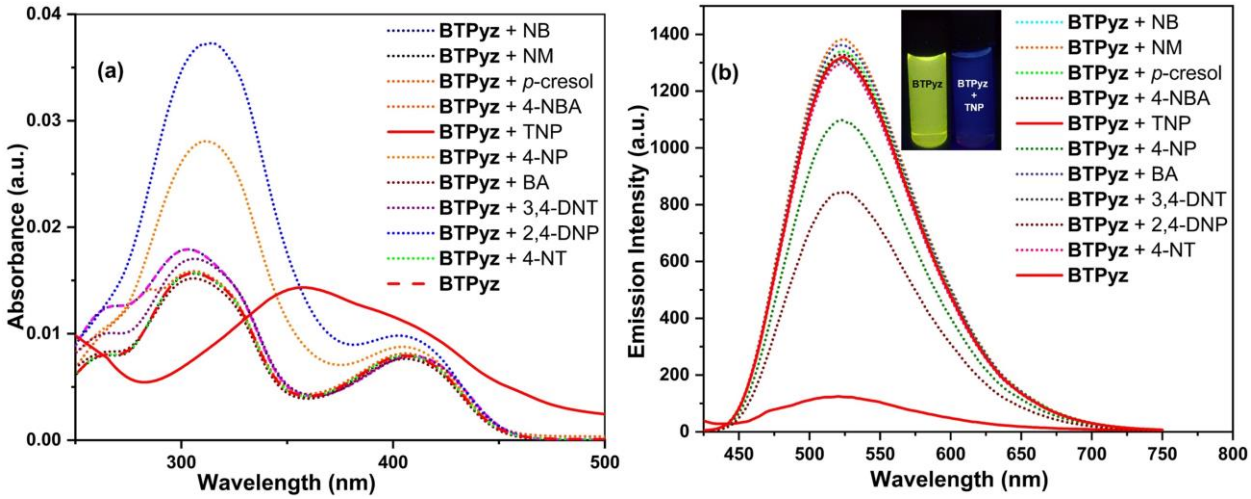

Figure 3A.6: (a) Absorption (b) fluorescence spectra of **BTPyz** (5×10^{-5} M) towards organic analytes in water

For UV-vis spectral titration, 5×10^{-5} M solution of the **BTPyz** was titrated with TNP solution. The intensity of absorption band at 305 nm decreased with a concomitant increase in the intensity of band at 370 nm, and an isosbestic point was observed at 331 nm (**Figure 3A.7a**). In the fluorescence titration studies, upon incremental addition of TNP, a gradual quenching in the initial fluorescence emission intensity was observed (**Figure 3A.7b**).

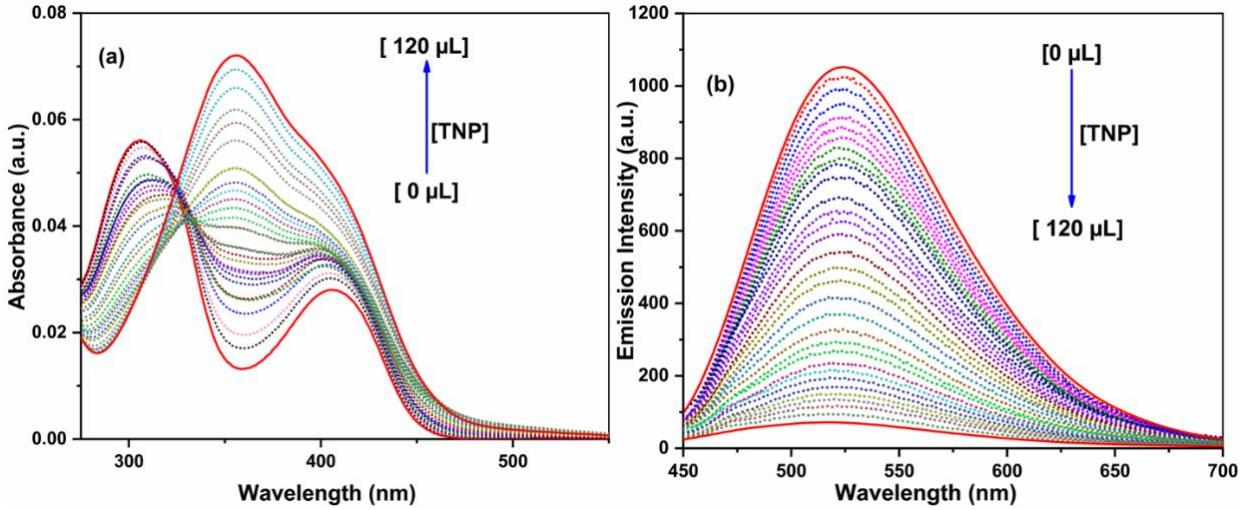

Figure 3A.7: Effect on the (a) absorption (b) emission spectrum of **BTPyz** (5×10^{-5} M) in water upon incremental addition of TNP (0.0-120.0 μL)

The limit of detection for TNP using the equation $3\sigma/K$, where σ is the standard deviation of 10 blank measurements and K is the slope from the intensity versus sample concentration plot, was calculated to be 11.6 nM (**Figure 3A.8a**). The Stern-Volmer constant was calculated to gain insight into the fluorescence quenching by TNP (**Figure 3A.8b**). The Stern-Volmer (S-V) equation is expressed as $I_0/I = 1 + K_{sv}[Q]$, where I_0 and I are the fluorescence intensities in the absence and presence of the analyte (TNP), respectively, [Q] is the analyte concentration, and K_{sv} is the Stern-Volmer constant. The Stern-Volmer constant was found to be 3.8×10^4 M^{-1}**.**

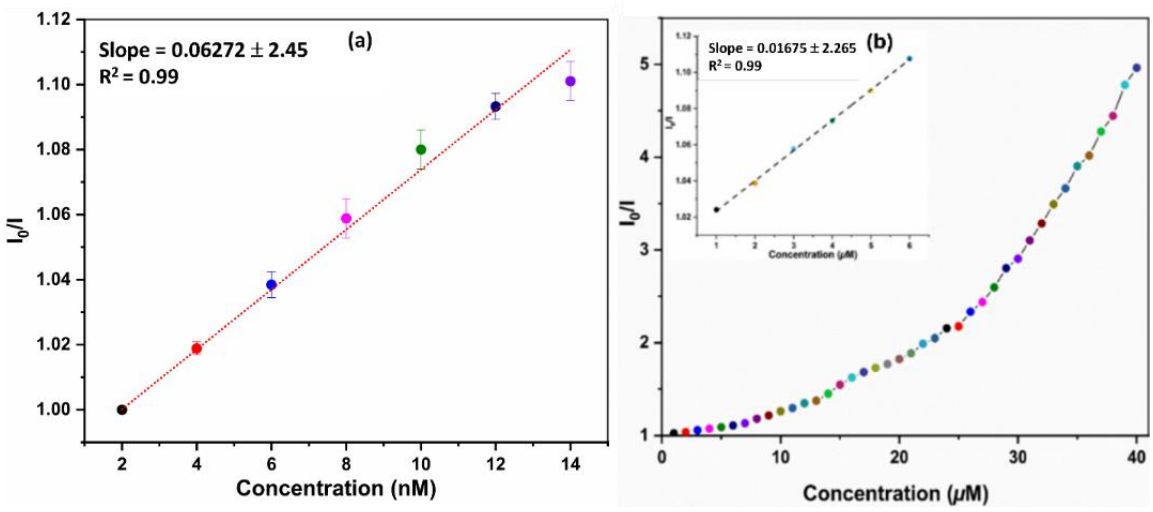

Figure 3A.8: (a) Calibration curve with error bar for calculating Limit of Detection for TNP (b) Stern−Volmer plot of **BTPyz** using TNP as a quencher

The linear quenching response at lower concentration upon incremental addition of TNP indicated the static quenching, which can be explained by the formation of the ground-state charge-transfer

complex. The appearance of a new absorption band at 370 nm and a decrease in emission peak at 524 nm also suggested the formation of the ground-state charge-transfer complex by deprotonation of phenolic -OH of TNP and consequential anion exchange with Br^- of **BTPyz**. At higher concentration, deviation of S-V curve from linearity, indicated dynamic quenching due to the resonance energy transfer (RET).

The maximum overlap between the absorption spectrum of TNP and the emission spectrum of **BTPyz** also indicated the highest probability of resonance energy transfer as compared to other analytes. The values of the overlap integral (J_λ = 1.49 × 10^{14} M^{-1} cm^{-1} nm^{-4}) and Förster distance (R_0 = 33.09 Å) for **BTPyz**-TNP indicated a significant RET process (**Figure 3A.9a**).

The spectral overlap among emission and/or the excitation spectrum of the fluorophore with the absorbance of quencher also suggests the possibility of IFE. Therefore, to check its presence, corrections were performed using the eq. (i).

$$I_{corr}/I_{obs} = 10^{(A_{ex}+A_{em})/2} \qquad \text{(i)}$$

where I_{corr} and I_{obs} are the emission intensities after and before IFE corrections, A_{ex} and A_{em} are the absorbances of the sensing system at the excitation and emission wavelength of **BTPyz**.[48] Insignificant changes in the emission intensity and quenching efficiency after performing IFE corrections suggested the absence of IFE (**Figure 3A.9b**).

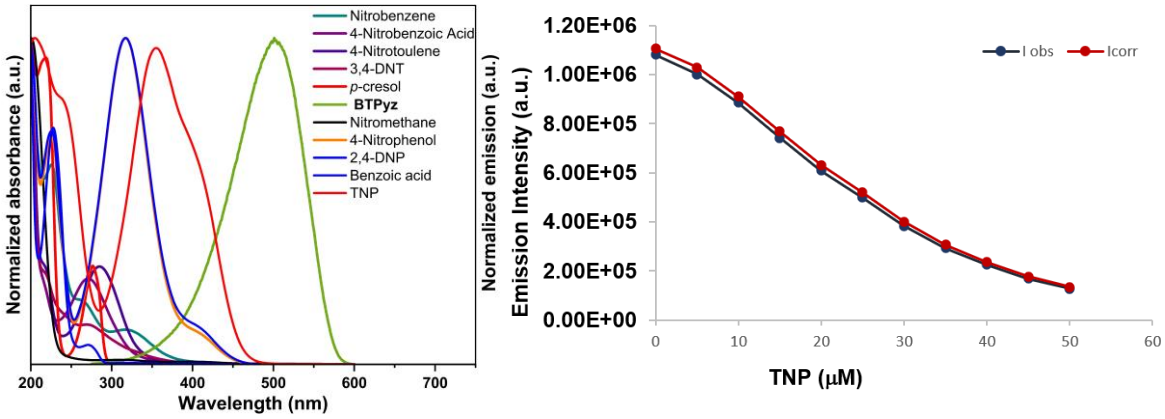

Figure 3A.9: (a) Spectral overlap between the normalized emission spectrum of **BTPyz** and normalized absorption spectra of different analytes (b) Emission intensity of **BTPyz** observed and after inner filter effect corrections

The decay profile from lifetime studies also supported the possibility of energy transfer mechanism. **BTPyz** showed a lifetime of 0.962 ns, which decreased to 0.526 ns upon addition of 50 μM TNP due to the dynamic quenching process (**Figure 3A.10**).

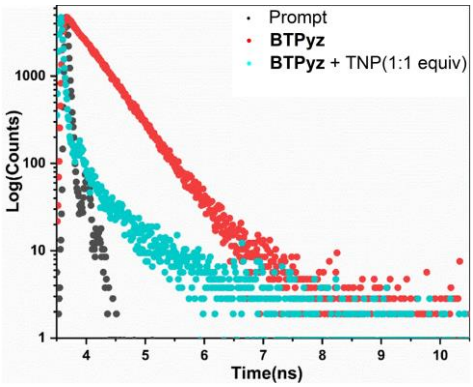

Figure 3A.10: Fluorescence lifetime decay curves of **BTPyz** and **BTPyz**-TNP

To validate the binding mode of the sensor, the **BTPyz**-TNP complex was prepared at room temperature and was characterized by ^{1}H NMR and single-crystal XRD. The ^{1}H NMR of the complex indicated the presence of TNP with a singlet at 8.58 ppm corresponding to picrate anion (**Figure 3A.11**) The proton signal at 9.56 ppm in **BTPyz** shifted downfield to 9.65 ppm in the complex. A slight shifting in the aromatic proton signals also indicated the formation of **BTPyz**-TNP complex. The relative integration of picrate protons to the **BTPyz** protons indicated a 1:1 ratio in the complex, which was confirmed by single-crystal XRD.

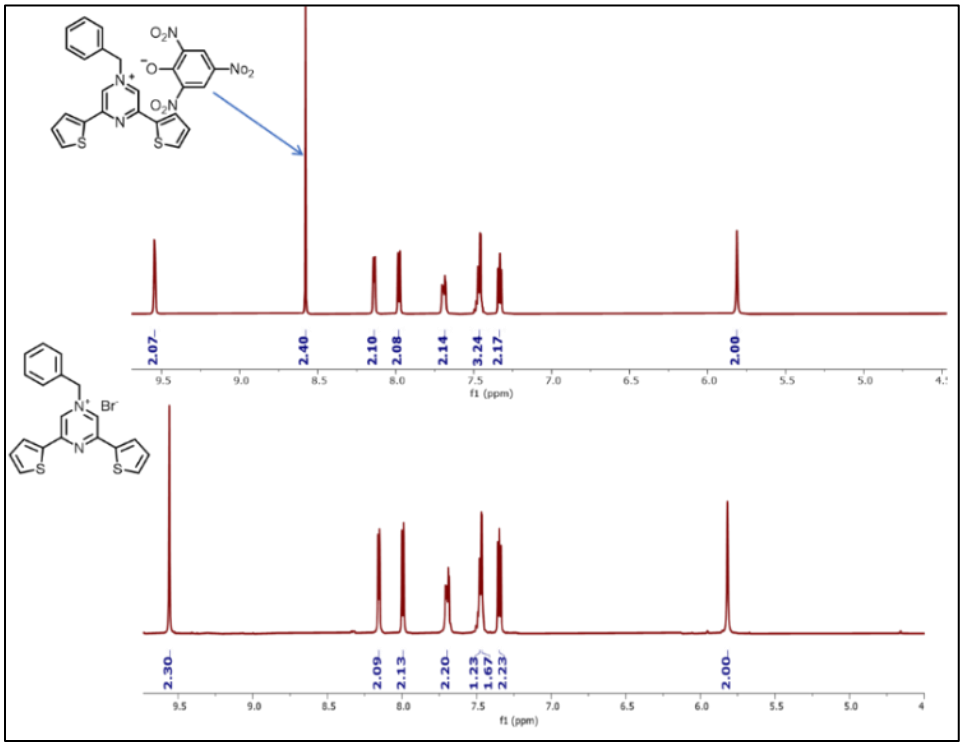

Figure 3A.11: ^{1}H NMR spectra of **BTPyz** with TNP in DMSO-d_6

The **BTPyz**-TNP complex with the molecular formula ($C_{25}H_{17}N_5O_7S_2$) crystallized in the monoclinic *C*2/c space group with one organic molecular cation, one picrate anion (**Figure 3A.12**, **Table A2, Appendix-A**).

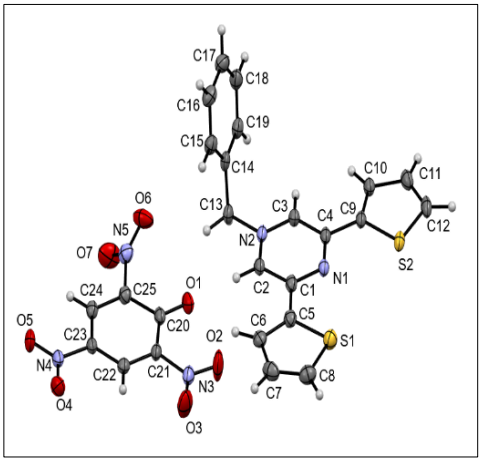

Figure 3A.12: ORTEP diagram of **BTPyz**-TNP complex (CCDC 2168277) showing thermal ellipsoids at 50% probability level

The HRMS of **BTPyz**-TNP revealed *m/z* peaks in negative and positive modes at 335.0658 (*m/z*, calcd. 335.0586) and 227.9525 (*m/z*, calcd. 227.9893) due to cationic [**BTPyz**-Br]$^+$ (**Figure 3A.13a**) and anionic [TNP-H]$^-$ (**Figure 3A.13b**) species, respectively.

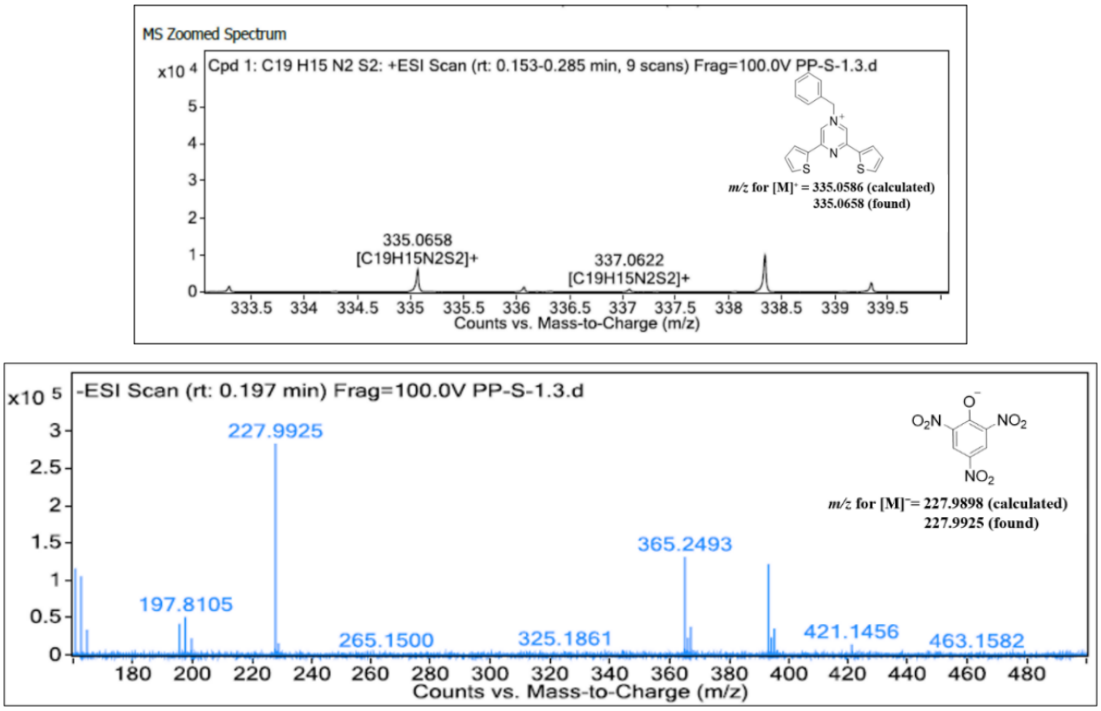

Figure 3A.13: HRMS of **BTPyz**-TNP complex in (a) negative and (b) positive modes

The pH-dependent sensing behavior of **BTPyz** was also studied. The fluorescence intensity was measured before and after TNP addition in different pH solutions. The maximum fluorescence quenching was found in the pH range of 3–10. No change was observed in the fluorescence intensity of **BTPyz** at different pH proposing its stability under such conditions (**Figure 3A.14a**). To rule out the fluorescence quenching by the acidity effect of TNP, the emission spectrum of **BTPyz** with TFA was recorded (**Figure 3A.14b**). TNP as a strong acid readily dissociates in an aqueous medium facilitating the electrostatic interaction between cationic **BTPyz** and TNP. TFA ($pK_a \sim 0.52$), being stronger acid than TNP ($pK_a \sim 0.38$), did not affect the emission spectra of **BTPyz**, contradicting the possibility of quenching by acidity effect. The efficient charge transfer and/or energy transfer mechanism facilitated by the close proximity of **BTPyz** and TNP *via* electrostatic interaction led to excellent fluorescence quenching towards TNP.

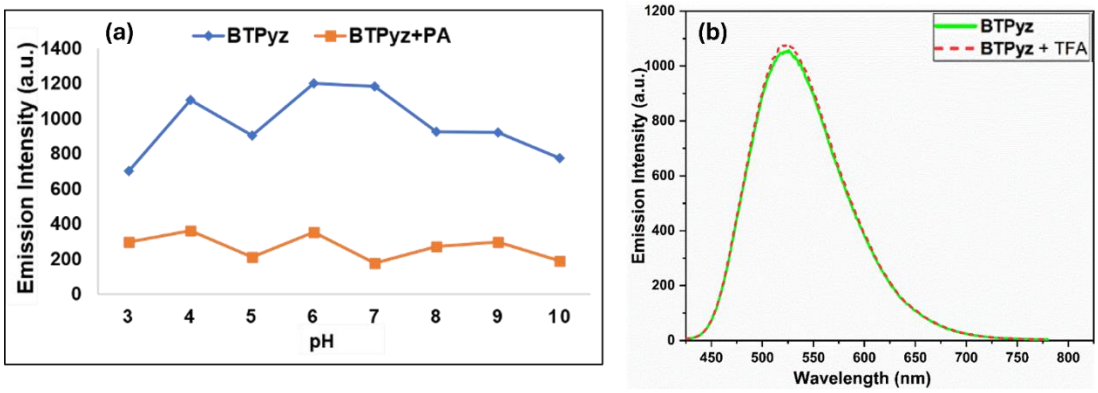

Figure 3A.14: (a) Effect of pH on fluorescence intensity of **BTPyz** (5×10^{-5} M) (b) Fluorescence spectra of **BTPyz** (5×10^{-5} M) and **BTPyz** with TFA

To study the selectivity of **BTPyz** in competitive environments, the interferences from metal ions (Na^+, Mg^{2+}, Al^{3+}, K^+, Ca^{2+}, Mn^{2+}, Fe^{2+}, Fe^{3+}, Co^{2+}, Ni^{2+}, Cu^{2+}, Zn^{2+}, Ag^+, Cd^{2+}, Hg^{2+}, Pb^{2+}, La^{3+}, Eu^{3+}, Gd^{3+} and Yb^{3+}), anions (F^-, Cl^-, Br^-, I^-, NO_3^-, HCO_3^- and CH_3COO^-) and organic analytes (BA, *p*-cresol, 2,4-DNP, 3,4-DNT, NB, 4-NBA, NM, 4-NP, and 4-NT) were evaluated at equimolar concentrations of TNP and these analytes in aqueous medium, and no apparent interference was observed (**Figure 3A.15**).

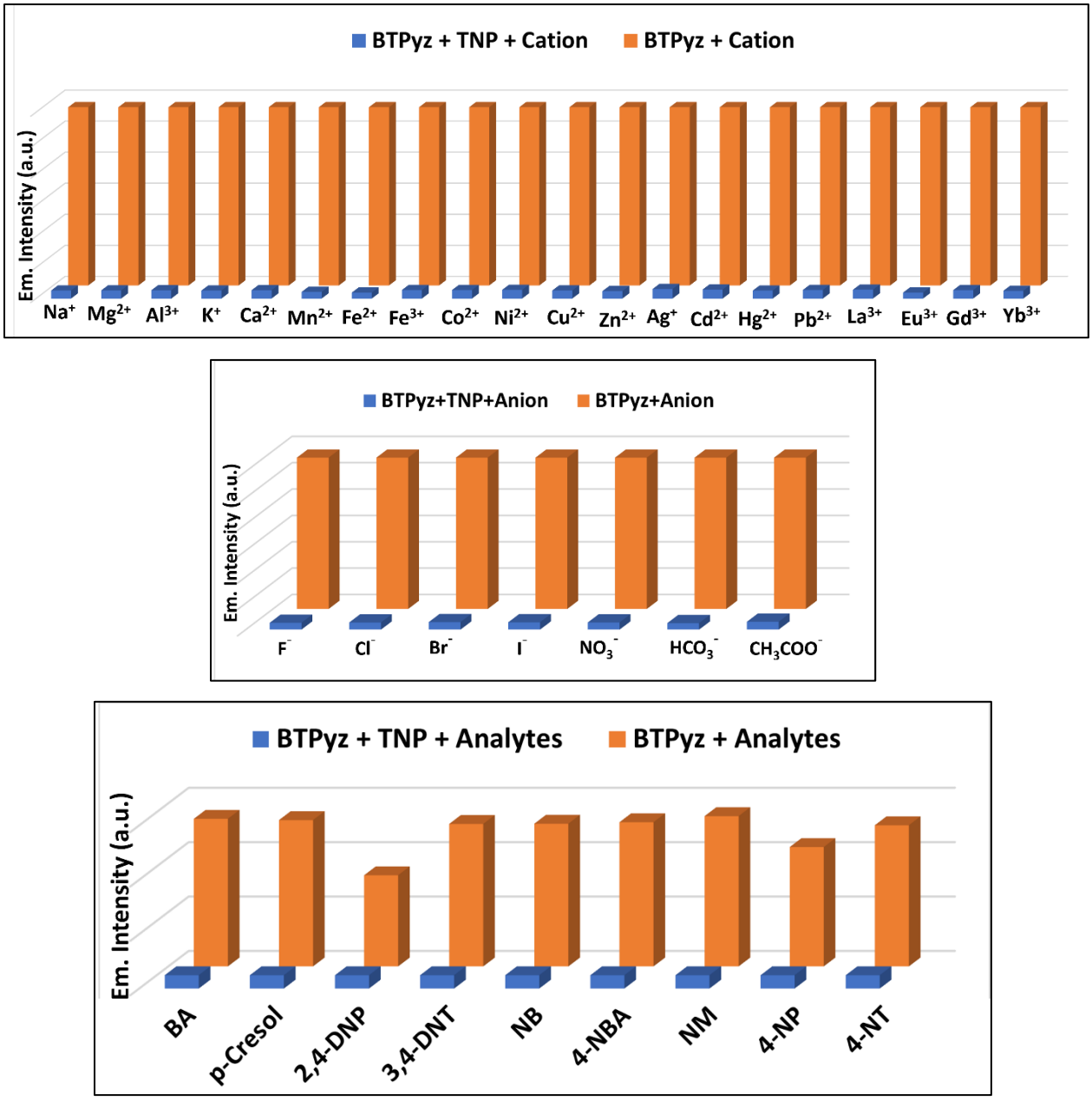

Figure 3A.15: Selectivity of **BTPyz** (5×10^{-5} M) towards TNP in the presence of (a) anions (b) cations (c) organic analytes

Density functional theory (DFT) calculations were performed to explain the ground-state electron transfer mechanism between the **BTPyz** and picrate anion. The geometrical structures were optimized using the B3LYP basis set and standard 6-311+G(d,p) in the gas phase. The energy calculation analysis revealed that the energies of HOMO and LUMO of cationic **BTPyz** were -9.5143 and -6.276 eV, whereas for picrate anion were -3.424 eV and +0.1417 eV, respectively (**Figure 3A.16**). Therefore, an electron from HOMO of picrate can be favourably transferred to

LUMO of **BTPyz**, which results in the highest quenching efficiency. Whereas the energy profile of other analytes showed HOMO at low energy levels compared to LUMO of **BTPyz** (**Figure A5, Appendix-A**).

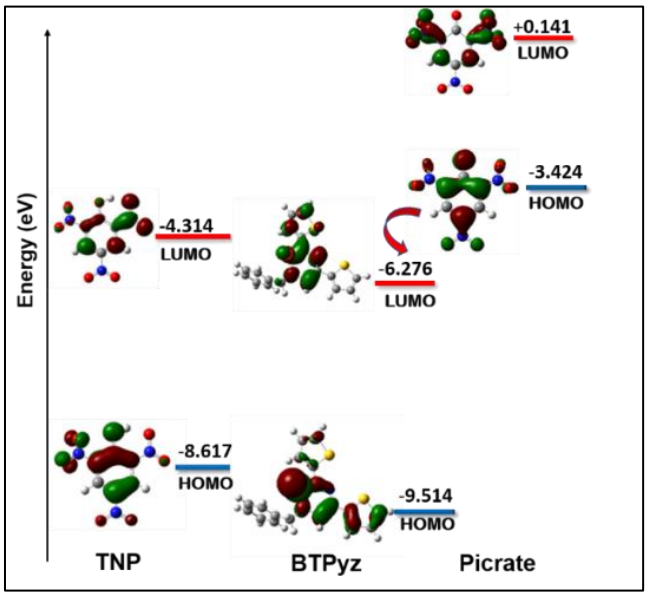

Figure 3A.16: Energy levels and frontier molecular orbitals of TNP, **BTPyz** and picrate

3A.2.3 Analytical Applications

Detection of TNP in environmental specimen

To assess the effectiveness of the proposed method in the presence of interferences, the probe was examined for detection of TNP in real samples from various sources. Each sample was spiked with 20 μM of TNP. The recovery rate was almost 100%, and the relative standard deviation was less than 5%, demonstrating the feasibility of the sensor in the real water sample analysis (**Table 1**).

Table 3.1 Detection of TNP in real water samples by **BTPyz**

Sample	TNP spiked (μM)	Recovery (%)	RSD
River water	20	99.75	0.10
Tap water	20	99.00	0.25
Mineral water	20	99.65	0.30

Implementation of test paper strips

In security scanning and prompt identification, visual detection of trace amounts of TNP is essential. Paper test strips were prepared by dipping commercially available Whatman filter paper in a concentrated solution of **BTPyz** for 10 min and drying for 2 h. 10 μL of TNP solutions (10^{-3}-10^{-6} M), were drop casted on these test strips and fluorescence quenching was observed by the naked eye and illumination under a 365 nm UV lamp (**Figure 3A.17**).

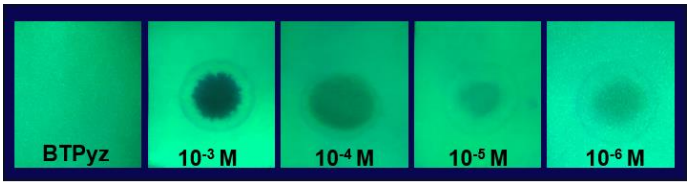

Figure 3A.17: Photographs of test paper strips for detection of TNP under 365 nm UV light

Detection of TNP in the soil is highly appreciable for tracking its accumulation in the ecosystem. **BTPyz** solution with soil sample in the absence of TNP showed no change in the emission intensity. In contrast, the soil samples with increasing amounts of TNP revealed increase in fluorescence quenching (**Figure 3A.18**).

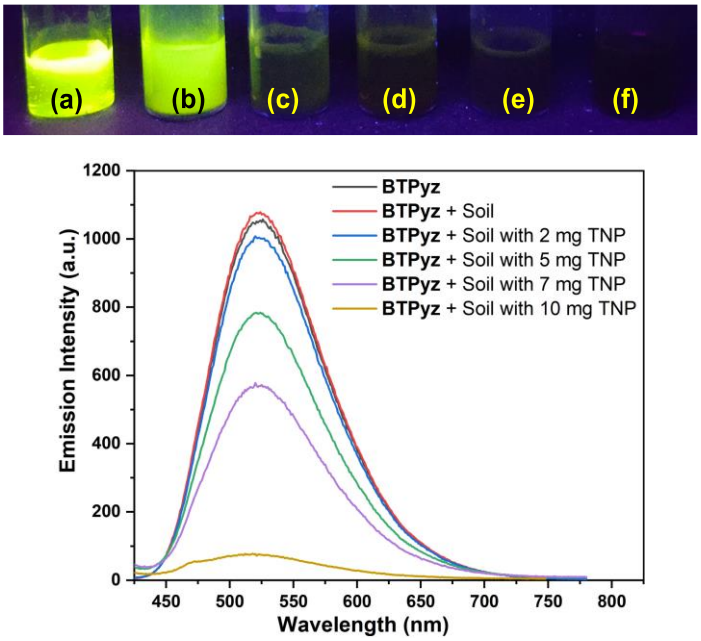

Figure 3A.18: TNP sensing in soil (a) only **BTPyz** (b) **BTPyz** and soil sample without TNP (c) (d) (e) (f) **BTPyz** with soil containing 2 mg, 5 mg, 7 mg and 10 mg TNP, respectively (top) Fluorescence quenching of TNP in soil samples (bottom)

A comparison of **BTPyz** with chemosensors reported in the literature is given in **Table A5, Appendix A**.

3A.3 CONCLUSION

A fluorescent pyrazinium salt, **BTPyz** was designed and synthesized and its photophysical properties were investigated in detail. The chemosensor showed high selectivity towards TNP, among other closely related nitroaromatic compounds, cations and anions. The pronounced fluorescence quenching upon titration revealed a high binding affinity of picrate to **BTPyz**, due to the formation of ground state charged transfer complex and resonance energy transfer. Furthermore, **BTPyz** was capable of sensing TNP in real water and soil samples indicating its feasibility for practical applications.

SECTION 3B

Benzene-Appended Pyrazinium Salt for Detection of TNP and Sulfite Ions

In this section, the synthesis, characterization and investigation of photophysical properties of benzene-appended pyrazinium salt, **BPPyz** is discussed. It is utilized for fluorometric detection of TNP and colorimetric and fluorometric detection of sulfite ions. A cost-effective method for sulfite detection via smartphone is also incorporated in this section.

3B.1 EXPERIMENTAL SECTION

3B.1.1 Synthesis of 2,6-diphenylpyrazine (PPyz)

A round bottom flask was charged with 2,6-dichloropyrazine (0.671 mmol), phenylboronic acid (1.476 mmol), Pd $(OAc)_2$ (0.033 mmol), K_2CO_3 (1.342 mmol) and dimethylformamide (2.5 mL). The reaction was irradiated in the microwave at 120 °C for 50 min. The reaction mixture was cooled to room temperature, quenched with water (5 mL), and diluted with EtOAc (15 mL). The layers were separated, and the aqueous layer was extracted three times with 10 mL of EtOAc. The organic layer was dried over Na_2SO_4, filtered, and concentrated under reduced pressure. The residue was purified by column chromatography on silica gel using a 15-20% EtOAc/hexane mixture. **PPyz** was obtained as a white solid (137 mg, 86% yield); mp = 98–100 °C; δ ^{1}H NMR (400 MHz, $CDCl_3$) δ 9.00 (s, 2H), 8.21 – 8.17 (m, 4H), 7.60 – 7.50 (m, 6H). $^{13}C\{^1H\}$ NMR (100 MHz, $CDCl_3$) δ 151.6, 139.9, 136.5, 129.9, 129.0, 127.0; HRMS (ESI) *m*/*z*: $[M+H]^+$ calcd. for $[C_{16}H_{12}N_2+H]^+$, 233.1002, found 233.1002.

3B.1.2 Synthesis of 1-benzyl-3,5-diphenyl pyrazin-1-ium bromide (BPPyz*)*

A mixture of **PPyz** (0.431 mmol) and benzyl bromide (0.517 mmol) was stirred in a round bottom flask for 8 h at 75 °C. The reaction mixture was washed with ethyl acetate, bright yellow solid obtained was filtered and dried under vacuum (169 mg, 97.1% yield); mp = 205–210 °C; ^{1}H NMR (400 MHz, DMSO-d_6) δ 9.77 (s, 2H), 8.37 – 8.29 (m, 4H), 7.73 (dd, *J* = 8.0, 2.4 Hz, 2H), 7.68 (dd, *J* = 5.2, 2.0 Hz, 6H), 7.49 – 7.44 (m, 3H), 5.95 (s, 2H); $^{13}C\{^1H\}$ NMR (100 MHz, DMSO-d_6) δ 153.1, 138.4, 134.4, 133.1, 131.2, 130.2, 130.1,130.0, 129.6, 129.5, 65.2; HRMS (ESI) *m*/*z*: $[M-Br]^+$ calcd. for $[C_{23}H_{19}N_2]^+$, 323.1543; found 323.1536.

3B.1.3 Synthesis of BPPyz-TNP complex

At room temperature, an ethanolic solution of TNP (0.247 mmol) was added dropwise to the solution of **BPPyz** (0.247 mmol) in ethanol. The reaction mixture was stirred for 5 h, and the obtained yellow precipitate was filtered and washed with ethyl acetate (130 mg, 95%); mp = 220–225 °C; ^{1}H NMR (400 MHz, DMSO-d_6) δ 9.75 (s, 2H), 8.56 (s, 2H), 8.32 (dd, *J* = 6.8, 2.8 Hz,

4H), 7.73 – 7.70 (m, 2H), 7.67 (dd, *J* = 5.2, 2.0 Hz, 5H), 7.46 (dd, *J* = 5.2, 1.8 Hz, 3H), 5.94 (s, 2H); HRMS (ESI) *m/z*: $[M\text{-}Br]^+$ calcd for $[C_{23}H_{19}N_2]^+$, 323.1543; found 323.1536

3B.1.4 Synthesis of BPPyz-SO_3^{2-} complex

An acetonitrile solution of **BPPyz** (0.247 mmol) was added dropwise to a solution of sodium sulfite (0.123 mmol) at room temperature. The reaction mixture was stirred for 5 min, and the yellow precipitated solid was filtered and washed with ethyl acetate, (125 mg, 70%); mp = 210–225 °C ^{1}H NMR (400 MHz, DMSO-d_6) δ 10.01 (s, 2H), 8.39 (dd, *J* = 6.6, 3.0 Hz, 4H), 7.86 – 7.82 (m, 2H), 7.68 (dd, *J* = 4.8, 1.6 Hz, 6H), 7.46 (dq, *J* = 3.7, 1.9 Hz, 2H), 6.05 (s, 2H). ^{13}C{^{1}H} NMR (100 MHz, DMSO-d_6) δ 157.3, 133.7, 133.6, 132.9, 132.5, 130.1, 130.0, 129.7, 129.6, 128.1, 65.1; HRMS (ESI) *m/z*: $[M\text{-}Br]^+$ calcd. for $[C_{23}H_{19}N_2]^+$, 323.1543; found 323.1538

3B.2 RESULTS AND DISCUSSION

3B.2.1 Synthesis and Characterization

The Suzuki coupling reaction of 2,6-dichloropyrazine with phenylboronic acid provided 2,6-diphenylpyrazine (**PPyz**) which was well characterized (**Figure A6, A7, A8 Appendix-A**). The solvent-free reaction between **PPyz** and benzyl bromide gave **BPPyz** (**Scheme 3B.1**).

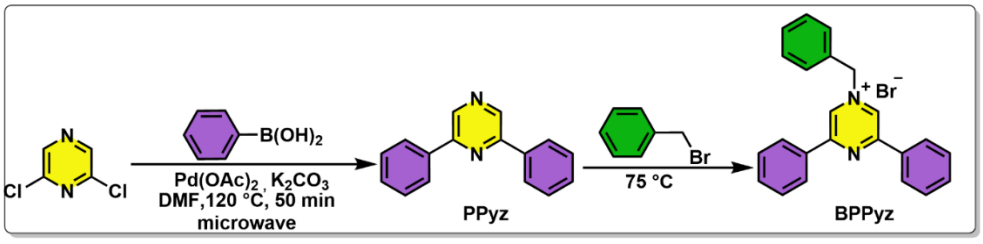

Scheme 3B.1: Synthesis route for **BPPyz**

BPPyz was characterized using different spectroscopic techniques and single crystal-XRD. In ^{1}H NMR of **BPPyz**, a two-proton singlet at 5.65 ppm indicated the presence of benzylic proton, and aromatic protons appeared in the range 7.09–8.26 ppm (**Figure 3B.1**). In the ^{13}C NMR spectrum of **BPPyz**, a signal at 65.1 ppm was due to the benzylic carbon, and the aromatic carbon signals appeared in the 128.1–157.4 ppm range (**Figure 3B.2**). ESI mass spectral analysis showed *m/z* peak at 323.1536 (*m/z*, calc. 323.1543), which may be attributed to [**BPPyz**-Br]$^+$ (**Figure 3B.3**).

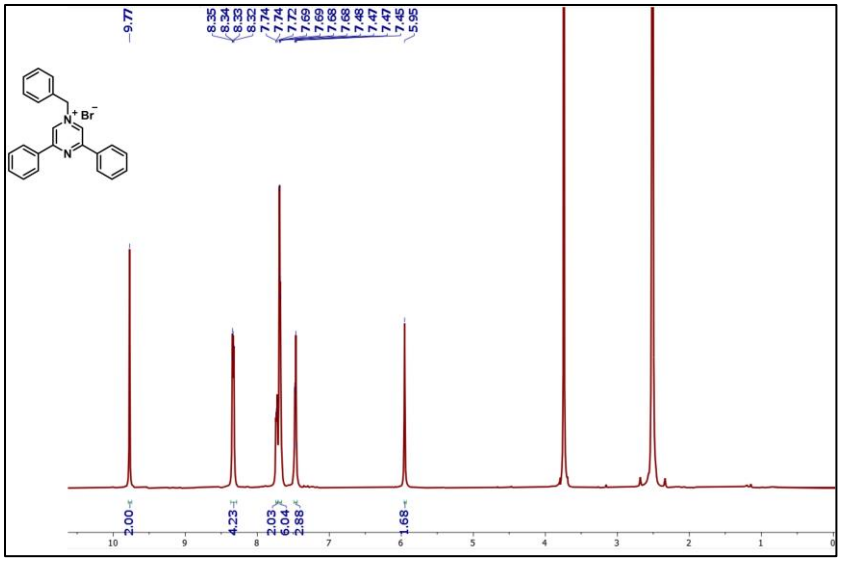

Figure 3B.1: ^{1}H NMR of **BPPyz** in DMSO-d_6

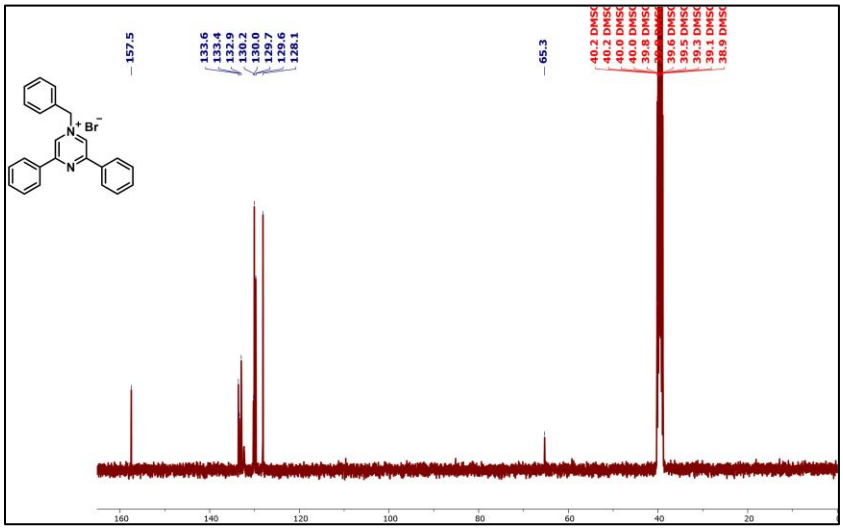

Figure 3B.2: ^{13}C NMR of **BPPyz** in DMSO-d_6

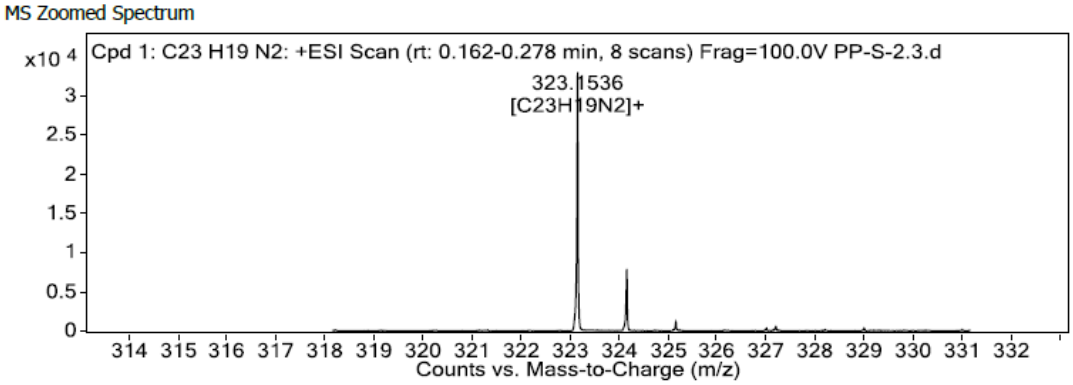

Figure 3B.3: HRMS of **BPPyz**

The structure of **BPPyz** was further confirmed by single-crystal XRD analysis (CCDC number 2189176). The compound crystallized in a monoclinic $P2_1/c$ space group. The ionic compound comprises an organic cation and bromide anion; three pairs of these ions are found in a crystallographic asymmetric unit, $Z' = 3$ (**Table A3, Appendix-A**). The ORTEP diagram is shown only for one molecule (**Figure 3B.4**).

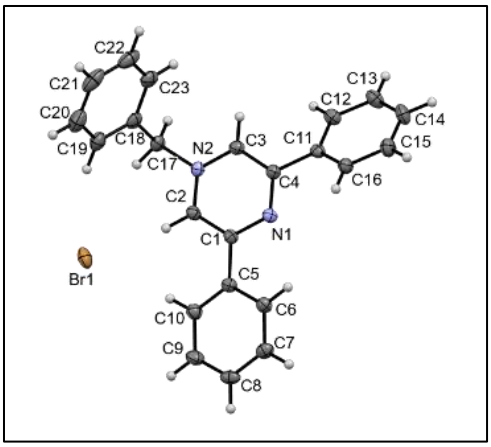

Figure 3B.4: ORTEP diagram of **BPPyz** (CCDC 2189176) showing thermal ellipsoids at 50% probability level

3B.2.2 Response of BPPyz toward TNP

Nitroaromatic compounds (NACs) can interact with fluorescent probes through non-covalent and electrostatic interactions resulting in a change in the absorption and emission properties. **BPPyz** showed three absorption bands at λ_{max} = 356 nm, 268 nm, and 236 nm in aqueous medium. It also showed a strong emission (Φ = 0.35) maximum at 438 nm (λ_{ex} = 359 nm) in the fluorescence spectra (**Figure 3B.5a**). The emission spctra of **BPPyz** was recorded in various solvents. The blue emission of **BPPyz** in aqueous medium motivated us to explore its potential application as a fluorescent chemosensor (**Figure 3B.5b**).

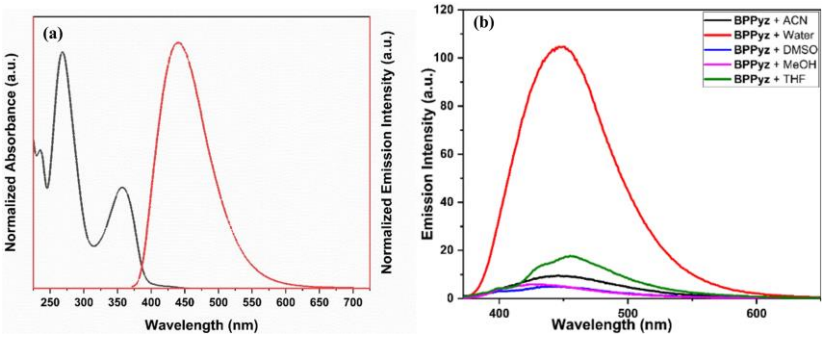

Figure 3B.5: (a) Absorption and fluorescence spectra of **BPPyz** (2×10^{-5} M) in water (b) Fluorescence spectra of **BPPyz** (2×10^{-5} M) in different solvents

The UV-vis absorption spectra of **BPPyz** was examined by adding nitroaromatics 4-NT, 4-NP, NM, 4-NBA, NB, 3,4-DNT, and 2,4-DNP in 2×10^{-5} M concentration. No alteration was observed in the absorbance with these NACs except TNP (**Figure A9, Appendix-A**), which showed an increase in the intensity with the appearance of a new band at 425 nm (**Figure 3B.6a**). The fluorescence intensity of **BPPyz** on the addition of 2,4-DNP, 4-NP, and TNP showed fluorescence quenching whereas, other NACs showed insignificant changes (**Figure 3B.6b**). The quenching efficiencies of TNP, 2,4-DNP, and 4-NP were found to be 97.3%, 75%, and 40%, respectively (**Figure A10 Appendix-A**).

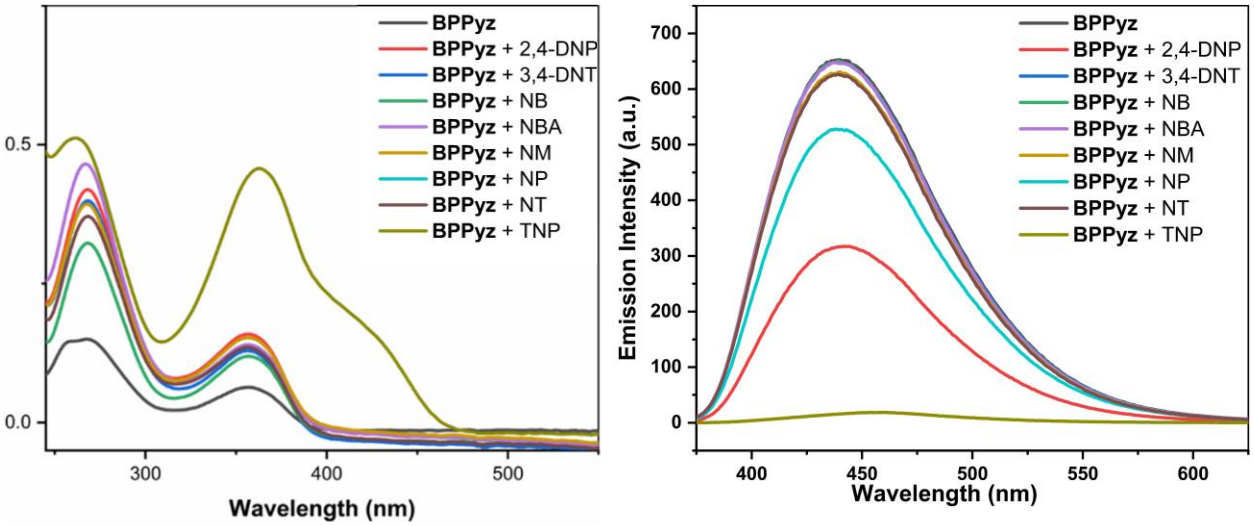

Figure 3B.6: (a) Absorption (b) Fluorescence spectra of **BPPyz** (2×10^{-5} M) with different nitroaromatic analytes in water

The general mechanisms of fluorescence quenching include static and/or dynamic quenching, Förster resonance energy transfer (FRET), photo-induced electron transfer (PET), and inner filter effect (IFE). The UV-vis absorption and fluorescence titrations were performed to elucidate the mechanism of interaction between **BPPyz** and TNP. On continuous addition of TNP, the absorption intensity of the band at 358 nm increased with an isosbestic point at 289 nm, and a new band at 425 nm appeared due to the formation of a ground state charge transfer complex (**Figure 3B.7a**). The intensity of the emission peak at 438 nm decreased with a gradual increase in the TNP concentration (**Figure 3B.7b**). This is due to the formation of the picrate anion by the deprotonation of phenolic -OH of TNP in aqueous medium, followed by an anion exchange with Br^-. The fluorescence titration studies were also performed for 2,4-DNP and 4-NP to investigate

the quenching of **BPPyz** (**Figure A11 and A12 Appendix-A**). The emission intensity at 438 nm decreased in the presence of 2,4-DNP and 4-NP, but to a lesser extent than TNP.

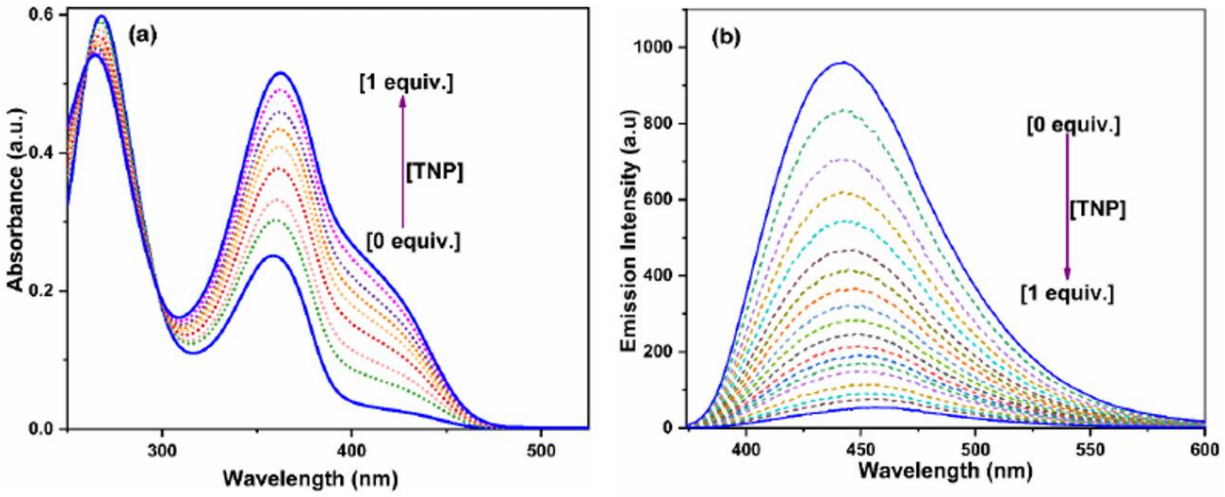

Figure 3B.7: (a) Absorption (b) Fluorescence spectra for **BPPyz** (2×10^{-5} M) with different amounts of TNP in water

The limit of detection (LOD) obtained from fluorescence titration studies at 438 nm was found to be 9 nM. It was estimated by the IUPAC standard method, $3\sigma/K$, where σ is the standard deviation of 10 blank measurements and K is the slope from the intensity versus sample concentration plot (**Figure 3B.8a**). To examine the sensitivity of **BPPyz** toward TNP, the Stern-Volmer (S-V) constant, K_{sv} was calculated using the Stern-Volmer equation, $I_0/I = 1 + K_{sv}[Q]$, where I_0 represents initial fluorescence intensity in the absence of analyte, I denotes intensity in the presence of the analyte, $[Q]$ is the molar concentration of analyte and K_{sv} is the quenching constant. The quenching constant, K_{sv} for **BPPyz** was found to be $4.12 \times 10^5\ M^{-1}$, confirming the high sensitivity of **BPPyz** toward TNP (**Figure 3B.8b**). The K_{sv} for 2,4-DNP and 4-NP were also calculated and found to be $6.7 \times 10^3\ M^{-1}$ and $2.3 \times 10^4\ M^{-1}$ respectively (**Figure A13 and A14, Appendix-A**). A Stern-Volmer plot may be linear or nonlinear depending on the static or dynamic quenching process. The linear S-V plot at the lower concentration indicated static quenching, which was attributed to the formation of the ground state charge transfer complex. This was confirmed by the appearance of a new band at 425 nm in UV-vis absorption spectra.

The deviation from linearity of the S–V plot at higher concentrations revealed the possibility of dynamic quenching. Dynamic quenching occurs as a result of collisional interactions or excited-state phenomena like Förster resonance energy transfer (FRET). Energy transfer through FRET is dependent on (i) a significant overlap between the absorption and fluorescence spectra of the acceptor and donor, respectively (ii) relative dipole orientations of the donor and acceptor, and (iii) Förster distance between the donor and acceptor.

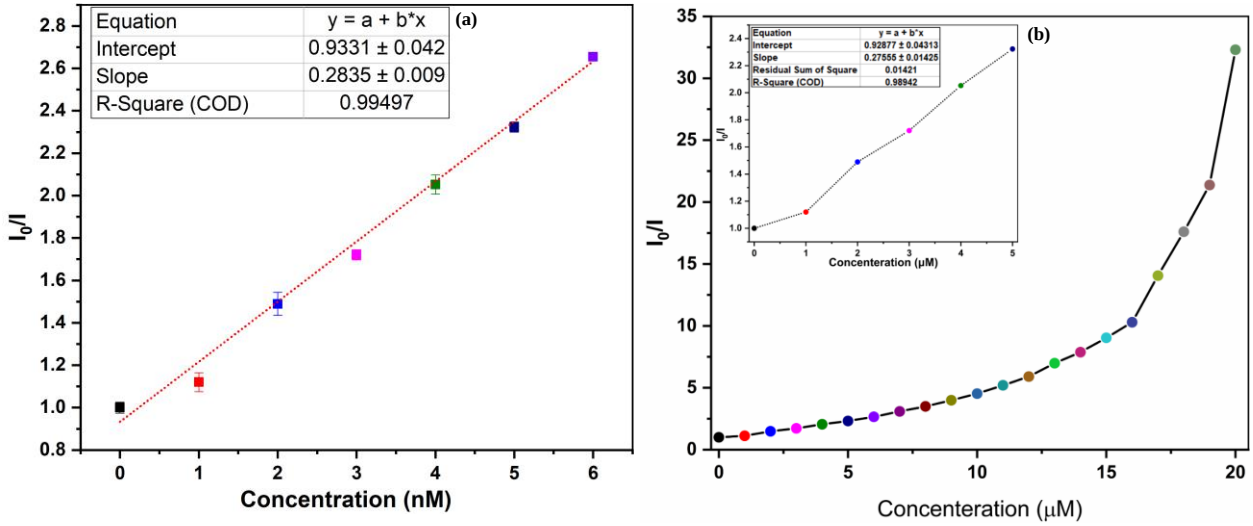

Figure 3B.8: (a) Calibration curve with error bar for calculating Limit of Detection for TNP (b) Stern-Volmer plot of **BPPyz** using TNP as a quencher

To validate the dynamic quenching mechanism, UV-vis absorption spectra of TNP were plotted together with the emission spectrum of **BPPyz,** and an effective overlap was observed with TNP only. Therefore, resonance energy can easily be transferred from the excited donor fluorophore (**BPPyz**) to the electron-deficient acceptor (TNP). To identify the extent of energy transfer, the overlap integral value (J_λ) for TNP was calculated and found to be 5.74×10^{14} M^{-1} cm^{-1} nm^{-4}. The Forster distance, R_0 for the **BPPyz**-TNP interaction, was 38.10 Å, which falls in the range for RET (**Figure 3B.9a**). The spectral overlap of the absorption spectra of the absorber with the emission/excitation spectra of fluorophore also indicates the possibility of an inner filter effect. The species in the IFE process should not chemically interact with each other, i.e., no new absorption band of the ground state charge transfer complex should be observed. Further, the quencher should not change the fluorescence lifetime of the fluorophore. In the current study, a new absorption band at 425 nm was observed due to ground state charge transfer complex formation.

Further, to exclude the possibility of IFE, corrections were performed using following eqn.

$I_{corr}/I_{obs} = 10^{(A_{ex}+A_{em})/2}$

where I_{corr} and I_{obs} indicate the fluorescence intensities of **BPPyz** after and before IFE corrections, respectively. A_{ex} and A_{em} denote the absorbances of the sensing system at the excitation and emission of **BPPyz**, respectively. No change in the emission intensity after performing IFE corrections clearly indicated the non-involvement of IFE in the TNP sensing mechanism (**Figure 3B.9b**).

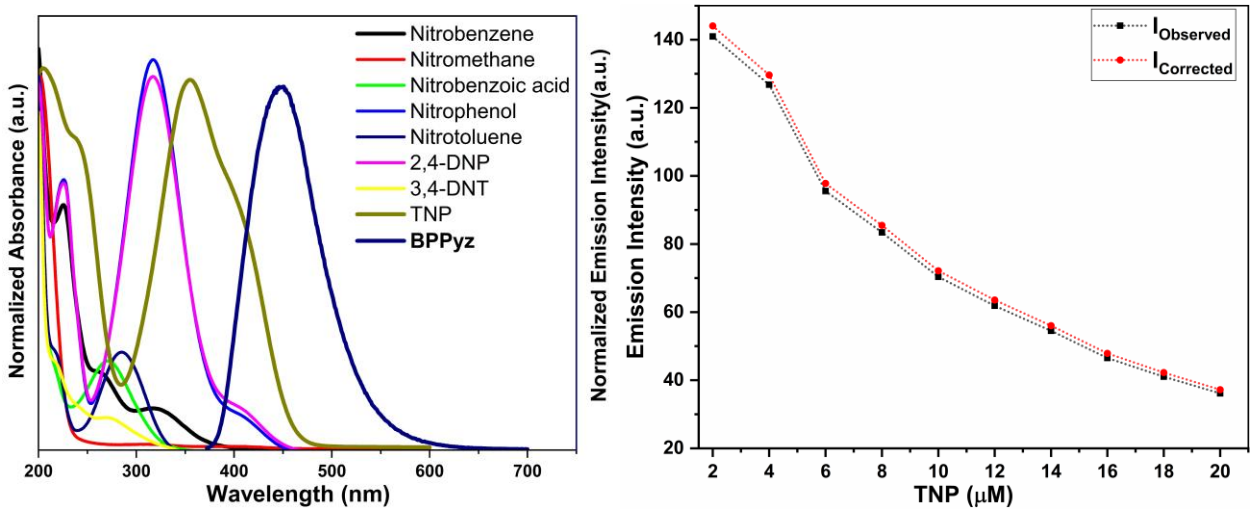

Figure 3B.9: (a) Spectral overlap between the normalized emission spectrum of **BPPyz** and normalized absorption spectra of different analytes (b) Emission intensity of **BPPyz** observed and after inner filter effect corrections

Furthermore, fluorescence lifetime decay profiles also showed a decrease in the lifetime of the **BPPyz**-TNP complex (0.5 ns) compared to **BPPyz** (3.50 ns). Moreover, it was observed that the reduction in fluorescence lifetime and intensity followed the relation $\tau_0/\tau = I_0/I$, which is a crucial feature of collisional or dynamic quenching (**Figure 3B.19**).

The nature of attenuation of fluorescence emission of **BPPyz** by TNP was inspected by ^{1}H NMR, HRMS, and theoretical studies. The stoichiometric ratio was confirmed by the spectroscopic analysis of the yellow complex isolated from the ethanolic solution of **BPPyz** and TNP at room temperature. Comparing ^{1}H NMR of **BPPyz** and **BPPyz**-TNP complex suggested the complexation of picrate ion with **BPPyz** cation (**Figure 3B.10**). In the ^{1}H NMR spectrum of the **BPPyz**-picrate complex, a new prominent signal at 8.58 ppm due to picrate protons and its relative integration confirmed the formation of a 1:1 molar complex between **BPPyz** and TNP. The HRMS

analysis of **BPPyz**-TNP demonstrated *m/z* peaks attributed to anionic $[TNP\text{-}H]^-$ and cationic $[\mathbf{BPPyz}\text{-}Br]^+$ species at 227.9525 (*m/z*, calcd. 227.9893) and 323.1536 (*m/z*, calcd. 323.1543), respectively (**Figure 3B.11**).

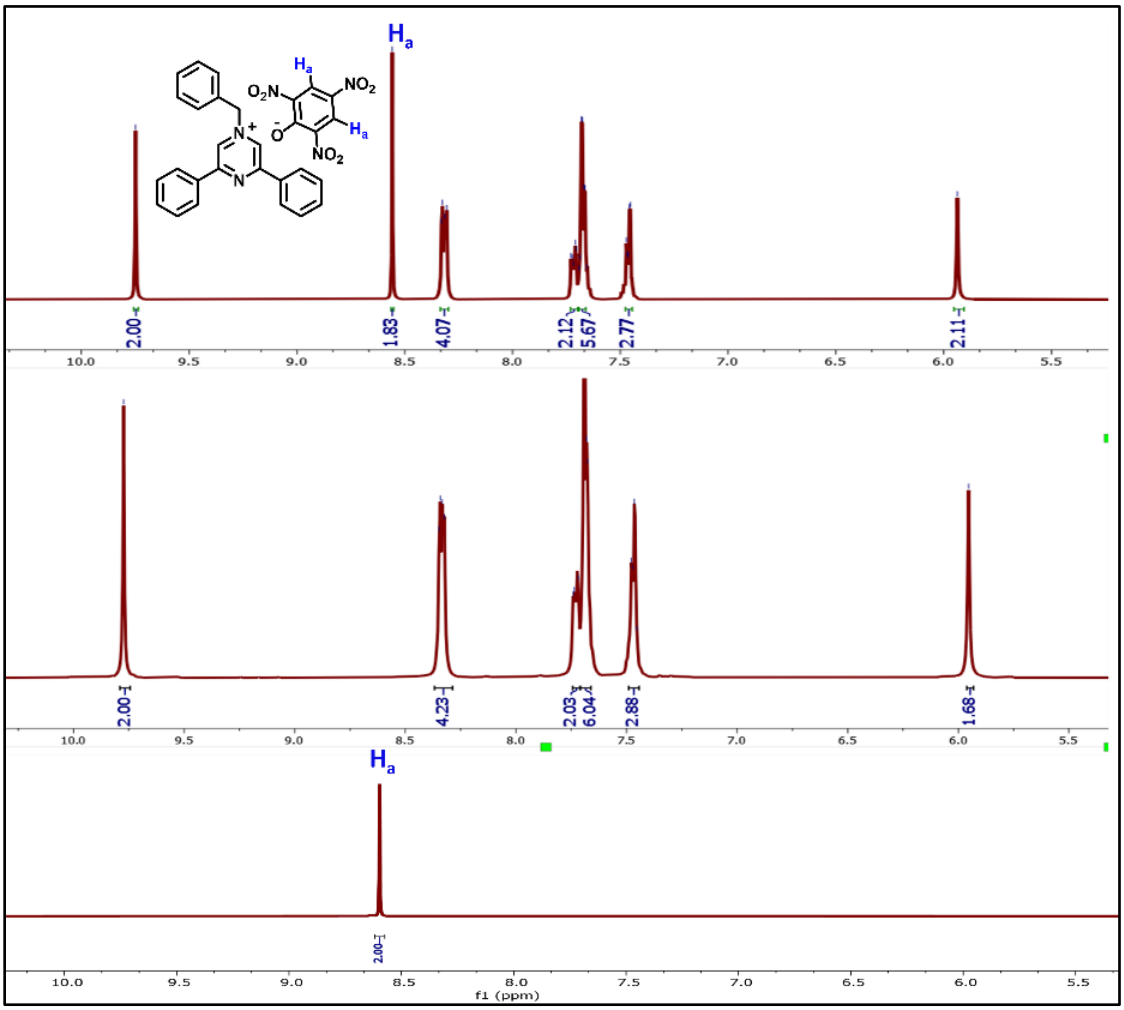

Figure 3B.10: ^{1}H NMR spectra of **BPPyz**-TNP complex in DMSO-d_6

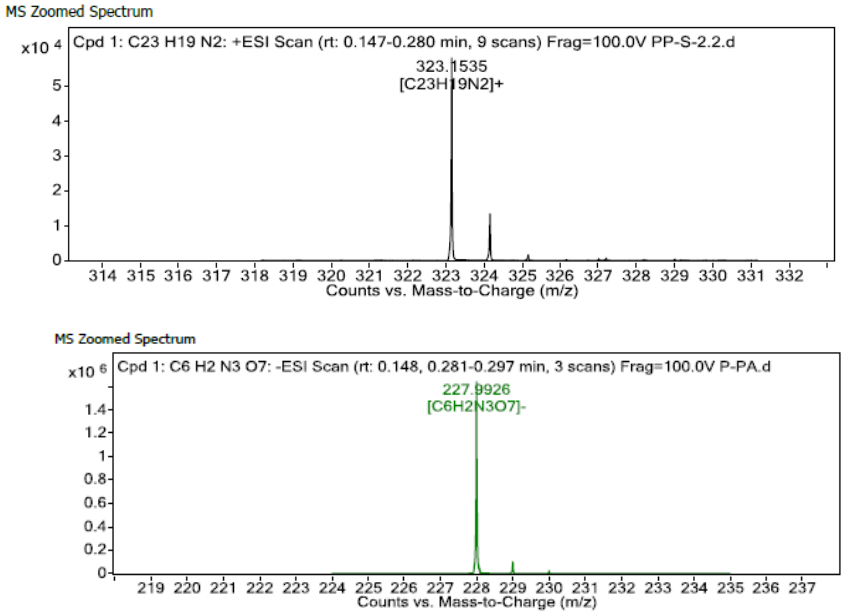

Figure 3B.11: HRMS of **BPPyz**-TNP complex in (a) positive (b) negative modes

The crystal of **BPPyz**-TNP grown from an acetonitrile-methanol solvent mixture crystallized in a monoclinic system, *C*2/c space group. One **BPPyz**$^{+}$ cation and one deprotonated picrate anion are found in a crystallographic asymmetric unit, $Z' = 1$. The ORTEP diagram of the **BPPyz**-TNP crystal is shown in (**Figure 3B.12**). **BPPyz**-TNP complex is stabilized through short C-H···O non-covalent interactions. The pyrazine ring C3-H3···O1, methylene C17-H17A···O1, and phenyl ring C3-H3···O1 non-covalent bond distances are 2.391, 2.471, and 2.533 Å, respectively, these bond distances are shorter than the hydrogen-oxygen van der Waals radius, 2.72 Å (**Table A3, Appendix-A**).

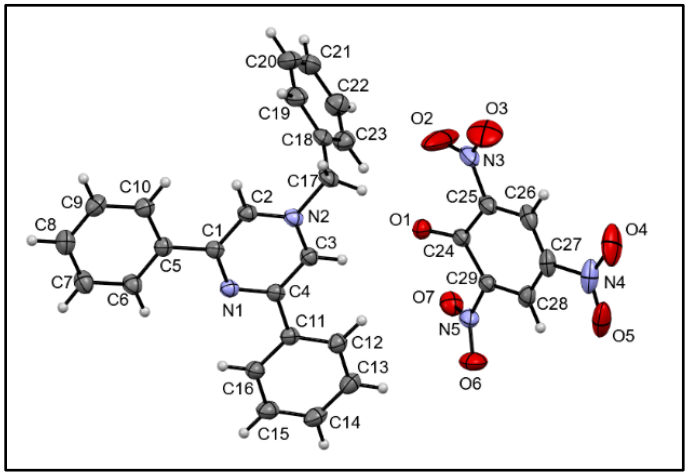

Figure 3B.12: ORTEP diagram of **BPPyz**-TNP (CCDC 2189177) showing thermal ellipsoids at 50% probability level

The behavior of **BPPyz** towards TNP in different pH solutions was also investigated. On addition of TNP, the maximum fluorescence quenching of **BPPyz** was found in the pH range of 6-8. This result indicated that **BPPyz** can be used efficiently as a fluorescent chemosensor for TNP detection under a neutral pH environment (**Figure 3B.22**). The emission of **BPPyz** was recorded in the presence of triflic acid (TFA) (p*K*a ~ 0.52), a stronger acid than TNP (p*K*a ~ 0.38) to investigate the acidity effect of TNP on fluorescence quenching. No change in the fluorescence emission suggested that the acidity effect was not involved in the fluorescence quenching mechanism (**Figure 3B.13**).

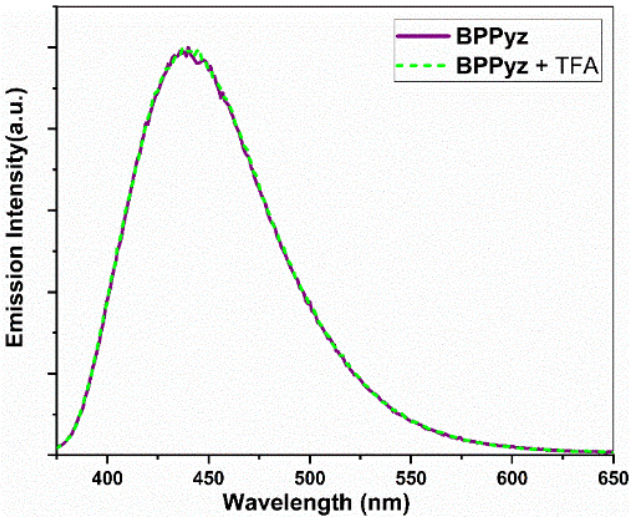

Figure 3B.13: Fluorescence spectra of **BPPyz** and **BPPyz** with TFA

So far, the selectivity of **BPPyz** towards TNP was established among different nitro compounds. Further, the interference studies were performed using competitive binding studies for the TNP with **BPPyz** in the presence of equimolar concentrations (2×10^{-5} M) of other metal ions (Na^{+}, Mg^{2+}, Al^{3+}, K^{+}, Ca^{2+}, Mn^{2+}, Fe^{2+}, Fe^{3+}, Co^{2+}, Ni^{2+}, Cu^{2+}, Zn^{2+}, Ag^{+}, Cd^{2+}, Hg^{2+}, Pb^{2+}, La^{3+}, Eu^{3+}, Gd^{3+} and Yb^{3+}), anions (CH_3COO^{-}, HCO_3^{-}, NO_3^{-}, I^{-}, Br^{-}, Cl^{-}, and F^{-}) and nitro compounds (4-NT, 4-NP, NM, 4-NBA, NB, 3,4-DNT, and 2,4-DNP) (**Figure 3B.14**). No perturbation of fluorescence quenching was observed, which established the selectivity of **BPPyz** for TNP in the presence of several other analytes.

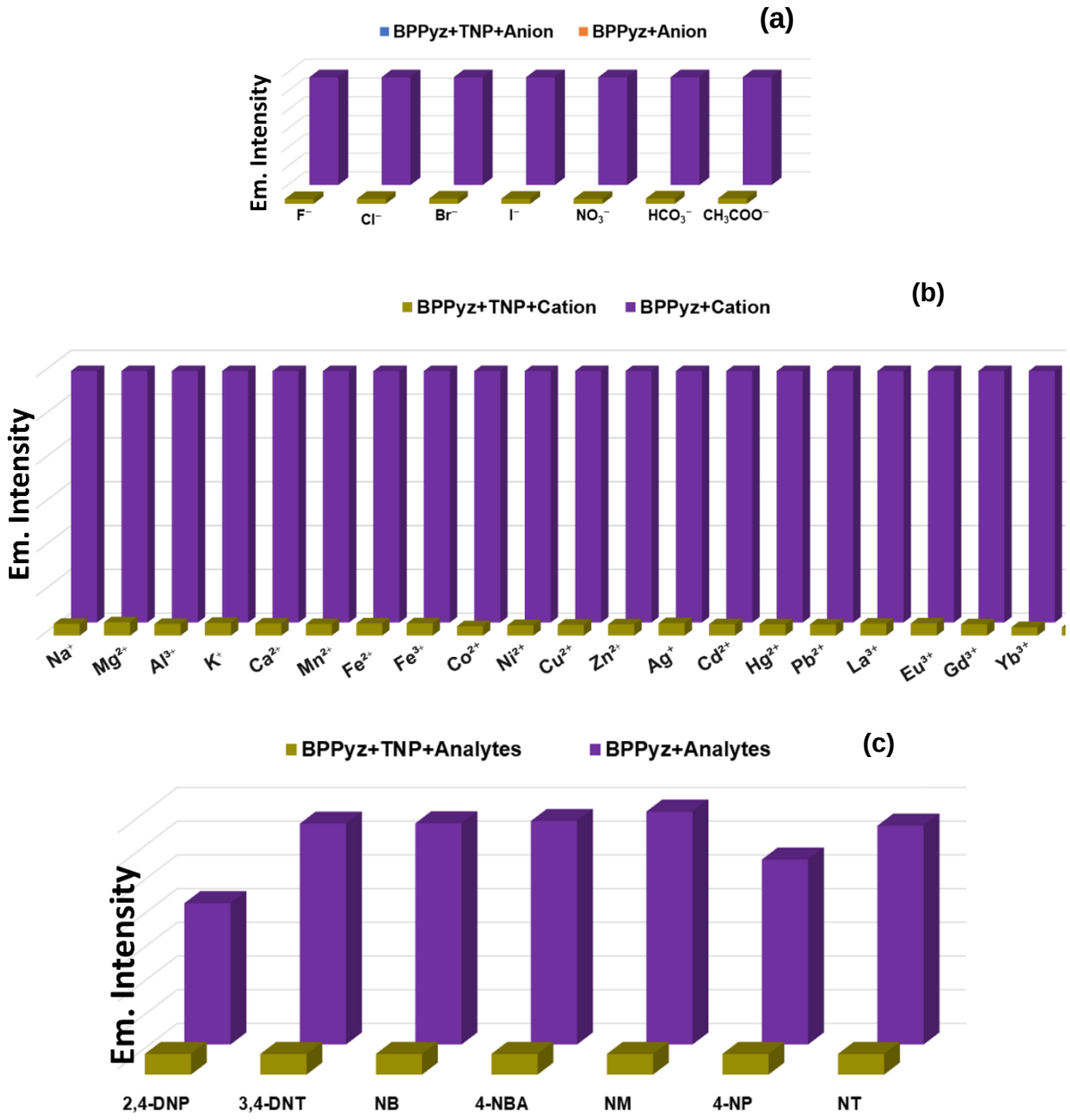

Figure 3B.14: Interference study of **BPPyz** (2×10^{-5} M) toward TNP selectivity in the presence of (a) anions (b) cations (c) organic analytes

To study the interaction between **BPPyz** and TNP, DFT calculations were performed at the level of B3LYP/ 6–311G(d,p) in the gas phase. The energies of HOMO and LUMO of **BPPyz** were -9.856 eV and -6.334 eV, respectively. The energies of HOMO and LUMO of picrate anion were found to be -3.424 eV and +0.1417 eV, respectively (**Figure 3B.15**). Hence, theoretical results direct the possibility of a ground state electronic charge transfer from the HOMO of picrate anion

to the LUMO of **BPPyz** which results in high quenching efficiency. However, HOMOs of other nitroaromatics were found to have low energy levels than the LUMO of **BPPyz**, thereby discarding the possibility of electronic charge transfer and leading to low quenching efficiencies (**Figure A15, Appendix-A**).

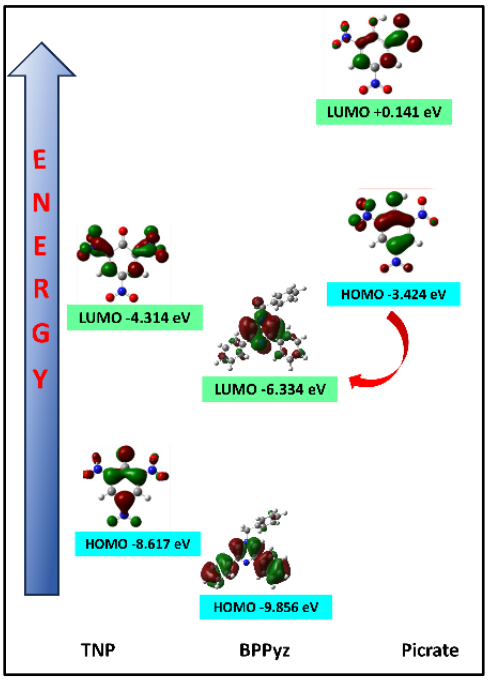

Figure 3B.15: Energy levels and frontier molecular orbitals of **BPPyz**, Picrate, and TNP

3B.2.3 Response of BPPyz toward SO_3^{2-}

The anion sensing ability of the probe **BPPyz** was elucidated by change in UV-vis absorption and fluorescence spectra upon the addition of various anions, SO_3^{2-}, HSO_3^-, NO_3^-, F^-, Cl^-, Br^-, I^-, ClO_4^-, $[Fe(CN)_5(NO)]^{2-}$, $C_2O_4^{2-}$, cystine, glutathione, methionine, $S_2O_3^{2-}$, SO_4^{2-}, PO_4^{2-}, CN^-, SCN^-, N_3^-, OH^-, $H_2PO_4^-$, OAc^- (2×10^{-5} M) in aqueous medium. Among these anions, **BPPyz** was interestingly selective for SO_3^{2-} with a visual change in the color of the solution from colorless to yellow. On addition of SO_3^{2-} ions, the UV-vis absorption bands of **BPPyz** at 268 nm and 358 nm showed a hypsochromic shift to 255 nm and 322 nm, respectively, with a simultaneous emergence of a new band at 439 nm. **BPPyz** solution emitted a dark brownish fluorescence in the presence of SO_3^{2-} anion under the 365 nm UV lamp. To ascertain the selectivity of the probe, emission spectra of **BPPyz** were recorded in the presence of various anions at 2×10^{-5} M concentration, and no alteration was observed in the emission behavior of **BPPyz**. The addition of

SO_3^{2-} resulted in 94.3% quenching of emission intensity at 438 nm. A ground state charge transfer complex might have formed due to the exchange of Br^- with SO_3^{2-} (**Figure 3B.16**).

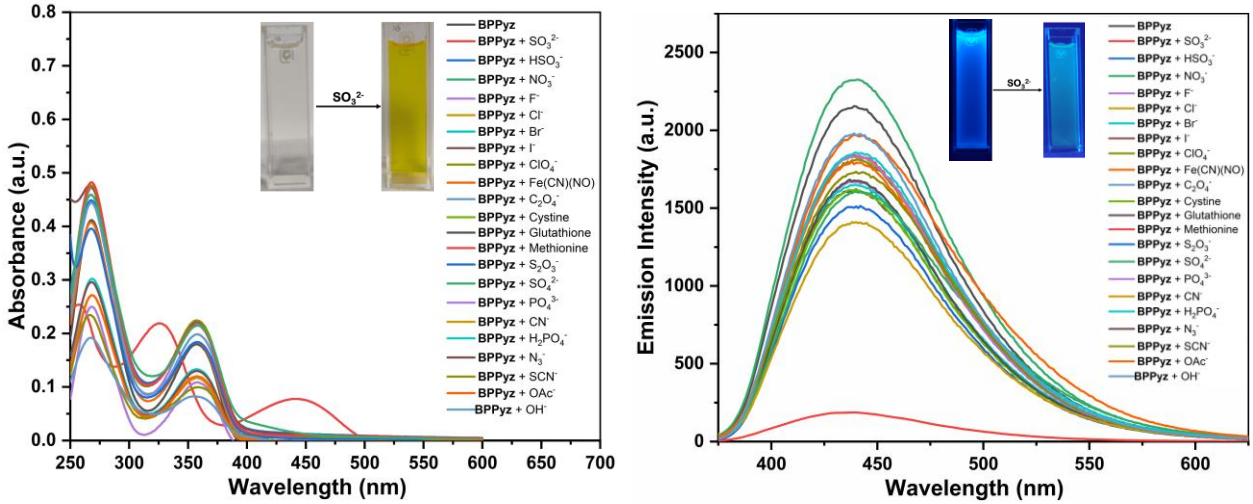

Figure 3B.16: (a) Absorption (b) Fluorescence spectra of **BPPyz** (2×10^{-5} M) with different anions in water

To further confirm the formation of the ground state charge transfer complex, UV-vis absorption spectra of **BPPyz** were recorded with the increasing concentration of the SO_3^{2-}. A well-defined isosbestic point at 385 nm suggested the formation of a new compound upon treatment of the probe with sulfite ions (**Figure 3B.17a**). To better understand the sensing ability of **BPPyz** for SO_3^{2-} anion, a fluorescence titration experiment of **BPPyz** was carried out with the gradual addition of SO_3^{2-}. The fluorescence intensity of **BPPyz** decreased gradually with the increasing concentration of the SO_3^{2-} anion (**Figure 3B.17b**).

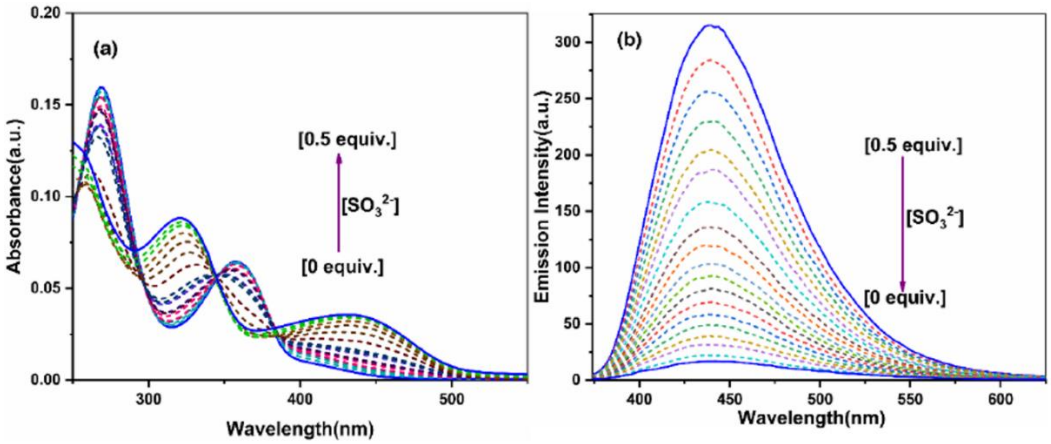

Figure 3B.17: (a) Absorption (b) Fluorescence spectra for **BPPyz** (2×10^{-5} M) with different amounts of SO_3^{2-} in water

The limit of detection is an important parameter that describes the sensing ability of sensors. The limit of detection of **BPPyz** for the SO_3^{2-} anion was found to be 31 nM (**Figure 3B.18a**). The linear variation at low concentration was due to static quenching. The linear fit of the plot provided $K_{sv} = 3.8 \times 10^5\ M^{-1}$ and a correlation coefficient (R^2) = 0.9936 (**Figure 3B.18b**).

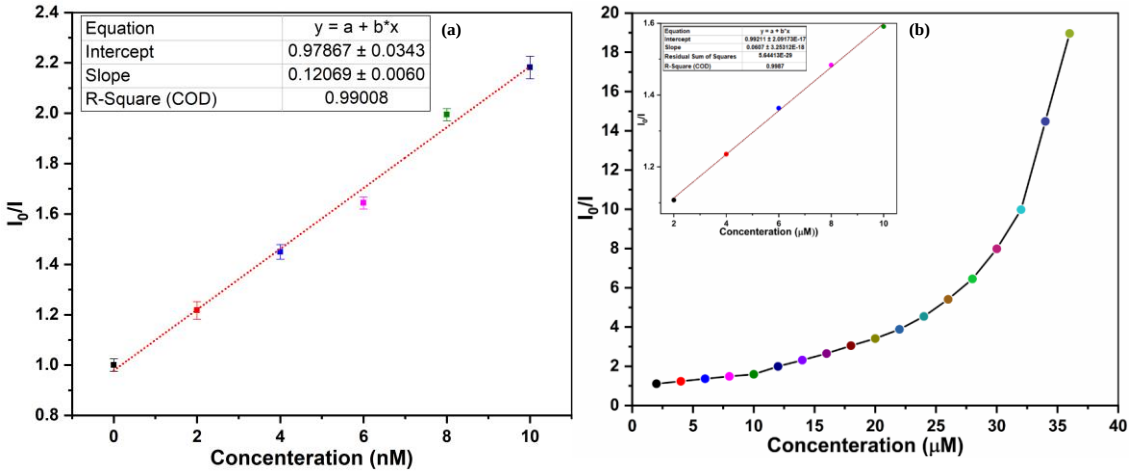

Figure 3B.18: (a) Calibration curve with error bar for calculating Limit of Detection for SO_3^{2-} (b) Stern−Volmer plot of **BPPyz** using SO_3^{2-} as a quencher

The deviation from linearity indicated dynamic quenching, which was further supported by lifetime measurements. Fluorescence lifetime decay profiles showed a decrease in the lifetime of **BPPyz**-SO_3^{2-} complex (0.9 ns) as compared to **BPPyz** (3.50 ns) due to dynamic quenching **(Figure 3B.19a**). Job's plot suggested a 2:1 stoichiometry between **BPPyz** and SO_3^{2-} anion (**Figure 3B.19b**). To further confirm the stoichiometric ratio of the complex, the dark yellow complex was isolated from an ethanolic solution of **BPPyz** and SO_3^{2-} at room temperature and was analyzed by ^1H and ^{13}C NMR (**Figure A16, Appendix-A**).

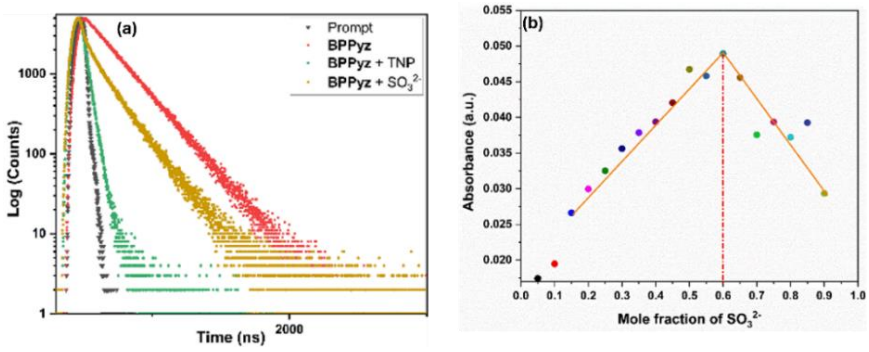

Figure 3B.19: (a) Fluorescence lifetime decay curves of **BPPyz**, **BPPyz**-TNP and **BPPyz**-SO_3^{2-} complexes (b) Job's Plot of **BPPyz** with SO_3^{2-}

In the ^{1}H NMR of the **BPPyz**-SO_3^{2-} complex, the pyrazinium proton H_a shifted downfield fom 9.77 ppm to 10.01 ppm. The prominent shift in the ^{1}H NMR indicated the hydrogen bonding between the pyrazinium proton (H_a) of **BPPyz** and the O atom of SO_3^{2-}. A downfield shift was also observed in the aliphatic proton (H_b) and aromatic proton (H_c) signals due to hydrogen bonding (**Figure 3B.20**). In HRMS of **BPPyz**-SO_3^{2-} complex *m/z* peak was observed at 323.1536 (*m/z*, calc. 323.1543) for [**BPPyz**-Br]$^{+}$ (**Figure 3B.21**).

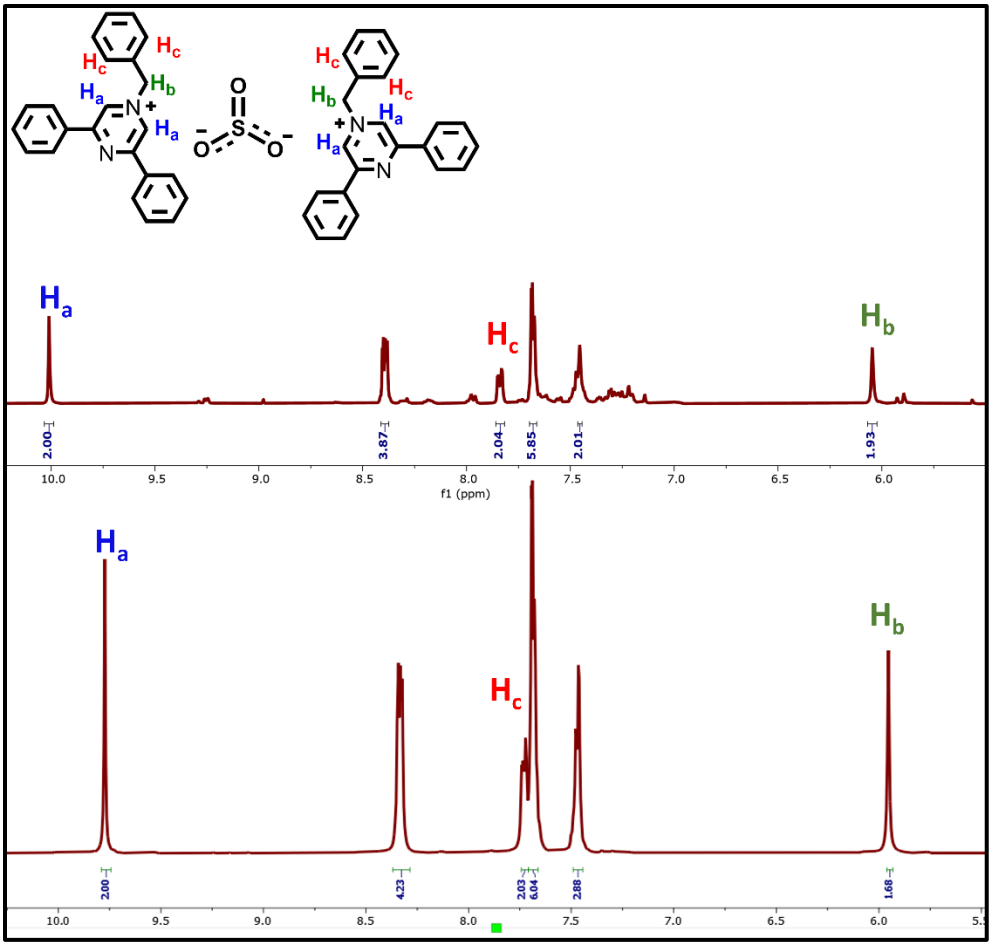

Figure 3B.20: ^{1}H NMR spectra of **BPPyz**- SO_3^{2-}complex in DMSO-d_6

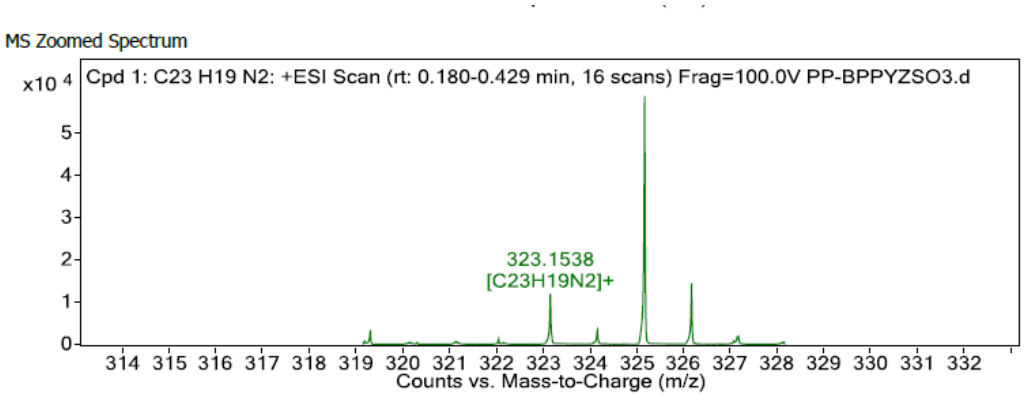

Figure 3B.21: HRMS of **BPPyz**-SO_3^{2-} complex in positive mode

The maximum fluorescence quenching of **BPPyz** in the presence of SO_3^{2-} was found in the pH range of 6-9, indicating its stability in a neutral pH environment (**Figure 3B.22**).

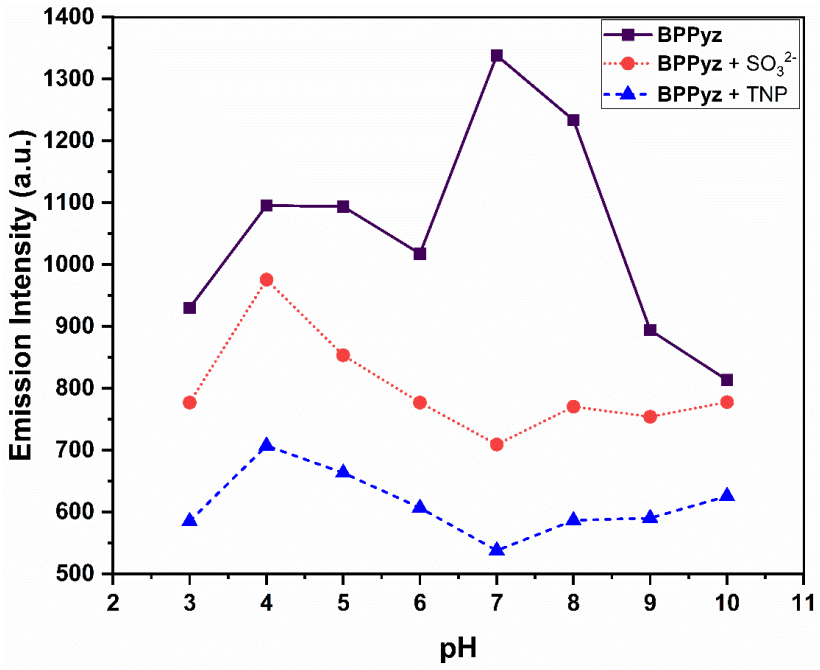

Figure 3B.22: Effect of pH on **BPPyz** (2×10^{-5} M), **BPPyz**-TNP and **BPPyz**-SO_3^{2-}

The selectivity of **BPPyz** for SO_3^{2-} was evaluated by monitoring the fluorescence response of **BPPyz** toward SO_3^{2-} in the presence of F^-, Cl^-, Br^-, I^-, NO_3^-, HCO_3^-, CH_3COO^-, $S_2O_3^{2-}$, SO_4^{2-}, and PO_4^{2-} (**Figure 3B.23**). Fluorescence quenching was unaffected, indicating that **BPPyz** can selectively discriminate the SO_3^{2-} anion in the presence of all other examined anions.

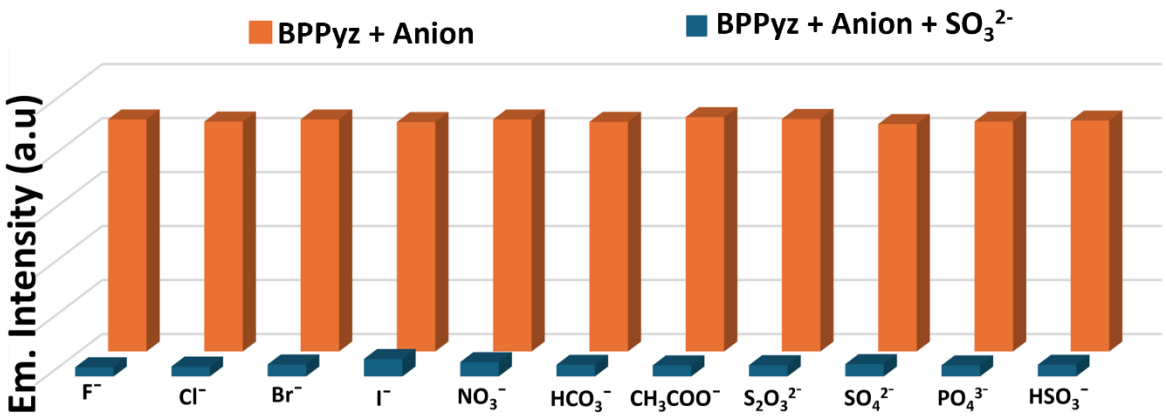

Figure 3B.23: Selectivity of **BPPyz** (2×10^{-5} M) toward SO_3^{2-} in the presence of anions

The DFT calculations were carried out at the B3LYP/6–311G(d,p) level of theory to understand the formation of the complex (**Figure 3B.24a**). The red-shifted absorption band in **BPPyz**-SO_3^{2-} can be explained by the molecular orbitals. In the **BPPyz**-SO_3^{2-}complex, the energy gap between HOMO and LUMO was -0.519 eV, which is much smaller than that in **BPPyz** (-1.95 eV). Such lowering of the HOMO-LUMO gap in the **BPPyz**-SO_3^{2-} complex can be attributed to the change in electron distribution due to anion exchange (**Figure 3B.24b**).

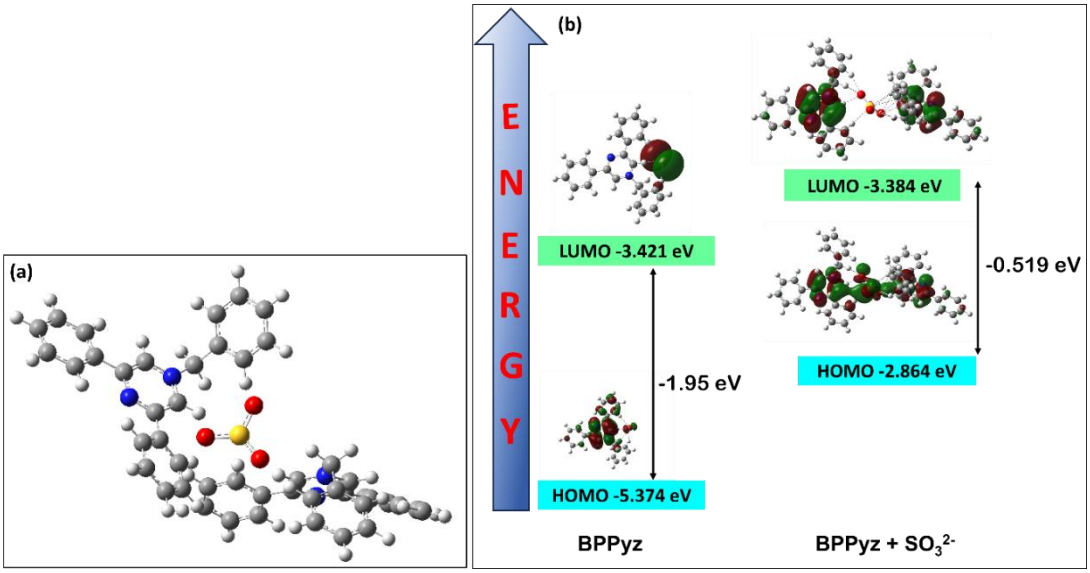

Figure 3B.24: (a) Optimized ball and stick model (b) Energy levels and frontier molecular orbitals of **BPPyz**-SO_3^{2-}

3B.2.4 Analytical Applications

Smartphone-Based Colorimetric Read-Out

An affordable on-site monitoring method was developed based on the naked-eye detectable change of **BPPyz** in the presence of SO_3^{2-} using a smartphone. The standard RGB scale is represented by whole number-values from 0 to 255 for red, green, and blue colors. The values [0,0,0] and [255, 255, 255] correspond to absolute black and white, respectively. The change in the RGB values of **BPPyz** on the addition of SO_3^{2-} was recorded by keeping the smartphone camera about 1 cm away from the vials enclosed inside a paper box. The changes were recorded using a smartphone app, which could directly output the RGB values (**Figure 3B.25**).

Figure 3B.25: Integration of the **BPPyz** with a smartphone

In order to compute the fitting parameters, several empirical formulae were used to assess the correlation of RGB values processed from the smartphone **(Figure A17, Appendix-A**). The optimal relationship was obtained when the ratio of R/(R+G+B) was used (**Figure 3B.26**). By using this ratio, a calibration curve was obtained with good linearity from 0 μM to 20.0 μM (R^2 = 0.9949). These results demonstrate that the developed smartphone-based colorimetric read-out method performs well and is more accessible, affordable, and portable than other chromatographic techniques.

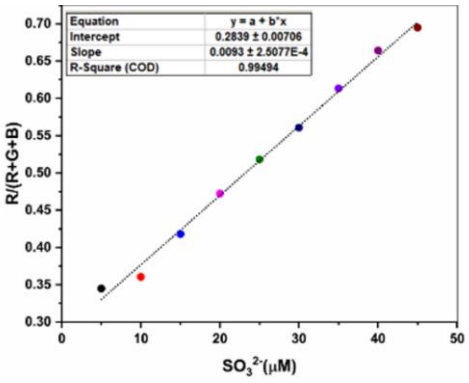

Figure 3B.26: Ratio of R/(R + G + B) versus SO_3^{2-} concentration in the range of 0 to 20.0 μM

Implementation of test paper strips

For rapid and on-site detection of TNP and sulfite, commercial Whatman filter paper was used to create paper test strips.[60] The strips were dipped in a concentrated **BPPyz** solution for 10 minutes, and then allowed to dry for two hours. These test strips were dipped in aqueous solutions of TNP and sulfite solutions (10^{-3}-10^{-6} M), and fluorescence quenching was observed under a 365 nm UV lamp (**Figure 3B.27**).

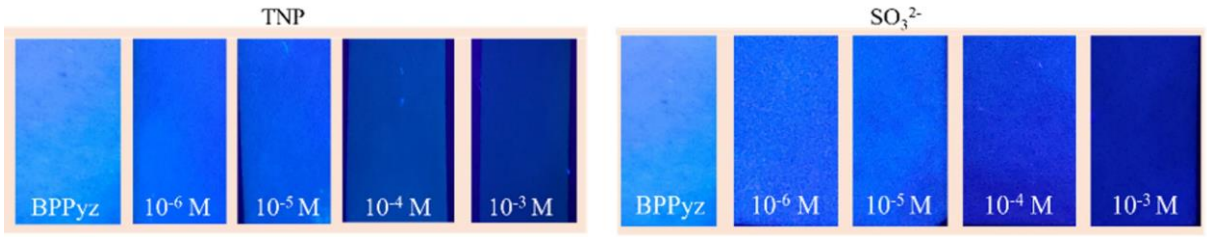

Figure 3B.27: Test paper strips for detection of TNP and SO_3^{2-} under 365 nm UV light

A comparative study of **BPPyz** with chemosensors reported in the literature is given in **Table A6 and A7, Appendix A**.

3B.3 CONCLUSION

In summary, a fluorescent pyrazinium salt, **BPPyz** was successfully synthesized, and its photophysical properties were studied in detail. In aqueous media, **BPPyz** showed high selectivity and high sensitivity for sensing TNP among nitrocompounds by fluorescence quenching, which can be due to the formation of ground state charge transfer complex and resonance energy transfer. Among anions, **BPPyz** exhibits good sensing ability towards SO_3^{2-} by colorimetric and fluorometric response attributed to hydrogen bond interaction between the pyrazinium of **BPPyz** and SO_3^{2-}. Moreover, **BPPyz** was integrated with a smartphone for sulfite detection. The developed strategy is portable and accessible for in situ sulfite analysis and does not require advanced instruments.

SECTION 3C

Pyrene-Appended Pyrazinium Salt for Detection of TNP and Nitrite Ions

In this section, pyrene-appended pyrazinium salt, **MPyPyz** has been synthesized and characterized. It is utilized as a chemosensor for the detection of TNP and nitrite ions *via* a fluorescence turn-off mechanism. Furthermore, it is also employed for the visualization of latent fingerprints.

3C.1 EXPERIMENTAL SECTION

3C.1.1 Synthesis of 2-(pyren-1-yl)pyrazine (PyPyz)

An oven-dried glass vial was charged with 2-chloropyrazine (0.436 mmol), pyrene-1-boronic acid (0.436 mmol), $Pd(PPh_3)_4$ (0.021 mmol), K_2CO_3 (0.654 mmol) in dimethylformamide (2.5 mL). The reaction was irradiated in the microwave at 120 °C for 50 min. After completion of the reaction (monitored by TLC), the reaction mixture was allowed to attain room temperature. The precipitate was filtered and washed with cold water to remove DMF. **PyPyz** was obtained as a pale white solid, (60 mg, 73% yield); mp = 125–130 °C; ^{1}H NMR (400 MHz, DMSO-d_6) δ 8.53 (d, J = 7.9 Hz, 1H), 8.43 – 8.25 (m, 5H), 8.21 (d, J = 7.4 Hz, 1H), 8.13 (t, J = 7.5 Hz, 1H), 8.04 (d, J = 9.2 Hz, 1H), 7.54 (d, J = 9.2 Hz, 1H); ^{13}C{^{1}H} NMR (100 MHz, DMSO-d_6) δ 157.4, 153.5, 153.0, 152.5, 151.4, 149.9, 148.3, 146.8, 145.4, 145.4, 144.8, 143.6, 142.6, 141.5, 133.5, 131.2, 129.8, 122.4, 51.5; HRMS (ESI) m/z: $[M+H]^+$ calcd. for $[C_{20}H_{12}N_2 + H]^+$, 280.0110, found 245.0105.

3C.1.2 Synthesis of 1-Methyl-3-(pyren-1-yl)pyrazi-1-ium iodide (MPyPyz)

A mixture of **PyPyz** (0.169 mmol) and methyl iodide (0.847 mmol) was taken in a round bottom flask and stirred for 15 h at 75 °C. The reaction mixture was washed with ethyl acetate. The obtained bright yellow solid was filtered and dried under a vacuum, (45 mg, 65% yield); mp = 218–222 °C; ^{1}H NMR (400 MHz, DMSO-d_6) δ ^{1}H NMR (400 MHz, DMSO) δ 8.66 (d, J = 3.4 Hz, 2H), 8.57 (d, J = 8.3 Hz, 2H), 8.54 – 8.49 (m, 4H), 8.33 – 8.28 (m, 2H), 8.23 (t, J = 7.6 Hz, 1H), 8.14 (d, J = 9.3 Hz, 1H), 4.64 (s, 3H); ^{13}C NMR (100 MHz, DMSO-d_6) δ 157.4, 153.5, 153.0, 152.5, 151.4, 149.9, 148.3, 146.8, 145.4, 145.4, 144.8, 143.6, 142.6, 141.5, 133.5, 131.2, 129.8, 122.4, 45.3; HRMS (ESI) m/z: $[M-I]^+$ calcd. for $[C_{21}H_{15}N_2\text{-}I]^+$, 295.1230, found 295.1212.

3C.2 RESULTS AND DISCUSSION

3C.2.1 Synthesis and Characterization

MPyPyz was prepared by Suzuki coupling of 2-chloropyrazine and pyrene boronic acid followed by quaternization reaction with methyl iodide (**Scheme 3C.1**). These were characterized by ^{1}H and ^{13}C NMR spectroscopy and HRMS (**Figure A18 and A19 Appendix-A**).

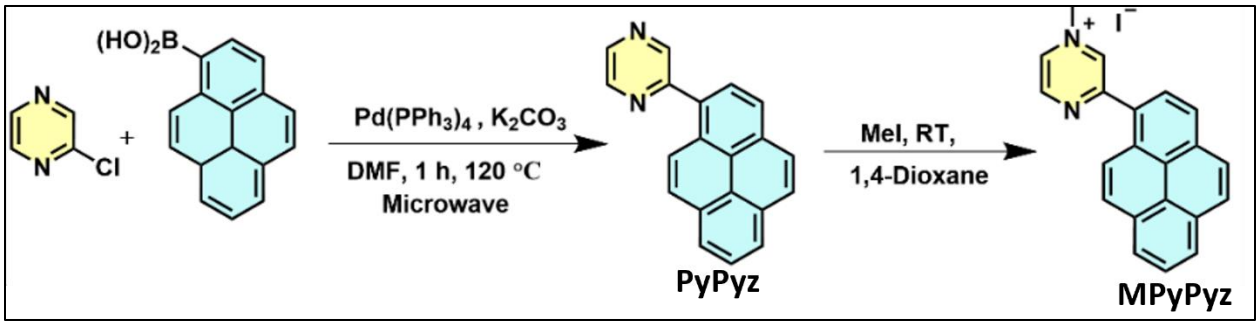

Scheme 3C.1: Synthetic route for **MPyPyz**

In ^{1}H NMR of **MPyPyz**, a proton singlet at 4.64 ppm indicated the presence of methyl protons, and aromatic protons appeared in the range 7.54-8.53 ppm (**Figure 3C.1**). In the ^{13}C NMR spectrum of **MPyPyz**, a signal at 48.5 ppm was due to the methyl carbon, and the aromatic carbon signals appeared in the 128.1–157.4 ppm range (**Figure 3C.2**). ESI mass spectral analysis showed *m/z* peak at 295.1515 (*m/z*, calc. 295.1230), which may be attributed to [**MPyPyz**-I]$^{+}$(**Figure 3C.3)**.

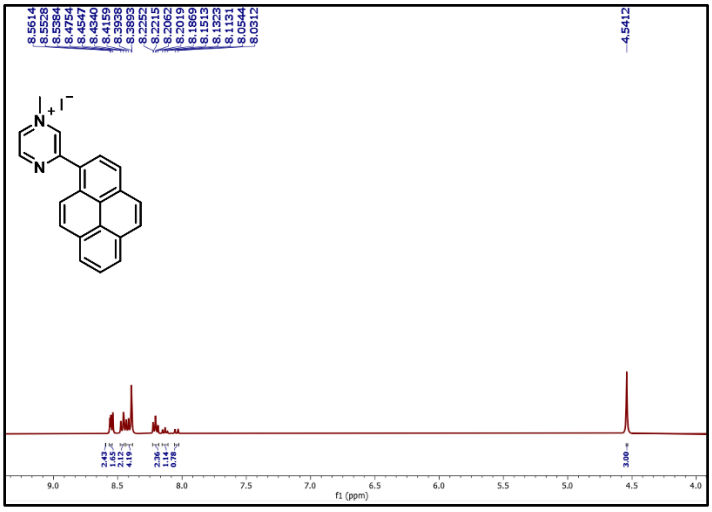

Figure 3C.1: ^{1}H NMR of **MPyPyz** in DMSO-d_6

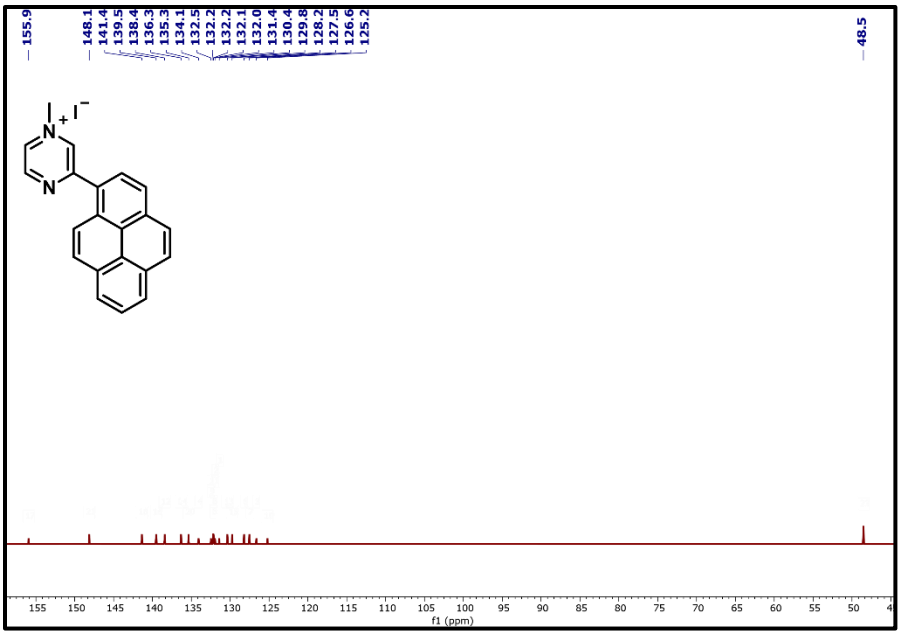

Figure 3C.2: ^{13}C NMR of **MPyPyz** in DMSO-d_6

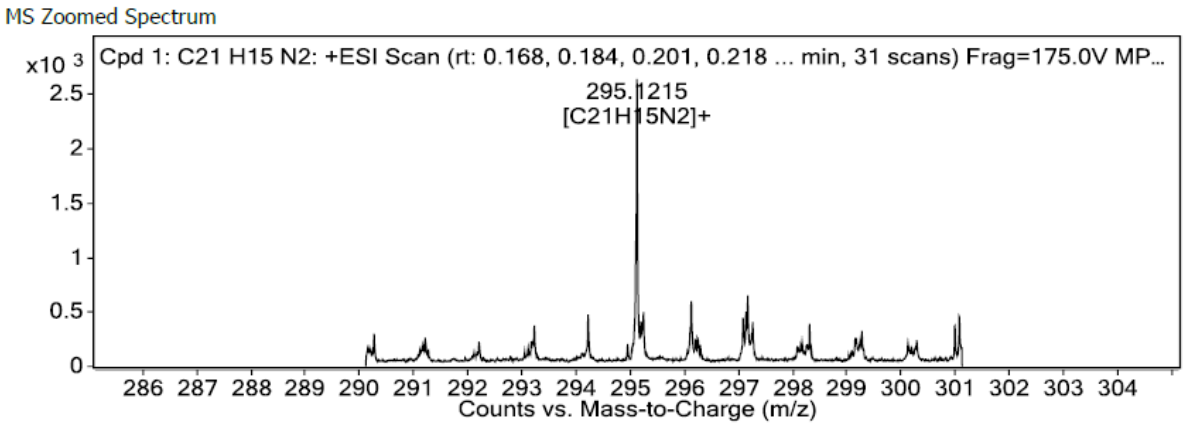

Figure 3C.3: HRMS of **MPyPyz**

MPyPyz showed high water solubility owing to the presence of positively charged pyrazinium ion with good hydrophilic properties. The Aggregation-induced emission (AIE) property of compound **MPyPyz** was evaluated in a water/DMSO mixture with varying fractions of DMSO (f_{DMSO}). **MPyPyz** was non-emissive in aqueous solution. However, when f_{DMSO} is gradually increased, the emission of **MPyPyz** enhanced. The highest emission was observed when f_{DMSO} concentration reached 80%. At this concentration, the fluorescence intensity enhanced by about 60 times compared to the aqueous solution. This confirms the aggregation-induced emission (AIE) property of **MPyPyz**.

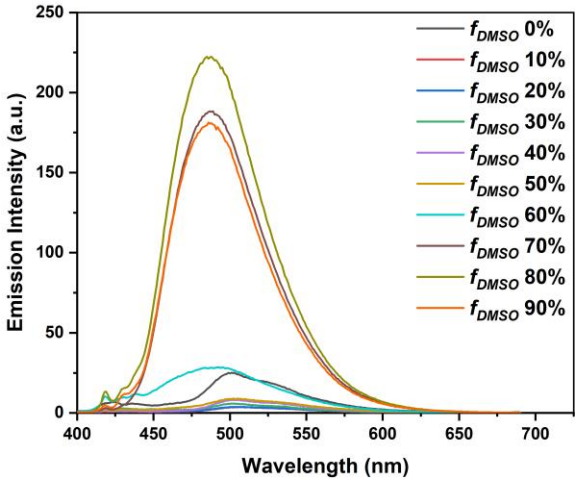

Figure 3C.4: Fluorescence spectra of **MPyPyz** in DMSO/water

3C.2.2 Response of MPyPyz toward TNP

Considering the AIE luminescent properties of **MPyPyz** in water-DMSO medium (v:v = 1:9), led to its application for the detection of nitroaromatics such as TNP, 2,4-DNB, 1-Cl,2,4-DNP, 4-NT, 4-NBA, 4-NP, DNBA and NM. Upon addition of 2.0 equivalents of the tested nitroaromatics the UV-vis absorption spectra, a new band appeared at 368 nm and 425 nm and the fluorescence emission of **MPyPyz** was quenched with TNP (**Figure 3C.5a**). No obvious change in the emission intensity of **MPyPyz** was found with other nitroaromatics except 2,4-DNP, and NP (**Figure 3C.5b**). In addition, under irradiation at UV 365 nm, the strong blue fluorescence of **MPyPyz** was quenched dramatically by TNP. The blue emission, however, was not significantly affected by other nitroaromatics.

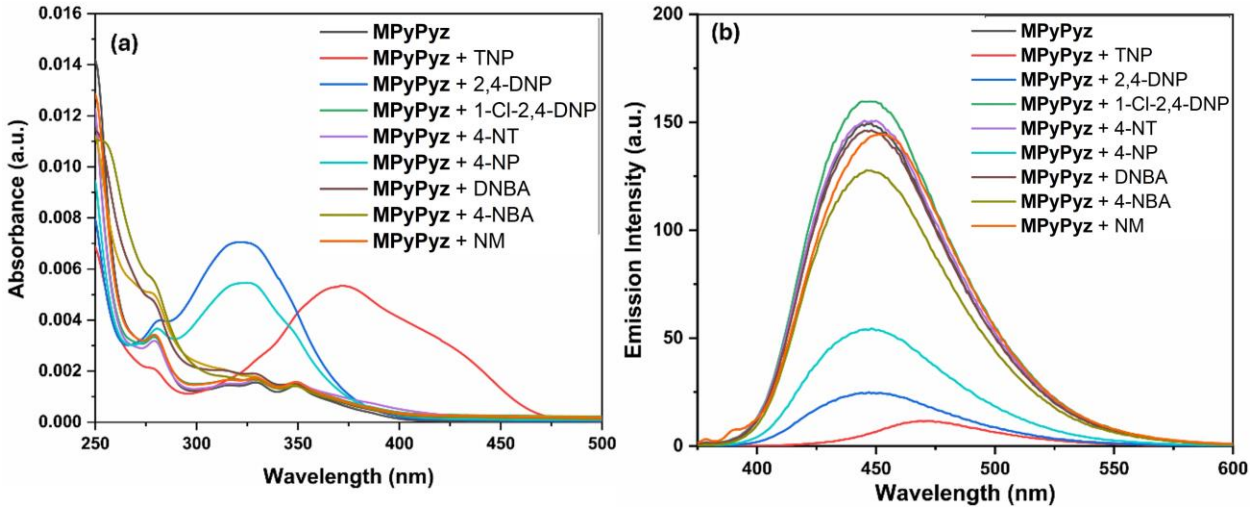

Figure 3C.4: (a) Absorption (b) Fluorescence spectra of **MPyPyz** (200 μM) in DMSO/water (8:2, v/v) toward analytes

Absorbance and fluorescence experiments were conducted to investigate the mechanism of interactions between **MPyPyz**. In the UV-vis absorption spectra, on continuous addition of TNP, the absorption intensity at 351 nm increased, and a new band appeared at 368 nm and 425 nm (**Figure 3C.6a**). In the fluorescence experiment the fluorescence emission intensity of **MPyPyz** at 449 nm was gradually quenched (95%) with the incremental addition of TNP (0 ~ 2 equivalents). The appearance of a new absorption band and decrease in emission intensity upon incremental addition of TNP can be attributed to the formation of the ground state charge transfer complex (**Figure 3C.6b**).

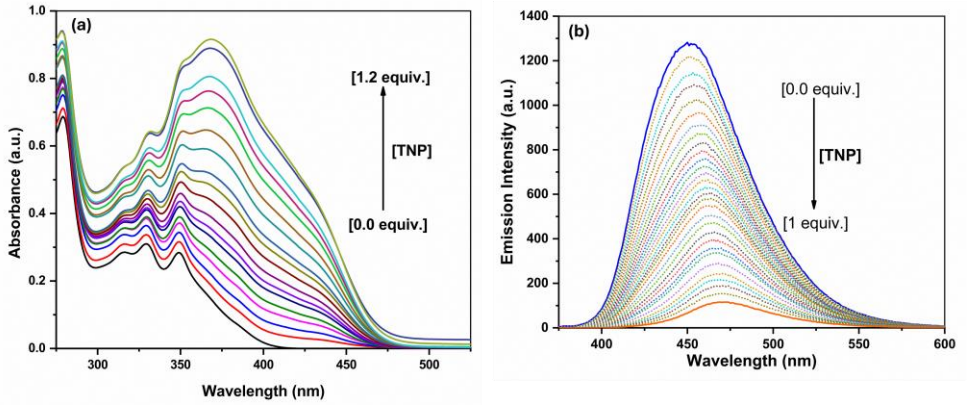

Figure 3C.6: (a) Absorption (b) Fluorescence spectra for **MPyPyz** (200 μM) in DMSO/water (8:2, v/v) with different amounts of TNP

The relative intensity of **MPyPyz** decayed linearly with 0–20 μM concentrations of TNP. In addition, the limit of detection (LOD) for TNP was calculated by $3\sigma/K$ and found to be 5 nM (**Figure 3B.7a**). The binding constant, K_B evaluated from the fluorescence data using the Benesi–Hildebrand plot was 2.18×10^6 M^{-1}, indicating efficient binding of **MPyPyz** with TNP (**Figure 3B.7b**).

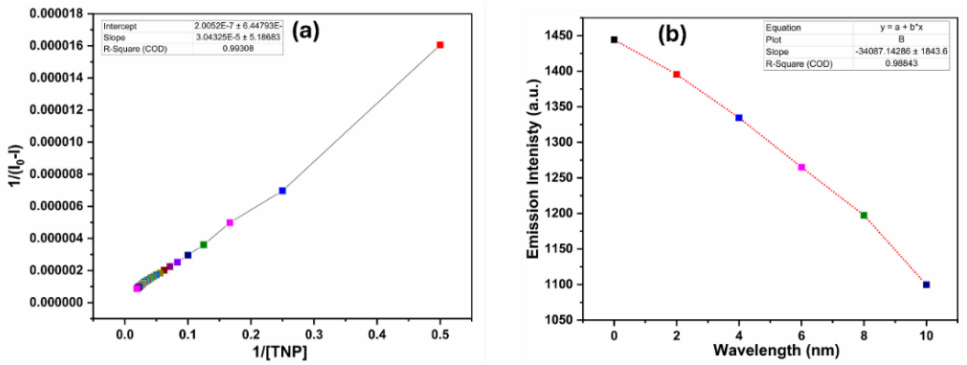

Figure 3C.7: (a) B–H plot of the fluorescence spectra of **MPyPyz** with different amounts of TNP (b) Calibration curve with error bar for calculating Limit of Detection for TNP

The fluorescence quantum yield of in water-DMSO (v:v = 9:1) was 45%, which decreased to 2.5% after interaction with TNP. Thus, the **MPyPyz** exhibited excellent sensitivity to TNP and was a potential candidate to detect TNP even at very low concentrations. The Stern-Volmer plot was linear at low concentrations of TNP, and the quenching constant, K_{sv} for TNP was estimated to be 2.70×10^5 M^{-1} (**Figure 3C.8a**). The high sensitivity of **MPyPyz** towards TNP and the non-linear nature of the S–V plot at higher concentrations of TNP suggested that an energy transfer process may also be involved in the quenching process. There is a possibility of RET from the fluorophore (donor) to non-emissive analytes (acceptor) if the emission band of the donor overlaps efficiently with the absorption band of the acceptor. Since RET has moderately higher efficiency compared to the electron transfer process, it can significantly enhance the quenching efficiency. Overlap between the absorption spectrum of TNP and the emission spectrum of **MPyPyz**, resulted in dramatic fluorescence quenching, unlike other analytes that had less overlap (**Figure 3C.8b**). To identify the extent of energy transfer, overlap integral values were calculated. The integral value, J_λ and Forster distance, R_0 was calculated to be 6.12×10^{14} M^{-1} cm^{-1} nm^{-4} and 39.21 Å for TNP indicating the possibility of energy transfer between **MPyPyz** and TNP.

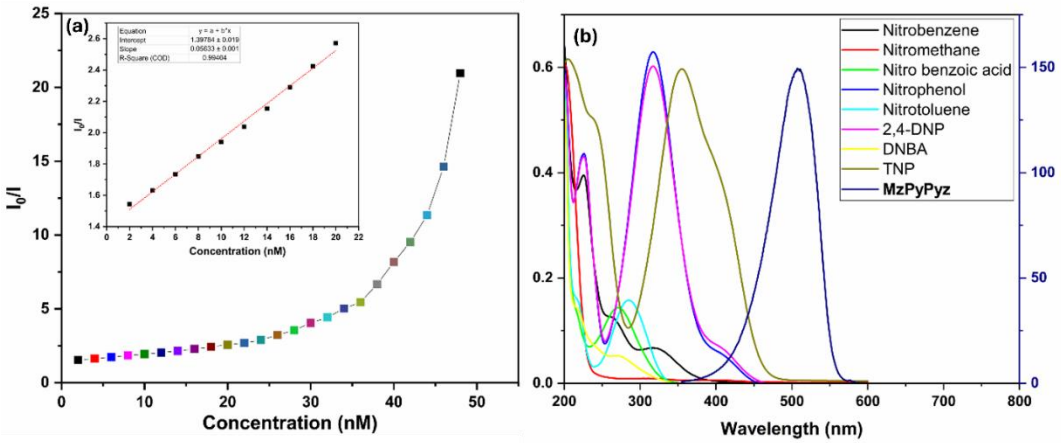

Figure 3C.8: (a) Stern−Volmer plot of **MPyPyz** using TNP as a quencher (b) Spectral overlap between the normalized emission spectrum of **MPyPyz** and normalized absorption spectra of different analytes

The nature of attenuation of fluorescence emission of **MPyPyz** by TNP was inspected by HRMS and theoretical studies. The HRMS analysis of **MPyPyz**-TNP demonstrated *m/z* peaks attributed to cationic [**MPyPyz**-I]$^+$ and anionic [TNP-H]$^-$ and species at 295.1212 (*m/z*, calc. 295.1230) and 227.9926 (*m/z*, calc. 227.9893), respectively (**Figure 3C.9**).

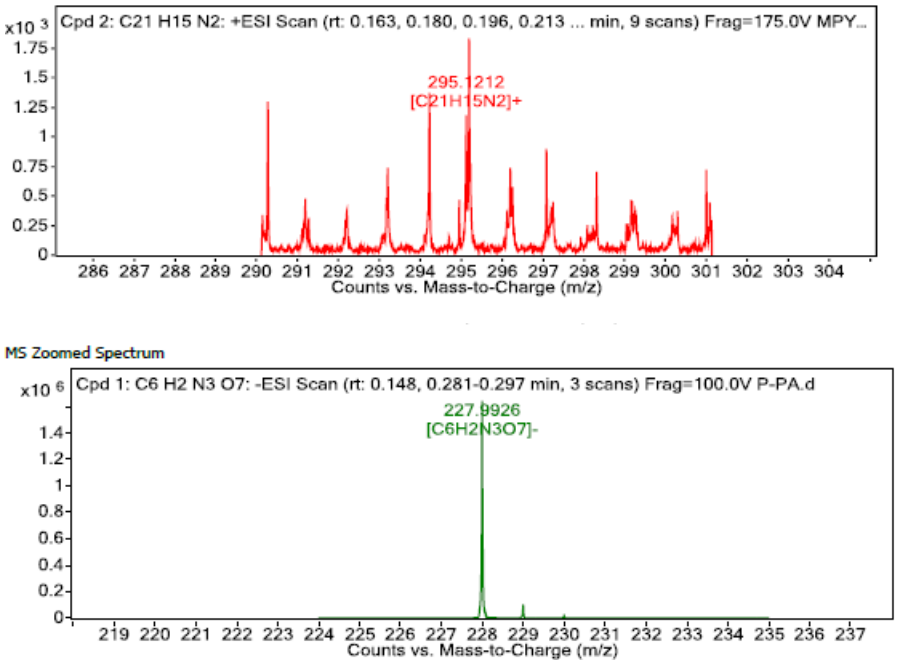

Figure 3C.9: HRMS of **MPyPyz**-TNP complex in (a) negative and (b) positive modes

To examine the interaction of **MPyPyz** and TNP, DFT calculations were conducted using the B3LYP/6–311G(d,p) method in the gas phase. The HOMO and LUMO energies of **MPyPyz** were -8.761 eV and -6.468 eV, respectively. The HOMO and LUMO energies of the picrate anion were determined to be -3.424 eV and +0.1417 eV, respectively (**Figure 3C.10**). Therefore, theoretical findings suggest that there is a potential for an electron charge transfer occur from the HOMO of the picrate anion to the LUMO of **MPyPyz**, leading to a significant reduction in energy and great efficiency in quenching.

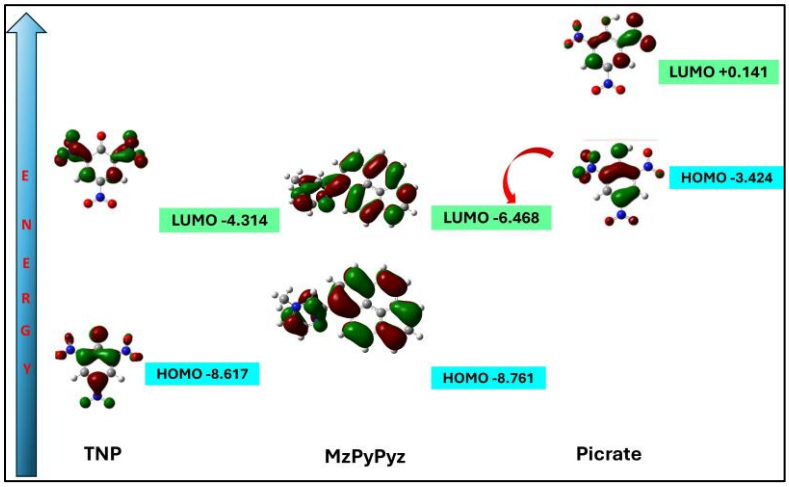

Figure 3C.10: Energy levels and frontier molecular orbitals of **BPPyz**, Picrate, and TNP

3C.2.3 Response of MPyPyz toward nitrite ions

MPyPyz was also explored the for possibility of binding different anions viz., F^-, Cl^-, Br^-, I^-, AcO^-, $H_2PO_4^-$, HSO_4^-, ClO_4^- and NO_3^- in water-DMSO medium solution. In the presence of nitrite ions, the UV–vis absorption band at 347 nm blue shifted to 358 nm (**Figure 3C.11a**). However, no such spectral change was observed with other competitive anions. These results indicated the formation of a ground state charge transfer complex between **MPyPyz** and NO_2^-. No obvious spectral changes were observed in the presence of other anions, due to their weaker interactions with the receptor. The emission spectra of **MPyPyz** were recorded in the presence of different anions, and no alteration was observed except NO_2^- (**Figure 3C.11b**). The change in the absorption and fluorescence spectra can be attributed to the formation of ground state charge transfer complex and exchange of I^- with NO_2^-.

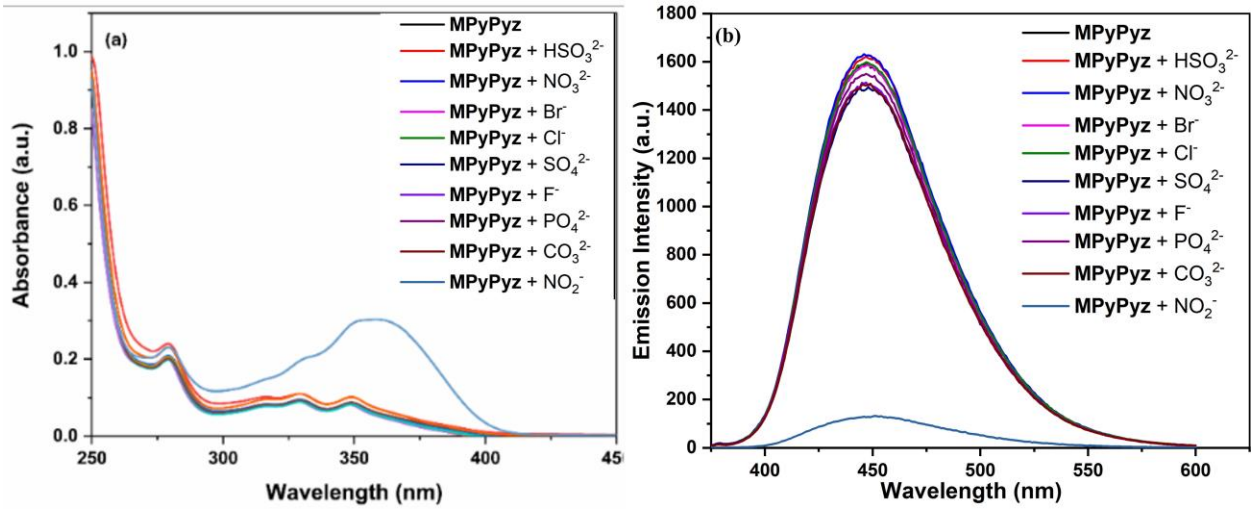

Figure 3C.11: (a) Absorption (b) Fluorescence spectra of **MPyPyz** (200 μM) in DMSO/water (8:2, v/v) toward anions

To further explore the quenching effect of NO_2^- anions on the emission of **MPyPyz**, UV-vis absorption and fluorescence spectra were recorded with different amounts of NO_2^-. In UV-vis absorption spectra, on continuous addition of NO_2^-, an increase in absorption intensity at 347 was observed (**Figure 3C.12a**). The emission intensity of **MPyPyz** was quenched steadily and quenching efficiency was found to be 90.07% (**Figure 3C.12b**).

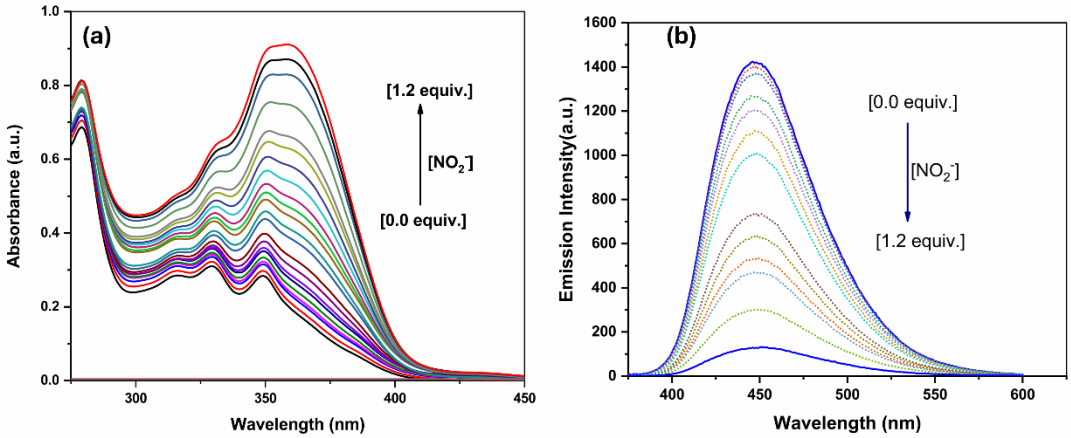

Figure 3B.12: (a) Absorption (b) Fluorescence spectra for **MPyPyz** (200 μM) in DMSO/water (8:2, v/v) with different amounts of NO_2^-

The limit of detection was calculated to be 12.0 nM. The linear variation at low concentrations was due to static quenching. The linear fit of the plot provided $K_{sv} = 3.8 \times 10^5\ M^{-1}$ and a correlation coefficient (R^2) = 0.9936. The deviation from linearity indicated dynamic quenching.

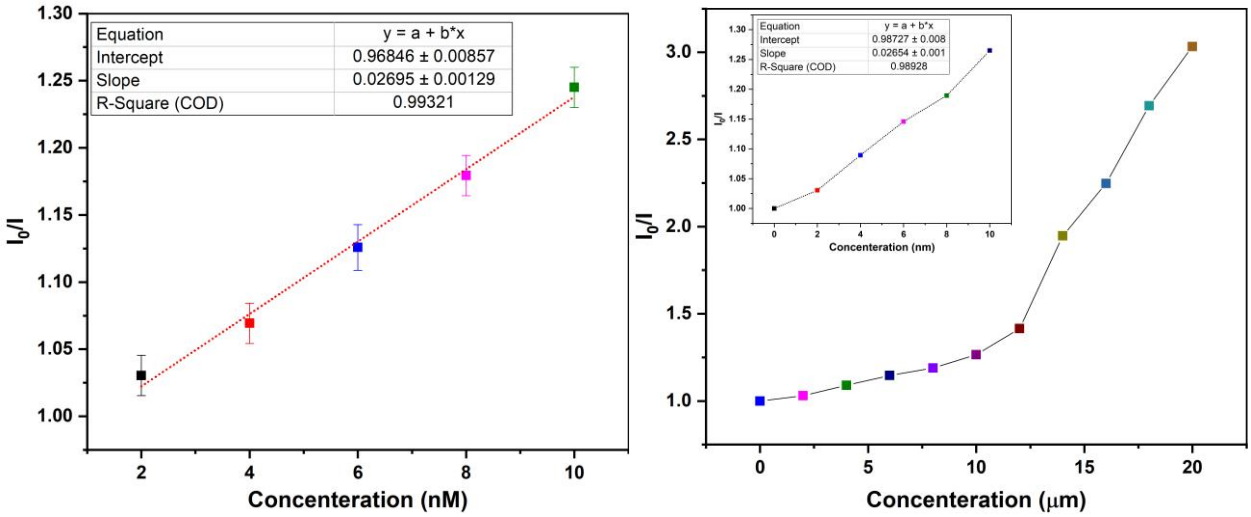

Figure 3B.13: (a) Calibration curve with error bar for calculating Limit of Detection for NO_2^- (b) Stern−Volmer plot of **MPyPyz** using NO_2^- as a quencher

The fluorescence response of **MPyPyz** for NO_2^- was evaluated in the presence of F^-, Cl^-, Br^-, I^-, NO_3^-, HCO_3^-, CH_3COO^-, SO_4^{2-}, and PO_4^{2-}. No change in fluorescence quenching suggested that **MPyPyz** can selectively distinguish the NO_2^- in presence of these competitive anions (**Figure 3C.14**).

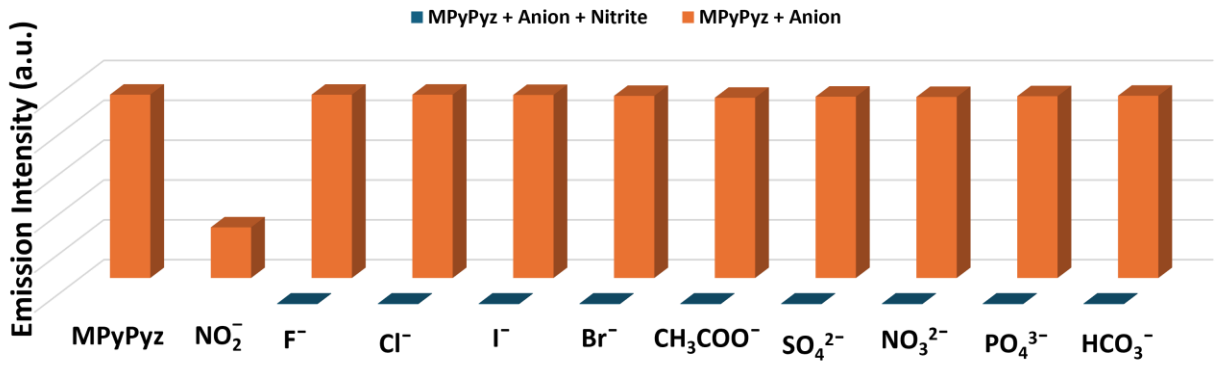

Figure 3B.14: Selectivity of **MPyPyz** (200 μM) in DMSO/water (8:2, v/v) toward anions in the presence of anions

The DFT calculations were performed using the B3LYP/6–311G(d,p) level of theory to investigate the detection NO_2^-. The electron density in HOMO and LUMO of **MPyPyz** was distrubuted around iodide and nitrogen atom of pyrazine. Upon anion exchange with NO_2^- the electron density was distributed all over the **MPyPyz**. Furthermore, the **MPyPyz**-NO_2^- complex had a significantly smaller energy gap between the HOMO and the LUMO compared to **MPyPyz**. Specifically, the energy gap in the **MPyPyz**-NO_2^- complex was measured to be -1.85 eV, whereas in **MPyPyz** it was -1.94 eV. The decrease in the HOMO-LUMO gap in the **MPyPyz**-NO_2^- complex can be explained by the alteration in electron distribution resulting from the exchange of anions (**Figure 3C.15)**.

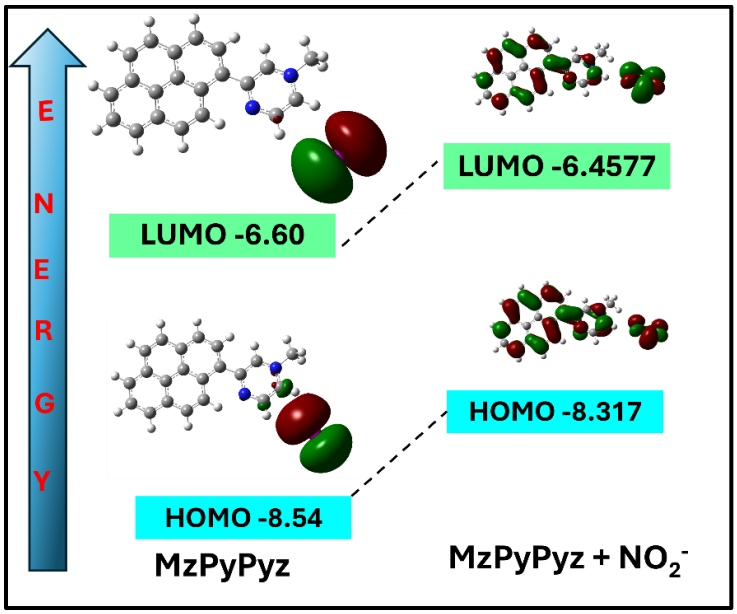

Figure 3A.15: Energy levels and frontier molecular orbitals of **MPyPyz**-NO_2^- complex

3C.2.4 Analytical Applications

Latent Fingerprints using MPyPyz

The solid-state emissive chromophores are effective in the forensic investigation of latent fingerprints. Fingerprints are distinctive and complex traces left on objects by eccrine gland secretions displayed as epidermal ridges containing inorganic salts, proteins, amino acids, and fatty acids in trace amounts. Forensic science frequently uses fingerprint analysis to identify criminals because of their distinctiveness. However, in most cases, fingerprints are latent and untreatable, making them invisible to the naked eye. Fingerprint characteristics are divided into three levels. The basic pattern *i.e.* level 1 refers to fingerprint macro details, including loop, delta, and whorl. Level 2 includes small details such as bifurcation, trifurcations, short ridges, bridges, lakes, and dots. These points are also referred to as "minutiae" points. Level 3 attributes to micro level features such as ridge path deviations and sweat pores. The features of level-2 such as, bifurcation, enclosure, ridge ends were extracted from the fingerprint developed using **MPyPyz** anions (**Figure 3C.16)**.

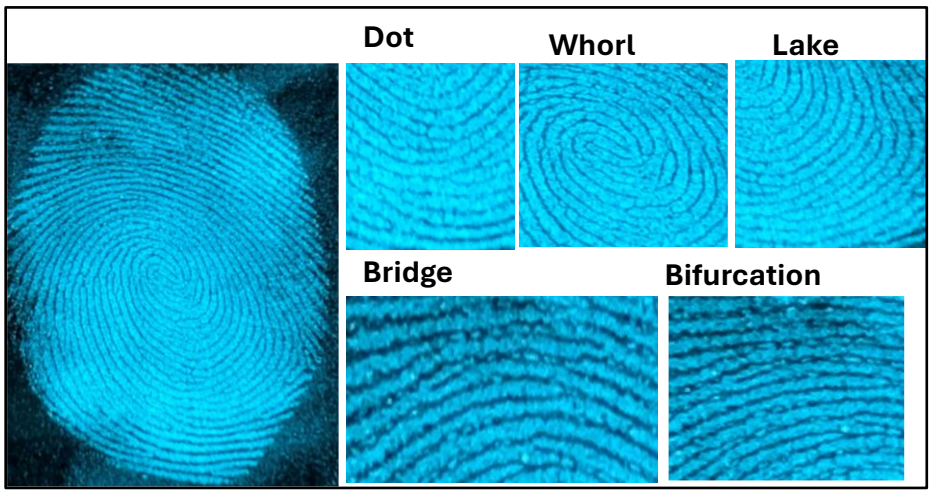

Figure 3C.16: Minutiae features of the fingerprints developed using **MPyPyz**-based fingerprint powder and exposed to UV light (365 nm)

Implementation of test paper strips

Commercial Whatman filter paper was utilized to make paper test strips for the quick and on-site identification of TNP and nitrite ions. The strips were immersed in a concentrated **MPyPyz** solution for a duration of 10 minutes, and thereafter left to air dry for a period of two hours. The test strips were immersed in aqueous solutions containing TNP or nitrite ions at concentrations

ranging from 10^{-3} to 10^{-6} M and the quenching in fluorescence of **MPyPyz** was observed anions (**Figure 3C.17)**.

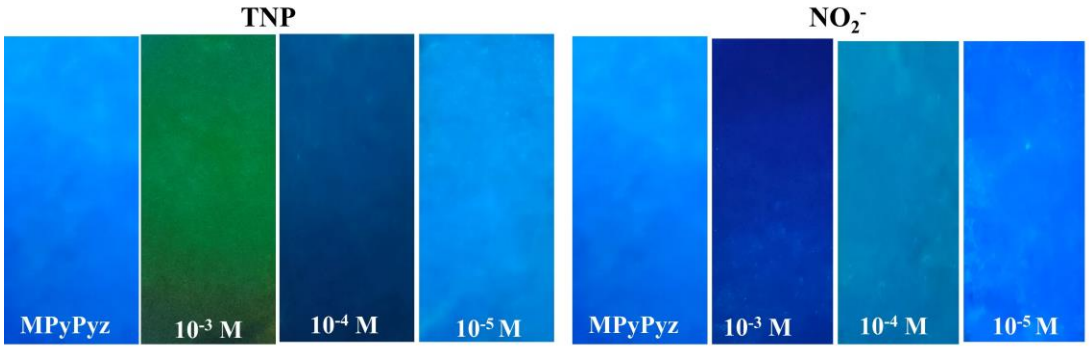

Figure 3C.17: Photographs of test paper strips for detection of TNP and NO_2^- under 365 nm UV light

Table A8 and A9, Appendix A show a comparison of **MPyPyz** with chemosensors reported in the literature.

3C.3 CONCLUSION

An AIE-based pyrazinium-salt, **MPyPyz** was synthesized and characterized. The studies showed that the AIE property arises due to restriction in rotation. The chemosensor gave a fluorescent turn-off response in the presence of TNP and nitrite ions. The mechanism for quenching for TNP was ascribed to the formation of the ground state charge transfer complex along with RET. The quenching in the presence of nitrite ions was attributed to the anion exchange of I^- with NO_2^-.

3.2 REFERENCES

1. Khan, S.; Valiyaneerilakkal, U.; Kumar, S.; Singh, A.; Ahmed, A.; Perera, H.; Mahadeva, R.; Alawatugoda, J.; Arya, S.; *Microchemical Journal*, **2024**, 110474.
2. Liu, X.; Han, Y.; Shu, Y.; Wang, J.; Qiu, H.; *Journal of Hazardous Materials*, **2022**, *425*, 127987.
3. Qian, Y.; Li, J.; Ji, M.; Li, J.; Ma, D.; Liu, A.; Zhao, Y.; Yang, C.; *Frontiers in Chemistry*, **2022**, *10*, 943813.
4. Rodgers, J. D.; Bunce, N. J.; *Water Research*, **2001**, *35* (9), 2101-2111.
5. Furton, K. G.; Myers, L. J.; *Talanta*, **2001**, *54* (3), 487-500.
6. Joarder, B.; Desai, A. V.; Samanta, P.; Mukherjee, S.; Ghosh, S. K.; *Chemistry–A European Journal*, **2015**, *21* (3), 965-969.
7. Barata, P. D.; Prata, J. V.; *Chemosensors*, **2020**, *8* (4), 128.
8. Samanta, P.; Dutta, S.; Ghosh, S. K., Metal-organic frameworks for detection and desensitization of environmentally hazardous nitro-explosives and related high energy materials. In *Metal-Organic Frameworks (MOFs) for Environmental Applications*, Elsevier: 2019; pp 231-283.
9. Sharma, V.; Mehata, M. S.; *Spectrochimica Acta Part A: Molecular and Biomolecular Spectroscopy*, **2021**, *260*, 119937.
10. Gogia, A.; Mandal, S. K.; *Dalton Transactions*, **2019**, *48* (7), 2388-2398.
11. Yan, Q.-L.; Gozin, M.; Zhao, F.-Q.; Cohen, A.; Pang, S.-P.; *Nanoscale*, **2016**, *8* (9), 4799-4851.
12. Kumar, V.; Saini, S. K.; Choudhury, N.; Kumar, A.; Maiti, B.; De, P.; Kumar, M.; Satapathi, S.; *ACS Applied Polymer Materials*, **2021**, *3* (8), 4017-4026.
13. Bauri, K.; Saha, B.; Mahanti, J.; De, P.; *Polymer Chemistry*, **2017**, *8* (46), 7180-7187.
14. Gowri, A.; Vignesh, R.; Kathiravan, A.; *Spectrochimica Acta Part A: Molecular and Biomolecular Spectroscopy*, **2019**, *220*, 117144.
15. Rai, R.; Bhandari, R.; Kaleem, M.; Shraogi, N.; Patnaik, S.; Mishra, H.; Misra, A.; *Industrial & Engineering Chemistry Research*, **2024**,
16. Khabarov, Y. G.; Patrakeev, A. A.; Veshnyakov, V. A.; Kosyakov, D. S.; Ul'yanovskii, N. V.; Garkotin, A. Y.; *Organic Preparations and Procedures International*, **2017**, *49* (2), 178-181.

17. Hebert, R. M.; Jackovitz, A. M., Wildlife toxicity assessment for picric acid (2, 4, 6-trinitrophenol). In *Wildlife Toxicity Assessments for Chemicals of Military Concern*, Elsevier: 2015; pp 271-277.
18. Wyman, J. F.; Serve, M. P.; Hobson, D. W.; Lee, L. H.; Uddin, D. E.; *Journal of Toxicology and Environmental Health, Part A Current Issues*, **1992**, *37* (2), 313-327.
19. Kimura, N.; Kitagawa, W.; Kamagata, Y.; *Biological Remediation of Explosive Residues*, **2014**, 1-13.
20. Bilal, M.; Bagheri, A. R.; Bhatt, P.; Chen, S.; *Journal of Environmental Management*, **2021**, *291*, 112685.
21. Patel, R.; Bothra, S.; Kumar, R.; Sahoo, S. K.; *Nano-Structures & Nano-Objects*, **2019**, *19*, 100345.
22. Goel, A.; Malhotra, R.; *Journal of Molecular Structure*, **2022**, *1249*, 131619.
23. Khan, I.; Shah, T.; Tariq, M. R.; Ahmad, M.; Zhang, B.; *Journal of Environmental Chemical Engineering*, **2024**, 112720.
24. Tanwar, A. S.; Meher, N.; Adil, L. R.; Iyer, P. K.; *Analyst*, **2020**, *145* (14), 4753-4767.
25. Noronha, V. T.; Aquino, Y. M.; Maia, M. T.; Freire, R. M., Sensing of Water Contaminants: From Traditional to Modern Strategies Based on Nanotechnology. In *Nanomaterials Applications for Environmental Matrices*, Elsevier: 2019; pp 109-150.
26. Tohora, N.; Sultana, T.; Mahato, M.; Ahamed, S.; Das, S. K.; *ChemistrySelect*, **2023**, *8* (21), e202301023.
27. Koç, O. m. K.; Üzer, A. e.; Apak, R. a.; *ACS Applied Materials & Interfaces*, **2023**, *15* (35), 42066-42079.
28. Yin, H.; Wu, Y.; Peng, X.; Song, F.; *Chemical Communication*, **2020**, *56* (72), 10549-10551.
29. Zhang, H.; Xue, S.; Feng, G.; *Sensors and Actuators B: Chemical*, **2016**, *231*, 752-758.
30. Liu, S.; Song, L.; Sun, Q.; Chen, Z.; Ge, Y.; Zhang, W.; Qian, J.; *RSC Advances*, **2015**, *5* (111), 91863-91868.
31. S Rocha, B.; Gago, B.; Pereira, C.; M Barbosa, R.; Bartesaghi, S.; O Lundberg, J.; Radi, R.; Laranjinha, J.; *Current drug targets*, **2011**, *12* (9), 1351-1363.
32. Tejero, J.; Shiva, S.; Gladwin, M. T.; *Physiological reviews*, **2019**, *99* (1), 311-379.
33. Martínez-Ruiz, A.; Cadenas, S.; Lamas, S.; *Free radical biology and medicine*, **2011**, *51* (1), 17-29.

34. Bryan, N. S.; *Free Radical Biology and Medicine*, **2006**, *41* (5), 691-701.
35. Jensen, F. B.; *Biochimica et Biophysica Acta (BBA)-Bioenergetics*, **2009**, *1787* (7), 841-848.
36. Lundberg, J. O.; Weitzberg, E.; Gladwin, M. T.; *Nature reviews Drug discovery*, **2008**, *7* (2), 156-167.
37. Hakeem, K. R.; Sabir, M.; Ozturk, M.; Akhtar, M. S.; Ibrahim, F. H.; *Reviews of Environmental Contamination and Toxicology Volume 242*, **2017**, 183-217.
38. Beligni, M.; Lamattina, L.; *Plant, Cell & Environment*, **2001**, *24* (3), 267-278.
39. Yilong, Z.; Dean, Z.; Daoliang, L.; *International Journal of Electrochemical Science*, **2015**, *10* (2), 1144-1168.
40. Tavker, N.; Gaur, U. K.; Sharma, M.; *Nanoscale Advances*, **2020**, *2* (7), 2870-2884.
41. Masime, J. O., Analysis of the levels of arsenic, nitrate, nitrite and phosphate in home made brews, spirits, in water and raw materials in nairobi county. Kenyatta University, 2011.
42. Bryan, N. S.; Loscalzo, J.; **2017**,
43. Avery, A. A.; *Environmental health perspectives*, **1999**, *107* (7), 583-586.
44. Johnson, S. F.; *Current problems in pediatric and adolescent health care*, **2019**, *49* (3), 57-67.
45. Ziarati, P.; Zahedi, M.; Shirkhan, F.; Mostafidi, M.; *SF Pharma J*, **2018**, *1* (3), 1-13.
46. Dawidziuk, B.; Nawała, J.; Dziedzic, D.; Gordon, D.; Popiel, S.; *Analytical Methods*, **2018**, *10* (43), 5188-5196.
47. Liu, M.; Zheng, W.; Yang, Y.; Shi, G.; Li, Y.; Zhou, S.; Zhao, Y.; Yao, Z.; *Microchemical Journal*, **2023**, *191*, 108889.
48. Terry, L. R.; Sanders, S.; Potoff, R. H.; Kruel, J. W.; Jain, M.; Guo, H.; *Analytical Science Advances*, **2022**, *3* (3-4), 113-145.
49. Tanwar, A. S.; Patidar, S.; Ahirwar, S.; Dehingia, S.; Iyer, P. K.; *Analyst*, **2019**, *144* (2), 669-676.
50. Pisoschi, A. M.; Pop, A.; Gajaila, I.; Iordache, F.; Dobre, R.; Cazimir, I.; Serban, A. I.; *Microchemical Journal*, **2020**, *155*, 104681.
51. Pisoschi, A. M.; Pop, A.; *Open Chemistry*, **2018**, *16* (1), 1248-1256.
52. Yilmaz, U. T.; Somer, G.; *Analytica Chimica Acta*, **2007**, *603* (1), 30-5.
53. Zhang, L.-J.; Wang, Z.-Y.; Cao, X.-J.; Liu, J.-T.; Zhao, B.-X.; *Sensors and Actuators B: Chemical*, **2016**, *236*, 741-748.

54. Săcărescu, L.; Chibac-Scutaru, A.-L.; Roman, G.; Săcărescu, G.; Simionescu, M.; *Environmental Chemistry Letters*, **2022**, *21* (1), 561-596.

55. Sirbu, D.; Zeng, L.; Waddell, P. G.; Benniston, A. C.; *Organic Biomolecular Chemistry*, **2019**, *17* (31), 7360-7368.

56. Tan, L.; Lin, W.; Zhu, S.; Yuan, L.; Zheng, K.; *Organic Biomolecular Chemistry*, **2014**, *12* (26), 4637-43.

57. Ma, X.; Liu, C.; Shan, Q.; Wei, G.; Wei, D.; Du, Y.; *Sensors and Actuators B: Chemical*, **2013**, *188*, 1196-1200.

58. Sun, Y. Q.; Wang, P.; Liu, J.; Zhang, J.; Guo, W.; *Analyst*, **2012**, *137* (15), 3430-3.

59. Paul, S.; Majumdar, T.; Mallick, A.; *Dalton Transactions*, **2021**, *50* (5), 1531-1549.

60. Wei, T.; Wang, F.; Chen, Y.; Qiang, J.; Zhang, Z.; Chen, T.; Chen, X.; *Dyes and Pigments*, **2018**, *159*, 322-330.

61. Wu, J.; Liu, W.; Ge, J.; Zhang, H.; Wang, P.; *Chemical Society Reviews*, **2011**, *40* (7), 3483-95.

62. Moragues, M. E.; Martinez-Manez, R.; Sancenon, F.; *Chemical Society Reviews*, **2011**, *40* (5), 2593-643.

63. Saini, V.; Gupta, A.; Rangan, K.; Khungar, B.; *Dyes and Pigments*, **2020**, *180*, 108447.

64. Kumari, S.; Joshi, S.; Cordova-Sintjago, T. C.; Pant, D. D.; Sakhuja, R.; *Sensors and Actuators B: Chemical*, **2016**, *229*, 599-608.

65. Harathi, J.; Thenmozhi, K.; *Chemosphere*, **2022**, *286* (Pt 2), 131825.

66. Harathi, J.; Selva Kumar, R.; Ashok Kumar, S. K.; Saravanakumar, D.; Senthilkumar, S.; Thenmozhi, K.; *Journal of Materials Chemistry C*, **2022**, *10* (20), 7949-7961.

68. Duan, C.; Zhang, J.-F.; Hu, Y.; Zeng, L.; Su, D.; Bao, G.-M.; *Dyes and Pigments*, **2019**, *162*, 459-465.

69. P, S.; Prakash, S.; Joseph, A.; *RSC Adv.*, **2023**, *13* (4), 2552-2560.

70. Venkatachalam, K.; Asaithambi, G.; Rajasekaran, D.; Periasamy, V.; *Spectrochimica Acta Part A: Molecular and Biomolecular Spectroscopy*, **2020**, *228*, 117788.

71. Uchacz, T.; Jajko, G.; Danel, A.; Szlachcic, P.; Zapotoczny, S.; *New Journal of Chemistry*, **2019**, *43* (2), 874-883.

72. Singh, L.; Ranjan, N.; *Journal of the American Chemical Society*, **2023**, *145* (5), 2745-2749.

73. Deniz Yilmaz, M.; *Microchemical Journal*, **2024**, *196*, 109554.

74. Yang, L.; Wang, F.; Zhao, J.; Kong, X.; Lu, K.; Yang, M.; Zhang, J.; Sun, Z.; You, J.; *Talanta*, **2021**, *221*, 121477.

75. Yu, K. K.; Pan, S. L.; Li, K.; Shi, L.; Liu, Y. H.; Chen, S. Y.; Yu, X. Q.; *Food Chemistry*, **2021**, *341* (Pt 2), 128254.

76. Wang, H.; Wen, Y.; Yang, X.; Wang, Y.; Zhou, W.; Zhang, S.; Zhan, X.; Liu, Y.; Shuai, Z.; Zhu, D.; *ACS Applied Material and Interfaces*, **2009**, *1* (5), 1122-9.

77. Ni, X. L.; Chen, S.; Yang, Y.; Tao, Z.; *Journal of the American Chemical Society*, **2016**, *138* (19), 6177-83.

78. Schmitt, V.; Moschel, S.; Detert, H.; *European Journal of Organic Chemistry*, **2013**, *2013* (25), 5655-5669.

Chapter 4

Pyridinium and Imidazolium Salts for Fluorometric/Colorimetric Detection of Metal Ions

4.1 INTRODUCTION

Aluminium is the third most abundant element (after oxygen and silicon) in the earth's crust.[1] It is extensively used as utensils, electrical components in different gadgets, food additives, and packaging material.[2] Besides, it also plays a pivotal role in pharmaceutical industries, water purification, dyes, and textile production.[3] As a consequence, humans are easily exposed to Al^{3+} through food, drugs, and water. Exposure for long periods results in slow aluminum accumulation and circulation to almost all tissues, which reaches plasma through iron-binding protein and is stored in the brain.[4] Alzheimer [5] and Parkinson [6] disease can happen even with a minimum dose of chronic exposure to aluminum from drinking water due to aluminum-induced oxidative deterioration in the CNS (central nervous system).[7] It is also referred to as a silent killer as it is a causative factor of smoking-related diseases,[8] bone softening,[9] chronic renal failure,[10] osteoporosis, osteomalacia,[11] breast cancer,[12] and amyotrophic lateral sclerosis.[13] In addition, the increase in the concentration of the soluble form of (Al^{3+}) in water harms aquatic animals and plants because Al^{3+} can acidify water.[14] The recommended aluminum intake by WHO is around 3–10 mg per day, and the permitted concentration of Al^{3+} is 7.4 μM in drinking water.[15]

Chemosensors with Schiff base molecules exhibiting fluorescence response for the detection of Al^{3+} ion are shown in **Figure 4.1**. The naphthalene-based azo-armed Schiff base chemosensor **1** was synthesized from a naphthalene fluorophore. Upon interaction with Al^{3+}, **1** emitted a greenish-yellow fluorescence. This reaction was driven by isomerization of the C=N bond and photoinduced electron transfer (PET) in combination with the metal-induced CHEF (chelation-enhanced fluorescence) process. The hydroxy group from naphthalene, the pyridine ring nitrogen, and imine nitrogen offer a perfect host pocket for guest Al^{3+}. Cell imaging and cytotoxicity studies showed the applicability of **1** in biological systems.[16] The practical applications of the sensor were explored by designing molecular logic gates and a paper strip study. Benzofuranone based chemosensor **2** was reported as a fluorescent chemosensor for Al^{3+} ions. The high binding constant and LOD reflected strong affinity between **2** and Al^{3+}. The accuracy to detect trace levels of Al^{3+} in water and tea was comparable to the results obtained from ICP-OES method.[17] A chemosensor **3** displayed increase in fluorescence intensity due to the inhibition of PET and C=N isomerization upon binding with Al^{3+}. The quantum yield and fluorescence lifetime of chemosensor also increased upon Al^{3+} addition. It offered a sensitive and selective method for detecting Al^{3+} in various samples including environmental water sources like rivers.[18] A tridentate Schiff base

receptor **4** showed a significant fluorescence enhancement upon adding Al^{3+} ions, while no other tested metal ions perturb the fluorescence profile. The selective complexation between **4** and Al^{3+} restricted the conformational flexibility in the excited state via inhibition of C=N isomerization, resulting in significant fluorescence enhancement. This affinity was attributed to three donor sites in **4**: phenolate-O, imine-N, and thiol-S.[19] 2-hydroxynaphthaldehyde skeleton based chemosensor **5** on addition of Al^{3+} led to a notable increase in fluorescence intensity up to ten times, along with a hypsochromic shift (blue shift) of 152 nm in emission maxima, indicating enhanced electronic interaction and stability of **5** with Al^{3+}. This interaction likely inhibited excited-state intramolecular proton transfer, favoring intramolecular charge transfer.[20]

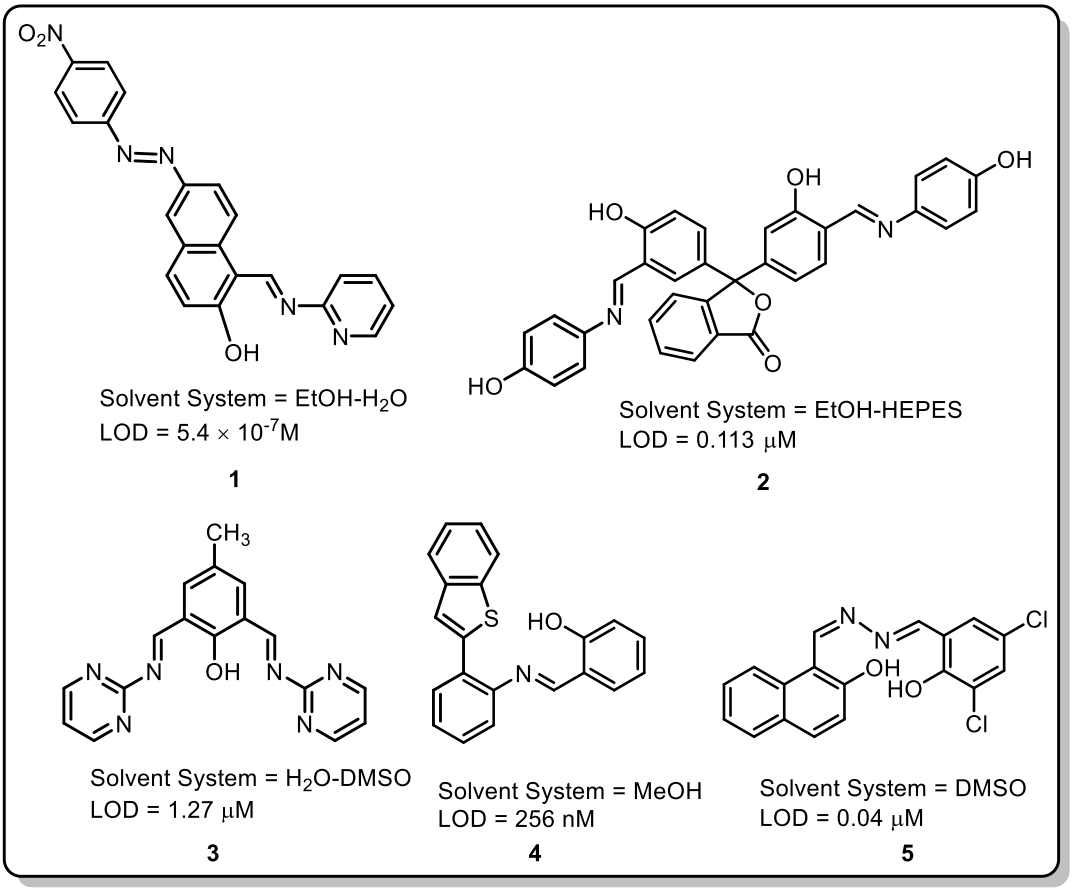

Figure 4.1: Chemosensors for detection of aluminum ions

The luminescent properties and longer wavelength emission of Schiff bases in the solid state may be useful for applications in latent fingerprinting.[21-22] The fluorescent powder has the advantage of developing latent fingerprints (LFPs) deposited on multicolor surfaces due to better resolution

and higher signal-to-noise ratio. Therefore, the fingerprints produced by fluorescent fingerprint powder can be readily viewed and photographed using an appropriate excitation light source.

Copper is the third most abundant trace element in the human body and plays a vital role in many elementary physiological processes.[23] Copper is an essential co-factor or structural component of many metalloenzymes, including cytochrome oxidase, and superoxide dismutase. Copper is involved in developing and functioning immune cells, helping the body to defend against infections and diseases.[24-26] Its antioxidant properties help to prevent cell damage and are required to produce bone and connective tissues. As a result, taking copper ions daily is quite important for maintaining good health.[27] It is also recognized to have an essential role in energy production, signal transduction, and dioxygen transport.[28] However, excessive entry of copper into food chains can cause major health problems such as gastrointestinal and renal system illnesses. Disruptions in the copper homeostasis have been linked to Alzheimer's, Wilson's, Prion, and Parkinson's diseases.[29] Copper is also frequently used in current industrial processes, and various industrial operations generate a large amount of wastewater containing copper species.[30] As a result, analytical methods with a low detection limit, excellent selectivity, and sensitivity for copper ions in aqueous media are critical for protecting human health and the environment.

Copper has been detected using a variety of approaches, including atomic absorption spectroscopy, ion-selective electrodes, inductively coupled plasma mass spectroscopy, inductively coupled atomic emission spectroscopy, voltammetry, and X-ray fluorescence.[31] However, unlike most analytical techniques, a colorimetric method may efficiently and conveniently monitor objective analytes in the visible range while remaining simple, sensitive, and cost-effective. Colorimetric assays often have a greater dynamic range, making it possible to detect a wider range of analyte concentrations. They are also versatile in terms of sample compatibility and stability over time.

Several organic compounds have been used as chemosensors because of their capacity to detect copper through a change in fluorescence or absorption spectrum (**Figure 4.2**). The colorless solution of chemosensor **6** became orangish-yellow with the addition of Cu^{2+}. The UV-vis absorption spectra revealed the formation of a new peak at 558 nm combined with a 23 nm redshift of the 359 nm peak of **6**.[32] N-azo dye ligand **7** was synthesized to provide a quick, sensitive, and selective way to measure copper (II) ions via formation of a deep yellow-colored complex at pH 10.0.[33] Colorimetric sensor **8** based on diaminomaleonitrile and 3-hydroxynaphthalimide chromophores for the selective detection of Cu^{2+} ions was reported. On addition of Cu^{2+} ions, a

strong absorption band appeared at 565 nm, combined with a striking color shift from yellow to pink, suggesting a Cu^{2+} selective colorimetric response. **8** was selective for Cu^{2+} as evidenced by the fact that no notable spectrum changes were observed with other environmentally relevant metal ions, such as alkali, alkaline earth, and transition metal ions. A smartphone was also used as a detection tool to assess Cu^{2+} levels in extracted simulated semiconductor wastewater samples based on the colorimetric response, demonstrating the usefulness of **8** in real-world applications.[34] Quinoline scaffold-based sensor **9**, which upon chelation with Cu^{2+} in CH_3OH/aqueous HEPES buffer (v/v, 8:2, pH = 7.4) medium produced a visible color change from light yellow to red. **9** originally showed broad absorption maxima at 330 nm and 385 nm, corresponding to the keto and enol forms. The UV–vis absorption spectrum showed the appearance of a new band at 505 nm and a well-defined isosbestic point at 430 nm.[35] A chelated-type colorimetric chemosensor **10** turned into yellow color complex upon the addition of Cu^{2+} ions. Well-defined isobestic points were found through extensive spectroscopic investigations, including UV-vis spectral titrations. The great sensitivity of **10** was demonstrated by the low detection limits for Cu^{2+} (0.88 μM) which were below the WHO safe standards.[36]

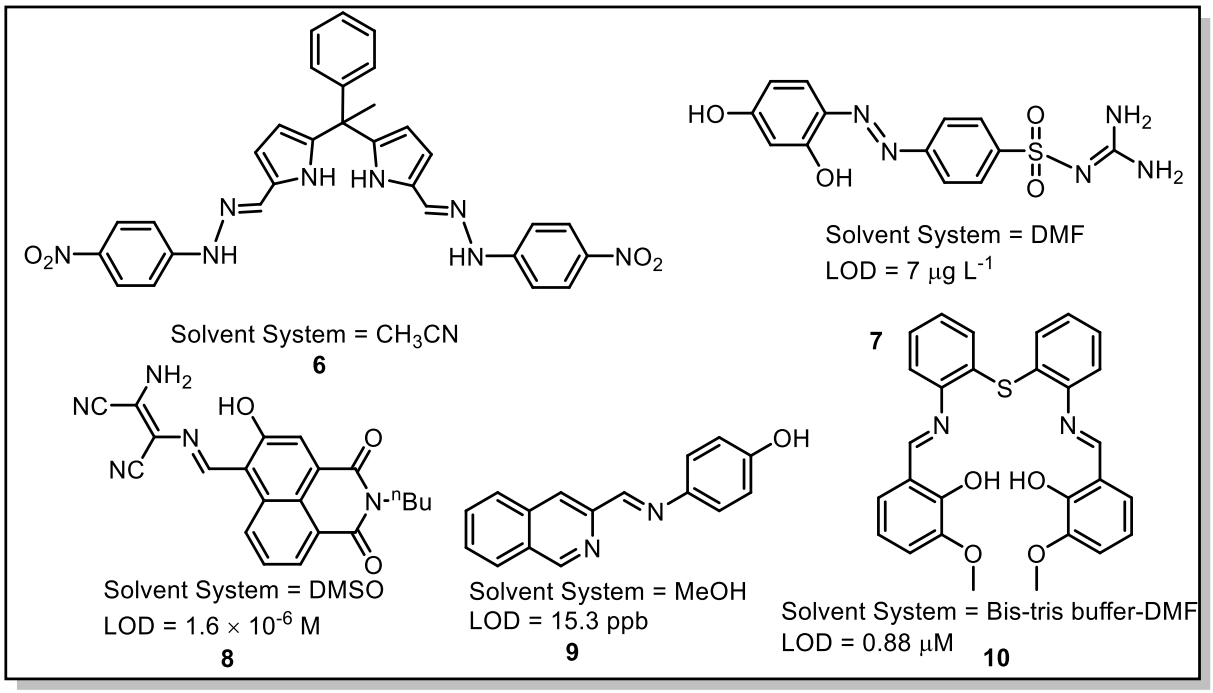

Figure 4.2: Chemosensors for detection of copper ions

Schiff-base compounds are the organic compounds produced when an aldehyde or ketone reacts with a primary amine. A chromophore group in the Schiff base molecule interacts with the target

analyte to cause a reversible color shift. Schiff base chemosensors are designed and synthesized by modifying the chemical structure of the receptor site to selectively bind to the target analyte having interactions like hydrogen bonding, coordination, or π-π stacking. The Schiff base precursor and its functional groups are critical in determining the selectivity and sensitivity toward the target analyte. The π electrons of the C=N group make the Schiff base an effective ligand for metal ions, chelated Schiff bases, for instance, may have a stronger affinity for metal ions. Fluorescent chemosensors derived from Schiff bases have gained much attention in recent years because of their low cost, simple synthesis methods, strong complexation ability, immediate response, and high sensitivity for multi-ion detection.[37] Schiff base derivatives with N & O donor atoms are more likely to form complexes with metal ion analytes.[38] After interaction with a metal ion, the suppressed C=N isomerization increases fluorescence intensity through the chelation-enhanced fluorescence (CHEF) mechanism.[39] Furthermore, alteration in spectrum in the presence of different analytes paves the way for detecting multiple ions.[40]

Therefore, Schiff base chemosensors have been synthesized to detect a variety of analytes, such as metal ions, anions, nitroaromatics, and biomolecules. Their simplicity, sensitivity, and cost-effectiveness make them useful in environmental monitoring, biomedical diagnostics, and industrial quality control, among other applications. Moreover, the urge for the development of water-soluble chemosensors for metal detection remains a challenge. The strive for the simplest, cheapest, and greenest chemosensor capable of selectively and sensitively detecting copper ions and featuring the lowest detection limit, wide pH range, and real-time application is in demand. In this regard, pyridinium and imidazolium salts as chemosensors have gained significant attention due to their unique properties such as water solubility and high stability.

A straightforward approach to synthesize pyridinium and imidazolium salts **BzPySB** and **IsImSB**, respectively, for the detection of metal ions is discussed in this chapter.

Section 4A

Schiff Base-Appended Pyridinium Salt for Detection of Aluminum(III) Ions

A Schiff base-appended pyridinium salt, **BzPySB** for the selective detection of Al^{3+} by a turn-on mechanism is discussed. In this work, the solid-state fluorescence behavior of **BzPySB** was utilized for latent fingerprint detection. The probe was also employed for the detection of Al^{3+} in plant and MCF-7 cells thereby highlighting its potential in biological systems.

4A.1 EXPERIMENTAL SECTION

4A.1.1 Synthesis of 1-(2-(4-formyl-3-hydroxyphenoxy)ethyl)pyridin-1-ium bromide (BzPy)

4-(2-Bromoethoxy)-2-hydroxybenzaldehyde (0.081 mmol) synthesized by previously reported method[44] was stirred with pyridine (0.081 mmol) for 6 h. The pale-white liquid obtained was washed with ethyl acetate and ether successively. The obtained white solid was filtered and dried under vacuum (26 mg, 96% yield); mp = 210–215 °C; ^{1}H NMR (400 MHz, DMSO-d_6) δ 9.96 (s, 1H), 9.12 – 9.05 (m, 2H), 8.62 (tt, J = 7.8, 1.4 Hz, 1H), 8.19 – 8.11 (m, 2H), 7.62 (d, J = 8.8 Hz, 1H), 6.56 (dd, J = 8.8, 2.4 Hz, 1H), 6.47 (d, J = 2.4 Hz, 1H), 5.03 (t, J = 5.0 Hz, 2H), 4.56 (dd, J = 5.6, 4.4 Hz, 2H); ^{13}C NMR (100 MHz, DMSO-d_6) δ 191.4, 164.4, 163.3, 146.6, 145.9, 132.5, 128.4, 117.3, 108.0, 102.0, 66.9, 60.2; HRMS (ESI) m/z: $[M\text{-}Br]^+$ calcd. for $[C_{14}H_{14}NO_3]^+$ 244.0968; found 244.0988.

4A.1.2 Synthesis of (E)-1-(2-(3-hydroxy-4-((pyridine-2-ylimino)methyl)phenoxy)ethyl) pyridinium-1-ium bromide (BzPySB)

Ethanolic solution of **BzPy** (0.061 mmol) and 2-aminopyridine (0.074 mmol) was refluxed at 80 °C for 6 h. The solvent was removed under reduced pressure and a yellow solid was obtained. The crude product was washed with ethyl acetate and ether several times. A free-flow bright turmeric-yellow solid was obtained, which was filtered and dried in vacuum (22 mg, 95.6% yield); mp = 220–225 °C, ^{1}H NMR (400 MHz, DMSO-d_6) δ 13.73 (s, 1H), 9.40 (s, 1H), 9.21 – 9.15 (m, 2H), 8.72 – 8.63 (m, 1H), 8.51 (dd, J = 2 Hz, 1H), 8.26 – 8.18 (m, 2H), 7.91 (td, J = 2.0 Hz, 1H), 7.68 (d, J = 8.4 Hz, 1H), 7.41 (d, J = 7.6 Hz, 1H), 7.37 – 7.29 (m, 1H), 6.59 – 6.47 (m, 2H), 5.10 (t, J = 4.8 Hz, 2H), 4.63 (t, J = 4.8 Hz, 2H), ^{13}C NMR (100 MHz, DMSO-d_6) δ 191.4, 164.6, 164.3, 163.6, 163.3, 162.9, 157.5, 149.4, 146.6, 145.9, 139.5, 135.6, 132.6, 128.4, 123.0, 119.6, 117.3, 113.7, 108.0, 107.9, 102.2, 102.1, 66.9, 60.2; HRMS (ESI) m/z: $[M\text{-}Br]^+$ calcd. for $[C_{19}H_{18}N_2]^+$, 320.1392; found 320.1377.

4A.2 RESULTS AND DISCUSSION

4A.2.1 Synthesis and Characterization

The synthesis of chemosensor followed a straightforward methodology. 4-(2-Bromoethoxy)-2-hydroxybenzaldehyde was quaternized with pyridine to yield 1-(2-(4-formyl-3-hydroxyphenoxy)ethyl)pyridin-1-ium bromide **BzPy (Figure A20, A21, A22, A23, A24, A25, Appendix-A**). (E)-1-(2-(3-hydroxy-4-((pyridine-2-ylimino)methyl)phenoxy)ethyl) pyridinium-1-ium bromide (**BzPySB)** was obtained as a bright yellow solid by the condensation reaction of **BzPy** and 2-amino pyridine in ethanol with 98% yield (**Scheme 4A.1**).

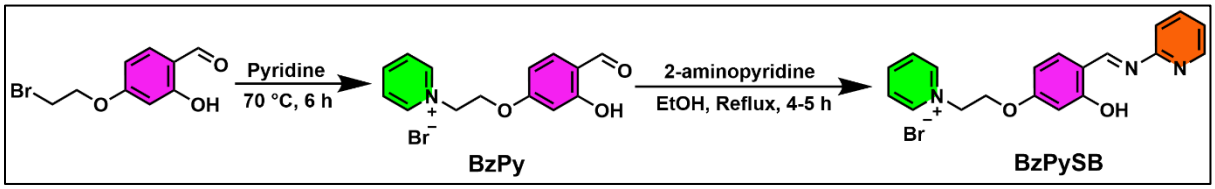

Scheme 4A.1: Synthetic route for **BzPySB**

The structure of the **BzPySB** was well characterized by FT-IR, ^{1}H and ^{13}C NMR spectroscopy, mass spectrometry, and X-ray crystallography. The FT-IR spectrum of **BzPySB** exhibited distinctive peaks at 1604 cm^{-1} for υ(C=N) stretching of the azomethine group and 3471 cm^{-1} for υ(O-H) (**Figure 4A.1**).

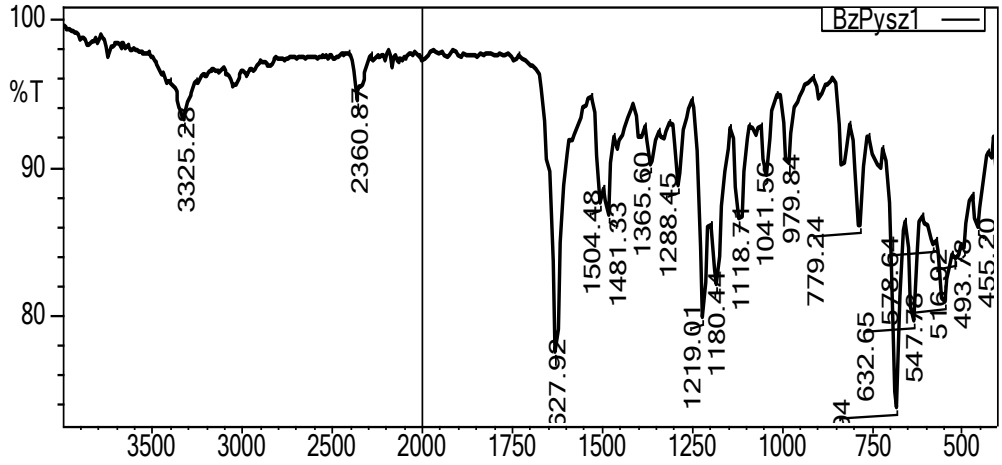

Figure 4A.1: FT-IR spectra of **BzPySB**

The ^{1}H NMR spectrum of **BzPySB** had a signature imine proton signal at 9.40 ppm and another important characteristic singlet at 13.72 ppm for –OH proton. In ^{1}H NMR, two triplets for aliphatic and aromatic protons appeared in the range 5.09–4.61 ppm and 8.69–7.31 ppm, respectively (**Figure 4A.2**). In ^{13}C NMR, the signals at 164.5 ppm and 163.5 ppm indicated the presence of

azomethine and phenolic carbons, respectively. The signals in the range 102.0–147.6 ppm and 60.93–61.26 ppm were assigned to aromatic and aliphatic carbons, respectively (**Figure 4A.3**). The molecular ion peak in the ESI-mass spectrum of **BzPySB** (**Figure 4A.4**) was observed at 320.1377 due to [**BzPySB**-Br] $^{+}$ (*m/z*, calc. 320.1392).

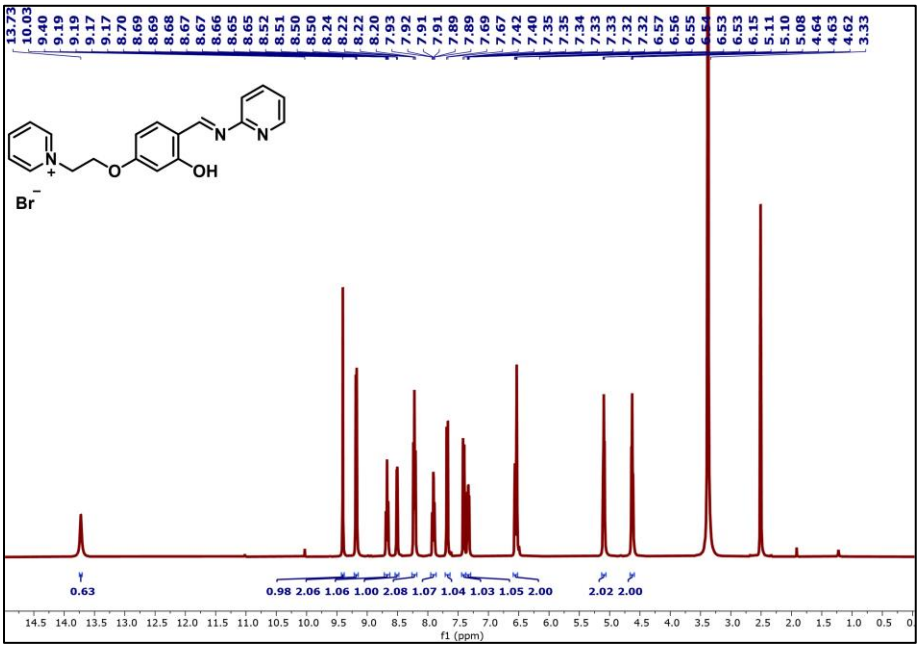

Figure 4A.2: ^{1}H NMR of **BzPySB** in DMSO-d_6

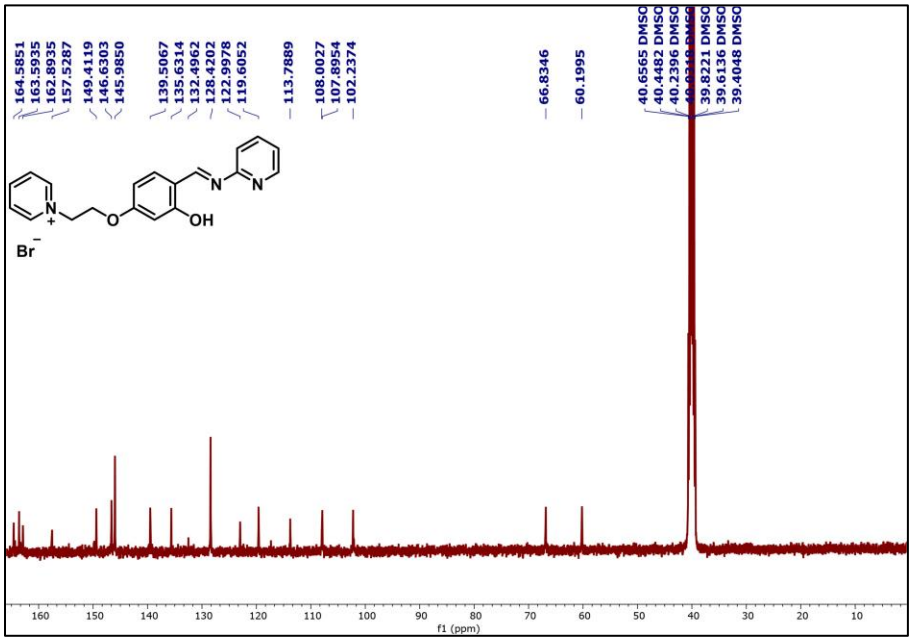

Figure 4A.3: ^{13}C NMR of **BzPySB** in DMSO-d_6

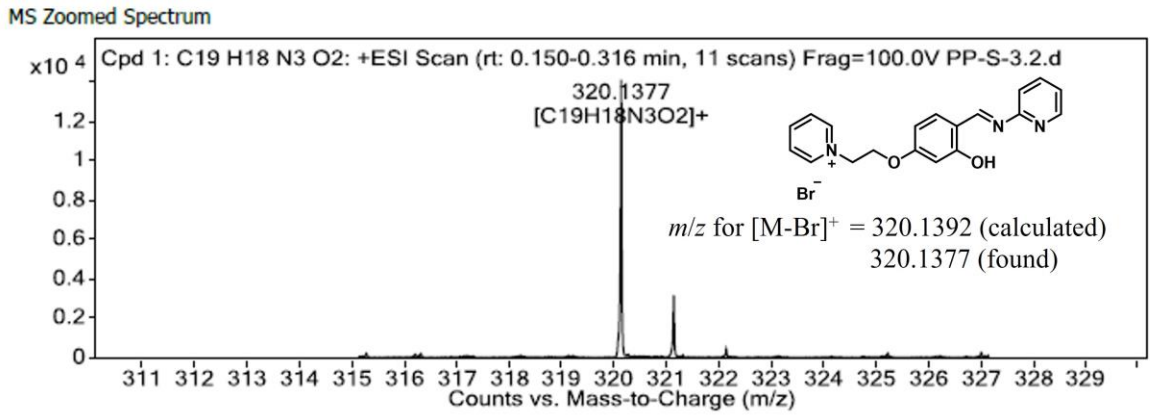

Figure 4A.4: HRMS of **BzPySB**

Suitable single crystals of diffraction quality were obtained from an ethanol solvent. The X-ray crystallographic characterization indicated the existence of **BzPySB** in the enolic form. The **BzPySB** crystallized in a triclinic, *P-1* space group. The ORTEP diagram of the **BzPySB** is depicted in **Figure 4A.5**.

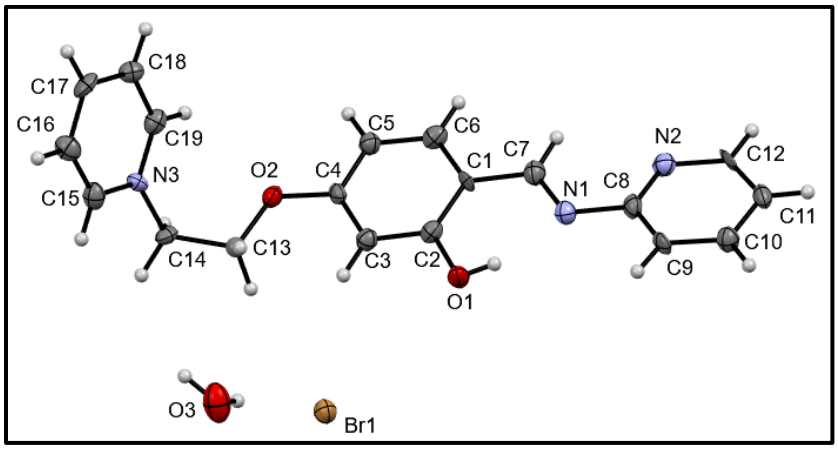

Figure 4A.5: ORTEP diagram of **BzPySB** (CCDC 2330395) showing thermal ellipsoids at 50% probability level

In an asymmetric unit, one organic molecular cation, one bromide anion, and one water of solvation are found during crystal structure solving. The X-ray single crystal structure of **BzPySB** shows an expected planar orientation of the molecule stabilized through intramolecular hydrogen bonding between phenolic O-H and imine N groups with a bent at the end. The phenyl ring (C1 C2 C3 C4 C5 C6) plane and pyridinium ring (N3 C15 C16 C17 C18 C19) plane arranged at 72.18° angle. Slipped π-π interactions of the aromatic rings with centroid (C1 C2 C3 C4 C5 C6 phenyl ring) to centroid (N2 C8 C9 C10 C11 C12 pyridine ring) distance of 3.878 Å allow the *π* stacking

of the molecules in head to tail fashion. The π-π interactions of the aromatic rings help the chemosensor to align in an alternate direction (**Figure 4A.6**). The crystallographic cell parameters and data are given in **Table A4, Appendix-A**.

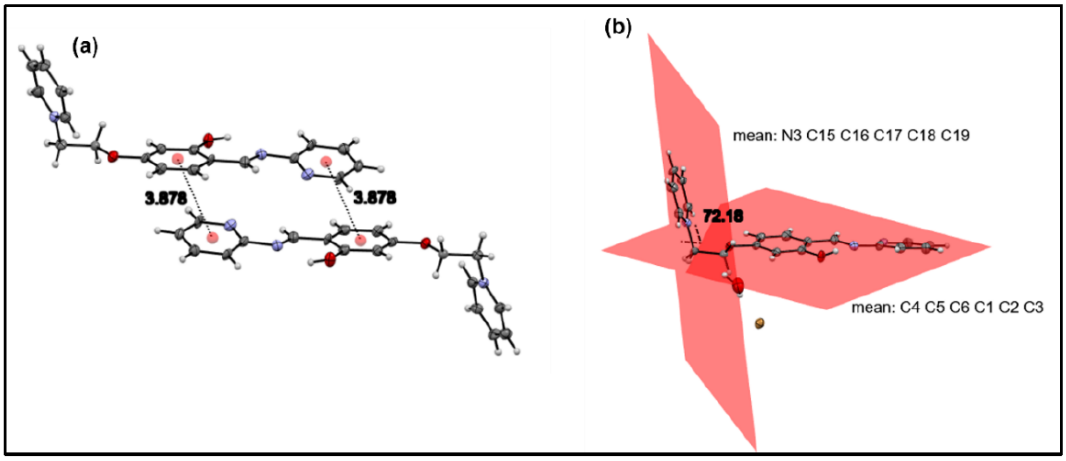

Figure 4A. 6: (a) π-π interaction between the centroids of two molecules of **BzPySB** (b) Ring plane diagram of **BzPySB**

The photophysical properties of **BzPySB** were studied in solution and solid state. The polarity of solvents affects the potential barrier of keto and enol forms of Schiff bases. The solvent effect depends upon the ability of solvents to form hydrogen bonding as proton donors and acceptors, thereby permitting proton transfer that results in the formation of the keto form. In the UV-vis absorption spectra of **BzPySB** in ACN, the absorption bands were observed at 272 nm and 311 nm due to π-π* and n-π* transitions, respectively, indicating the presence of only enolic form. The absorption bands at 226 nm, 276 nm, and 310 nm in water and 213 nm, 270 nm, and 313 nm in MeOH indicated the presence of enol-imine tautomers. The absorption band at 425 nm in water and 416 nm in MeOH were ascribed to the keto-enamine form of **BzPySB** (**Figure 4A.7**).

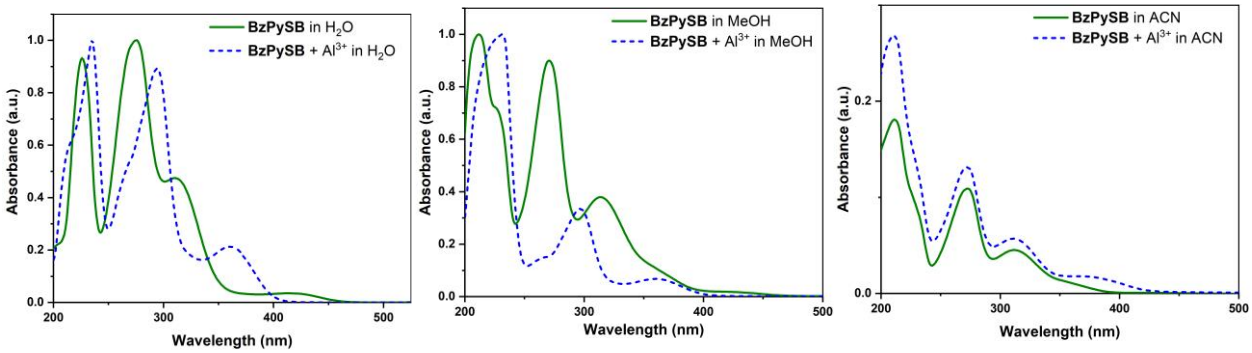

Figure 4A.7: UV-vis absorption spectra of **BzPySB** (1×10^{-5} M) in (a) H_2O (b) MeOH (c) ACN

In solid-state UV-vis absorption spectra of **BzPySB,** absorption bands at 303 nm, 355 nm, and 466 nm were observed (**Figure 4A.8**).

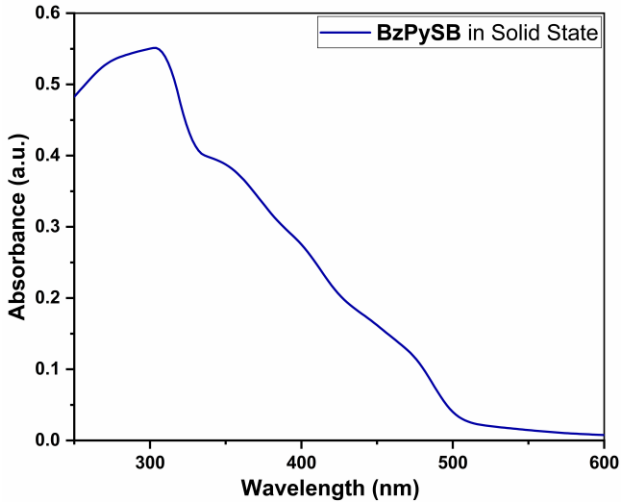

Figure 4A.8: Solid state UV-vis absorption spectra of **BzPySB**

The fluorescence spectra of **BzPySB** in water showed an emission peak at 375 nm (10^{-6} M, Φ = 0.036) and 514 nm (10^{-2} M, Φ = 0.0004). In solid-state fluorescence spectra, an emission peak was observed at 545 nm (**Figure 4A.9a**). The appearance of a red-shifted absorption band at λ_{max} = 466 nm and emission peak at λ_{max} = 545 nm supported *J*-aggregation formation in the solid state of **BzPySB** (**Figure 4A.9b**).

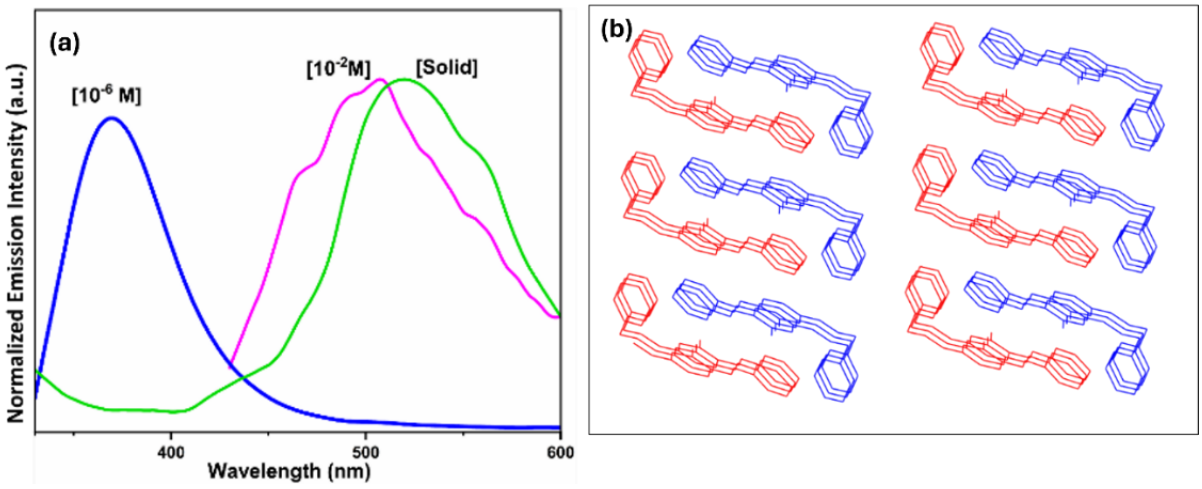

Figure 4A.9: (a) Solution and solid-state fluorescence spectra **BzPySB** (b) *J*-aggregate (head to tail arrangement) in crystal structure of **BzPySB**

The presence of enol-imine tautomer was confirmed by recording fluorescence spectra of **BzPySB** at different excitation wavelengths (**Figure 4A.10**). A sharp emission peak at (λ_{em} = 425 nm) was observed, indicating the presence of keto form. The appearance of two emission peaks at λ_{ex} = 325 nm indicated the keto-enol tautomerism in **BzPySB**.

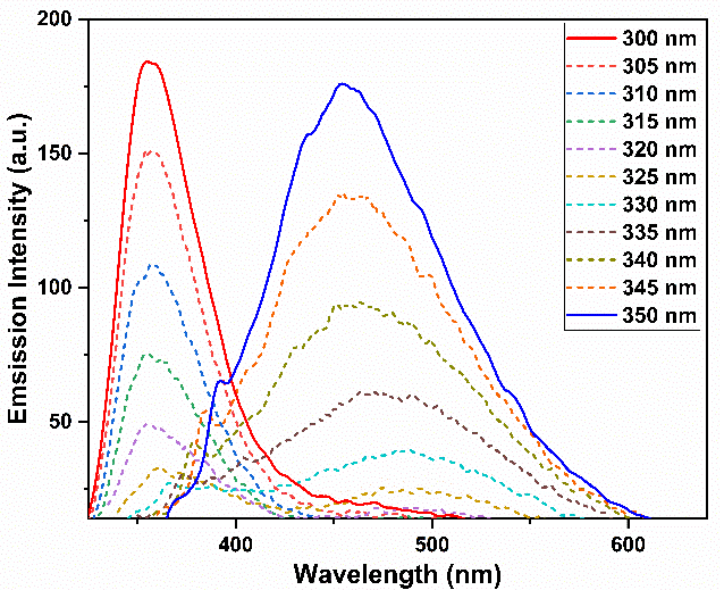

Figure 4A.10: ESIPT investigation of **BzPySB**

4A.2.2 Response of BzPySB toward Al^{3+} ions

The UV-vis absorption spectra of **BzPySB** were recorded in the presence of different metal ions (Na^+, K^+, Ca^{2+}, Mn^{2+}, Cu^{2+}, Ni^{2+}, Co^{2+}, Fe^{2+}, Fe^{3+}, Zn^{2+}, Hg^{2+}, $La^{3+,}$ and Lu^{3+}). In the presence of Al^{3+}, the absorption bands at 225 nm and 263 nm shifted to 230 nm and 293 nm, respectively. A new absorption band appeared at 362 nm, with the disappearance of the absorption band at 310 nm, indicating the formation of the **BzPySB**-Al^{3+} complex. The behavior of **BzPySB** in the presence of metal ions was also explored using fluorescence spectroscopy by recording the emission spectra of **BzPySB** upon excitation at 310 nm in water. Among various metal ions, fluorescence enhancement was observed in the presence of Al^{3+} ion at an emission wavelength of 453 nm. There was no appreciable change in the fluorescence intensity with other metal ions Na^+, K^+, Ca^{2+}, Mn^{2+}, Cu^{2+}, Ni^{2+}, Co^{2+}, Fe^{2+}, Fe^{3+}, Zn^{2+}, Hg^{2+}, La^{3+}, and Lu^{3+}. The enhancement in the emission intensity showed the cyan fluorescence turn-on behavior of the **BzPySB** (Φ = 0.611) in the presence of Al^{3+} ion. Further, the emission intensity gets shifted from 375 nm to 453 nm (redshift of 78 nm), confirming the coordination of **BzPySB** to the Al^{3+} ion. The change in emission intensity may be explained by photo-induced electron transfer (PET) mechanism. The

weak fluorescence of the **BzPySB** was due to a lone pair of electrons on the nitrogen atom, which led to the PET process. The emission intensity of **BzPySB** was enhanced by the addition of Al^{3+} ion due to PET inhibition, leading to chelation enhanced fluorescence (**Figure 4A.11**).

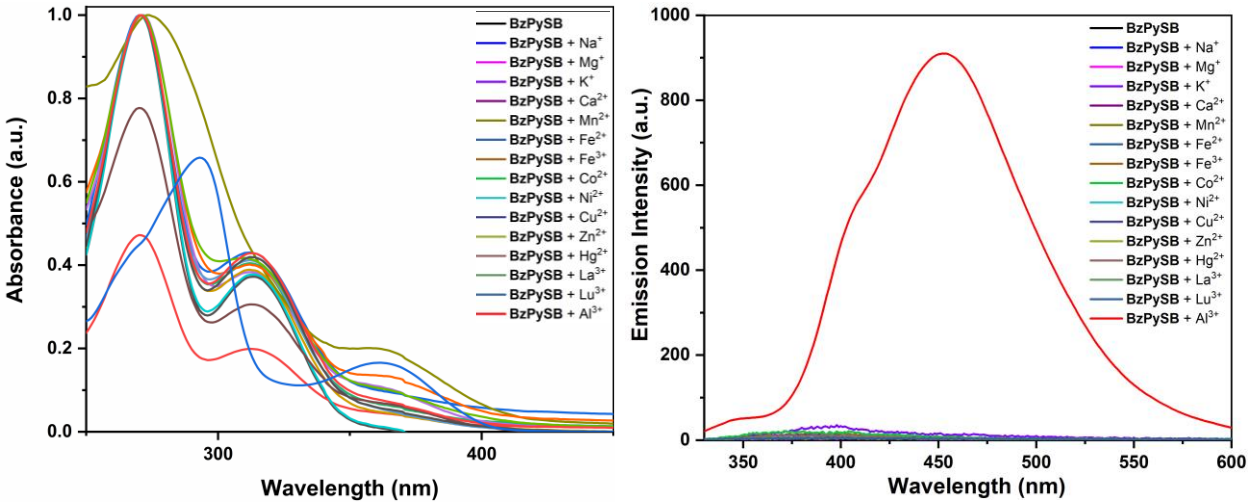

Figure 4A.11: (a) Absorption (b) Fluorescence response of **BzPySB** (1×10^{-5} M) toward different metal ions in water

Furthermore, to investigate the effect of increasing the amount of Al^{3+} ion on **BzPySB**, the absorption and fluorescence spectra were recorded upon increasing the concentration of the Al^{3+} ion. In UV-vis absorption spectra, two isosbestic points at 279 nm, 308 nm, and 340 nm appeared. A distinct new absorption band at 362 nm confirmed the formation of the **BzPySB**-Al^{3+} complex. A continuous increase in fluorescence emission intensity at 453 nm was observed upon the addition of aluminum (**Figure 4A.12**).

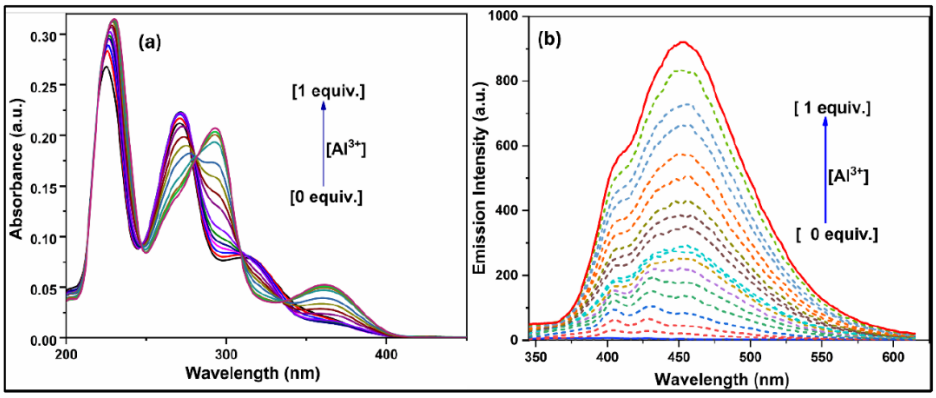

Figure 4A.12: (a) Absorption (b) Fluorescence spectra of **BzPySB** (1×10^{-5} M) with different amounts of Al^{3+} ions in water

The phenomena of enhanced fluorescence emission could be explained by restriction in the intermolecular rotation due to the increased rigidity of the system. The Benesi-Hildebrand equation was used to fit the data from the fluorescence titration experiment of **BzPySB** with Al^{3+}, and the results showed that the association constant for **BzPySB**-Al^{3+} was 4.19×10^5 M^{-1} (**Figure 4A.13a**). Using equation $3\sigma/K$, the limit of detection for Al^{3+} was calculated as 0.024 nM, which is significantly less than the WHO-recommended limit (**Figure 4A.13b**). Therefore, **BzPySB** could act as an effective chemosensor for the detection of Al^{3+} in drinking water.

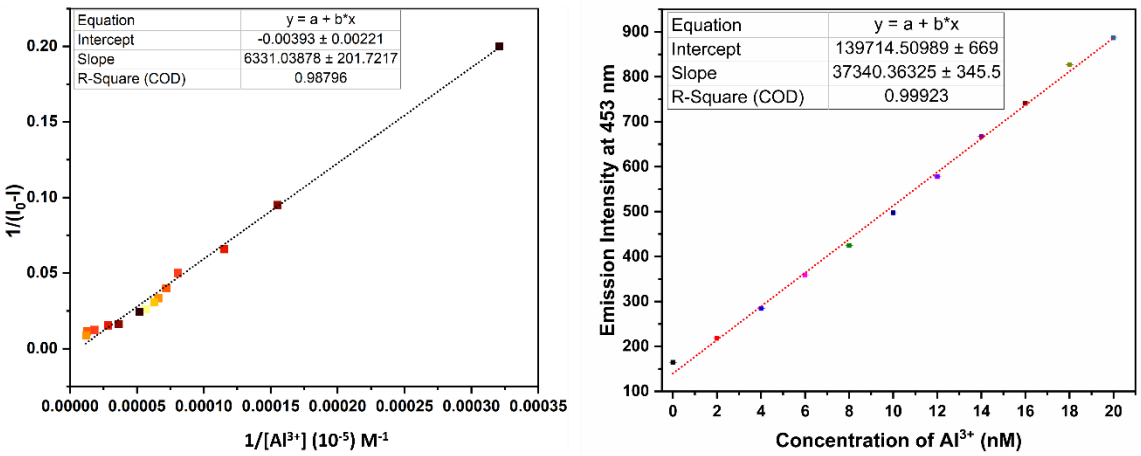

Figure 4A.13: (a) Benesi-Hildebrand plot of the absorption spectra of **BzPySB** with different amounts of Al^{3+}
(b) Calibration curve with error bar for calculating Limit of Detection for Al^{3+} ions

To study the stoichiometric binding of **BzPySB** with Al^{3+} metal, Job's plot was investigated. The data was recorded using an equimolar solution of **BzPySB** and Al^{3+} in aqueous medium. The breakpoint was observed in the graph at a 0.5-mole fraction of Al^{3+} in the receptor solution, indicating the stoichiometric ratio as 1:1 (**Figure 4A.14a**). In addition, fluorescence lifetime measurements were recorded to investigate the mechanism underlying the enhanced fluorescence response of **BzPySB** in the presence of Al^{3+} ion (**Figure 4A.14b**).

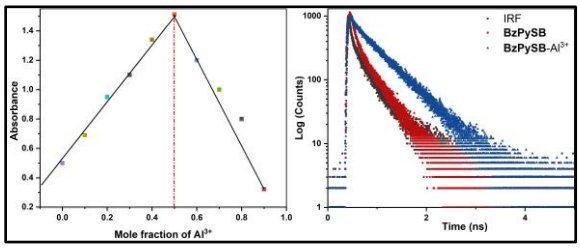

Figure 4A.14: (a) Job's plot of **BzPySB** with Al^{3+} ions (b) Fluorescence lifetime decay plot of **BzPySB** and **BzPySB**-Al^{3+} complex

The radiative decay rate constant k_r and total nonradiative decay rate constant k_{nr} of **BzPySB** were calculated using equation $\tau^{-1} = k_r + k_{nr}$ and $k_r = \Phi/\tau$. The data indicate (**Table 4A.1**) that fluorescence enhancement occurs due to the decrease in the ratio of k_{nr}/k_r from 30.36 for **BzPySB** to 0.648 for **BzPySB**-Al^{3+}, which agrees with the chelation-enhanced fluorescence (CHEF) process.

Table 4A.1 Fluorescence lifetime measurement of **BzPySB** and **BzPySB**-Al^{3+} complex

Entry	Φ	τ_{avg} (ns)	$k_r \times 10^9$ (S^{-1})	$k_{nr} \times 10^9$ (S^{-1})	χ^2
BzPySB	0.032	0.253	0.126	3.826	0.972
BzPySB + Al^{3+}	0.611	5.23	0.116	0.075	0.966

To further comprehend the UV-vis and fluorescence spectroscopic experiments for binding of **BzPySB** and Al^{3+}, ^{1}H NMR spectra of **BzPySB**-Al^{3+} was recorded (**Figure 4A.15**). In ^{1}H NMR spectra of **BzPySB**-Al^{3+}, the disappearance of phenolic -OH signal at 13.72 ppm (H_a) and shift in imine proton signal to 9.68 ppm (H_b) indicated the complexation of **BzPySB** with Al^{3+}. This was further verified by ESI-MS analysis which showed a peak at 470.0544, due to [**BzPySB**+Al^{3+}+2NO_3^- Br]$^+$ (*m/z*, calcd. 470.0888), which supported the 1:1 stoichiometry (**Figure A.16**).

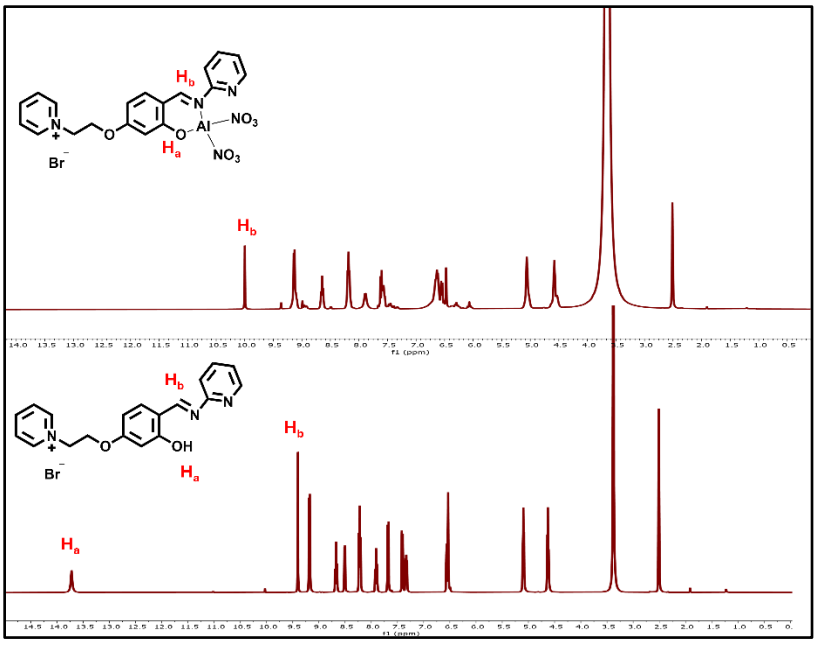

Figure 4A.15: ^{1}H NMR spectra of **BzPySB**-Al^{3+} complex in DMSO-d_6

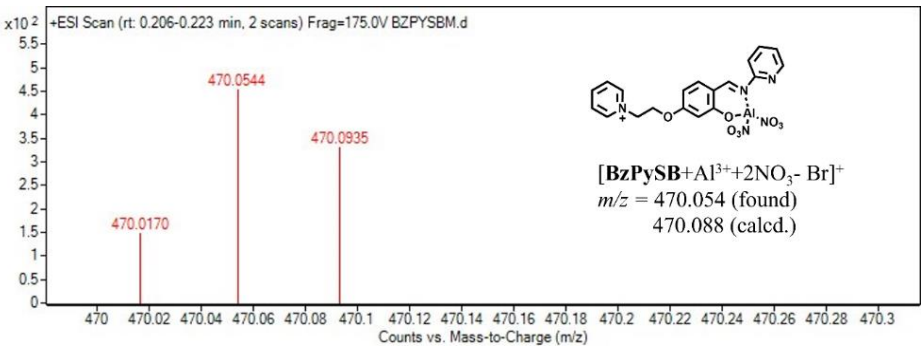

Figure 4A.16: HRMS of **BzPySB**-Al^{3+} complex

The fluorescence spectral nature of **BzPySB** was investigated with and without Al^{3+} as a function of pH (from 2.0 to 12.0) in aqueous solution at 310 nm. The emission intensity of **BzPySB** was negligible throughout the pH range, whereas the emission intensity of the **BzPySB**-Al^{3+} ensemble reached a maximum in the pH 6.0–9.0 region. In the acidic zone (pH < 6.0), dissociation of the complex due to protonation decreases the emission intensity. At higher pH values (pH > 9.0), OH^- ions compete with **BzPySB** for Al^{3+}, causing aluminum hydroxide precipitation and thus lowering the emission intensity (**Figure 4A.17a**). The alternating addition of Al^{3+}/Na_2H_2EDTA established the reversibility of the sensing process. Upon increasing the concentration of EDTA to the solution of **BzPySB**-Al^{3+}, a gradual decrease in the fluorescence was observed, indicating the binding of EDTA with $Al^{3+,}$ leaving uncomplexed **BzPySB**. The sequential addition of Al^{3+} and EDTA to the aqueous solutions of **BzPySB** indicates the reversible nature of **BzPySB** up to five cycles with a progressive decline in efficiency (**Figure 4A.17b**).

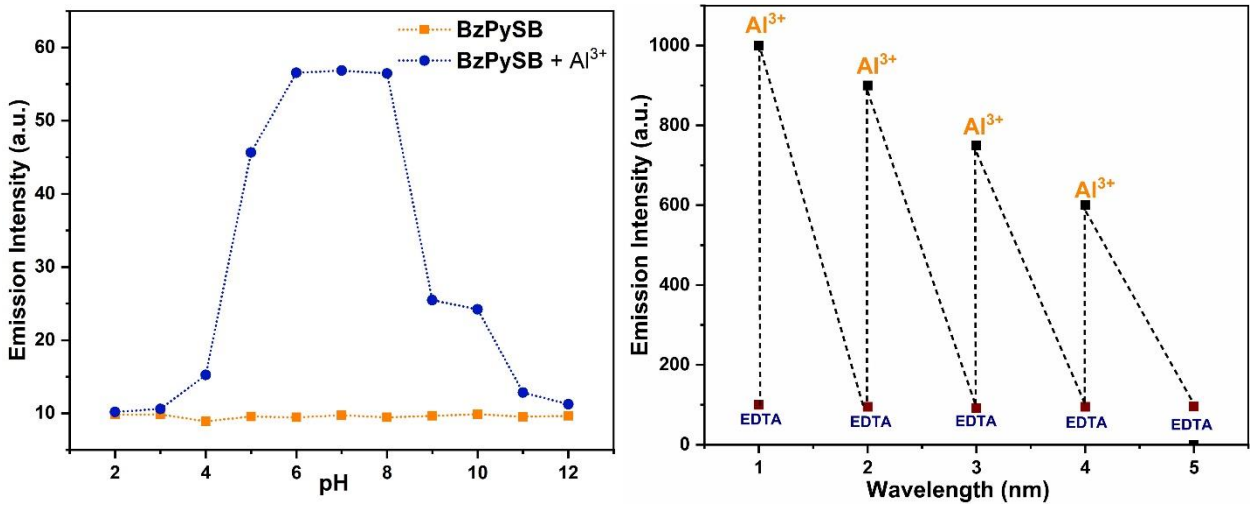

Figure 4A.17: Effect of pH on **BzPySB** (1×10^{-5} M) and **BzPySB**-Al^{3+} complex (b) Reversibility chart of **BzPySB** (1×10^{-5} M) after the sequential addition of Al^{3+} and EDTA

Then, equimolar concentrations of other pertinent metal ions and anions, Na^+, K^+, Mg^{2+}, Mn^{2+}, Fe^{2+}, Fe^{3+}, Co^{2+}, Ni^{2+}, Zn^{2+}, La^{3+}, Eu^{3+} , F^-, Cl^-, Br^-, I^-, CH_3COO^-, SO_4^{2-}, NO_2^-, PO_4^{3-} and HCO_3^- were screened to assess competitive binding interactions. No noticeable change in fluorescence emission was observed with these ions (**Figure 4A.18 a and b**). **BzPySB** was selective to Al^{3+} because of its high charge (+3) and small ionic radius, among the other elements in the series.

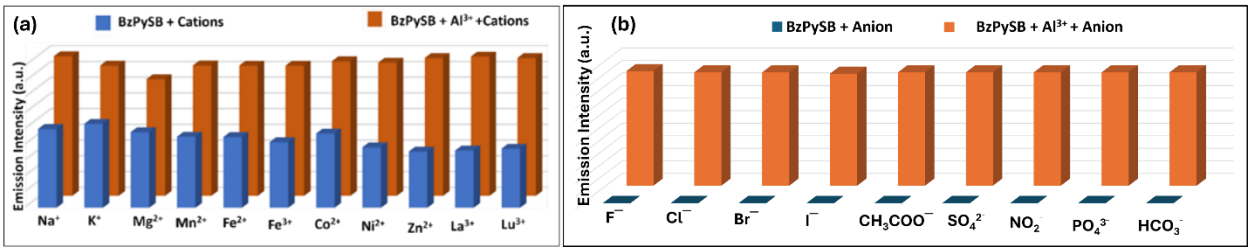

Figure 4A.18 Interference study of **BzPySB** (1×10^{-5} M) toward Al^{3+} selectivity in the presence of (a) cations (b) anions

To investigate the sensing mechanism of **BzPySB**, geometrical optimization of **BzPySB** (keto and enol form), **BzPySB**$^+$ (without Br), and **BzPySB**-$Al(NO_3)_2$, were performed. In the ground state, of **BzPySB** in both enolic and ketonic forms, the electron density in HOMO and LUMO was distributed over the molecule except the alkyl chain and pyridine ring. The energy difference between the HOMO and LUMO in the enolic and ketonic form were 1.69 eV and 1.19 eV, respectively (**Figure 4A.19a**). The calculated lowest-lying absorption band can be assigned to S_0-S_1 occurring from the electronic transitions, HOMO→LUMO, HOMO-1→LUMO and HOMO→LUMO+1 (**Figure 4A.19b**).

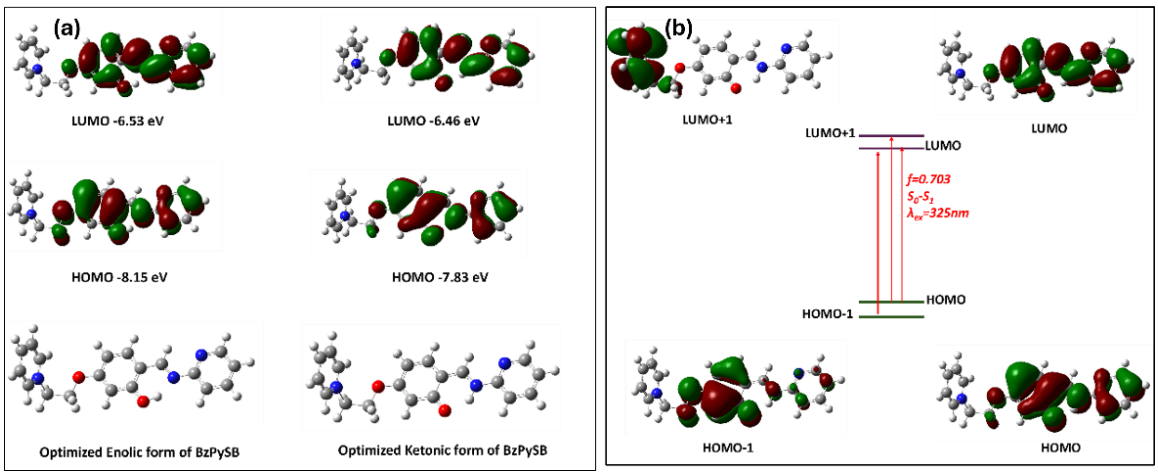

Figure 4A.19: (a) Optimized structures and HOMO-LUMO orbitals of **BzPySB** in keto and enolic forms (b) Molecular orbitals involved in the UV-vis absorption of the **BzPySB**

It was observed that electrostatic potential (ESP) around oxygen and nitrogen atoms of **BzPySB** are more negative therefore, it has a strong attractive force for cation, Al^{3+}, as also inferred from the experiment results (**Figure 4A.20**).

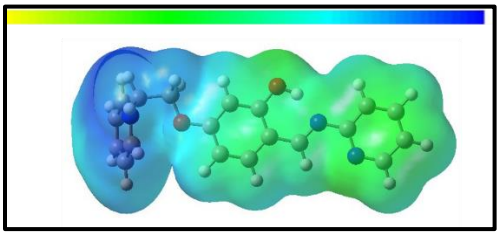

Figure 4A.20: Electrostatic Potential of **BzPySB**

The electron density over oxygen and nitrogen atoms of **BzPySB** in the ground state decreased on complexation with Al^{3+}. **BzPySB** exhibited less stabilized HOMO and LUMO energy levels than **BzPySB**-Al^{3+}, indicating the formation of a complex (**Figure 4A.21a**). In the electronic absorption spectra, the redshift was observed, which can be explained by the less energy gap between HOMO and LUMO of **BzPySB**-Al^{3+}. In the TD-DFT calculation for **BzPySB**-$Al(NO_3)_2$, the absorption bands at 363 nm, 293 nm, and 230 nm were due to HOMO→LUMO, HOMO→LUMO+1 and HOMO→LUMO+2 transition respectively (**Figure 4A.21b**).

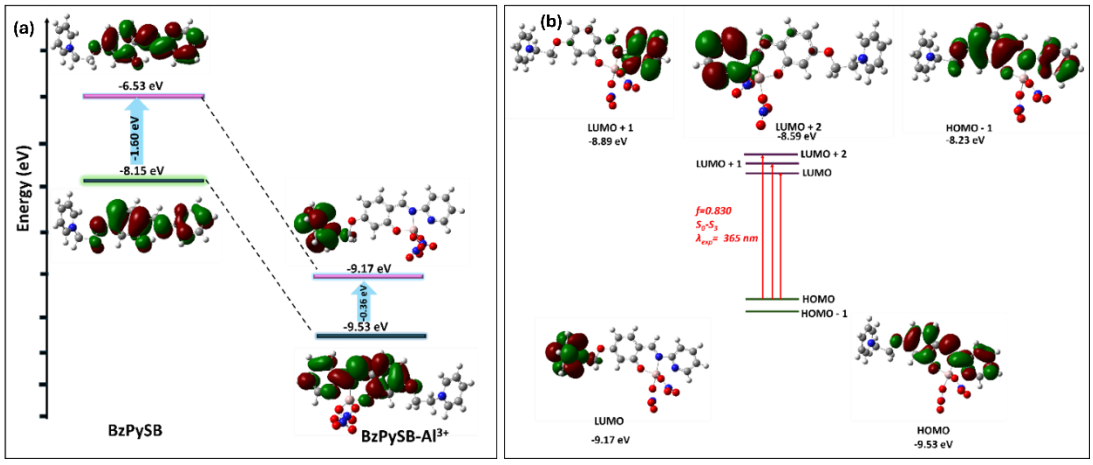

Figure 4A.21: (a) Energy levels and frontier molecular orbitals of **BzPySB** and the **BzPySB**-$Al(NO_3)_2$ complex (b) Frontier molecular orbitals involved in the lowest-lying observable UV-vis absorption bands of the **BzPySB**-$Al(NO_3)_2$ complex

4A.2.3 Analytical Applications

Latent Fingerprints using BzPySB

The solid-state emissive property of **BzPySB** was effective in the investigation of latent fingerprints. The features such as bridge, bifurcation, core, delta, dot, enclosure, ridge ends, short

ridge, trifurcation, and lake can be extracted from the fingerprint developed by **BzPySB**: neutral alumina powder (**Figure 4A.22**). Hence, level-2 information was extracted from the fingerprints developed by the fingerprint powder.

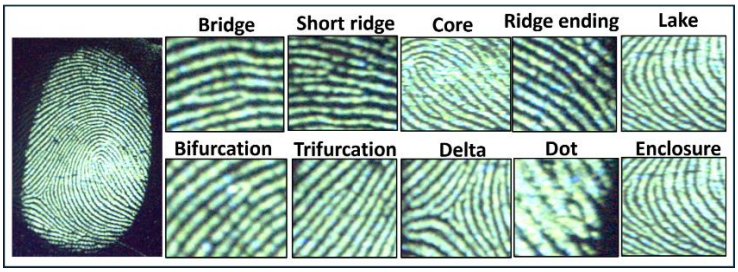

Figure 4A.22: Minutiae features of the fingerprints developed using **BzPySB**-based fingerprint powder and exposed to UV light (365 nm)

Cytotoxicity Assay

The MTT assay was used to examine the effects of **BzPySB** on cell metabolic activity and cell viability of MCF-7, a human breast cancer cell line. The measured cell viability is demonstrated in **Figure 4A.23**, which shows decreased % viability with increasing concentration of the test compound. The assay demonstrated that the **BzPySB** is relatively less cytotoxic as it showed more than 90% cell viability upto 25 μM concentration of the test compound. The cell viability was more than 80% even at 100 μM concentration.

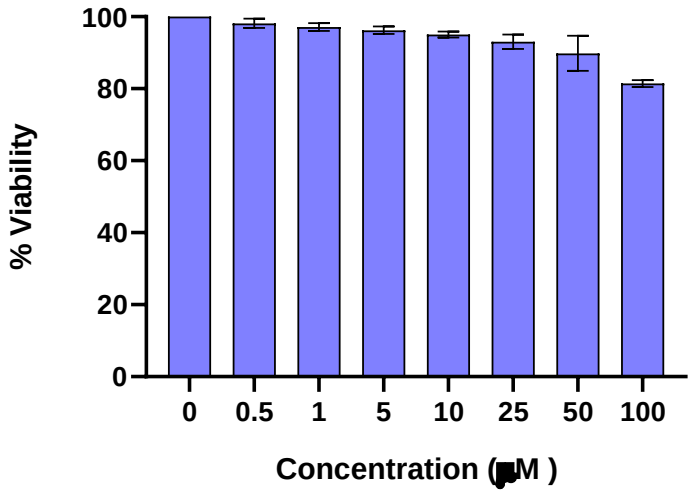

Figure 4A.23: Cell viability percentage of the MCF-7 cells against different concentration of **BzPySB**

Cell-culture and imaging

The biological applicability of the **BzPySB** compound as a fluorescent probe for *in-vitro* living cell imaging and detection of Al^{3+} ions was studied on the human breast cancer cell line, MCF-7 and images were acquired using a Carl Zeiss LSM 880 confocal microscope equipped with a 40X objective lens. The cells were incubated with **BzPySB** (30 μM) for 40 min at room temperature. These cells treated with the test compound only showed minimal fluorescence (**Figure 4A.24e**), whereas the combination of **BzPySB** compound and Al^{3+} solution (30 μM **BzPySB** + 30 μM Al^{3+}, 20 min incubation) provided striking intense fluorescence as seen in **Figure 4A.24h**, These results proved that **BzPySB** can be vital in sensing Al^{3+} intracellularly in human tissues. The treatment of cells with only Al^{3+} solution did not show any fluorescence (**Figure 4A.24k**) and acted as the control set in the study. Overall, the results demonstrated that **BzPySB** can play an indispensable role in intracellular fluorescence imaging of Al^{3+}.

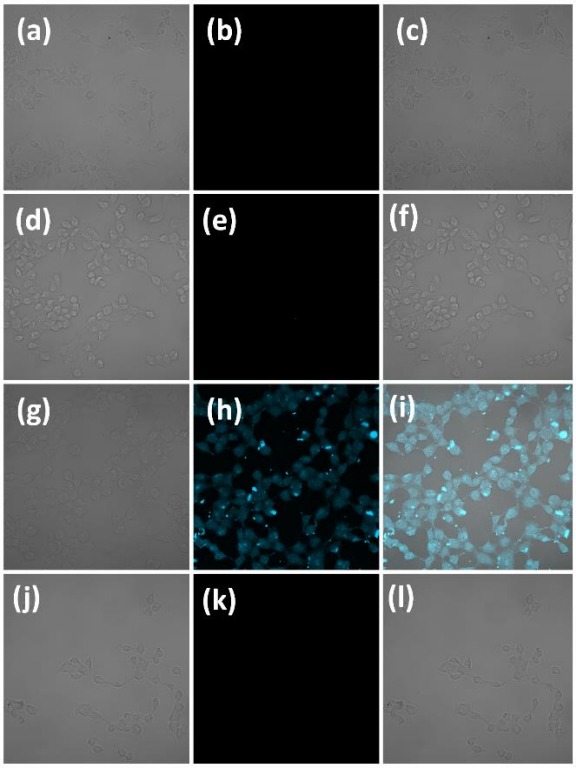

Figure 4A.24: Confocal microscopic images of MCF-7 cells under bright field, Fluorescence and overlay conditions respectively, (a-b-c) MCF-7 Cells without **BzPySB** treatment as control; (d-e-f) MCF-7 cells treated with **BzPySB**; (g-h-i) MCF-7 cells treated with **BzPySB** and $Al^{3+}$and, (j-k-l) MCF-7 cells treated only with Al^{3+} solution as control.

In vitro cellular imaging of onion epidermal cells

The fluorescence microscopy images of **BzPySB** and **BzPySB**-Al^{3+} in a pure aqueous medium are utilized demonstrate the practical application of **BzPySB** in monitoring aluminum in biological systems. The onion epidermal cells treated with **BzPySB** exhibited weak fluorescence which enhanced upon addition of Al^{3+}. The cells exhibited blue fluorescence, with the nuclei of the cells being distinctly labelled (**Figure 4A.25a**). It was observed that **BzPySB** had the ability to enter the cytoderm and plasma membrane of onion epidermal cells for the detection of Al^{3+}. Interestingly, it was noted that the specific blue fluorescence signal was only present in the nucleus when Al^{3+} was present. This indicates that **BzPySB** can serve as a fluorescent sensor for Al^{3+} in plant cells.

Plant imaging by BzPySB

BzPySB was explored for plant imaging in bean sprouts. Bean sprouts cultured with **BzPySB** exhibited weak fluorescence, which, upon addition of Al^{3+}, emitted cyan fluorescence under UV light (365 nm), indicating that **BzPySB** could be used for the determination of Al^{3+} in plant tissues (**Figure 4A.25b**).

Recognition of Al^{3+} by polymeric film

The practical applicability of **BzPySB** was investigated by preparation of fluorescent polymeric films. The yellow colour and yellow fluorescence of **BzPySB** changed to cyan after being exposed to the solution of Al^{3+} highlighting its potential for Al^{3+} detection (**Figure 4A.25c**). Moreover, the film can be bent, folded with good flexibility, indicating its utilization for real sample analysis.

Recognition of Al^{3+} on test strips

The real field application is always desired for the detection of targeted analytes. The test kits were prepared by soaking Whatman-40 filter paper strips in the aqueous solution of **BzPySB** for 3-4 h. The dried test strips were non-fluorescent when seen under UV light. Then, an aqueous solution of Al^{3+} (10^{-3}M - 10^{-6} M) was added to the test paper strip (**Figure 4A.25d**). The spot with Al^{3+} exhibited cyan color fluorescence emission. The fluorescence quenching was observed under a 365 nm UV lamp, revealing the utility of **BzPySB** for practical applications.

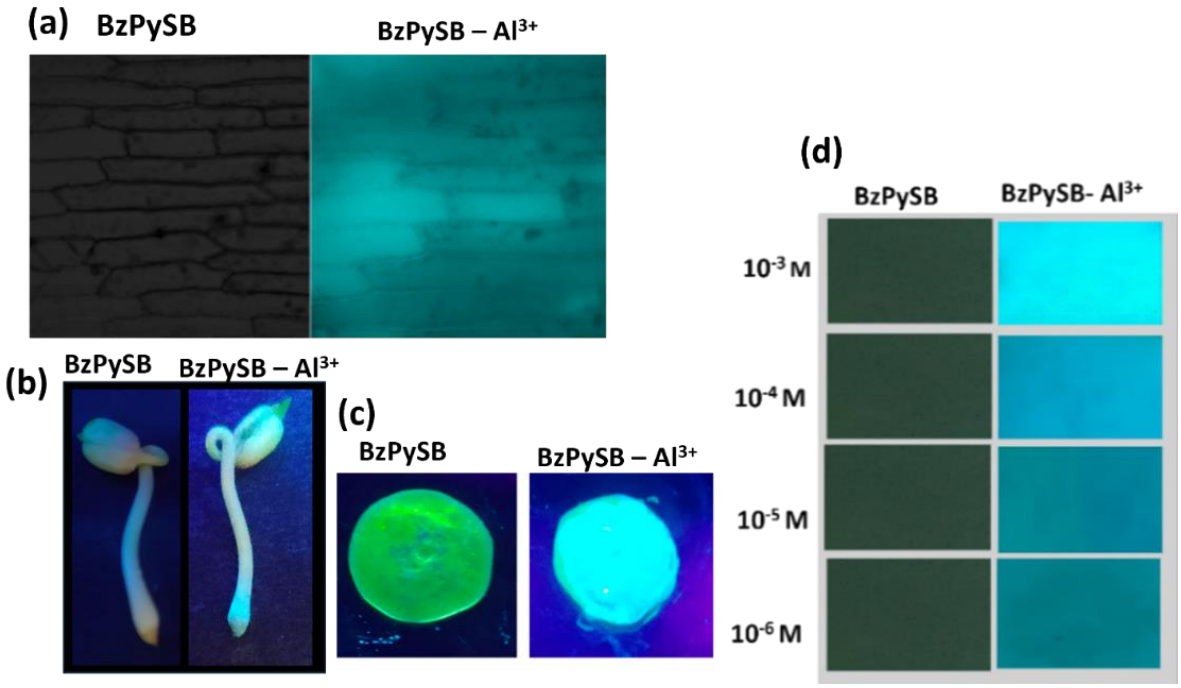

Figure 4A.25: (a) Fluorescence microscopy images of onion epidermal cells (b) Image of sprouts (c) Polymeric film (d) Test paper strips for detection of Al^{3+}

Molecular Logic Gates

The reversible property of **BzPySB** was utilized to create a molecular logic gate with two binary inputs. The two inputs consist of Al^{3+} and Na_2EDTA, while the output is observed by measuring the alteration in the fluorescence emission spectrum at a wavelength of 453 nm. If both inputs are absent, there is no noticeable alteration in the emission band, indicating that the gate is in the 'OFF' state. Upon the addition of Na_2EDTA to the chemosensor, no substantial alterations were observed. Instead, the emission band remained unaltered. Therefore, in the presence of Na_2EDTA, the result was deemed to be null. However, when only the Al^{3+} ion solution was added to the chemosensor, there is a noticeable increase in the fluorescence intensity at 453 nm. The output signal is now 1, indicating that the gate is 'ON'. However, when both inputs are present, the fluorescence intensity is much reduced, resulting in an output of zero, indicating that the gate is once again in the 'OFF' state. These investigations indicate that the molecular gate functions as an INHIBIT logic gate.

The inputs to the gate are Al^{3+}, Na_2EDTA, and the output is the change in fluorescence intensity at 453 nm. The respective truth table and pictorial diagram of the INHIBIT logic gate is depicted in **Figure 4A.26**.

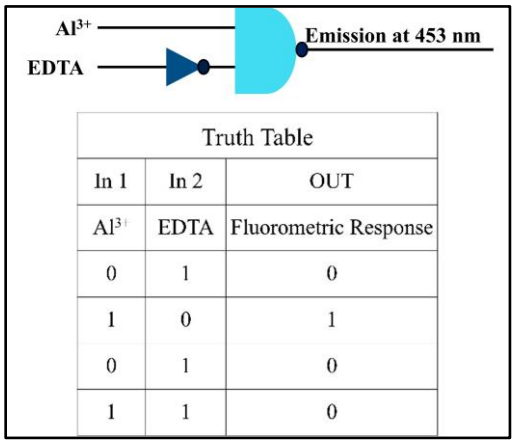

Truth Table		
In 1	In 2	OUT
Al^{3+}	EDTA	Fluorometric Response
0	1	0
1	0	1
0	1	0
1	1	0

Figure 4A.26: Molecular logic gates and truth table based on Al^{3+} and EDTA for **BzPySB**

Table A10, Appendix A shows a comparison of **BzPySB** with chemosensors reported in the literature.

4A.3 CONCLUSION

A pyridinium salt was synthesized and well-characterized by FT-IR, NMR, SC-XRD, and mass spectroscopy. **BzPySB** demonstrated high selectivity and sensitivity for recognizing Al^{3+} metal ions among various other metal ions. The B-H plot and LOD estimation supported the high affinity of **BzPySB**. The fluorescence emission phenomena may be attributed to chelation-enhanced fluorescence (CHEF) due to the restriction of C=N isomerization. The solid-state fluorescence of **BzPySB** was utilized to visualize latent fingerprints on glass surfaces, revealing information about the peculiar individual characteristics of the fingerprints under investigation. Additionally, the fluorescence properties of **BzPySB** were also investigated in biological systems.

Section 4B

Schiff Base-Appended Imidazolium Salt for Detection of Copper(II) Ions

In this section the synthesis and characterization of Schiff base-appended imidazolium-salt, **IsImSB** is discussed. The developed chemosensor was applied in real water and urine samples for Cu^{2+} ions detection. It was also applied for the development of commercially reliable and low-cost μPADs for Cu^{2+} detection.

4B.1 EXPERIMENTAL SECTION

4B1.1 Synthesis of 3-(2-(2,3-dioxoindolin-1-yl)ethyl)-1-methyl-1H-imidazol-3-ium bromide (IsIm)

To an ethanolic solution of N-alkylated Istain (0.0790 mmol), 1-methyl imidazole (0.0790 mmol) was added. The solution was stirred for 6 h under reflux conditions. The bright orange liquid obtained was washed with ethyl acetate and ether successively. The obtained orange solid was filtered and dried under vacuum (26 mg, 96% yield); mp = 215–220 °C; ^{1}H NMR (400 MHz, DMSO-d_6) δ 8.96 (s, 1H), 7.68 (s, 1H), 7.49 – 7.35 (m, 1H), 7.01 – 6.89 (m, 1H), 4.27 (t, 2H), 3.93 (t, 2H), 3.57 (s, 3H). ^{13}C NMR (100 MHz, DMSO-d_6) δ 187.9, 163.8, 155.2, 143.2, 142.6, 129.8, 128.7, 128.1, 122.9, 115.4, 52.2, 45.5, 45.2, 45.0, 44.8, 44.6, 44.4, 44.2, 44.0, 40.9.; HRMS (ESI) *m*/*z*: $[M\text{-}Br]^+$ calcd. for $[C_{14}H_{14}N_3O_2]^+$ 256.1081; found 256.1102.

4B1.2 Synthesis of 2-((Z)-3-(((E)-2-hydroxybenzylidene) hydrazineylidene)-2-oxoindolin-1-yl)-1-(1-methyl-1H-3l4-imidazol-3-yl)ethan-1-ylium bromide (IsImSB)

The ethanolic solution of **IsIm** (0.0595 mmol) was stirred with an ethanolic solution of (E)-2 (hydrazineylidemehyl)phenol (0.0595 mmol). This mixture was stirred for 6 h under reflux. The solvent was removed under reduced pressure to obtain a dark yellow viscous liquid. The crude product was further washed with ethyl acetate and diethyl ether several times and precipitated as a bright yellow solid (30 mg, 95% yield); mp = 220–225 °C; ^{1}H NMR (400 MHz, DMSO-d_6) δ 12.38 (s, 1H), 9.73 (d, J = 7.9 Hz, 1H), 9.45 (s, 1H), 8.63 (d, J = 7.5 Hz, 1H), 8.56 – 8.49 (m, 1H), 8.45 – 8.36 (m, 1H), 8.24 (ddd, J = 15.9, 6.5, 3.2 Hz, 3H), 8.21 – 8.16 (m, 1H), 8.10 – 7.95 (m, 2H), 7.75 – 7.63 (m, 2H), 7.62 – 7.46 (m, 3H), 5.03 (d, J = 5.5 Hz, 2H), 4.74 (q, J = 6.4 Hz, 2H), 4.33 (d, J = 11.6 Hz, 3H); ^{13}C NMR (100 MHz, DMSO- d_6) δ 173.3, 170.9, 164.2, 160.5, 159.2, 150.2, 145.1, 138.5, 137.8, 137.6, 134.8, 134.0, 128.9, 124.1, 123.7, 123.4, 120.4, 119.7, 117.2, 116.6, 109.8, 60.3, 47.5, 36.2.; HRMS (ESI) *m*/*z*: $[M\text{-}Br]^+$ calcd. for $[C_{21}H_{19}N_5O_2]^+$ 373.1612; found 373.1632.

4B.2 RESULTS AND DISCUSSION

4B.2.1 Synthesis and Characterization

The proposed chemosensor **IsImSB** was synthesized through an easy and economical procedure. The synthetic procedure comprises of quaternization of N-alkylated isatin with 1-methyl imidazole to yield 3-(2-(2,3-dioxoindolin-1-yl)ethyl)-1-methyl-1H-imidazol-3-ium bromide (**IsIm**) which was well characterized **(Figure A26, A27, A28 Appendix-A**). The 1:1 condensation reaction of **IsIm** and (E)-2-(hydrazineylidemehyl)phenol gave **IsImSB** with good yield (**Scheme 4B.1**).

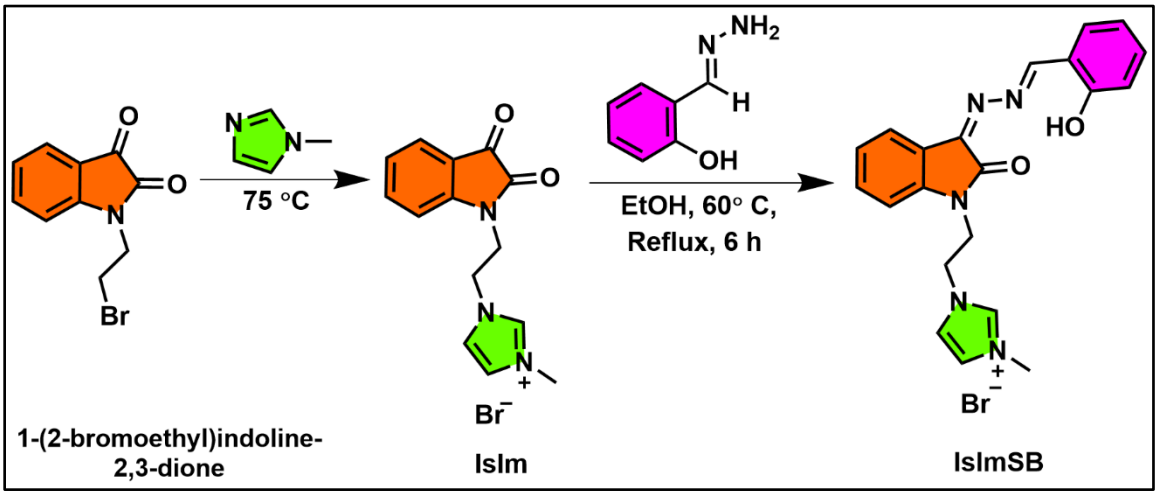

Scheme 4B.1: Synthetic route for **IsImSB**

Its structure was characterized by FT-IR, ^{1}H, and ^{13}C-NMR spectroscopy, and ESI-MS spectrometry. The infrared spectrum of the **IsImSB** exhibited a broad band from 3195-3640 cm^{-1} which can be attributed to hydrogen-bonded OH. Two bands due to CH=N groups appeared at 1585 cm^{-1} and 1574 cm^{-1} and an intense band at 1703 cm^{-1} appeared due to (C=O) of isatin (**Figure 4B.1**).

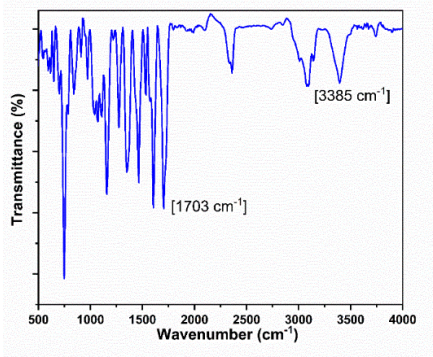

Figure 4B.1: IR spectra of **IsImSB**

The appearance of two triplets for CH_2 of the alkyl at 3.92 and 4.26 ppm, singlet at 3.57 ppm for imidazole methyl proton, and singlet at 8.96 ppm for imidazole C-H proton in ^{1}H NMR indicated the quaternization. The ^{13}C NMR signals were also well-matched with the structure. The 1:1 condensation reaction of **IsIm** and (E)-2-(hydrazineylidemehyl)phenol gave **IsImSB** in 90% yield. In ^{1}H of **IsImSB,** the appearance of singlet at 12.38 pm and 8.40 ppm indicated the presence of phenolic and imine proton (**Figure 4B.2**). In ^{13}C NMR the signals at 173.3, 170.93 and 164.2 ppm indicated the presence of ketonic, phenolic and imine carbon, respectively (**Figure 4B.3**). ESI mass spectral analysis showed *m/z* peak at 373.1534 (*m/z*, calcd. 373.1612), which may be attributed to [**IsImSB**-Br]$^-$ (**Figure 4B.4**).

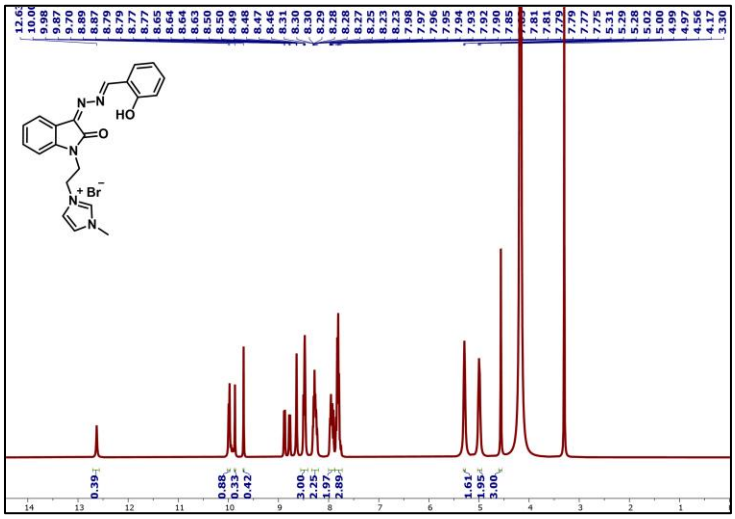

Figure 4B.2: ^{1}H NMR of **IsImSB** in DMSO-d_6

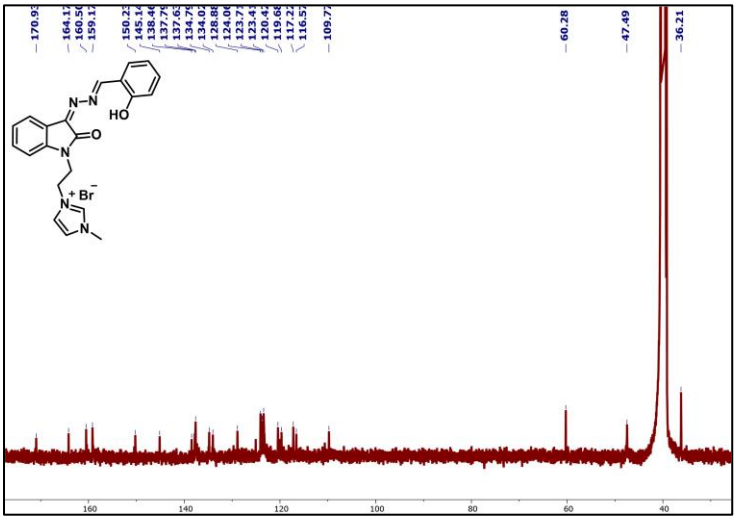

Figure 4B.3: ^{13}C NMR of **IsImSB** in DMSO-d_6

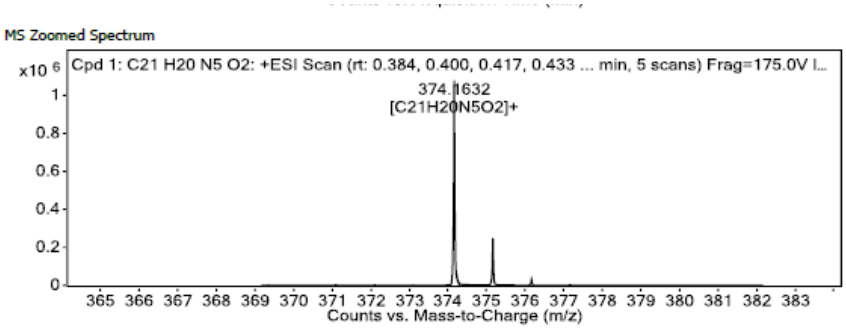

Figure 4B.4: HRMS of **IsImSB**

4B.2.2 Response of IsImSB toward Cu^{2+} ions

The selectivity of **IsImSB** was observed by the naked-eye detectable color change in the presence of Na^{+}, Mg^{2+}, Al^{3+}, K^{+}, Ca^{2+}, Mn^{2+}, Fe^{2+}, Fe^{3+}, Co^{2+}, Cu^{2+}, Zn^{2+}, Ag^{+}, Sn^{+}, Hg^{+}, Pb^{+}, Nd^{3+}, and Yb^{3+} metal ions in aqueous media. The noticeable color change of **IsImSB** was observed only with Cu^{2+}, the solution changed from yellow to dark red. The UV−vis spectra of **IsImSB** (50 μM) were recorded in the presence of 1.5 equiv. of these metal ions. **IsImSB** exhibited an absorption band at 246 nm assigned to π-π* transition and other two bands at 330 nm and 385 nm due to n-π* transitions of the ketimine and aldimine moieties, respectively. Upon interaction of **IsImSB** with Cu^{2+}, the two bands were red-shifted to 250 nm and 336 nm while no shift was observed in the third band. Moreover, the appearance of a new absorption band at 489 nm indicated the complexation of **ImIsSB** with Cu^{2+}. **IsImSB** did not show noticeable spectral responses with other metal ions, which indicated the high selectivity of **IsImSB** for Cu^{2+} (**Figure 4B.5a**). The criteria for selectivity depend on the cationic charge, ionic radii, type of bonding in the complexes (ionic/ covalent), and coordination numbers. **IsImSB** with two imine linkages and -OH group provided a cavity-like structure that can easily host metal ions. Moreover, **IsImSB** being a hard donor (due to the presence of N and O atoms) easily coordinated with the hard acceptor (Cu^{2+}). Therefore, the sensitivity of **IsImSB** toward Cu^{2+} was investigated by UV-vis absorption experiments. The aqueous solution of Cu^{2+} was added successively to the solution of **IsImSB** at an interval of 2 μM. Upon increasing the concentration of the Cu^{2+}, the absorption at 330 nm decreased while at 489 nm increased. The isosbestic point appeared at 359 nm, 372 nm, and 435 nm, indicating the formation of new species in solution (**Figure 4B.5b**). The increase in absorption band at 489 nm along with color change could be explained by the ligand-to-metal charge transfer (LMCT) mechanism.

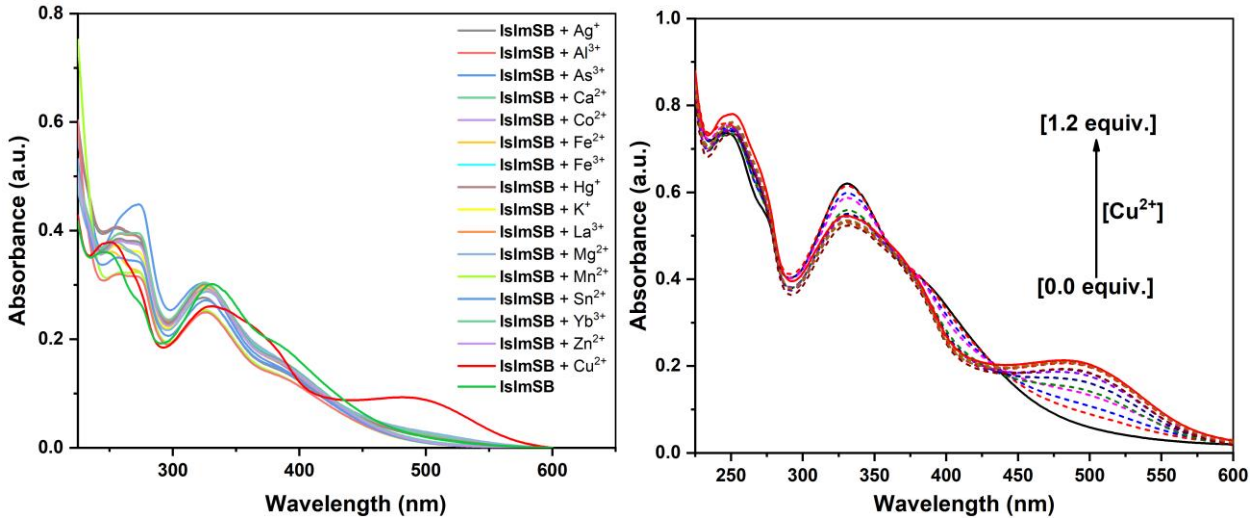

Figure 4B.5: (a)Absorption spectra of **IsImSB** (5×10^{-5} M) in water with (a) different metal ions (b) different amounts of Cu^{2+} ions

Based on UV-vis absorption spectra, the binding constant of **IsImSB** was estimated using a B-H plot drawn with a change in absorbance ($1/\Delta A$) vs concentration ($1/[Cu^{2+}]$) which gave the best fit for 1:1 binding stoichiometry and the magnitude of binding constant (K_a) was 4.18×10^{-4} M for the complex species (**Figure 4B.6a**). Further, these UV−vis spectral changes were found to obey Lambert Beer's law by showing a linear response at 489 nm against the concentration of Cu^{2+}. According to the IUPAC standard, the limit of detection (LOD) was calculated and found to be 10 nM (**Figure 4B.6b**).

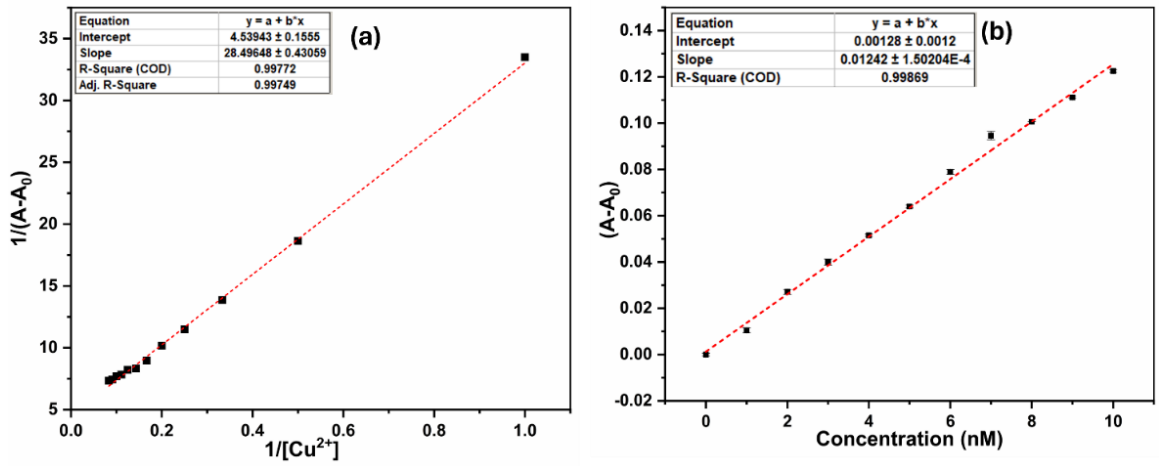

Figure 4B.6: (a) B–H plot of the absorption spectra of **IsImSB** with different amounts of Cu^{2+} (b) Calibration curve with error bar for calculating Limit of Detection of Cu^{2+} ions

For the Job's plot, the absorbance change at 489 nm was plotted against the mole fraction of the **IsImSB** under the constant total concentration. When the mole fraction was 0.5, the change in absorbance became maximum, which indicated a 1:1 binding stoichiometry between **IsImSB** and Cu^{2+} (**Figure 4B.7**).

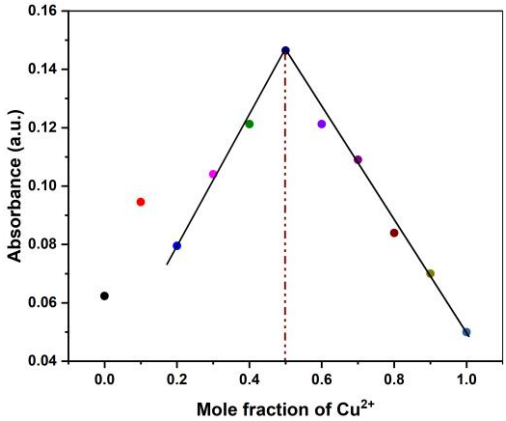

Figure 4B.7: Job's Plot of **IsImSB** with Cu^{2+}

The binding mode of **IsImSB** with Cu^{2+} was investigated by FT-IR, HRMS, and X-ray photoelectron spectroscopy (XPS). The evidence for binding was obtained by infrared spectra of the **IsImSB**-Cu^{2+} complex. The stretching frequency of ν(C=O) of **IsImSB** observed at 1703 cm^{-1} decreased to 1690 cm^{-1}. The decrease in frequency was also observed for ν(C=N) of the aldimine group from 1571 cm^{-1} to 1550 cm^{-1}. The disappearance of the broad signal at 3392 cm^{-1} for -OH also supported the binding of Cu^{2+} with O and N of **IsImSB** (**Figure 4B.8**).

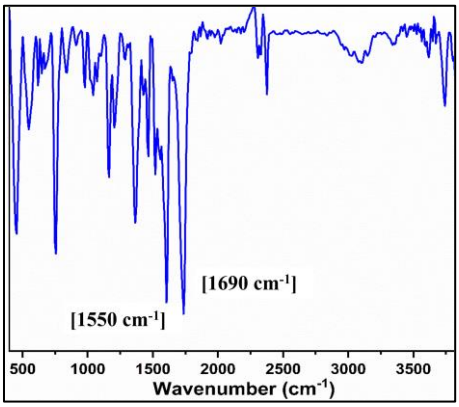

Figure 4B.8: IR of **IsImSB**-Cu^{2+} complex

The HRMS spectra further confirmed the proposed composition for the complex. The observed m/z value for [**IsImSB**+Cu+Cl-Br]$^{+}$ was found to be 471.0527 (calcd. 471.0518) also supported the complex formation (**Figure 4B.9**).

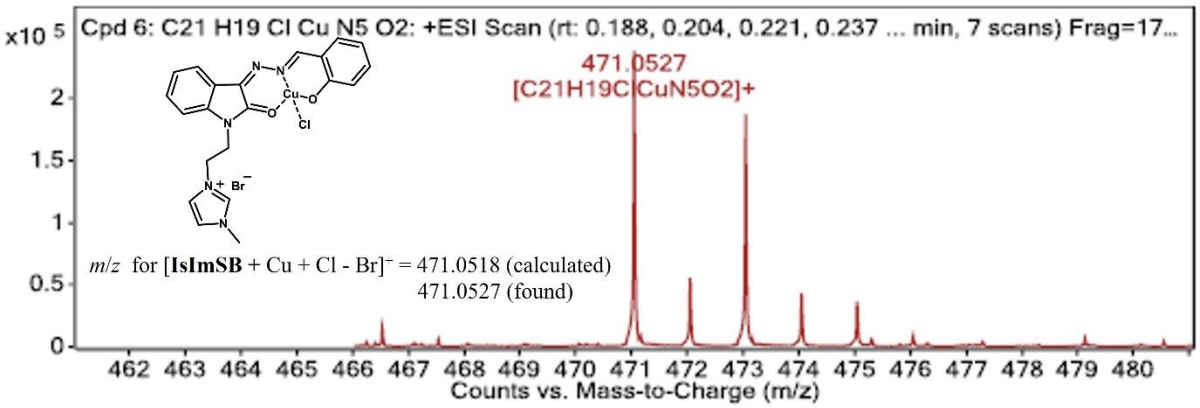

Figure 4B.9: HRMS of **IsImSB**-Cu^{2+} complex

The speculation of the interaction of O and N of **IsImSB** with Cu^{2+} was also confirmed by the results of XPS measurements (**Figure 4B.10a and b**). A comparison of the change in peaks in the XPS spectra before and after complex formation with Cu^{2+} showed that N 1s peaks shifted from free nitrogen atom at 400 eV to 401 eV, while the oxygen 1s peaks shifted from 532 eV to 533 eV. The binding energies of 935.3 eV and 955.4 eV correspond to Cu $2P_{3/2}$ and Cu $2P_{1/2}$ orbitals, indicating the presence of Cu in the +2 oxidation state (**Figure 4B.10c**).

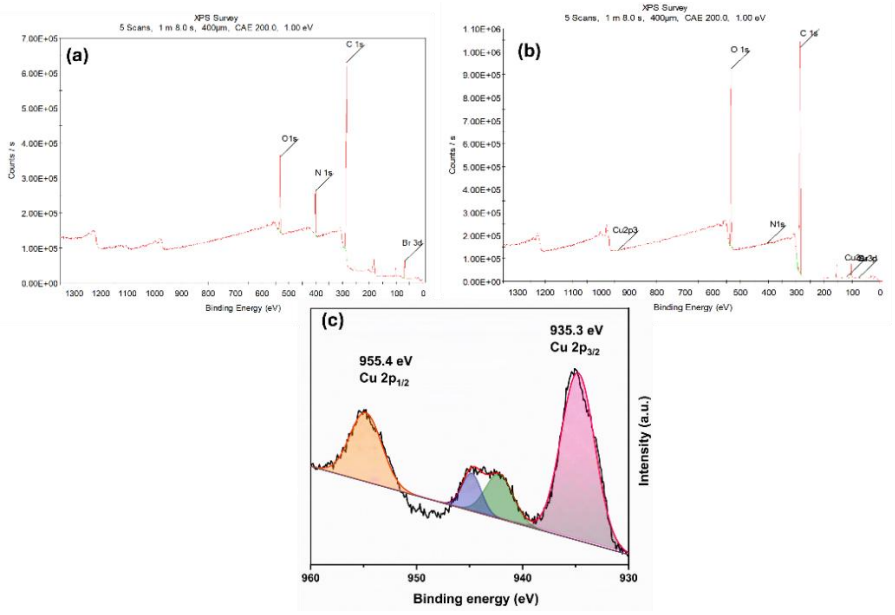

Figure 4B.10: XPS wide scan survey spectrum of (a) **IsImSB** (b) **IsImSB**-Cu^{2+} complex (c) XPS spectra of the Cu-2p core peak of the **IsImSB**-Cu^{2+} complex

The chemosensors with nitrogen donors have a high level of sensitivity to changes in ambient pH. This is because the degree of protonation of the nitrogen atoms is greatly influenced by the pH level. Therefore, to investigate the impact of pH on the detection of Cu^{2+} by **IsImSB**, pH titration studies were conducted in the pH range of 2 to 10. On addition of Cu^{2+} ions, the absorbance at 489 nm was high in the pH range 5-8 while low at pH 2-4 and 9-10 (**Figure 4B.11a**). The limited absorption response of **IsImSB** towards Cu^{2+} ions in acidic and alkaline solutions may be attributed to the protonation of nitrogen and formation of $Cu(OH)_2$, respectively which obstructs the interactions between **IsImSB** and Cu^{2+}. The findings demonstrate that **IsImSB** is very sensitive in detecting Cu^{2+} ions within the pH range of 5-8, therefore it can be utilized efficiently for Cu^{2+} detection in real samples. The reversibility of the spectral response of **IsImSB**-Cu^{2+} was investigated by adding a stronger chelating agent ethylenediaminetetraacetate (EDTA). Because of the high stability constant of the EDTA-Cu^{2+} complex, it was expected that EDTA would preferentially complex Cu^{2+} ion releasing **IsImSB** from the **IsImSB**-Cu^{2+}. The absorbance of the **IsImSB**-Cu^{2+} decreased with the addition of EDTA and was recovered with the addition of Cu^{2+}, which indicated that the binding of **IsImSB** with Cu^{2+} was reversible (**Figure 4B.11b**). Therefore, **IsImSB** could be recyclable after treatment with EDTA.

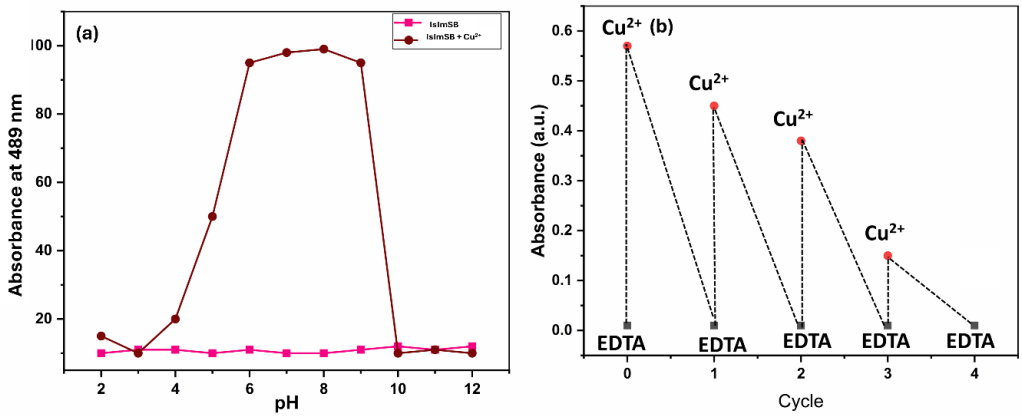

Figure 4B.11: (a) Effect of pH on **IsImSB** and **IsImSB**-Cu^{2+} complex (b) Reversibility chart of **IsImSB** after the sequential addition of Cu^{2+} and EDTA

To study the interference of other metal ions on the behavior of **IsImSB** to Cu^{2+}, competitive experiments were carried out in the presence of Cu^{2+} mixed with other metal ions (Na^+, Mg^{2+}, Al^{3+}, K^+, Ca^{2+}, Mn^{2+}, Fe^{2+}, Fe^{3+}, Co^{2+}, Cu^{2+}, Zn^{2+}, Ag^+, Sn^+, Hg^+, Pb^+, Nd^{3+}, and Yb^{3+}) and anions (F^-, Cl^-, Br^-, I^-, SO_4^{2-}, NO_2^-, HCO_3^-) at equimolar concentration. These competitive metal ions and anions did not produce significant absorption changes except Cu^{2+} (**Figure 4B.12a and b**). This

indicated that **IsImSB** can be used to detect Cu^{2+} even in the presence of other competitive metal ions in high concentrations.

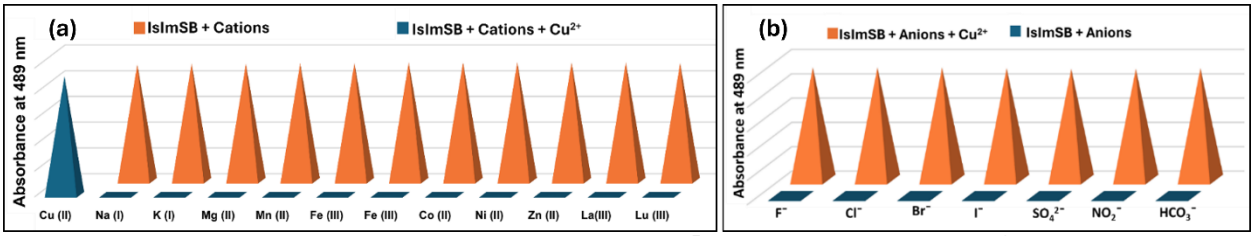

Figure 4B.12: Interference study of **IsImSB** (5×10^{-5} M) in water toward Cu^{2+} selectivity in the presence of (a) cations (b) anions

To better understand the interaction between **IsImSB** and Cu^{2+}, theoretical DFT computations were performed for **IsImSB** and its 1:1 complex **IsImSB**-Cu^{2+}. In **IsImSB** the electron density in HOMO was distributed over the conjugated part of isatin and salicylaldehyde. While in LUMO there was a decrease in the electron density at oxygen atoms of isatin and salicylaldehyde. On the other hand in **IsImSB**-Cu^{2+}, the electron densities of HOMO and LUMO were allocated over the −OH and −NH groups, which lead to the complexation of Cu^{2+} with **IsImSB**. The calculated energy gap between HOMO and LUMO for **IsImSB** was found to be 1.58 eV (**Figure 4B.13**). Similarly, for **IsImSB**-Cu^{2+} complex, the energy gap was found to be 0.0268 eV. The energy gap of free **IsImSB** (1.573 eV) was larger than that of the **IsImSB**-Cu^{2+} complex (0.0268 eV). The decrease in the energy gap indicated energetically favourable conditions for complex formation. These results also supported the redshift in the experimental UV–vis spectra upon addition of the Cu^{2+}.

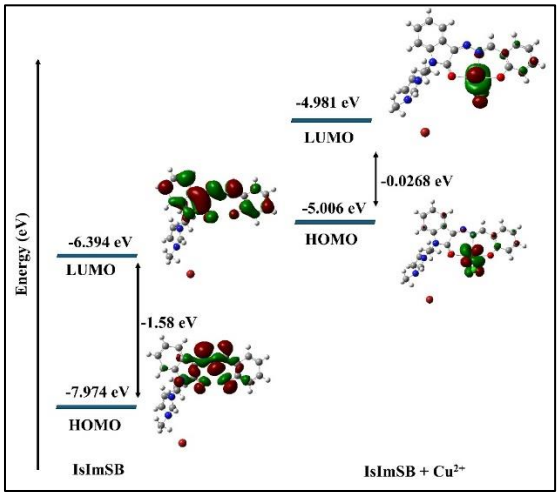

Figure 4B.13: Energy levels and frontier molecular orbitals of **IsImSB** and the **IsImSB**-Cu^{2+} complex

4B.2.3 Analytical Applications

Microfluidic paper-based analytical device (*μ*PAD) for detection of Cu^{2+}

Fast, selective, proprietary, and inexpensive tools are especially meaningful for on-site environmental surveys. For the development of such devices, papers have been considered an appropriate substrate due to their advantages such as low cost, commercial availability, and easy design. In addition, papers are made of cellulosic fibers and are environmentally friendly, and due to their capillary properties, they can flow fluids into their channels without the need for a pump or external force. Efforts to develop paper-based microfluidics for the detection of heavy metal ions have attracted tremendous research attention due to the increasing environmental pollution of metals and their adverse effects on human health. These tools have all the features of the WHO-approved diagnostic devices such as sensitivity, cost-effectiveness, user-friendliness, and portability. Hence, μPADs have recently been used for the on-site monitoring of environment sites. Due to its excellent variability and hydrophilicity, the paper can facilitate the adsorption and stabilization of target analytes and prevent excessive separation and dispersion by creating clear detection zones. Probe–metal complexes are effectively detected by the naked eye and can be measured using inexpensive optical patterns. Therefore, in this part of the study, the efficiency of paper microfluidics in the diagnosis of Cu^{2+} has been evaluated.

In the production of microfluidic paper chips, hydrophilic capillary channels are created on paper using hydrophobic materials, in which no chemical reaction takes place between cellulose and hydrophobic materials. Different types of paper can be applied depending on the sensor application and how it is made. Because 30% to 90% of paper is porous and the shape is not the same in different types of paper, the structure of the pores can help in the use of paper in diverse fields. Therefore, the choice of paper type is of particular importance and several factors such as non-decomposition and deformation after immersion in the liquid phase, heat loss and sufficient tolerance must be considered in this selection. In addition, microfluidic paper chips highly require water-absorbent paper. Therefore, filter paper can be considered the best matrix in the construction of microfluidic paper chips due to its large pores and high absorption ability. In this work, filter paper with wax coating was used to make μPADs.

The optical images on the μPADs were captured under natural light, in which the color alternations of **IsImSB** were evaluated through the l-channels. Furthermore, the colorimetric sensing was performed by capillary method, in which the **IsImSB** probe was placed on the central part of the

μPADs. In the presence of Cu^{2+}, the color changed from yellow to red while there was no color change in the presence of the other ions. The reason for more adsorption of the **IsImSB** solution in the presence of Cu^{2+} is attributed to the interactions between Cu^{2+} ion and **IsImSB**, leading to the complexation of the Cu^{2+} and **IsImSB** (**Figure 4B.14**).

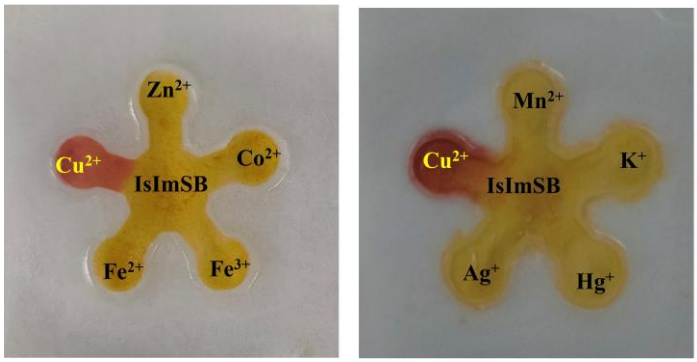

Figure 4B.14: μPADs for colorimetric detection of Cu^{2+}

Smartphone Application for the Detection of Cu^{2+}

The color change of **IsImSB** in the presence of varied concentrations of Cu^{2+} provided the prerequisites for the smartphone colorimetric detection strategy for Cu^{2+}. Therefore, **IsImSB** was integrated with a smartphone to monitor the change in the RGB values. The color (red, green, and blue) on the standard RGB scale is represented by whole numbers ranging from 0 to 255. The number [255,255,255] on that scale denotes true white, while [0,0,0] denotes absolute black. The RGB values can be recorded to monitor color changes using a smartphone. The change in RGB (red, blue, green) values of the vails containing **IsImSB** solutions with different concentrations of Cu^{2+} were measured by using a back camera. The results showed that the color intensity of R and G decreased gradually. By considering the ratio between the red channel and the green channel (G/B) as the signal, a linear trend between the concentration of Cu^{2+} and the R/G value can be obtained. The R/G value is linear in the concentration range 15.39–153.85 M of Cu^{2+} ($R^2 = 0.9917$) (**Figure 4B.15a**). The calculated LOD measured 5.55 nM, which is lower than the maximum amount of drinking water specified by the WHO (7 M). These results show that the detection of Cu^{2+} in a "portable" way is possible by using a simple smartphone.

Recognition of Cu^{2+} on test strips

To investigate the practicability of the **IsImSB** for Cu^{2+} detection, a simple paper-based sensor was used for real-time monitoring. The Whatman filter paper was immersed in the aqueous solution of **IsImSB** for 10 min and dried in air. On addition of various concentrations of Cu^{2+}

(10^{-3} M to 10^{-5} M) showed different shades of red color on the paper strip depending on the concentration of Cu^{2+} (**Figure 4B.15b**). Thus, the paper strip experiment supported efficient and convenient techniques for the detection of Cu^{2+}.

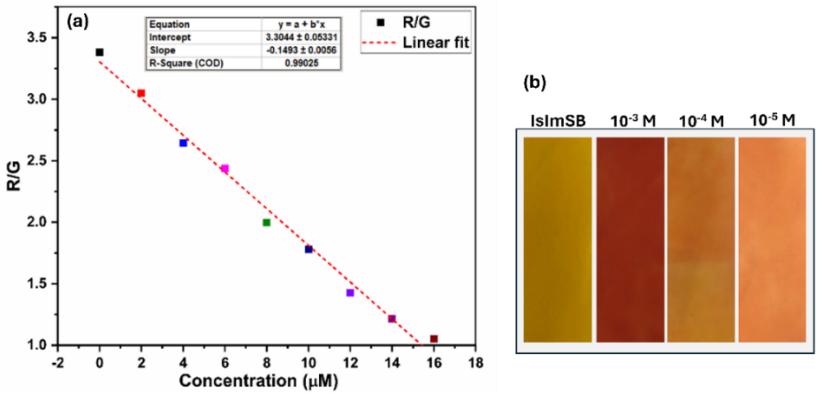

Figure 4B.15: (a) Ratio of R/G versus Cu^{2+} concentration in the range of 0 to 16 μM (b) Test paper strips for detection of Cu^{2+}

Real sample Analysis

The practical feasibility of **IsImSB** as a colorimetric chemosensor was evaluated using water and urine samples. Different Water samples were first filtered and then spiked with various concentrations of Cu^{2+}. According to the obtained calibration curve with a wide linear range (0.3-30 mM), the **IsImSB** could be appropriate for the quantitative detection of Cu^{2+} in environmental samples. As can be seen in **Table 4B.1**, considerable recoveries and R.S.D. values obtained for the determination of Cu^{2+} ions in water samples confirmed that the developed sensor could be useful for the quantitative detection of Cu^{2+} in real samples.

Table 4B.1 Determination of copper ion in water

Sample	Cu^{2+} Spiked (μM)	Cu^{2+} recovered (μM)	Recovery %
Mineral Water	20	19.87	99.35
Tap Water	20	19.80	99
River Water	20	19.90	99.5

Wilson disease is an inherited disorder in which excessive amounts of copper accumulate in the body, particularly in the liver, brain, and eyes, a urinary copper excretion of more than 100 μg/24 h (>1.6 μmol/24h) is considered diagnostic for symptomatic Wilson's disease. Consequently, there is an elevated likelihood of copper being excreted through urine. Thus, the identification of urine copper through a chemoreceptor could serve as a biomarker for diagnosing this condition. The ability of **IsImSB** to detect Cu^{2+} with a distinct naked eye colorimetric change from yellow to dark

red from human urine samples could as a diagnostic chemosensor for Wilson disease (**Table 4B.2**). The concentrations of copper ions in the spiked urine samples determined by the developed method were in good agreement with those of the added Cu^{2+} indicating that the present method is promising in practical applications.

Table 4B.2 Determination of copper ion in Urine samples

Sample	Cu^{2+} Spiked (μM)	Cu^{2+} recovered (μM)	Recovery %
	5	4.85	97
Human Urine	10	9.89	98.9
	20	19.70	98.5

Molecular logic gate

The creation of molecular logic circuits, like logic gates, is an advancement in molecular perception analysis. The reversible colorimetric signaling of the probe **IsImSB** was used to create a molecular circuit diagram that mimics logic gate behavior. The molecular logic gate was activated using a variety of chemical inputs, including Cu^{2+} and EDTA, and its outputs were the strong absorbance signals at 489 nm. The absence and existence of inputs in digital coding were represented by the binary digits ‟0″ and ‟1″ For output, colorimetric ON mode (‟1″) denoted a significant absorbance at 489 nm, whereas OFF mode (‟0″) denoted a loss in the absorbance, therefore the output signal for **IsImSB** in the presence of Cu^{2+} was ‟1″ indicating that the system was in the ON state. The system status was OFF with no absorbance for the other input combinations, which showed that the output signal was ”0″. Thus, the aforementioned results conclusively show that INHIBIT molecular logic gates are designed for the potent reversible properties of the probe (**Figure 4B.16**).

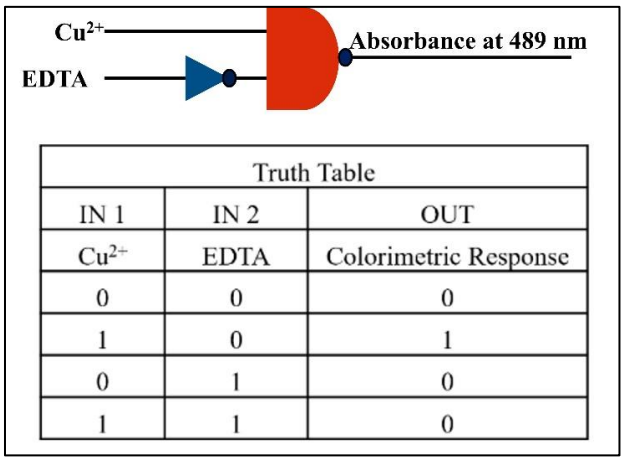

Truth Table		
IN 1	IN 2	OUT
Cu^{2+}	EDTA	Colorimetric Response
0	0	0
1	0	1
0	1	0
1	1	0

Figure 4B.16: Molecular logic gates and truth table based on Cu^{2+} and EDTA for **IsImSB**

A comparative literature report of chemsensor with **IsImSB** is presented in **Table A11, Appendix A**

4B.3 CONCLUSION

A simple and rapid colorimetric imidazolium-based chemosensor **IsImSB** has been developed to detect Cu^{2+} with a high sensitivity and good specificity. In the presence of Cu^{2+}, an alteration in the absorption spectra of **IsImSB** was directly recognized by the naked eye. The **IsImSB** exhibited a color change from yellowish to red upon complexation with Cu^{2+}. A good linearity was obtained between the absorption of **IsImSB** and the concentration of Cu^{2+}, with an LOD of 10 nM. In addition, **IsImSB** served as a reversible colorimetric sensor for Cu^{2+} using EDTA as a restoring agent. Thus, **IsImSB**–Cu^{2+} can be used as a probe for the detection of EDTA via a reversible chelation process. **IsImSB** was successfully used to detect Cu^{2+} in real water and urine samples. In addition to the quantitative analysis, the qualitative capability of **IsImSB** was achieved by paper-based microfluidic devices (μPADs).

4B.4 REFERENCES

1. Singh, G.; Priyanka; Singh, A.; Satija, P.; Sushma; Pawan; Mohit; Singh, J.; Singh, J.; *New Journal of Chemistry*, **2021**, *45* (17), 7850-7859.
2. Banerjee, S.; Brandão, P.; Saha, A.; *RSC Advances*, **2016**, *6* (104), 101924-101936.
3. Liu, F.; Fan, C.; Tu, Y.; Pu, S.; *RSC Advances*, **2018**, *8* (54), 31113-31120.
4. Ghorai, P.; Pal, K.; Karmakar, P.; Saha, A.; *Dalton Transactions*, **2020**, *49* (15), 4758-4773.
5. Ghorai, A.; Mondal, J.; Chandra, R.; Patra, G. K.; *Dalton Transactions*, **2015**, *44* (29), 13261-71.
6. Mukherjee, S.; Betal, S.; Chattopadhyay, A. P.; *New Journal of Chemistry*, **2020**, *44* (29), 12692-12703.
7. Liu, Z.; Yang, W.; Tian, B.; Liu, J.; Zhu, W.; Ge, G.; Xiao, L.; Meng, Y.; *New Journal of Chemistry*, **2018**, *42* (21), 17665-17670.
8. Alasfar, R. H.; Isaifan, R. J.; *Environmental Science and Pollution Research International* , **2021**, *28* (33), 44587-44597.
9. Li, Z.; Zhao, J. L.; Wu, Y. T.; Mu, L.; Zeng, X.; Jin, Z.; Wei, G.; Xie, N.; Redshaw, C.; *Organic Biomolecular Chemistry*, **2017**, *15* (40), 8627-8633.
10. Robertson, J. A.; Felsenfeld, A. J.; Haygood, C. C.; Wilson, P.; Clarke, C.; Llach, F.; *Kidney International*, **1983**, *23* (2), 327-35.
11. Vallejos, S.; Munoz, A.; Ibeas, S.; Serna, F.; Garcia, F. C.; Garcia, J. M.; *ACS Applied Material and Interfaces*, **2015**, *7* (1), 921-8.
12. Moussaron, A.; Alexandre, J.; Chenard, M. P.; Mathelin, C.; Reix, N.; *Journal of Trace Elements in Medicine and Biology*, **2023**, *79*, 127247.
13. Bhuvanesh, N.; Suresh, S.; Kannan, K.; Rajesh Kannan, V.; Maroli, N.; Kolandaivel, P.; Nandhakumar, R.; *New Journal of Chemistry*, **2019**, *43* (6), 2519-2528.
14. Botté, A.; Zaidi, M.; Guery, J.; Fichet, D.; Leignel, V.; *Aquatic Ecology*, **2022**, *56* (3), 751-773.
15. Sharma, S.; Hundal, M. S.; Walia, A.; Vanita, V.; Hundal, G.; *Organic Biomolecular Chemistry*, **2014**, *12* (25), 4445-53.
16. Mabhai, S.; Dolai, M.; Dey, S. K.; Choudhury, S. M.; Das, B.; Dey, S.; Jana, A.; Banerjee, D. R.; *New Journal of Chemistry*, **2022**, *46* (15), 6885-6898.
17. Aydin, D.; Dinckan, S.; Karuk Elmas, S. N.; Savran, T.; Arslan, F. N.; Yilmaz, I.; *Food Chemistry*, **2021**, *337*, 127659.
18. Hazra, A.; Roy, P.; *Inorganic Chemistry Communications*, **2021**, *130*, 108694.

19. Kshirsagar, N.; Sonawane, R.; Patil, P.; Nandre, J.; Sultan, P.; Sehlangia, S.; Pradeep, C. P.; Wang, Y.; Chen, L.; Sahoo, S. K.; *Inorganica Chimica Acta,* **2020**, *511*, 119805.
20. Al Anshori, J.; Ismalah, D.; Abror, A. F.; Zainuddin, A.; Wiani Hidayat, I.; Yusuf, M.; Maharani, R.; Tatang Hidayat, A.; *RSC Advances*, **2022**, *12* (5), 2972-2979.
21. Wang, M.; Li, M.; Yu, A.; Zhu, Y.; Yang, M.; Mao, C.; *Advance Functional Material*, **2017**, *27* (14),
22. Nirmala, M.; Vadivel, R.; Chellappan, S.; Malecki, J. G.; Ramamurthy, P.; *ACS Omega*, **2021**, *6* (15), 10318-10332.
23. Singh, N.; Chandra, R.; *New Journal of Chemistry*, **2021**, *45* (23), 10340-10348.
24. Sahu, M.; Kumar Manna, A.; Rout, K.; Mondal, J.; Patra, G. K.; *Inorganica Chimica Acta*, **2020**, *508*, 119633.
25. Chopra, T.; Sasan, S.; Devi, L.; Parkesh, R.; Kapoor, K. K.; *Coordination Chemistry Reviews*, **2022**, *470*, 214704.
26. Mandegani, F.; Zali-Boeini, H.; Khayat, Z.; Scopelliti, R.; *Talanta*, **2020**, *219*, 121237.
27. An, Y.; Li, L.; Li, L.; Sun, Y.; Li, B.; Wang, P.; *Journal of Hazardous Materials*, **2024**, *465*, 133192.
28. Chereddy, N. R.; Thennarasu, S.; Mandal, A. B.; *Sensors and Actuators B: Chemical*, **2012**, *171-172*, 294-301.
29. Mergu, N.; Gupta, V. K.; *Sensors and Actuators B: Chemical*, **2015**, *210*, 408-417.
30. Teixeira Alves Duarte, L. G.; Coelho, F. L.; Germino, J. C.; Gamino da Costa, G.; Berbigier, J. F.; Rodembusch, F. S.; Zambon Atvars, T. D.; *Dyes and Pigments*, **2020**, *181*, 108566.
31. Senthil Murugan, A.; Abel Noelson, E. R.; Annaraj, J.; *Inorganica Chimica Acta*, **2016**, *450*, 131-139.
32. Muwal, P. K.; Nayal, A.; Jaiswal, M. K.; Pandey, P. S.; *Tetrahedron Letters*, **2018**, *59* (1), 29-32.
33. Mohammed, G. I.; El-Ghamry, H. A.; Saber, A. L.; *Spectrochim Acta A Molecular Biomolecular Spectroscopy*, **2021**, *247*, 119103.
34. Chang, I. J.; Choi, M. G.; Jeong, Y. A.; Lee, S. H.; Chang, S.-K.; *Tetrahedron Letters*, **2017**, *58* (5), 474-477.
35. Mohan, V.; Das, N.; Jain, V. K.; Khan, T.; Pandey, S. K.; Faizi, M. S. H.; Daniel, J.; Sen, P.; *ChemistrySelect*, **2020**, *5* (30), 9435-9442.

36. An Kim, P.; Lee, H.; So, H.; Kim, C.; *Inorganica Chimica Acta*, **2020**, *505*, 119502.

37. Liu, H.; Ding, S.; Lu, Q.; Jian, Y.; Wei, G.; Yuan, Z.; *ACS Omega*, **2022**, *7* (9), 7585-7594.

38. Goshisht, M. K.; Patra, G. K.; Tripathi, N.; *Materials Advances*, **2022**, *3* (6), 2612-2669.

39. Afrin, A.; Jayaraj, A.; Gayathri, M. S.; P, C. A. S.; *Sensors & Diagnostics*, **2023**, *2* (5), 988-1076.

40. Kumar, A.; Virender; Saini, M.; Mohan, B.; Shayoraj; Kamboj, M.; *Microchemical Journal*, **2022**, *181*, 107798.

Chapter 5

Conclusion and Future Scope

5.1 General Conclusion

Sensing target analytes in the environment or biological samples using abiotic receptors is the major thrust area at the boundaries of organic, inorganic, environmental, and medicinal chemistry. Though several strategies have been employed for detecting analytes, colorimetric and fluorometric detection accomplishes many advantages over other methods because it is cheap and easy to assess. However, the low solubility of chemosensors in aqueous media hampers their applications for biological and environmental samples. This limitation can be circumvented by using hydrophilic pyrazinium-, imidazolium- and pyridinium-salt as chemosensors. Therefore, it is essential to design and synthesize fluorometric and colorimetric receptors that can selectively and sensitively recognize analytes in aqueous medium.

The current thesis entitled **"Azinium and Azolium Salts as Fluorometric/Colorimetric Chemosensors"** deals with the synthesis and application of chemosensor and their application in the detection of nitro explosives, anion and metal ions in a pure aqueous medium. The pyrazinium-salt as chemosensors were synthesized by a simple Suzuki coupling approach followed by a nucleophilic substitution reaction. The synthesis of pyridinium and imidazolium-salt involved incorporation of O-alkylation and N-alkylation, respectively followed by condensation reaction to provide Schiff base chemosensors.

5.2 Specific Conclusions

The chapter-wise description of the thesis is as follows:

Chapter 1: Introduction

The first chapter of the thesis presents the general discussion related to the brief discussion about chemosensors, the necessity of chemosensor systems, and the performance of optical sensors. The basic principles of colorimetric and fluorescent chemosensors are described. The sensing mechanisms such as fluorescence resonance energy transfer, photoinduced electron transfer, aggregation-induced emission, monomer/excimer formation, C=N isomerization, CHEF/CHEQ, Ground-state complex formation, ESIPT, and IFE have been presented with brief explanations in this chapter. In the latter part, various examples of imidazolium, pyridinium, and pyrazine-based chemosensors exhibiting colorimetric and fluorometric responses for different analytes have been discussed.

Chapter 2: Material, Methods and Instrumentation

This chapter explains the details of chemicals, instruments, software, and general methods used for the synthesis of pyrazinium, pyridinium, and imidazolium-salt as chemosensor. It also discusses the basic principles of various analytical instruments such as FT-IR, NMR, ESI-MS, single-crystal X-ray diffraction, UV-vis, fluorescence, time-resolved spectroscopy, XPS, and theoretical calculation.

Chapter 3: Pyrazinium Salts for Fluorometric/Colorimetric Detection of TNP and Anions

This chapter of the thesis is divided into three parts:

Section 3A: **Thiophene-Appended Pyrazinium Salt for Detection of TNP**

It deals with the synthesis of thiophene-appended pyrazinium salt, **1**-benzyl-3,5-di(thiophen-2yl) pyrazin-1-ium bromide, **BTPyz**. The synthetic procedure included a microwave-assisted palladium-catalyzed reaction of 2,6-dichloropyrazine with thiophene-2-boronic acid followed by a nucleophilic addition reaction with benzyl bromide. **BTPyz** exhibited a selective response toward TNP, among other closely related nitroaromatic compounds and other commonly interfering cations/anions. The fluorescence quenching revealed a high binding affinity of picrate to **BTPyz**, due to the formation of ground state charged transfer complex (GSC) and resonance energy transfer (RET) as evident from ^{1}H NMR spectra, single-crystal XRD, and density functional theory calculations. Contact mode detection using paper strips of **BTPyz** confirmed the technique to be widely applicable for instant on-site detection of TNP. Detection of TNP in real water and soil samples demonstrated **BTPyz** as a promising detecting tool in environmental specimens**.**

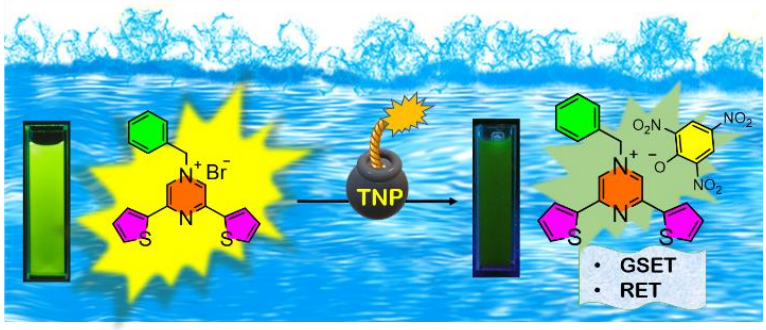

Figure 5.1: BTPyz for the detection of TNP

Section 3B: Benzene-Appended Pyrazinium Salt for Detection of TNP and Sulfite Ions

This chapter discusses the synthesis and investigation of the photophysical property of benzene-appended pyrazinium salt, 1-benzyl-3,5-diphenylpyrazin-1-ium bromide, **BPPyz**. It exhibited a

decrease in the blue fluorescence emission in the presence of TNP as compared to other nitroaromatic compounds. **BPPyz** showed fluorescence quenching and rapid naked-eye detection with a significant color change in the presence of sulfite ions. The selectivity of **BPPyz** towards TNP was ascribed to the GSC formation and RET. The sulfite ion detection involved the formation of a GSC through hydrogen bonding with the pyrazinium proton. Moreover, **BPPyz** was integrated with a smartphone to develop a cost-effective approach for the on-site monitoring of sulfite ions.

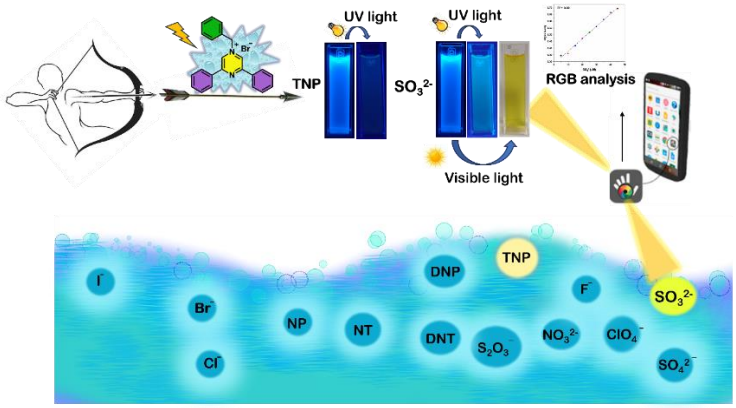

Figure 5.2: BPPyz for the detection of TNP and sulfite ions

Section 3C: Pyrene-Appended Pyrazinium Salt for Detection of TNP and Nitrite Ions

This chapter incorporates the design, synthesis and characterization of pyrene-appended pyrazine salt**,** 1-Methyl-3-(pyren-1-yl)pyrazi-1-ium iodide, **MPyPyz** for detection of TNP and nitrite. **MPyPyz** showed a fluorescence turn-off response for both analytes. The solid-state luminescent property was utilized for the visualization of latent fingerprints.

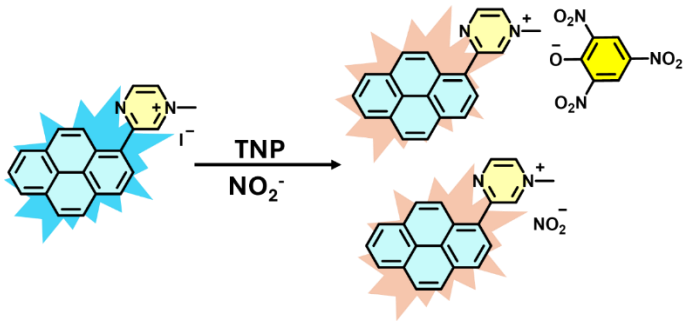

Figure 5.3: MPyPyz for the detection of TNP and nitrite ions

Chapter 4: Pyridinium- and Imidazolium Salts for Fluorometric/Colorimetric Detection of Metal Ions

This chapter of the thesis is divided into two sections:

Chapter 4A: Schiff Base-Appended Pyridinium Salt for Detection of Aluminum(III) Ions

This chapter incorporates the synthesis and application of Schiff base-appended pyridinium salt, (E)-1-(2-(3-hydroxy-4-((pyridine-2-ylimino)methyl)phenoxy)ethyl) pyridinium-1-ium bromide**,** **BzPySB**. It exhibited bright yellow color in the solid state with yellow fluorescence when examined under UV-vis light. In polar protic solvents, **BzPySB** existed in both keto and enol form while in polar aprotic solvents, enol form was predominant. The chemosensor **BzPySB** was utilized as a turn-on chemosensor for aluminum ions with high selectivity and sensitivity elucidated through ^{1}H NMR, Mass spectrometry, and DFT calculations. The fluorescence emission phenomena may be attributed to chelation-enhanced fluorescence (CHEF) due to the restriction of C=N isomerization. The utilization of **BzPySB** was for the detection of aluminum in plant and living cells was investigated by fluorescence microscopy images. The solid-state fluorescence of **BzPySB** was utilized to visualize latent fingerprints on glass surfaces, revealing information about the peculiar individual characteristics of the fingerprints under investigation.

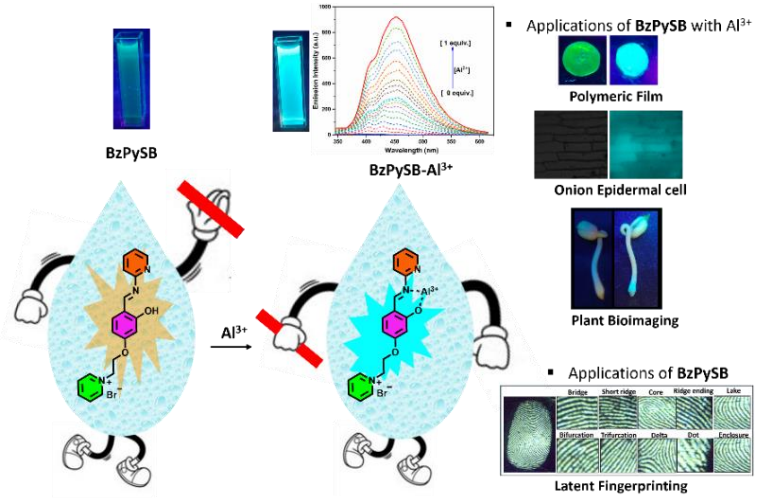

Figure 5.4: BzPySB for the detection of Al^{3+} ions

Chapter 4B: Schiff Base-Appended Imidazolium Salt for Detection of Copper(II) Ions

This chapter discusses the synthesis and application of Schiff base-appended Imidazolium salt as colorimetric chemosensor, 2-((Z)-3-(((E)-2-hydroxybenzylidene) hydrazineylidene)-2-oxoindolin-1-yl)-1-(1-methyl-1H-3l4-imidazol-3-yl)ethan-1-ylium bromide, **IsImSB**. The chemosensor incorporated imidazolium-salt based isatin in conjugation with (E)-2-(hydrazineylidemehyl) phenol, resulting in a selective chemosensor for Cu^{2+}. When applied to the detection of Cu^{2+} ions, the probe prompts a noticeable color change from yellow to red.

Furthermore, investigations revealed that the probe operates ligand-to-metal charge transfer (LMCT) in its interaction with Cu^{2+}, with a binding stoichiometry of 1:1. This was substantiated by Benesi-Hildebrand studies, Job's plot analysis, and density functional theory calculations. The practical real applications extended to a variety of substances, including paper strips, water, solid, and urine samples affirming the versatility and utility of the probe across different sample matrices. A selective, simple, fast, sensitive, quantitative, cost-effective, and eco-friendly approach for naked-eye detection of Cu^{2+} was developed through μPADs.

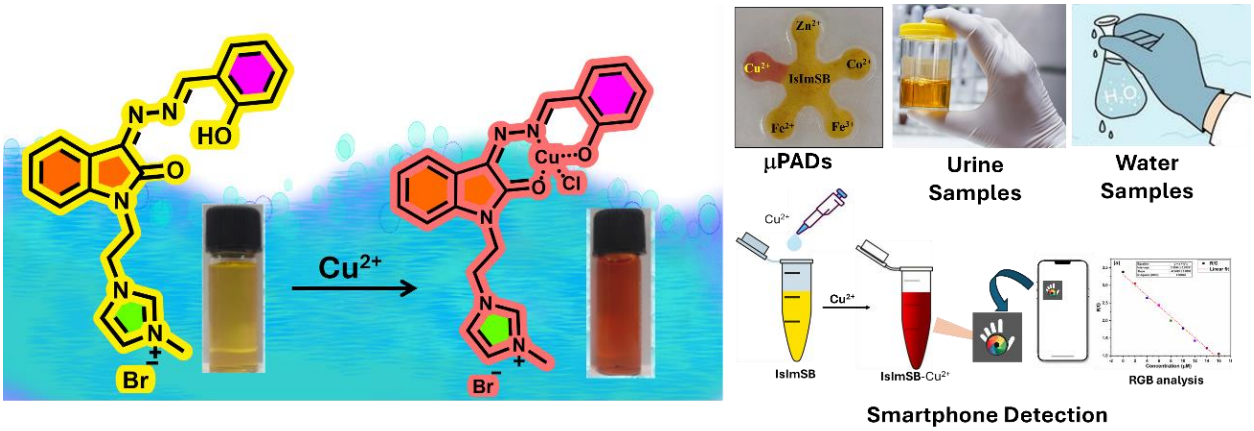

Figure 5.5: IsImSB for the detection of Cu^{2+} ions

5.3 Future scope of the research work

Imidazolium and Pyridinium-salt as chemosensors have gained significant attention due to their properties like water solubility, high stability, tuneable properties, and wide applicability. The imidazolium and pyridinium-salt as chemosensor has been applied for the detection of Al^{3+} and Cu^{2+}. In the future, through the incorporation of different chromophores, these salt-based chemosensors can be applied for the detection of various other analytes. The variation in amine group can yield different Schiff bases of **BzPy** and **IsIm**.

Pyridinium and imidazolium-salt as water-soluble chemosensor have been previously reported for analyte detection, but only a few reports are available for the use of pyrazinium-salt as chemosensors. New chemosensors with various derivatives of pyrazine viz., 2-amino pyrazine, 2,3-diamino pyrazine, pyrazine carbaldehyde/dicarbaldehyde can give chemosensors based on Schiff bases. Pyrazine on coupling reaction with pyrene-1-boronic acid can give various regio isomers having distinct AIE properties. The derivatives of pyrazine can be used for the synthesis of cagelike structures with aryl halides. Therefore, there is a wide scope for the synthesis and

application of pyrazinium-salt as chemosensors in analyte detection. As these chemosensors exhibit high water solubility, therefore, they can be applied for live cell imaging. The solid-state fluorescent properties of the pyrazinium, pyridinium, and imidazolium-salt can be used for investigating micro-level details of fingerprints.

Appendices

Appendix-A

Chapter 3

Section A

Section B

Section C

Chapter 4

Section A

Section B

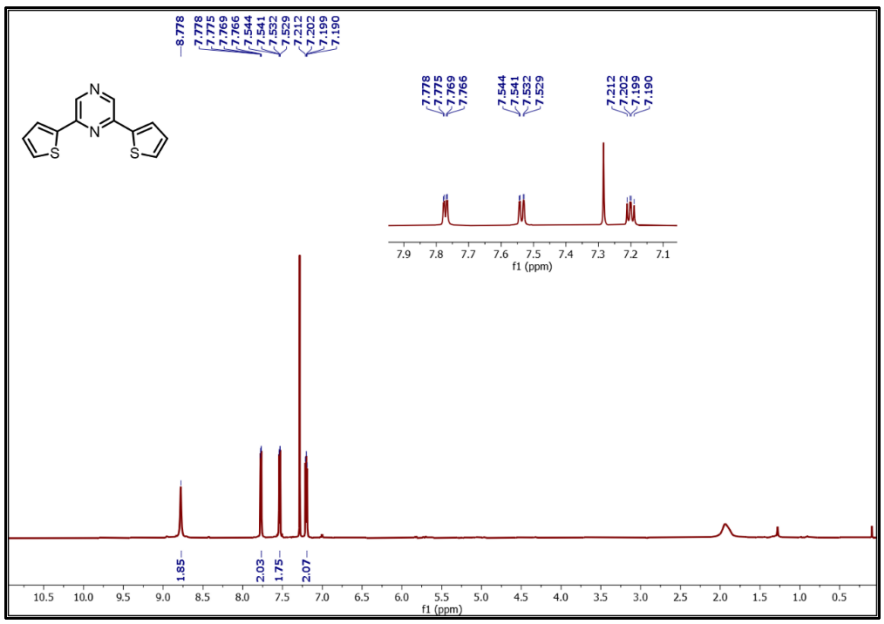

Figure A1: ^{1}H NMR of **TPyz** in $CDCl_3$

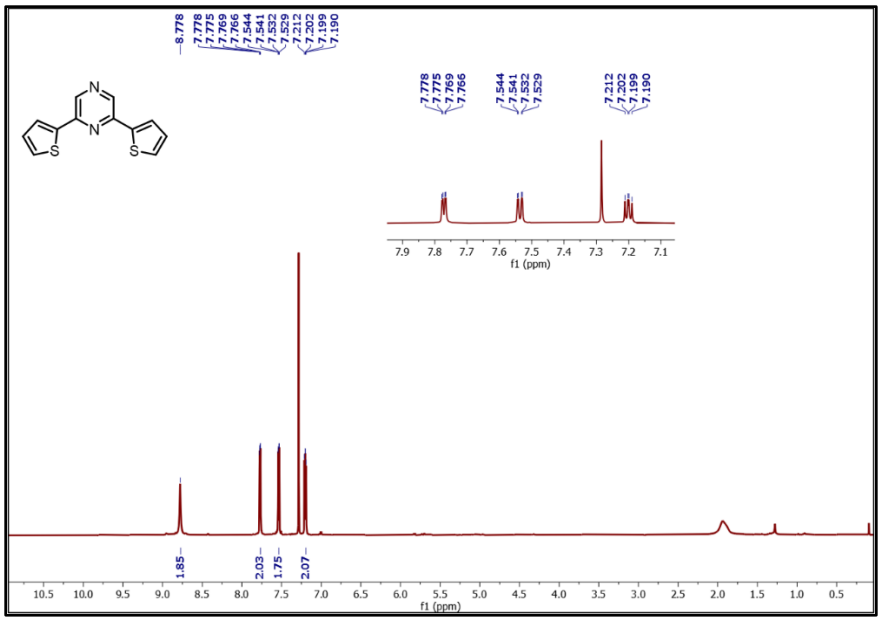

Figure A2: ^{13}C NMR of **Tpyz** in $CDCl_3$

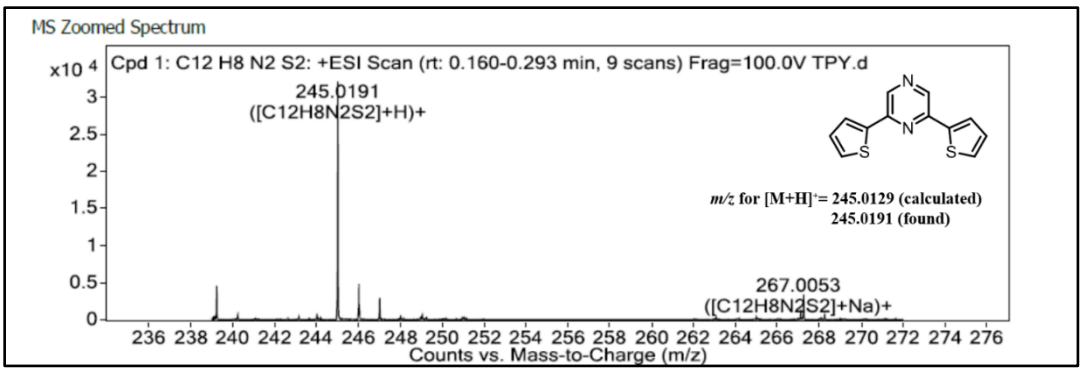

Figure A3: HRMS of **TPyz**

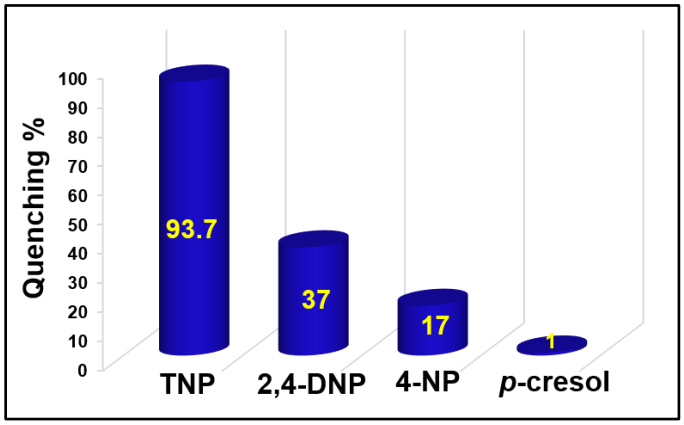

Figure A4: Fluorescence quenching percentage of *p*-cresol, 4-NP, 2,4-DNP and TNP

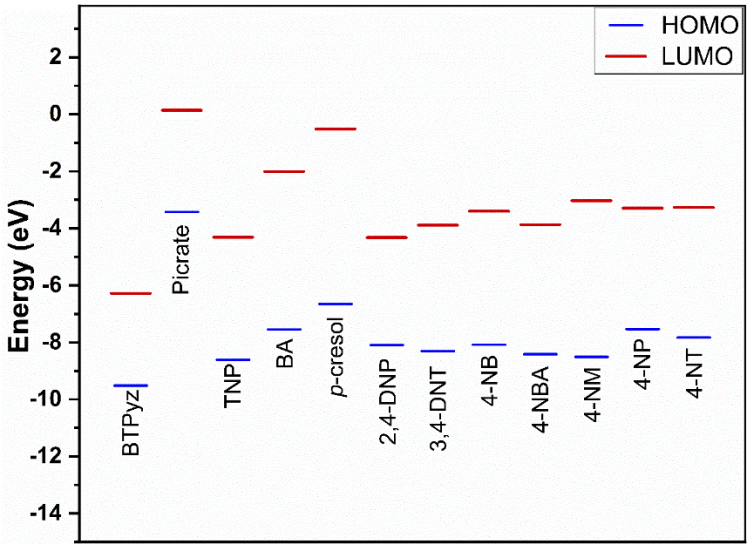

Figure A5: HOMO-LUMO energy levels of **BTPyz** and organic analytes

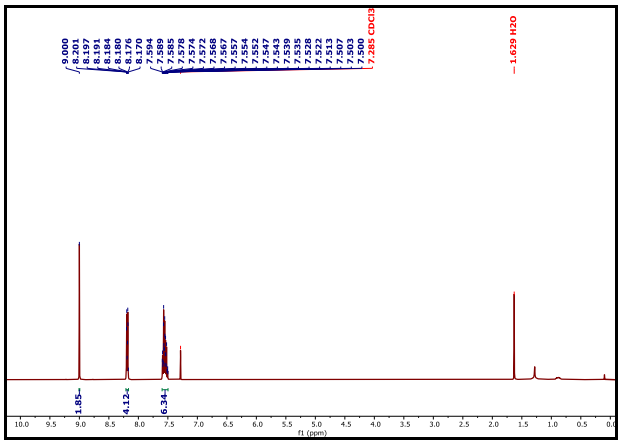

Figure A6: ^{1}H NMR of **PPyz** in $CDCl_3$

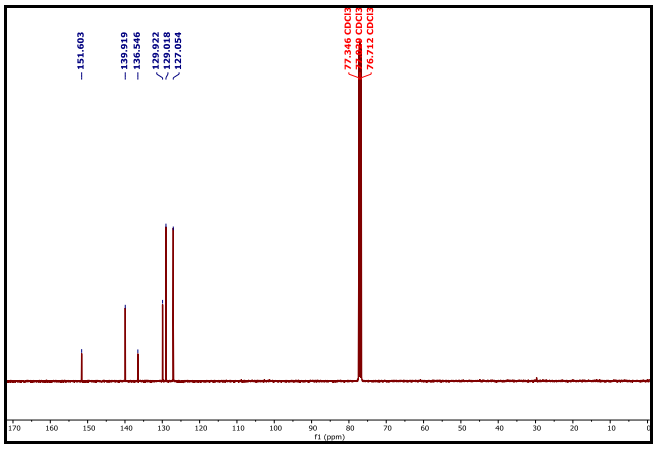

Figure A7: ^{13}C NMR of **PPyz** in $CDCl_3$

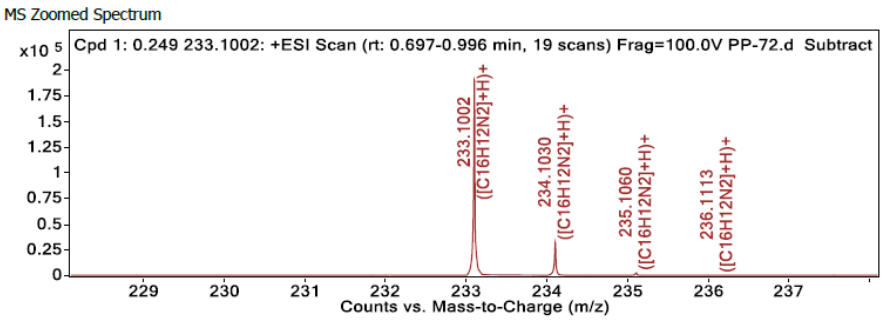

Figure A8: HRMS of **PPyz**

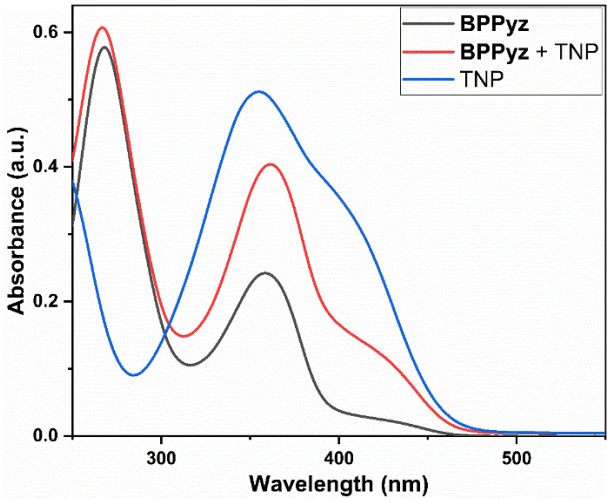

Figure A9: Individual UV-vis spectra of **BPPyz** (2×10^{-5} M), **BPPyz**-TNP and TNP

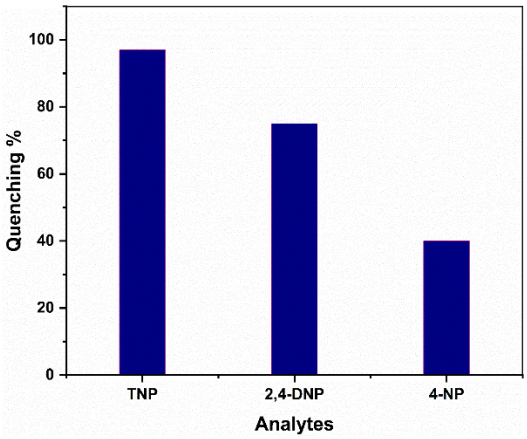

Figure A10: Comparison of percentage fluorescence quenching obtained on addition of TNP, 2,4- DNP and 4-NP to the solution of **BPPyz** in water (2×10^{-5} M)

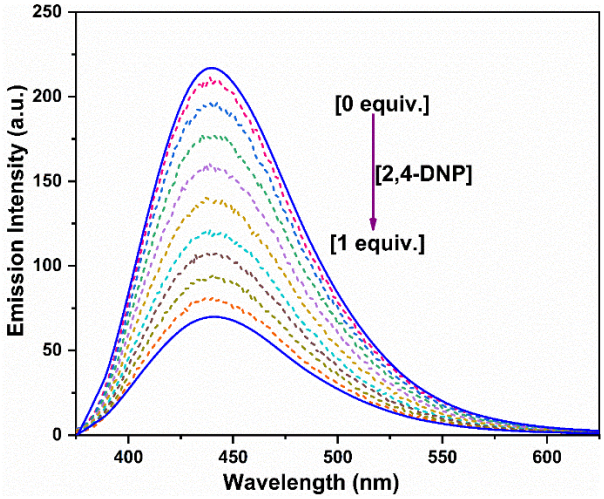

Figure A11: Fluorescence spectra for **BPPyz** (2×10^{-5} M) with different amounts of 2,4-DNP

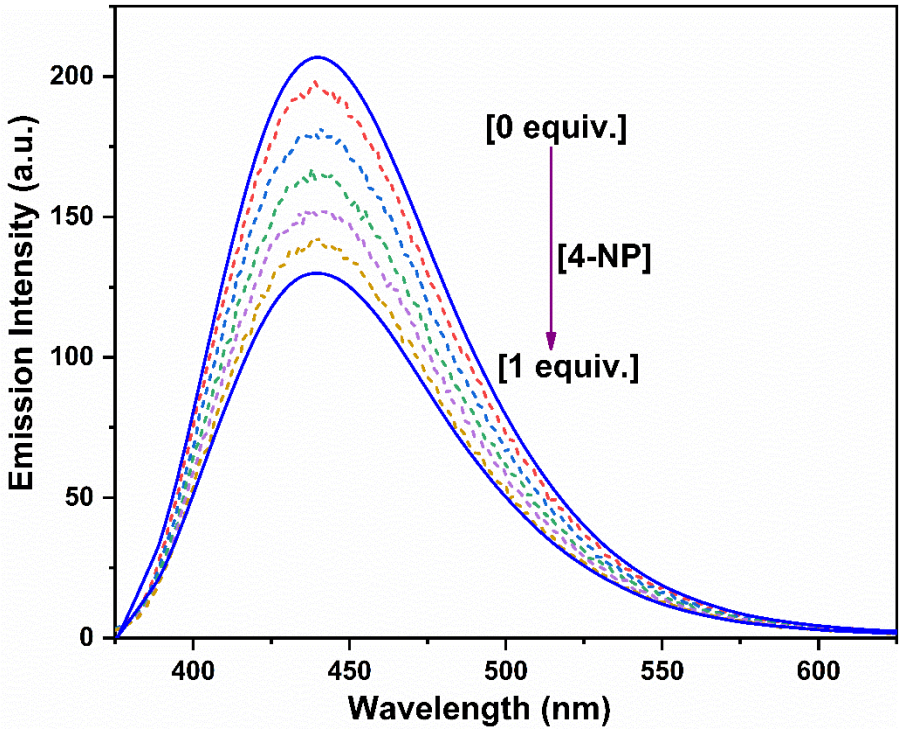

Figure A12: Fluorescence spectra for **BPPyz** (2×10^{-5} M) with different amounts of 4-NP

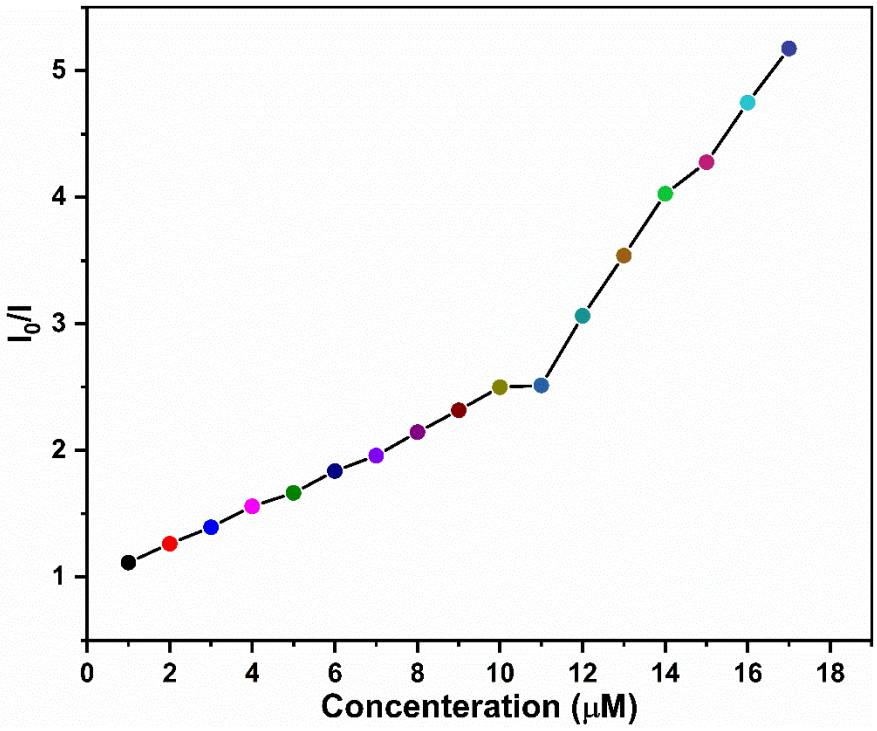

Figure A13: Stern-Volmer plot of **BPPyz** using 2,4-DNP as a quencher (2×10^{-5} M)

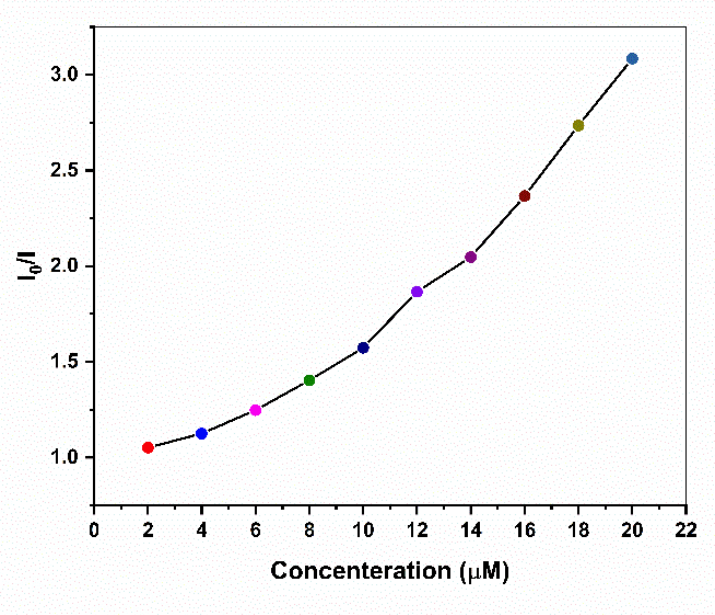

Figure A14: Stern-Volmer plot of **BPPyz** using 4-NP as a quencher (2×10^{-5} M)

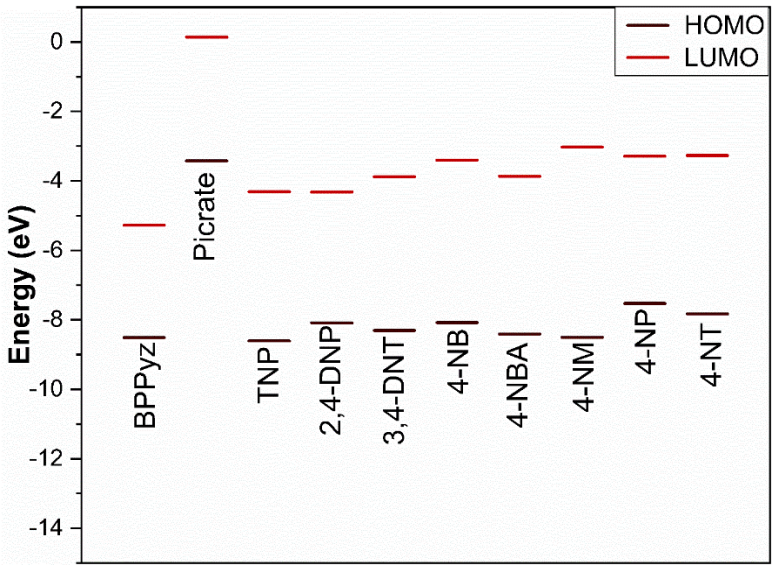

Figure A15: HOMO-LUMO energy levels of **BPPyz** and organic analytes

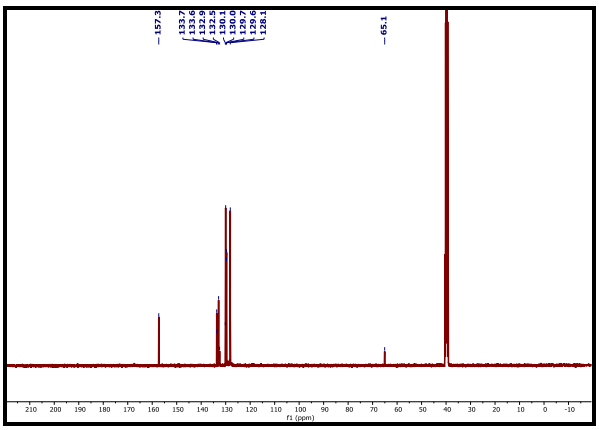

Figure A16: ^{13}C NMR of **BPPyz**-SO_3^{2-} complex in DMSO-d_6

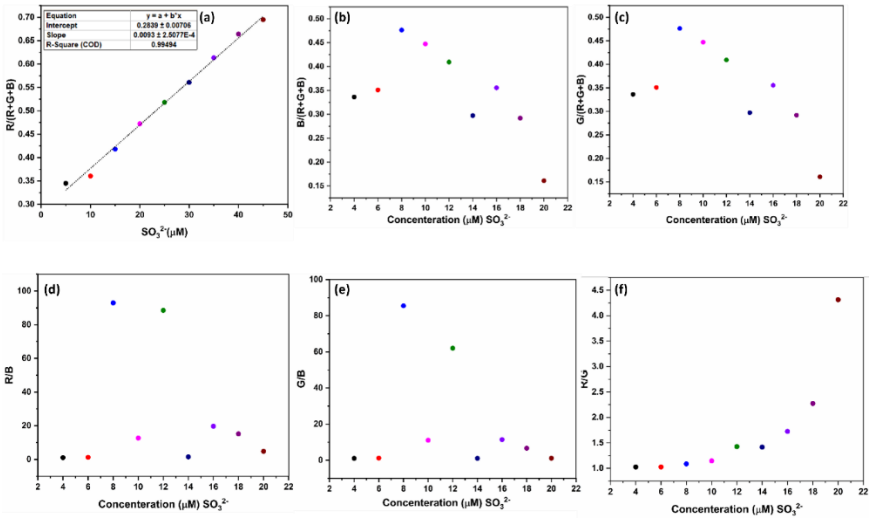

Figure A17: The ratio of RGB (a) R/(R+G+B) (b) G/(R+G+B) (c) B/(R+G+B) (d) R/G (e) R/B (f) G/B versus SO_3^{2-} concentration in the range of 0 to 20.0 µM

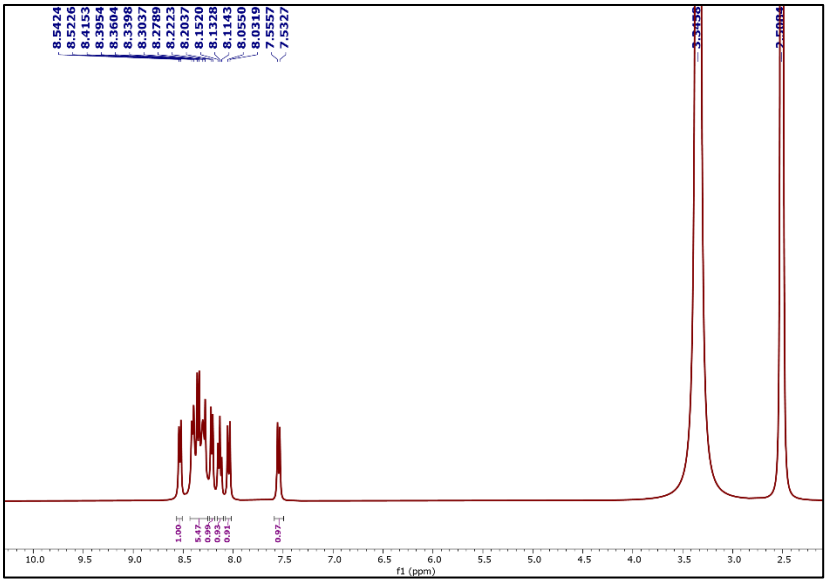

Figure A18: ^{1}H NMR of **PyPyz** in DMSO-d_6

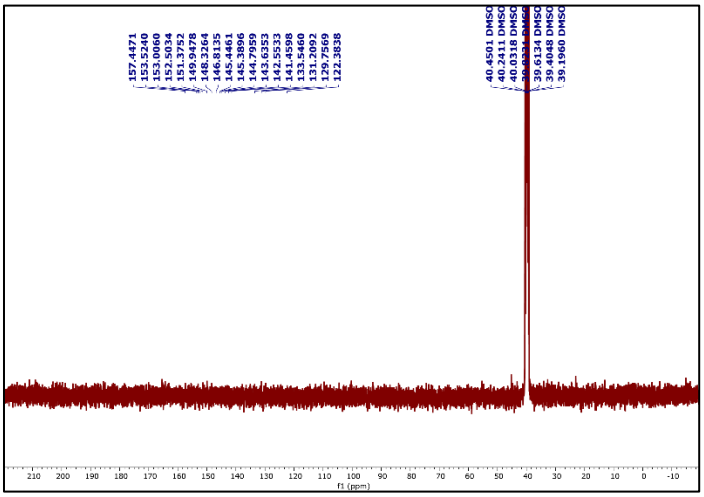

Figure A19: ^{13}C NMR of **PyPyz** in DMSO-d_6

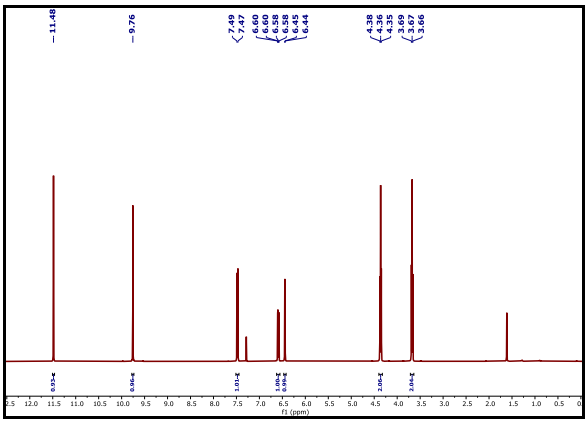

Figure A20: ^{1}H NMR of 4-(2-bromoethoxy)-2-hydroxybenzaldehyde in $CDCl_3$

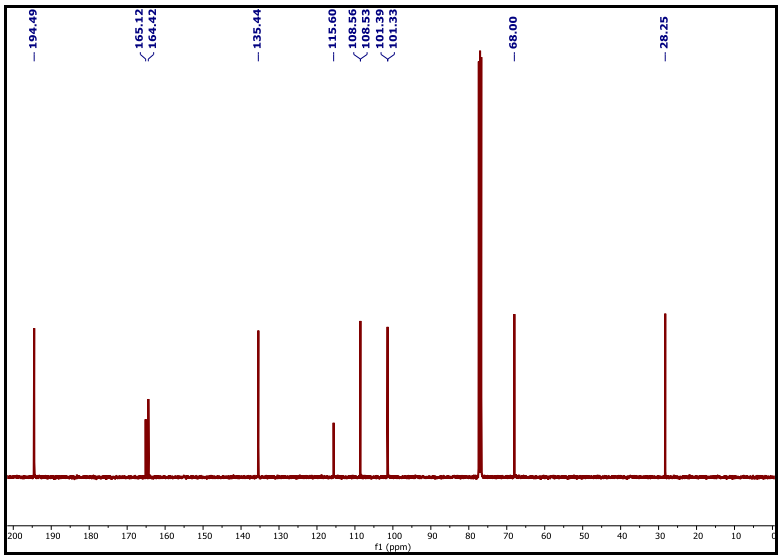

Figure A21: ^{13}C NMR of 4-(2-bromoethoxy)-2-hydroxybenzaldehyde in $CDCl_3$

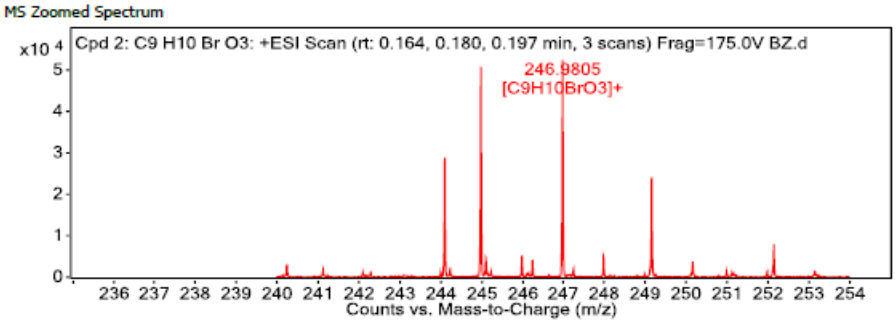

Figure A22: HRMS of 4-(2-bromoethoxy)-2-hydroxybenzaldehyde

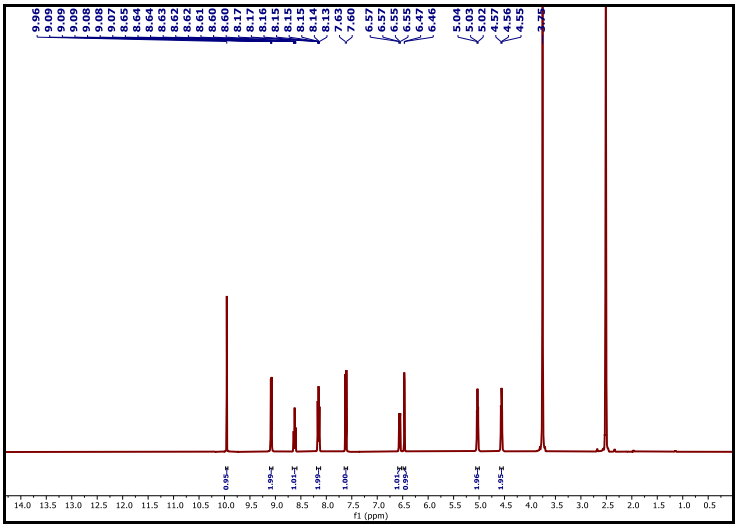

Figure A23: ^{1}H NMR of **BzPy** in $CDCl_3$

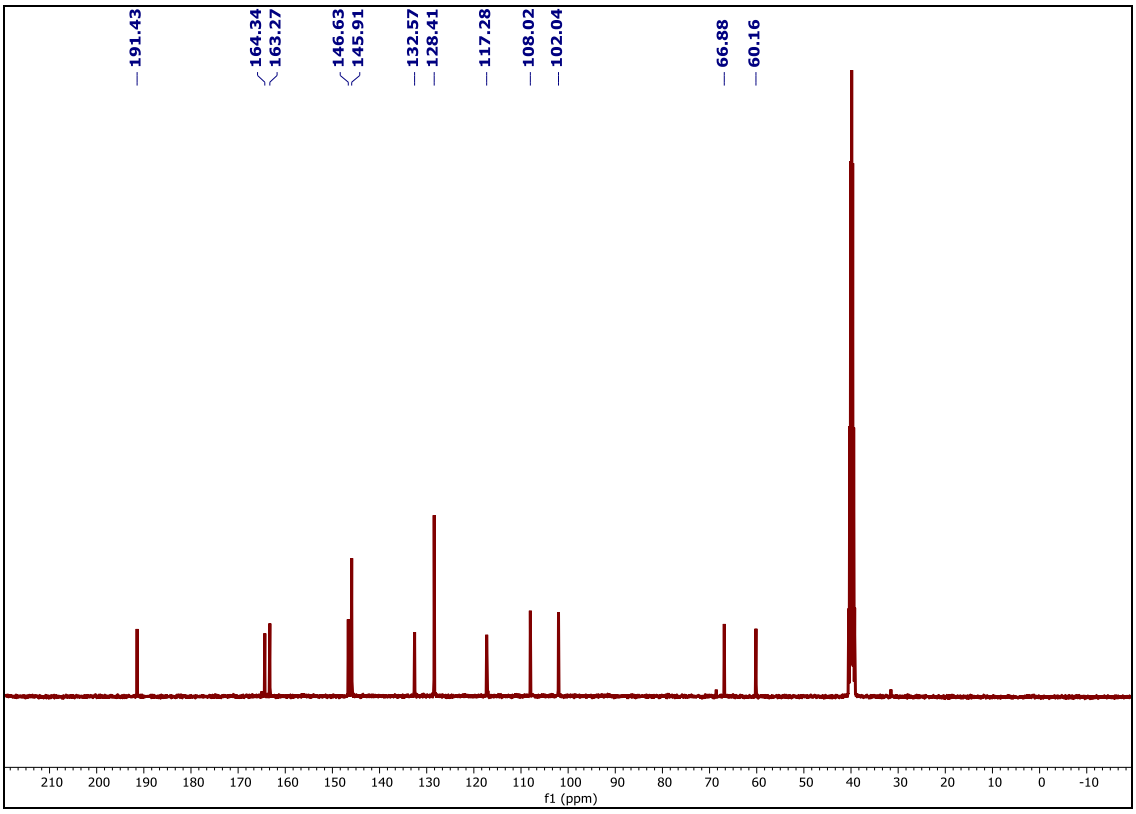

Figure A24: ^{13}C NMR of **BzPy** in $CDCl_3$

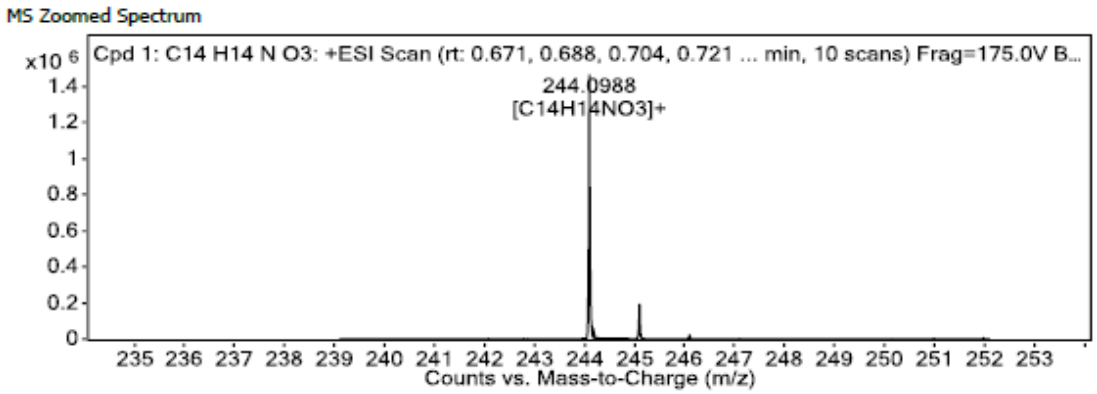

Figure A25: HRMS of **BzPy**

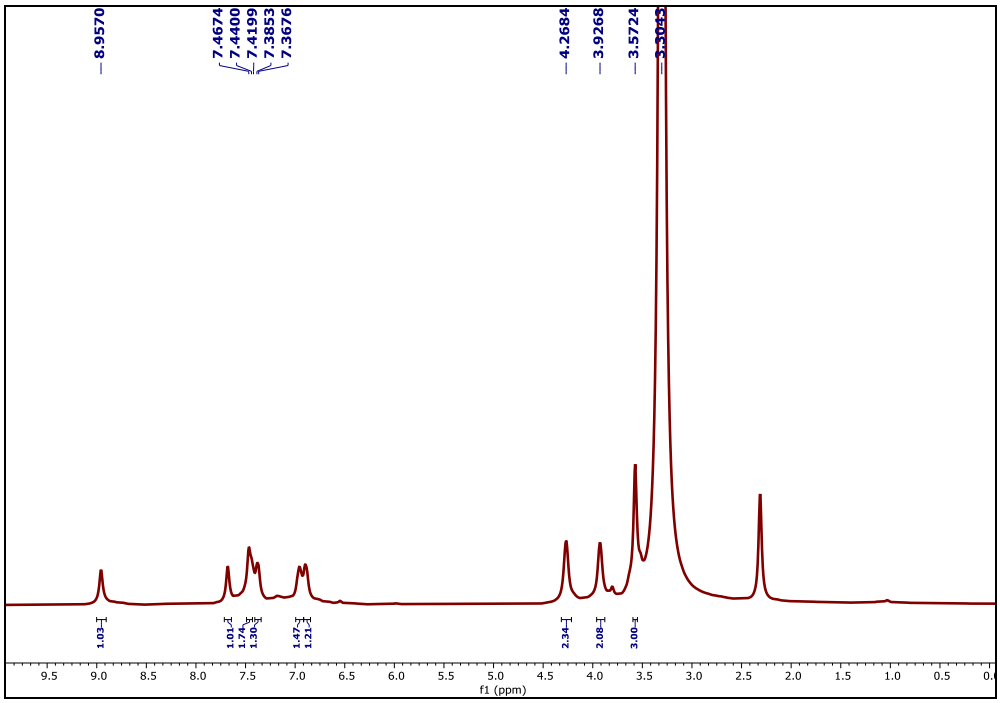

Figure A26: ^{1}H NMR of **IsIm** in DMSO-d_6

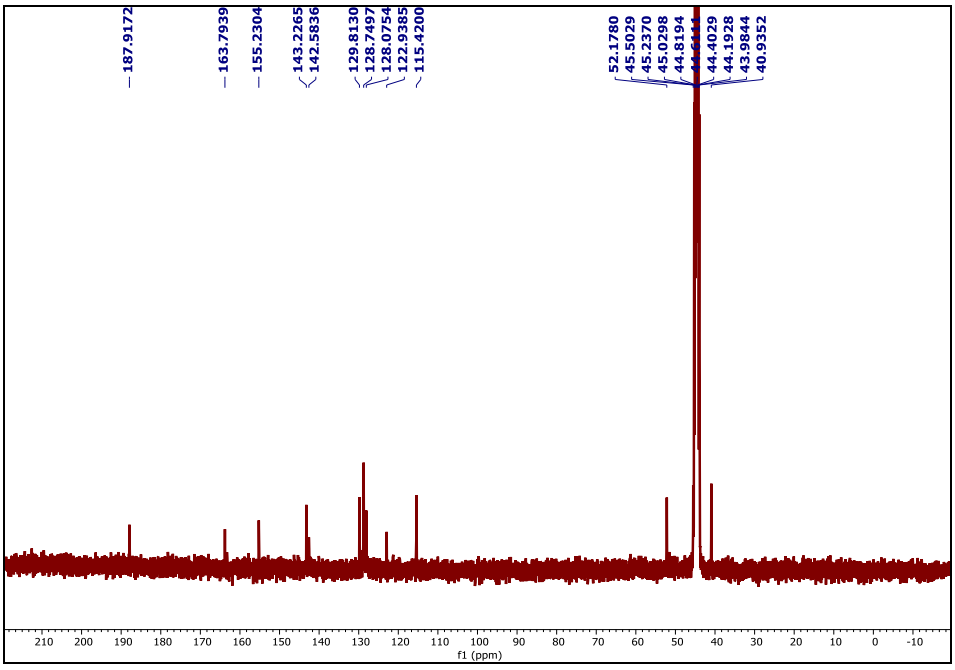

Figure A27: ^{13}C NMR of **IsIm** in DMSO-d_6

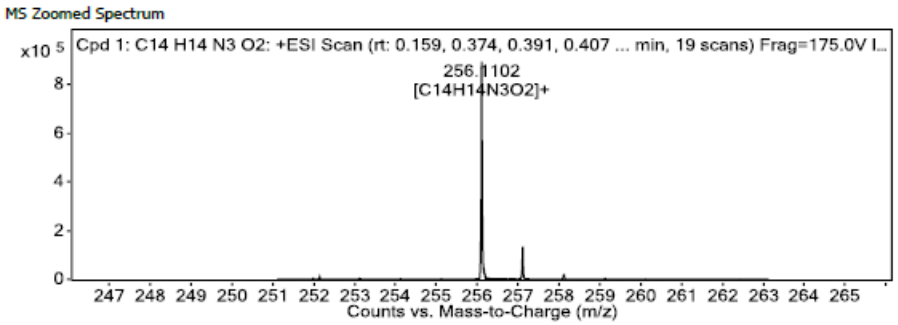

Figure A28: HRMS of **IsIm**

Table A1: Inner filter effect Corrections

TNP[μM]	A_{em}	A_{ex}	I_{obs}	I_{corr}	I_{corr}/I_{obs}	$I_{corr}/I_{obs},0$	E_{obs}	E_{corr}
0	0.000152	0.01867	1080000	1104967	1.021906	0	0	0
5	0.000426	0.02137	1000000	1028167	1.024959	0.93049	7.407407	6.950434
10	0.000211	0.02499	884830	910878.6	1.029439	0.82434	18.0713	17.56509
15	0.00157	0.02871	742340	768675.2	1.035476	0.69565	31.26481	30.43456
20	0.00252	0.03054	608020	631608.4	1.038795	0.57160	43.70185	42.83916
25	0.00395	0.03063	499450	519735.1	1.040615	0.47036	53.75463	52.96374
30	0.00573	0.03168	384120	401025.4	1.044011	0.36292	64.43333	63.70702
35	0.00688	0.03224	293830	307366.2	1.046068	0.27816	72.79352	72.18322
40	0.00755	0.03474	225310	236551.4	1.049893	0.21407	79.13796	78.59199
45	0.00786	0.03685	169340	178284.9	1.052822	0.16134	84.32037	83.86514
50	0.00761	0.0395	128660	135830.9	1.055735	0.12292	88.08704	87.70724

Table A2: Single-crystal XRD data and structure refinement of **BTPyz** and **BTPyz**-TNP complex

Compound	**BTPyz**	**BTPyz**-TNP complex
Empirical formula	$C_{19.5}H_{17}BrN_2O_{0.5}S_2$	$C_{25}H_{17}N_5O_7S_2$
Formula weight	431.38	563.55
Temperature/K	293(2)	93(2)
Crystal system	Monoclinic	monoclinic
Space group	$P2_1/n$	C2/c
a/Å	13.6130(2)	18.0779(3)
b/Å	18.6032(2)	20.0433(3)
c/Å	15.0166(2)	14.3377(3)
α/°	90	90
β/°	90.2640(10)	111.423(2)
γ/°	90	90
Volume/Å^3	3802.84(9)	4836.20(16)
Z	8	8
ρ_{calc}g/cm^3	1.507	1.548
μ/mm^{-1}	5.049	2.513
F(000)	1752.0	2320.0
Crystal size/mm^3	0.1 × 0.1 × 0.08	0.15 × 0.1 × 0.04
Radiation	Cu Kα (λ = 1.54184)	Cu Kα (λ = 1.54184)
2Θ range for data collection/°	7.566 to 159.874	8.094 to 159.676
Index ranges	$-14 \le h \le 17$, $-23 \le k \le 22$, $-16 \le l \le 19$	$-21 \le h \le 23$, $-25 \le k \le 24$, $-17 \le l \le 18$
Reflections collected	15315	14206
Independent reflections	7340 [R_{int} = 0.0249, R_{sigma} = 0.0296]	5121 [R_{int} = 0.0327, R_{sigma} = 0.0347]
Data/restraints/parameters	7340/0/453	5121/0/352
Goodness-of-fit on F^2	1.104	1.093
Final R indexes [I>=2σ (I)]	R_1 = 0.0487, wR_2 = 0.1321	R_1 = 0.0473, wR_2 = 0.1418

Final R indexes [all data]	R_1 = 0.0504, wR_2 = 0.1333	R_1 = 0.0504, wR_2 = 0.1451
Largest diff. peak/hole / e Å^{-3}	1.48/-0.93	0.44/-0.34
CCDC No.	2110747	2168277

Table A3: Single-crystal XRD data and structure refinement of **BPPyz** and **BPPyz-TNP** complex

Identification code	**BPPyz**	**BPPyz-TNP**
Empirical formula	$C_{23}H_{19}BrN_2$	$C_{29}H_{21}N_5O_7$
Formula weight	403.31	551.51
Temperature/K	93(2)	93(2)
Crystal system	monoclinic	monoclinic
Space group	$P2_1/c$	C2/c
a/Å	23.0173(3)	17.3755(2)
b/Å	10.11520(10)	19.6061(2)
c/Å	26.4430(3)	15.0107(2)
α/°	90	90
β/°	113.4840(10)	103.3710(10)
γ/°	90	90
Volume/Å^3	5646.64(12)	4975.02(10)
Z	12	8
ρ_{calc}g/cm^3	1.423	1.473
μ/mm^{-1}	3.023	0.903
F(000)	2472.0	2288.0
Crystal size/mm^3	0.13 × 0.08 × 0.05	0.14 × 0.12 × 0.1
Radiation	Cu Kα (λ = 1.54184)	Cu Kα (λ = 1.54184)
2Θ range for data collection/°	8.376 to 159.512	6.904 to 159.878
Index ranges	-28 ≤ h ≤ 29, -12 ≤ k ≤ 6, -28 ≤ l ≤ 33	-11 ≤ h ≤ 21, -24 ≤ k ≤ 24, -18 ≤ l ≤ 19
Reflections collected	35513	15324

Independent reflections	12044 [R_{int} = 0.0318, R_{sigma} = 0.0322]	5281 [R_{int} = 0.0248, R_{sigma} = 0.0244]
Data/restraints/parameters	12044/0/703	5281/0/371
Goodness-of-fit on F^2	1.076	1.058
Final R indexes [I>=2σ (I)]	R_1 = 0.0361, wR_2 = 0.0999	R_1 = 0.0557, wR_2 = 0.1389
Final R indexes [all data]	R_1 = 0.0383, wR_2 = 0.1014	R_1 = 0.0592, wR_2 = 0.1412
Largest diff.peak/hole / e $Å^{-3}$	0.72/-0.71	0.70/-0.72
CCDC	2189176	2189177

Table A4: Single-crystal data and structure refinement for **BzPySB**

Identification code	**BzPySB**
Empirical formula	$C_{19}H_{20}BrN_3O_3$
Formula weight	418.29
Temperature/K	133(2)
Crystal system	triclinic
Space group	P-1
a/Å	7.5119(8)
b/Å	7.5970(7)
c/Å	16.9739(5)
α/°	92.436(5)
β/°	97.446(6)
γ/°	109.972(9)
Volume/$Å^3$	898.81(14)
Z	2
ρ_{calc}g/cm^3	1.546
μ/mm^{-1}	3.327
F(000)	428.0
Crystal size/mm^3	0.14 × 0.04 × 0.03
Radiation	Cu Kα (λ = 1.54184)
2Θ range for data collection/°	10.558 to 158.106
Index ranges	-9 ≤ h ≤ 9, -6 ≤ k ≤ 9, -21 ≤ l ≤ 21
Reflections collected	6808
Independent reflections	3551 [R_{int} = 0.0963, R_{sigma} = 0.0902]
Data/restraints/parameters	3551/0/234
Goodness-of-fit on F^2	1.146

Final R indexes [I>=2σ (I)]	R_1 = 0.0687, wR_2 = 0.1779
Final R indexes [all data]	R_1 = 0.0994, wR_2 = 0.2420
Largest diff. peak/hole / e $Å^{-3}$	1.54/-1.38

Table A5: A comparison of literature reported Chemosensors for TNP detection

S. No.	**Publication**	**Material used**	**Detection Limit**	**Stern-Volmer constant**	**Medium used**
1	**BTPyz**	Pyrazinium-based	11.6 nM	3.8×10^4 M^{-1}	Aqueous
2	*Ind. Eng. Chem. Res.*, 2021, **60**, 7987–7997.	Triazine derivative	209 nM	1.02 mM	Aqueous
3	*CrystEngComm*, 2019, **21**, 6252–6260.	Organic framework	13.08 ppb	4.56×10^5 M^{-1}	Aqueous
4	*New J. Chem.*, 2017, **41**, 8739–8747.	Pyridinium-based	10^{-13} M	6.73×10^8 M^{-1}	Aqueous
5	*ACS Omega*, 2017, **2**, 4424–4430.	Pyridinium-based	295 nM	–	HEPES Buffer (pH-7)
6	*Sens. Actuators B Chem.*, 2016, **229**, 599–608.	Imidazolium-based	107 nM and 87 nM	5×10^4 M^{-1} and 2.2×10^4 M^{-1}	Aqueous

Table A6: A comparison of literature reported Chemosensors for TNP detection

S.No.	Publication	Material used	Detection Limit	Stern-Volmer constant	Medium used
1	**BPPyz**	Pyrazinium-based	9 nM	$4.12 \times 10^5\ M^{-1}$	water
2	*Analytica Chimica Acta*, 2017, **965**, 111e122.	Schiff base	500 nM	$4.4 \times 105\ M^{-1}$	HEPES buffer
3	*Journal of Photochemistry & Photobiology, A: Chemistry*, **428** ,2022, 113865.	Fluorenone	0.5 nm	$5.17 \times 10^7\ M^{-1}$	H_2O/THF
4	*Anal. Chim. Acta*, 2013, **793**, 99–106	Hexaphenylbenzene derivative	6.87 ppb	$1.92 \times 10^5\ M^{-1}$	Aqueous medium
5	*Dalton Trans*., 2021, **50**, 3816–3824.	Acylamide-based	61.5 ppb	$2.4 \times 10^4\ M^{-1}$	H_2O
6	*ACS Appl. Mater. Interfaces*, 2015, **7**, 10491–10500	Benzimidazolium-based	5×10^{-13} M	$4.8 \times 10^5\ M^{-1}$	H_2O: DMSO
7	*Journal of Molecular Structure*, **2023,** 1289, 135886.	MOF	$3.91 \times 10^4\ M^{-1}$	$3.8 \times 10^4\ M^{-1}$	H_2O

Table A7: A comparison of literature reported Chemosensors for SO_3^{2-} detection

S. No	Publication	Material used	Detection Limit	S-V constant	Medium used	Colorimetric/ Fluorometric
1	**BPPyz**	Pyrazinium-based	31 nM	$3.8 \times 10^5\ M^{-1}$	Aqueous medium	Colorimetric and fluorometric
2	*New J. Chem.*, 2017, **41**, 10096	Pyrazoline-based	7.56 mM, 4.87 mM	−	HEPES / DMF	Colorimetric and fluorometric
3	*RSC Adv.*, 2015, **5**, 91863	BODIPy - based	6.4 μM	−	Aqueous	Colorimetric and fluorometric
4	*Sens. Actuators B Chem.*, 2016, **231**, 752–758	Naphthofluorescein-based	1.74 M	−	DMSO/ PBS buffer	Colorimetric and fluorometric
5	*Org. Biomol. Chem*., 2014, **12**, 4637.	Coumarin-quinolinium based	8.9×10^{-8} M	−	PBS buffer	Colorimetric and fluorometric
6	*J. Agric. Food Chem*. 2011, **59**, 11935–11939.	Boron-dipyrromethene-based	5.8×10^{-5} M	−	H_2O/ DMSO	Colorimetric and fluorometric
7	*Chem. Commun*, 2020, **56**, 10549.	Fluorescein based	2.98 mM	−	CH_3CN / PBS buffer	Fluorometric

Table A8: A comparison of literature reported Chemosensors for TNP detection

S.No.	**Publication**	**Material used**	**Detection Limit**	**Stern-Volmer constant**	**Medium used**
1	**MPyPyz**	Pyrazinium-based	05 nM	$4.12 \times 10^5\ M^{-1}$	water
3	*Journal of Solid-State Chemistry*,2020, **290**, 121561.	AIE MOF	0.326 μM	$1.8 \times 10^5\ M^{-1}$	H_2O
4	*ACS Omega*, 2018, **3**, 10306−10316	Dabsyl based	7.2×10^{-6} M	$1.4 \times 10^4\ M^{-1}$	H_2O/ACN
5	*Spectrochimica Acta Part A: Molecular and Biomolecular Spectroscopy*, 2023, **285,** 121867.	Imidazole-based	7.2×10^{-8} M	$2.70 \times 10^5\ M^{-1}$	DMSO/ water
6	*Journal of Photochemistry & Photobiology, A: Chemistry*, **434** (2023) 114224	Dansyl-based	4.3 μM	$2.17 \times 10^4\ M^{-1}$	ACN
7	*Journal of Molecular Structure*, 2023, **1289,** 135886.	Phenothiazine	0.2 ppb	$4.05 \times 10\ M^{-1}$	DMF/H_2O

Table A9: A comparison of literature reported Chemosensors for NO_2^- detection

S. No	Publication	Material used	Detection Limit	Medium used
1	**MPyPyz**	Pyrazinium-based	12 nM	Aqueous medium
2	*Chem. Commun.*, 2019, **55**, 9947-9950.	Anthracene carboxyimide-based	84 nM	EtOH/HCl
3	*Talanta*, **2021**, **221**, 121477.	Aniline - based	60.63 nM	HCl-ACN
4	*Adv. Sci.*, 2020, *7*, 2002991.	Benzothiazole	2.2 fg	DMSO-PBS buffer
5	*Talanta*, 2016 **152**, 155–161.	Coumarin-quinolinium based	4.3×10^8 M	HCl/H_2O
6	*Food Chemistry*, 2021, **341,** 12825.	Aminophenyl	6.7 nM	PBS Buffer
7	*Anal. Chem.*, 2015, **87**, 1274−1280.	Diaminonaphthale	2.6 nM	HCl/H_2O

Table A10: A comparison of literature reported Chemosensors for detection of Al^{3+}

S.No	Publication	Material used	Detection Limit of Al^{3+}	Medium used	Bio imaging
1	**BzPySB**	Pyridinium	0.024 nM	Water	Yes
2	*ChemistrySelect*, 2023, ***8***, e202301023.	Benzoxazole based	13 nM	Water-DMSO mixture	No
3	*Dalton Trans*., 2018, **47**, 15907.	Schiff base	11.34×10^{-9} M	HEPES buffer	Yes
4	*J. Lumin., 2020*, **219**, 116908.	Cu(I)-MOF based	2.1×10^{-6} M	MeOH	No
5	*J. Photochem. Photobiol. A Chem.*, 2022, **433,** 114168.	Coumarin based	0.638 μM	Water-DMF	Yes
6	*ACS Omega*, 2019, **4,** 18520−18529.	Hydrazone based	2.53 nM	DMSO:HEPES	No
7	*Photochem. Photobiol. Sci*., 2019, **18**, 2717.	Antipyrine based	30 nM	MeOH	No

Table A11: A comparison of literature reported Chemosensors for Cu^{2+} detection

S. No	Publication	Material used	Detection Limit	Medium used
1	**IsImSB**	Imidazolium-based	10 nM	Aqueous medium
2	*Dalton Trans.*, 2015, **44**, 9120–9129.	Pyridine based	31.5 μM	Bis–tris buffer
3	*Inorganica Chimica Acta*, 2016, **450**, 131–139.	Terephthalic acid	0.25 M	DMSO
4	*Inorganica Chimica Acta*, 2020, **508**, 119633.	Thiosemicarbazide	1.7 μM	Methanol–water
5	*Journal of Photochemistry and Photobiology A: Chemistry*, 2017, **332,** 505–514.	Naphthalene quinoline	1.31×10^{-5} M	CH_3OH/aqueous HEPES buffer
6	*ChemistrySelect* 2020, ***5***, 9435 – 9442.	Quinoline based	15.3 ppb	MeOH
7	*Talanta,* 2020, ***219***, 121237.	Quinoline-indolin-2-one based	27.25×10^{-6} M	DMSO/H_2O

B-1 List of Publications

1. **Pragya,** Vaishali Saini, Krishnan Rangan and Bharti Khungar, "A pyrazinium-based fluorescent chemosensor for the selective detection of 2, 4, 6-trinitrophenol in an aqueous medium " *New J. Chem.*, **2022**, *46*(35), 16907-16913.
2. **Pragya,** Krishnan Rangan and Bharti Khungar, "Detection of TNP and sulfite ions in an aqueous medium using a pyrazinium-based chemosensor " *Sens. Diagn.*, **2024**, *3*(5), 872-882.
3. Vaishali Saini, Vimal Kumar Madduluri, **Pragya,** Krishnan Rangan and Bharti Khungar, "Abnormal NHC/CNN Pincer Palladium(II) Complex: Synthesis, Characterization and Application in Microwave-assisted Suzuki-Miyaura Coupling of Aryl Chlorides in Water" *Asian J. Org. Chem.*, **2023**, *12*(6), e202300072.
4. **Pragya** and Bharti Khungar, Pyridinium-based chemosensor for detection of Al^{3+} and its various application. (Manuscript Communicated- asia.202401158)
5. **Pragya** and Bharti Khungar, An imidazolium based colorimetric sensor for detection of Cu^{2+} in aqueous media: practical performance of Cu^{2+}. (Manuscript under preperation)
6. **Pragya**, Nitika and Bharti Khungar, An AIE-based pyrazinium salt for detection of TNP and Nitrite. (Manuscript under preparation)

Appendix B

B-2 List of conferences and workshops attended

Oral Presentations

1. Pragya, B. Khungar. "Pyrazinium and Imidazolium based Fluorescent Chemosensor for Analyte detection in Aqueous Medium" at **ICLMFA-LOCI** (GNDU, Amritsar) Mar 14-16, 2024. (**Best RSC Oral Presentation**)

Poster Presentations

1. Pragya, B. Khungar. "Pyrazinium-based Fluorescent Chemosensor for Selective Detection of TNP" held at **ISCB-22 international Conference**, BIT Mesra Ranchi, Nov 17-19, 2022.
2. Pragya, B. Khungar. "Pyrazinium-based Fluorescent Chemosensor for Selective Detection of TNP and Sulfite" held at **FCASI-23** international conference University of Rajasthan, 20-21 April, 2023.
3. Pragya, B. Khungar. "Pyrazinium-based Fluorescent Chemosensor for Selective Detection of Analytes" held at (**CRSI-NSC-32**) BITS Pilani, Pilani Campus, Feb 4-6, 2024.
4. Pragya, B. Khungar. "Fluorescent chemosensor for selective recognition of Picric acid in aqueous medium." One-day **MINI-SYMPOSIUM**, Department of Chemistry, BITS Pilani, Pilani (Rajasthan), India 28th February 2022
5. Pragya, B. Khungar. "Pyridinium-based Chemosensor for Relay detection of Al^{3+} and TNP " held at **MTIC-2023** (IISc, Bangalore) 16-18 Dec, 2023.

Workshops Attended

1. International Workshop on "**Supporting Chemistry Research with modern DFT (Density Functional Theory): Software, Techniques, and Applications**."

2. Workshop on **INUP Basic Training Program in Nano Science and Technology** held from 13th to 15th March 2023 at Centre for Nano Science and Engineering (CeNSE), Bangalore.

3. DST-STUTI Workshop organized on "**Analytical Advances in studing Molecules**" by the Department of Chemistry from October 15-21, 2022.

4. Workshop on "**Confocal and Fluorescence Microscope**" on April 12-13, 2024 held at Dept. of Biological Sciences, BITS Pilani, Pilani Campus.

Appendix C

C-1 Brief Biography of candidate

Pragya was born in Khetri, Rajasthan and her native place is Bihar. She obtained her B.Sc. Degree (Biology, Chemistry and Mathematics) from Patna Women's College. She obtained her M.Sc. degree (Organic Chemistry) from Patna University. She has joined BITS as research scholar in 2019 under the guidance of Dr. Bharti Khungar. During the tenure of Ph.D. programme, she was actively involved in the synthesis of pyrazinium, imidazolium- and pyridinium-based compounds for chemosensing for selective detection of toxic metal ions and explosive nitroaromatics. To the date she has published three research paper in the peer-reviewed international journals and presented research works in various national and international conferences in form of poster. Her research interest lies in the development of new chemosensors based on azinium and azolium salts to perform fluorometric/colorimetric applications in pure aqueous medium.

C-2 Brief Biography of Supervisor

Dr. Bharti Khungar is a Professor at the Department of Chemistry, BITS Pilani, Pilani Campus. She carried out her doctoral research in Chemistry from the Department of Chemistry, University of Rajasthan, Jaipur and obtained the Ph.D. degree in 2002. After this, she worked as a Lecturer in the Department of Chemistry, Laxmi Devi Institute of Engineering and Technology, Alwar, Rajasthan till 2005. Before joining BITS, she worked at the post of Senior Lecturer at Banasthali University, Rajasthan for two years.

Her research interests lie in the area of material science to develop pyrazinium, imidazolium-and pyridinium-based compounds for chemosensory applications in pure aqueous medium. Another recent area of her interest is green chemistry with a special focus on the synthesis of transition metal complexes as catalysts for carrying out simple organic transformation and screening their biological applications in water. She is the author of more than twenty-five publications in international journals of repute and has participated in more than thirty national and international conferences. She is the recipient of the Summer Research Fellowship for Teachers from Academies' of Science, India 2013 and 2014 and executed research work at Bhabha Atomic Research Centre, Mumbai. She was selected for the University Immersion Abroad Scheme of BITS Pilani, 2016 and worked at Chapman University, Irvine, California, USA. She has successfully executed three sponsored projects funded by DST, SERB and UGC, India. Prof. Khungar has supervised three PhD students and currently four students are pursuing PhD under her supervision.